Bielefeld University

Faculty of Physics, Bielefeld University

PhD. Thesis

on the subject:

Energy loss and equilibration of a highly energetic parton in QCD plasmas

Author

Ismail Soudi

Submitted in partial fulfillment of the requirements
for the degree of Doctor of Natural Sciences

1. Supervisor & Examiner	Jun-Prof. Dr. Sören Schlichting
2. Examiner	Prof. Dr. Nicolas Borghini

Bielefeld, 08, 2021

Abstract

While a hard parton (gluon or quark) traverses the medium, it loses its energy as a result of interactions with the medium. In this thesis, we describe the full in-medium kinetic and chemical equilibration of hard particles, using a linearized effective kinetic description of QCD at leading order. Since we include $2 \leftrightarrow 2$ elastic processes, collinear radiation, and the back-reaction of the jet constituents onto the medium, we are able to follow the energy from the hard scales $\sim E$ all the way to the medium scales $\sim T$.

In the first analysis, we consider the energy evolution only in the longitudinal direction and describe the elastic processes using the small angle approximation. After a direct energy deposition into the medium scales due to elastic and radiative interactions at early times, we find that the energy loss is mainly driven by successive splittings, which lead to an energy cascade from the hard sector to the medium scale akin to weak wave turbulence. The turbulent cascade is characterized by a stationary solution known as the Kolmogorov-Zakharov spectrum, which is recovered at intermediate energy scales. This Kolmogorov-Zakharov spectrum leads to a scale invariant energy flux that we investigate in detail.

In the second analysis, we consider the evolution of the distribution in the longitudinal direction as well as in the polar angle with respect to the initial parton, which allows us to study the angular structure of the cascade. In order to account for large angle elastic scatterings, we extend the framework by using the full matrix element in Hard Thermal Loop approximation. Similarly to the first analysis, the energy loss is dominated by collinear radiation, which transport energy to the soft scales. However, the radiation does not transport energy to large angles, rather, the soft energy equilibrates due to elastic scatterings, which starts already at early times, and leads to the deposition of energy at large angles.

Recent studies, using the dimensionally reduced theory of QCD on a lattice (EQCD) valid at high temperature, have obtained non-perturbative contributions to the collisional broadening kernel [1, 2]. The last part of this work is dedicated to computing the medium splitting rates using these results. First, since EQCD is an infrared effective theory of QCD, we employ a matching to supply the correct ultraviolet behavior to the computed kernel. Second, the non-perturbative kernel being in impact parameter space is Fourier transformed back to momentum space. We then compute medium-induced radiation rates in infinite and finite medium lengths and compare with leading order and next-to-leading order kernels that are usually used in the literature. We also compare several traditional and novel approximations to the radiation rates that are commonly used and discuss their range of validity.

List of Publications

Parts of this thesis are based on the work:

[3] Soeren Schlichting and Ismail Soudi.
'Medium-induced fragmentation and equilibration of highly energetic partons'.
Journal of High Energy Physics, 2021(7):77, July 2021.
DOI: 10.1007/JHEP07(2021)077

[4] Guy D. Moore, Soeren Schlichting, Niels Schlusser, and Ismail Soudi.
'Non-perturbative determination of collisional broadening and medium-induced radiation in QCD plasmas'.
e-Print: 2105.01679 [hep-ph]

At the time of writing, [4] is under peer review in the *Journal of High Energy Physics*. Furthermore, some results have been presented at the following conference and proceeding:

[5] Soeren Schlichting and Ismail Soudi.
'Energy loss and equilibration of jets in a QCD plasma'.
In: *10th International Conference on Hard and Electro-magnetic Probes of High-Energy Nuclear Collisions: Hard Probes 2020*. Sept.2020.
e-Print: 2009.02973 [hep-ph]

Contents

List of Figures

List of Tables

1 Introduction

Throughout scientific history, the pursuit of a better understanding of nature meant breaking down matter into more and more fundamental pieces. Needless to say, this quest led us to the discovery of the electrons and nucleons (protons and neutrons) that make up the atom. Soon afterwards, the success of the parton model [6] alluded to the fact that nucleons are also made up of even more fundamental particles that we now know as quarks and gluons and can be studied using the theory of Quantum Chromodynamics (QCD). QCD is a non-abelian gauge theory that describes how partons, which carry the color charge, interact with each other via the exchange of gluon gauge bosons [7]. Although there are further theoretical explorations that try to go beyond the standard model of particles to explain matter with even more fundamental objects (e.g., strings), it seems that experimentally we have many years ahead of us before we can reach beyond QCD, due to the fact that QCD exhibits a phenomenon known as confinement, which traps all color charged particles inside color neutral bound states. Concretely, the force holding together the quarks inside the proton grows linearly when one separates them until the energy required is large enough to create another pair of quarks in between. Hence, quarks at normal conditions of pressure and temperature can only be found in bound states, making it hard to study QCD.

QCD at high energies possess a property known as asymptotic freedom, leading to weaker interactions as the energy scale increases (or distance decreases) [8, 9]. Consequently, when taken to extreme conditions of high density and temperature, QCD matter experiences a smooth cross-over transition where the bound states start overlapping and melt into a soup of effectively free quarks and gluons in a new state of matter known as the quark-gluon plasma (QGP) [10]. In nature, such densities can potentially be achieved in very massive and compact neutron stars [11] and are known to exist in the early Universe microseconds after the Big Bang [12].

On Earth, several collisions have been developed in order to probe very short distances to attain asymptotic freedom. However, to form a QGP not only high energy is needed but also a sufficiently large system to form a medium. When two nuclei collide head-on at high velocities in high energy heavy-ion collisions (HIC), they can produce high multiplicity of particles. Such high multiplicity events at

the Relativistic Heavy-Ion Collider (RHIC) and Large Hadron Collider (LHC), can reach very high temperatures and densities that a QGP is formed in the laboratory. QGP formation is manifested by different signatures from the collective behavior of low energy hadrons to the modification of quarkonia states, as well as enhanced production of strange particles [13–16]. Additionally, hard collisions at the early stages produce jets of back-to-back high energy particles that traverse the medium, losing some of their energy before being detected. Known as jet quenching, this phenomenon has been a crucial issue of experimental and theoretical studies [17].

The study of jets is not exclusive to HIC, in fact it was essential in the development of QCD; starting with the early experiments of electron-positron annihilation to hadrons $e^- e^+ \to$ hadrons. Due to a hard scattering event, the electron-positron pair produces a pair of quark (q) and anti-quark ($\bar{q}$), which travel back-to-back because of momentum conservation, and as they separate further away from each other they undergo fragmentation and a parton shower into additional partons ending with a recombination which gives rise to two back-to-back hadronic jets[1]. For high energy events, perturbative QCD (pQCD) can be used to study this final state hadronic jet structure. Aside from representing important evidence of the existence of three color charges[2], the study of this process led to the development of pQCD jet physics in vacuum and allowed further calculations in more complex processes with hadronic initial states, such as proton-proton collisions [18–20]. While the physics of jets in vacuum is well established theoretically, the studies of medium modification of the parton shower are still ongoing [21–24]. By comparing against the expected fragmentation in the absence of the medium, one hopes to understand how the jet loses part of its energy to the medium, and how the presence of the medium modifies the parton shower.

The full study of jet quenching is an involved task, requiring a theoretical description of each stage of the evolution from the parton creation to the hadronization of the parton shower. Nonetheless, we will not attempt to describe such a comprehensive picture, instead we focus solely on a highly energetic parton interacting with the medium. The evolution and equilibration of the hard parton inside the QGP is characterized by two distinct processes, the elastic collision with the medium giving rise to many soft scatterings as well as a few hard collisions which lead to para-

[1] Note that two jets are only the leading order process, additional jets can be obtained with lower probability.

[2] One can infer the number of quark colors by computing the famous R-ratio, the ratio between the cross-section of the hadronic final state to a leptonic one, given by $R = \frac{\sigma(e^- e^+ \to \text{hadrons})}{\sigma(e^- e^+ \to \mu^+ \mu^-)} = N_c \sum_f Q_f$, where Q_f is the electric charge of the different quark flavors f [7, 18, 19].

metrically similar energy deposition [25, 26]. Similar to the classic Bremsstrahlung process, the multiple soft scatterings with the medium induce radiation from the highly energetic partons which dominate the in-medium energy loss [27, 28]. This medium cascade has been shown to display a universal behavior akin to a turbulent cascade [29, 30]. Based on an effective kinetic theory of QCD [31], we will describe the evolution of highly energetic partons in a thermal QGP medium. As opposed to earlier studies where they focus on the hard particles [29, 30, 32, 33], we keep track of the parton energy from the early collisional and radiative energy loss all the way to the full thermalization into the soft sector. Since the relevant dynamics of energy loss are similar to the QGP thermalization itself [34–38], we will also investigate to what extent the physics of near-equilibrium excitations is relevant to the problem of jet quenching. The main purpose of this thesis is to extract the universal dynamics and develop a (semi-)analytical understanding of the equilibration of highly energetic partons inside the QGP. Furthermore, since energy loss is dominated by the radiative splittings, we devote the last chapter to a novel approach of computing the in-medium splitting using non-perturbative input for describing the multiple soft scattering with the medium [1, 2]. We further compare different theoretical approaches to compute the in-medium splitting rates and discuss their respective range of validity.

The present thesis is structured as follows: chapter 2 provides a short introduction to the physics at play during heavy-ion collisions, and section 2.3 is used to contextualize the present work within the full evolution of jets in HIC. In chapter 3, we will go on to introduce the effective kinetic theory of QCD used to describe the evolution. We present the relevant QCD processes, discuss the Landau-Pomeranchuk-Migdal effect in QCD and include in the last section a brief introduction of weak wave turbulence and a derivation of the Kolmogorov-Zakharov spectrum. The in-medium energy loss in the longitudinal direction is studied in chapter 4, where we consider the elastic processes in the small angle approximation, as well as medium-induced radiation. In chapter 5, we extend the evolution to include the full elastic processes and angular structure in the polar angle around the initial leading parton. We dedicate the last chapter 6 to the determination of medium-induced radiation rates using a new collisional broadening kernel which includes non-perturbative contribution extracted from lattice EQCD. We obtain the rates in both infinite medium (sec. 6.2) and finite medium (sec. 6.3) and compare our results with a variety of approximations, either using broadening kernels from perturbative results or by using a simplified rate. We conclude in Chapter 7 with a brief summary of the most important findings and discuss possible directions for future work. Furthermore, at the end of the thesis, we provide appendices for the following derivations: the derivation

of the small angle approximation of the elastic collision integral is given in App. A, while the numerical implementation of the kinetic evolution is in App. B. App. C describes the derivation of the rate equation in the Bethe-Heitler regime and App. D provides the numerical implementation of the finite medium splitting.

Conventions Throughout this work we will make use of the following standard high-energy physics conventions :

- We work in natural unit system by setting the Plank constant $\hbar$, the speed of light c and the Boltzmann constant k_B to $\hbar = c = k_B = 1$.
- Bold letters are used for vector quantities and Minkowski 4-vectors are capitalized, e.g., $P = (E(\boldsymbol{p}), \boldsymbol{p})$, K.
- We will use the metric convention $(+, -, -, -)$.

2 Primer on heavy-ion collisions

The main topic of this work is the use of jets as tomographic probes to learn more about the QGP medium. However, the study of jet quenching in heavy-ion collisions is a broad subject which requires a vast array of phenomena. The purpose of this chapter is to provide the broader context of our work and justify the approximations we take.

Starting from a brief presentation of the characteristics of QCD theory, leading naturally to a discussion about the deconfinement transition to the quark-gluon plasma. We end the chapter with a description of the different stages of the collision and the relevance of jets in HIC.

2.1 Basics of Quantum Chromodynamics

QCD is a non-abelian gauge theory based on the special unitary group $SU(N_c)$ with $N_c = 3$ color charges, governing the interactions of quarks and gluons. The color symmetry group admits eight generators ($N_c^2 - 1 = 8$) written T^a and obey the commutation relations [40]

$$[T^a, T^b] = if^{abc}T^c \,, \tag{2.1}$$

where f^{abc} are the structure constants of the group. In the fundamental representation, T^a are represented by 3×3 Gell-Mann matrices. The quarks ψ_f are fermionic fields (spin-$\frac{1}{2}$ particles) which are observed in nature in six flavors ($f = u, d, s, \cdots$) with different masses (c.f. table 2.1), in addition to their electromagnetic charge carry the color charge of QCD and live in its fundamental representation. They

Flavor	up (u)	down (d)	strange (s)	charm (c)	bottom (b)	top (t)
mass $\sim$	2.16MeV	$2m_u$	$43m_u$	$588m_u$	$1935m_u$	$79981m_u$
charge	$2/3e$	-1/3	-1/3	2/3	-1/3	2/3

Table 2.1: Different quark flavors with their approximate masses relative to the quark up mass m_u and charge relative to the electron charge e [39].

transform according to

$$\psi_f(x) \to e^{igT^a\alpha_a(x)}\psi_f \ , \tag{2.2}$$

under the local gauge transformation $G(x) = e^{iT^A\alpha_a(x)}$, generated by α_a.

The boson fields ($A_\mu = A^a_\mu T_a$) of QCD are the gluons which, as opposed to photon in electromagnetism, also carry color charges a and live in the adjoint representation transforming as

$$A^a_\mu \to G(x)A_\mu G^\dagger(x) - \frac{i}{g}G(x)\partial^\mu G^\dagger(x) \ , \tag{2.3}$$

where for infinitesimal gauge transformation is written

$$A^a_\mu \to A^a_\mu + gf_{abc}A^\mu_b\alpha_c - \partial^\mu\alpha_a \ . \tag{2.4}$$

The QCD Lagrangian is written [7]

$$\mathcal{L}_{\rm QCD} = \sum_f \bar\psi_f(x)(i\gamma^\mu D_\mu - m)\psi_f(x) - \frac{1}{4}G^a_{\mu\nu}G^{\mu\nu}_a \ , \tag{2.5}$$

where γ^μ are the Dirac gamma matrices. The covariant derivative is defined as

$$D_\mu = \partial_\mu + igT^aA^a_\mu \ , \tag{2.6}$$

here g is the dimensionless QCD coupling. The QCD field strength tensor is given by

$$G^a_{\mu\nu} = \partial_\mu A^a_\nu - \partial_\nu A^a_\mu + gf^{abc}A^b_\mu A^c_\nu \ . \tag{2.7}$$

The quadratic term in the gluon field stems from the non-abelian nature of the theory and leads to the infamous gluon self-interaction.

The QCD Lagrangian is one of the hardest standard model theory to solve due to the gluon self-interaction and strong coupling constant. At large energies, one expects the coupling to be small to be able to employ standard perturbation techniques. Our analysis will rely on weak coupling techniques to describe interactions of hard partons with the medium at leading order of the QCD coupling constant.

Besides standard perturbative methods, one can use numerical simulation known as Lattice QCD, where the fields are discretized numerically on a lattice and by taking the continuum limit one can extract different observables [41–43]. However, because this discretization requires the evaluation of statistical averages weighted by the exponential of the QCD action in Euclidean time, when applied to a system with finite baryon chemical potential or to observables involving real-time calculations in Minkowski space, it leads to the so-called sign problem where the Euclidean

action acquires an imaginary contribution which does not correspond to a probability density [44, 45]. Consequently, Lattice QCD can only be applied for a system with zero baryon densities[1] or static (Euclidean) quantities.

Another approach to QCD is to enact effective theories that make use of the separation between different scales of the system. One such theory is known as Electrostatic QCD (EQCD) which describes QCD at high temperature [47, 48]. EQCD is motivated by the infrared (IR) problem of thermal QCD. As first pointed out by Lindé [49], at high temperatures the perturbative expansion encounters an IR wall when additional gluon loops are not suppressed with the coupling, because each loop give rise to the following factor [50]

$$\frac{1}{E_p}\left(1+\frac{1}{e^{E_p/T}-1}\right) \sim \frac{T}{E_p^2}+\mathcal{O}\left(\frac{1}{T}\right) . \tag{2.8}$$

By inserting the soft scale generated by the medium $p_{\text{soft}} \sim gT$, we find $\frac{1}{g^2 T}$ which spoils the coupling expansion even for small values of $g \ll 1$, as many diagrams contribute at the same order and thus have to be resummed. EQCD deals with this problem by making use of the generated hierarchy of scales for QCD at high temperatures, between a soft scale p_{soft} and a hard scale p_{hard} :

$$p_{\text{soft}} = gT \ll p_{\text{hard}} = \pi T , \tag{2.9}$$

where at high temperature one expects the coupling g to be small. By integrating out the hard scale and defining effective parameters which account for its effects [50], it turns out that the only dynamics left in the system is the boson zero mode as the nonzero modes and the fermionic frequencies are considered hard. EQCD is then a purely bosonic three-dimensional theory, where the A_0 field becomes an adjoint scalar field which couples to the three-dimensional gauge field A_i. EQCD can be solved either perturbatively or on a lattice, and it has been successfully used to determine thermodynamic quantities at higher precision [51, 52]. Recent studies were able to obtain lattice results for other quantities such as the collisional broadening kernel and thermal masses [1, 2, 53–55]. We will use the non-perturbative determined EQCD broadening kernel from [2] to study in-medium splitting rates in chapter 6.

2.1.1 Quark-Gluon Plasma

Due to the strong confinement of color charges, quarks and gluons at low energies are only present inside colorless bound states known as hadrons. The only

[1] Ongoing work studies small baryon density as an expansion around zero [46].

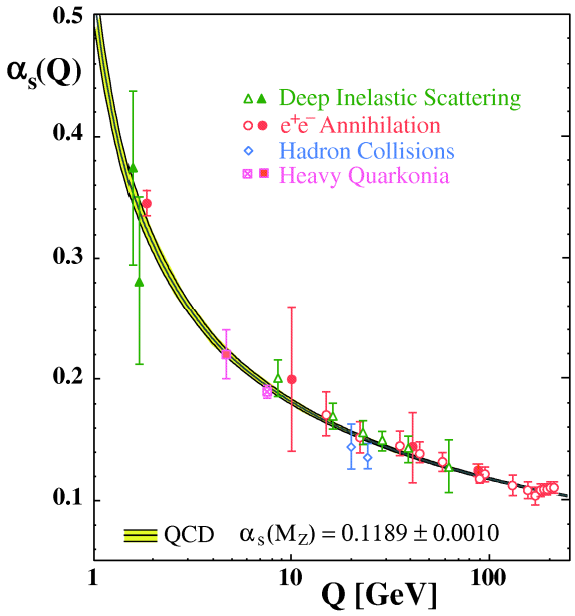

Figure 2.1: Experimental evidence of the QCD running coupling as a function of the exchange momentum. Figure from [56].

allowed hadrons are singlet under color transformation leading to the combination of so-called valence quark-antiquark pairs along with sea quark/antiquarks and gluons as mesons or three valence quarks (antiquarks) together with additional sea quark/antiquarks and gluons known as baryons.

Nevertheless, the QCD coupling exhibits a property known as the running coupling, which describes how at high energies the coupling constant depends on the four-momentum exchange Q^2. Using perturbative QCD at first order, one writes the effective coupling as [8, 9, 57]

$$\alpha_s(Q) = \frac{g^2}{4\pi} = \frac{4\pi}{(11 - \frac{2}{3}N_f)\ln(Q^2/\Lambda^2_{\mathrm{QCD}})} , \tag{2.10}$$

with the characteristic infrared scale $\Lambda_{\mathrm{QCD}} \sim 0.22\mathrm{GeV}$. The running coupling was confirmed through experiments [56] (c.f. Fig. 2.1) and explains the asymptotic freedom nature of QCD as it decreases logarithmically at large energies ($Q^2 \gg 1\mathrm{GeV}$).

As illustrated in figure 2.2, when nuclear matter is compressed to high baryon densities such that hadrons start overlapping, eventually, quarks cannot distinguish between neighboring hadrons. Alternatively, if one increases the temperature

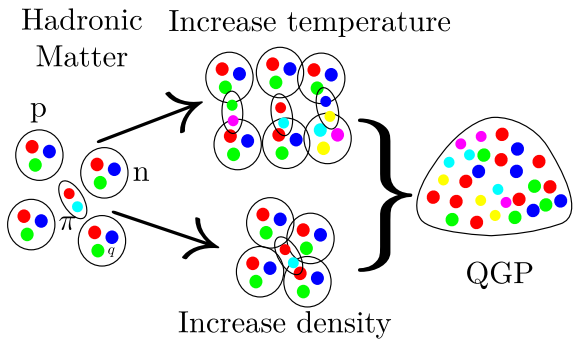

Figure 2.2: Illustration of QGP formation. When the temperature increases, newly created quark matter leads to screening of QCD interactions and formation of QGP. Similar conditions are created for QGP formation, due to high baryon densities. Figure inspired by [58, 59].

of strong interacting matter to extremes, the creation of additional mesons effectively reduces the distances between color charges giving rise to similar overlapping hadrons. Due to the short distances at play, quarks interactions are weak thanks to asymptotic freedom, leading to effectively free color charges interacting in a quark-gluon plasma (QGP). This transition to a system where color charges can move more freely over a larger volume is known as the deconfinement transition. The deconfinement transition has been extensively studied using Lattice QCD which allowed to extract the equation of state at vanishing baryon chemical potential [43].

In an equilibrium system the pressure is proportional to the degrees of freedom of the system, the results of [43] depicted in Fig. 2.3 show how at low energies the equation of state is equivalent to a hadron resonance gas where color charges are confined in hadrons leading to only few degrees of freedom. When the temperature increases, a transition occurs, color charges are freed, and the system exhibits a large number of (colored) degrees of freedom. The transition has been identified by lattice QCD to be a crossover transition at zero baryon chemical potential at around the critical temperature $T_c \sim 155\text{MeV}$ for two light flavors and a heavy strange quark flavor.

We note that color confinement is not actually violated by the QGP, but it is thanks to color screening that quarks are effectively free [60]. Color screening can be pictured similarly to screening in electromagnetic plasmas, where the electric charge is surrounded by a cloud of opposite charges, effectively scaling down the range of the Coulomb force. Analogously, we anticipate that color charges are screened in

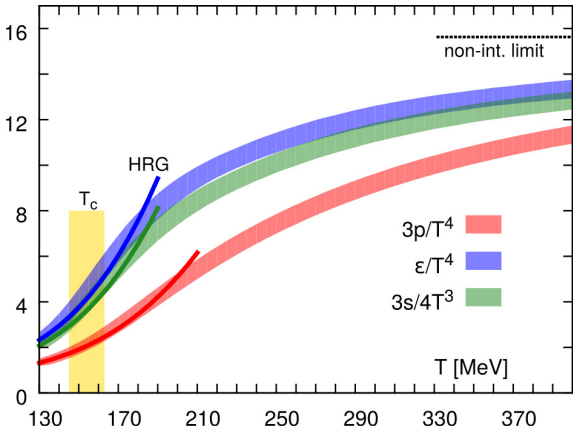

Figure 2.3: QCD equation of state extracted from lattice calculation by the HotQCD collaboration [43]. Pressure and energy density as a function of temperature display a transition from the Hadron Resonance Gas to a quark-gluon plasma.

the QGP. However, partons can still interact between each other as can be seen in Fig. 2.3, where the non-interacting limit is not reached. Nevertheless, modern perturbative calculation, based on Hard Thermal Loop perturbation, can achieve a good description of thermodynamic quantities at temperatures above $T \gtrsim 2T_c$ [61–65].

2.2 Heavy-ion collisions

In order to create a QGP on Earth at low baryon densities, one must reach extremely high temperatures of > 170MeV, which exceeds even what the core of the sun can reach ($1.57 \cdot 10^7$K $\sim 10^{-3}$MeV) [66]. Throughout recent history, advancement in collider technology and dedication from numerous physicists allowed us to create such conditions in ultra-relativistic heavy-ion collisions. These heavy-ion collision (HIC) experiments accelerate two nuclei at such high velocities ($\sim 99.995\%c$ at RHIC [67] and $\sim 99.99999c$ at the LHC [68]) that they almost pass through each other and only energy is deposited at the collision, creating a fireball with low baryon density but very high temperatures. However, the fireball is short-lived ~ 10fm/c, as soon after its creation it expands and cools down until it eventually turns into a hadron gas, who's remnants are detected long after the collision in the experimental detectors. Consequently, the study of the QGP in HIC is a complex task, and we can only rely on signatures of QGP formation.

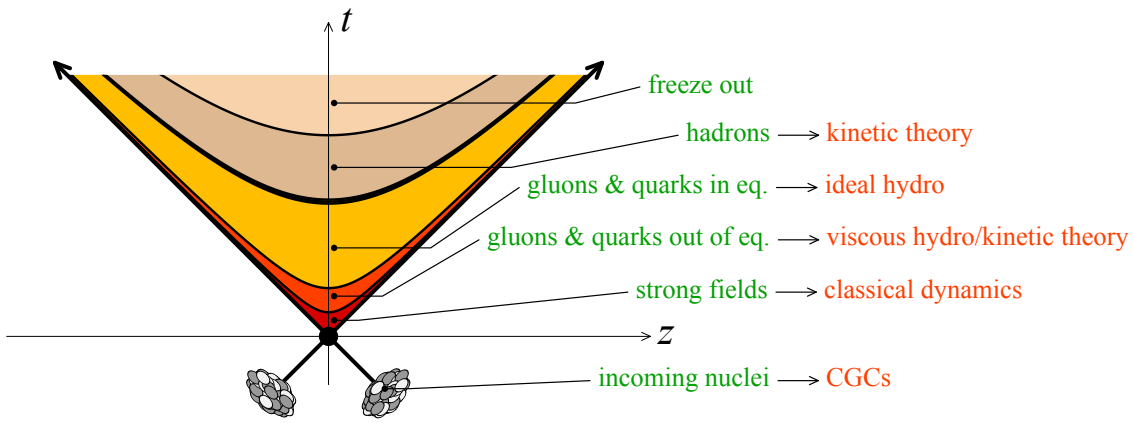

Figure 2.4: Different phases of heavy-ion collisions. Starting with the two incoming nuclei, which are close to the speed of light and are represented by 45° lines in the lab frame. The nuclei deposit energy in the form of strong gluon fields, which is modeled by classical dynamics towards an out of equilibrium plasma; the plasma evolution can be studied using kinetic theories and viscous Hydrodynamics. After the QGP thermalizes, it follows an ideal Hydrodynamic evolution, cooling down below the critical temperature when partons are confined in hadrons. The hadron gas itself expands and loses its kinetic energy towards a kinetic freeze out. Slightly modified version of a figure in [15].

Following [15], we will give a brief description of the different stages of the collision as shown in the schematic illustration in Fig. 2.4. Starting with Lorentz contracted ions with a high boost factor of nearly $\gamma \sim 100$ at RHIC [67] and $\gamma \sim 2675$ at the LHC [68]. At such high rapidity, QCD matter consists mostly of gluons, which are modeled by the effective theory of Color Glass Condensate (CGC) [69, 70].

Right after the collision of the two nuclei $t \sim 0$, hard processes with large momentum exchange ($Q > 10$GeV) occur first, due to the uncertainty principle $t \sim 1/Q$ and produce high energy particles such as hard partons, photons, heavy quarks or vector bosons.

Shortly after, the CGC describes how the bulk of the energy is deposited into a very dense glasma, i.e., a plasma constituted of mostly highly energetic gluons. This initial far-from equilibrium state undergoes kinetic and chemical thermalization, leading to the creation of quarks and antiquarks [34]. This thermalization is referred to as the bottom-up thermalization scenario [36] and can be studied using effective kinetic approaches [34, 35, 37, 38, 71–73]. The now formed QGP proceeds to expand and because the collision is not perfectly head-on, the asymmetric pressures give rise to an asymmetric expansion in the transverse plane.

Although the system size is small, due to the strong interactions, the system maintains a state sufficiently close to local thermal equilibrium that it can be successfully described by relativistic viscous hydrodynamics [74]. After the system expands and the temperature reaches below the critical temperature, color is confined once again inside hadrons, leading to an interacting hadron gas described by kinetic theory. Eventually, the hadron gas also expands to a point when interactions become weaker than the expansion in a stage known as kinetic freeze-out. Lastly, the hadrons continue in free streaming until they decay or reach the detector.

The QGP state of matter is only part of the complex evolution of HIC, extracting information about this medium is certainly challenging and would require a solid grasp on a lot of different physics characterizing each stage. Nevertheless, in the 80's Bjorken suggested that due to the short timescales of hard partonic collisions, the production of hard particles is not affected by the plasma [17] and can be reliably calculated using perturbative QCD. The highly energetic partons produced by these collisions traverse the medium before being detected, by doing so they interact with the medium and lose their energy in a process known as '*jet quenching*'. By studying how these hard particles lose their energy, one can infer information about the medium properties and evolution of the fireball. In the next section, we will briefly introduce the physics of QCD jets and discuss where exactly our analysis lies in this context.

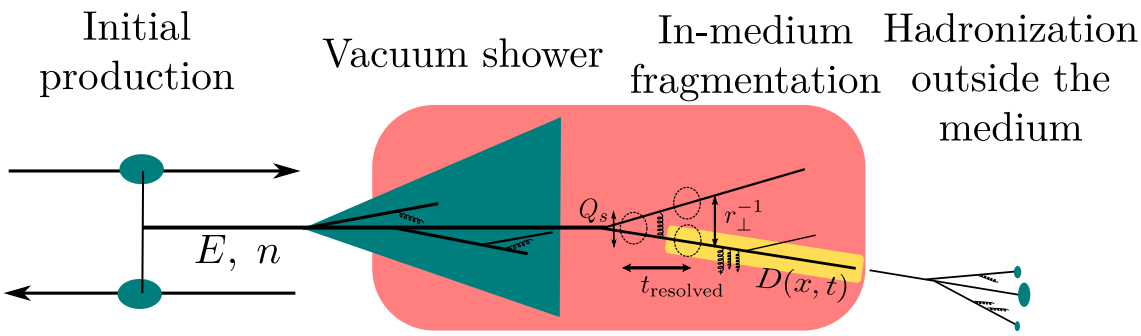

Figure 2.5: Visualization of jet evolution in heavy-ion collisions. We focus on the in-medium evolution of the partons once they are resolved by the medium.

2.3 Basics of QCD jets

Jets are defined, via a suitable clustering algorithm, as collimated sprays of hadrons that are produced from a hard collision process. Starting from a highly virtual parton produced in an initial hard scattering, in the vacuum the jet constituents evolve toward mass-shell following a collinear parton shower (akin to the time-like DGLAP equation) [75, 76]. In the presence of a QCD medium, the evolution involves additional processes and different approaches have been used to study the modification of the jet shower by the medium (see, [23, 24, 77] for a review). One approach consists of a modification of the DGLAP evolution to include medium modifications, as done in some MonteCarlo event generators [24, 78–80]; a different approach is to follow the kinematics of hard partons inside the medium and study how the jet constituents interact with the medium, as e.g., done in [29, 30, 32, 33]. Even though this work is not intended to provide a comprehensive description of in-medium jet evolution, we will generally follow the latter approach by studying the energy loss of hard partons inside a thermal medium.

Besides the scales relevant for vacuum dynamics, the dynamics of jets inside the medium are sensitive to additional scales emerging from the medium (as discussed in [23, 81]), including the typical transverse momentum acquired during scatterings $Q_s = \sqrt{\hat{q}L}$ where L is the medium size and $\hat{q}$ is the momentum broadening parameter; and the typical inverse size of the jet in the medium $r_\perp^{-1} = (\Theta L)^{-1}$, where Θ is the opening angle of the jet [23, 81]. Vacuum-like emissions can be factored out [82, 83] and degrade the virtuality of the partonic constituents as in the vacuum; however, individual jet constituents embedded in the medium are only resolved by the medium when the separation length is larger than the medium resolution scale

$Q_s^{-1} \ll r_\perp$, and it is thus useful to define a decoherence time $t_{\text{resolved}} \sim \left(\frac{1}{\hat{q}\theta_{12}^2}\right)^{1/3}$ [23] where constituents of the jet become resolved by the medium. Subsequently, the resolved constituents interact with the medium as uncorrelated colored partons, which undergo elastic and inelastic interactions with the medium leading to energy loss of the highly energetic partons and energy transfer to the thermal medium. Throughout the in-medium evolution, vacuum-like emissions at smaller and smaller angles continue to form, effectively providing a source of partons as they become resolved by the medium. Eventually, after a time $\sim L$ the hard constituents of the jet leave the medium and the vacuum-like evolution continues outside the medium [83], until it reaches non-perturbative scales where the constituents confine into hadrons.

Based on this discussion, it is clear that a complete picture of jet evolution in HIC will have to start from the jet creation all the way to hadronization, as is schematically illustrated in Fig. 2.5. Since such a description necessarily involves a variety of different processes at different scales, it is essential to develop a robust theoretical understanding of each stage, in order to devise suitable observables to probe e.g., the properties of medium-induced emissions or study connections between jet quenching and equilibration. We will therefore not attempt to develop a complete description of in-medium jet evolution, but rather focus on the particular aspect of the energy loss and equilibrium of highly energetic partons due to interactions with the surrounding medium. While our discussion thus ignores effects of vacuum-like emissions and the (lack of) color coherence of the vacuum shower, which are known to be important to describe some experimental observables such as e.g., fragmentation functions [83, 84], we anticipate that in a more complete theoretical description of jet vacuum-like emissions can be absorbed into the initial conditions or factored out into a source term depending on their decoherence time. By investigating how uncorrelated colored partons lose their energy and eventually become part of the medium, our results can therefore be seen as a Green's function propagating a single medium-resolved highly energetic parton through the medium. Since the evolution is linear, more realistic initial conditions including an early vacuum-like cascade can be implemented by a simple convolution with the corresponding Green's function. Vacuum-like splittings could in principle appear at any spacial position along the path-length of the medium, producing new sources not included in our approach. However, such vacuum-like emissions inside the medium are sub-leading in the double log approximation [83]. Even though the complicated interplay of initial conditions, source terms and in-medium evolution will inevitably modify observables such as momentum spectra, our qualitative conclusions regarding energy loss and equilibration mechanism are thus not expected to be modified by such a

more refined implementation.

2.3.1 Measurement of jets or high-p_T particles in heavy-ion collisions

A number of observables are used to study medium modification of jets or high-p_T particles in HIC, during this section we will provide a brief overview of the current status of the field (c.f. [22–24] for more extensive reviews).

The main purpose of probing medium modification of hard partons can be achieved using a class of observables known as the nuclear modification factor R^X_{AA}, which computes the ratio of the single-particle inclusive spectra in a nucleus-nucleus collision (AA) to the baseline proton-proton (pp) collisions [85]. For a given particle species X with inclusive yields N^X_{AA} and N^X_{pp} in AA and pp collisions, respectively, the ratio is given by

$$R^X_{\mathrm{AA}}(p_T, y, \phi) \equiv \frac{1}{N_{AA}} \frac{\frac{d^2 N^X_{\mathrm{AA}}}{dp_T^2 dy}}{\frac{d^2 N^X_{\mathrm{pp}}}{dp_T^2 dy}} , \tag{2.11}$$

where N_{AA} is the number of elementary nucleon-nucleon collisions expected at a given centrally which can be computed using a standard probabilistic Glauber model [86], and ensures the ratio is 1 if no suppression occurs.

In Fig. 2.6, hadron R_{AA} is shown for different experiments with energies $\sqrt{s_{NN}} = 17.3\mathrm{GeV}, 200\mathrm{GeV}, 2.76\mathrm{TeV}$ for SPS (PbPb), RHIC (AuAu) and LHC (PbPb) respectively, compared to a range of theoretical models [87]. One observes a clear suppression of high-p_T hadrons in the high energy collisions of RHIC and LHC compared to low energies at SPS where it is absent. We also observe less suppression of high p_T particles at LHC, as they lose less energy because they can escape the medium [21, 88]. The nuclear modification factor is well described by theoretical models and constitutes a strong signal for QGP formation at HIC.

While the hadron R_{AA} measures the suppression of only the leading hadron resulting from the parton cascade, one can also measure the modification of the complete parton showers. Parton fragmentation at small angles leads to collimated quarks and gluons, which combine into collimated hadrons, which form jets. However, whether a particle is considered part of the jet is not clear, one must establish a jet definition. At the core of jet definition is the jet recombination algorithm, which uses a set of parameters (e.g., distance R in the rapidity-azimuth $(y - \phi)$ plane) to cluster different hadrons into a jet. Moreover, using a recombination scheme one obtains the kinematics of the jet from its constituents, for example 'E-*scheme*' sim-

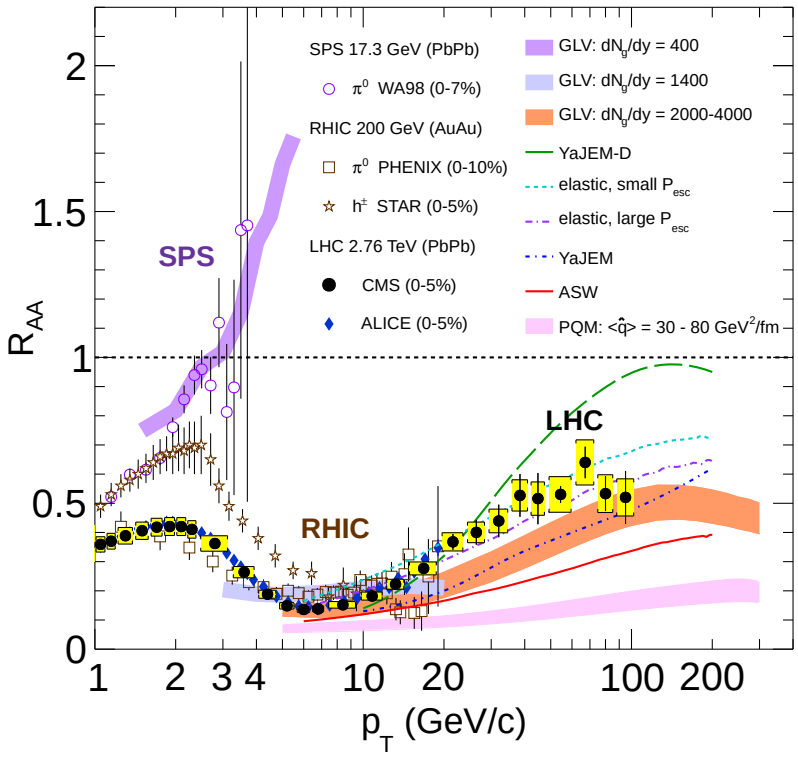

Figure 2.6: Measurement of the nuclear modification factor R_{AA} by different experiments RHIC, LHC and SPS compared with a range of theoretical models. Figure from [87].

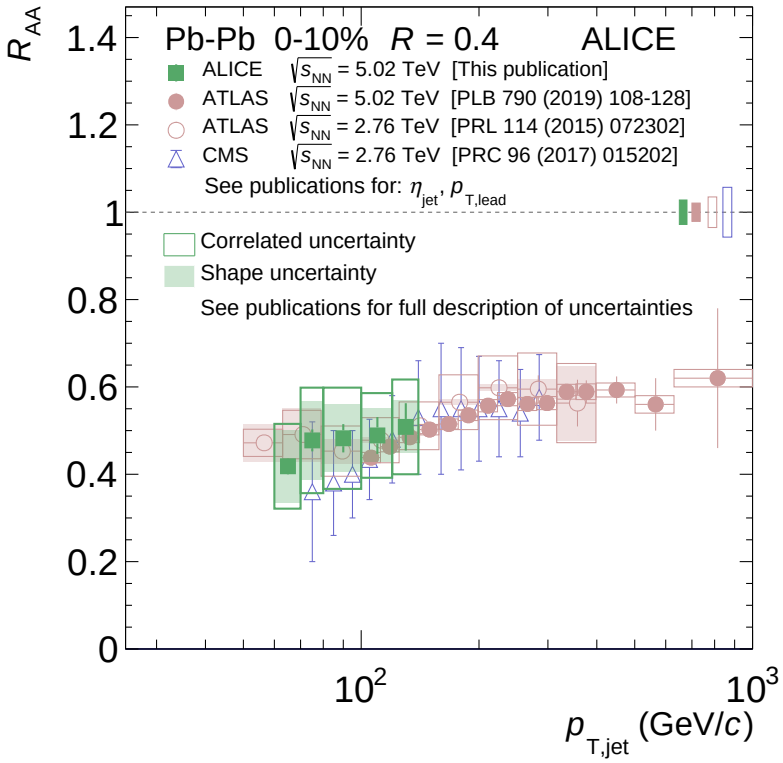

Figure 2.7: A comparison of the jet modification factor R_{AA}^{jet} between different experiments (ALICE, ATLAS, CMS) using anti-k_T clustering algorithm with $R = 0.4$. Figure from [89].

ply sums the components of the four-vectors to obtain the jet kinematics. One of the mostly used jet algorithms at LHC is the anti-k_T algorithm, which clusters hard particles first and successively aggregate soft particles around them until reaching a distance R away from the jet axis [90–92]. Similarly to the hadron R_{AA}, one defines a jet suppression

$$R_{\rm AA}^{\rm jet}(p_T, y, \phi) \equiv \frac{1}{\langle T_{AA} \rangle} \frac{\frac{d^2\sigma_{\rm AA}^{\rm jet}}{dp_T^2 dy}}{\frac{d^2\sigma_{\rm pp}^{\rm jet}}{dp_T^2 dy}} \,, \tag{2.12}$$

where $d\sigma^{\rm jet}$ is the cross-section of single inclusive jet production [24] and $\langle T_{AA} \rangle$ is the nuclear thickness function, which can also be determined using Glauber model [86]. We show in Fig. 2.7 the $R_{AA}^{\rm jet}$ for a single inclusive jet clustered using anti-k_T algorithm with radius $R = 0.4$ for different experiments Pb-Pb collisions at ALICE, ATLAS and CMS. As for the inclusive hadron, We observe a comparable suppression of jets, which further corroborates medium modification arguments.

Besides the nuclear modification factor, another set of observables are used to study the jet substructure, which measures how energy-momentum is distributed within jets. For example, jet fragmentation function, defined as

$$D(z) \equiv \frac{1}{N_{\rm jet}} \frac{dN_h}{dz} \,, \tag{2.13}$$

measures the hadrons number N_h distribution as a function of their longitudinal momentum fraction ($z \equiv \frac{\boldsymbol{p}_T^h \cdot \boldsymbol{p}_T^{\rm jet}}{|p_T^{\rm jet}|^2}$), usually normalized to 1. Interactions with the medium are expected to modify not only the inclusive yields, but also the substructure of jets. One can measure modification of the fragmentation function as shown in Fig. 2.8 for ATLAS experiment for Pb+Pb collisions compared to p+p [93]. Interestingly, we observe enhancement both at small and large momentum fractions which, due to energy conservation, is compensated by a depletion in the intermediate scale. Medium-induced radiation by hard partons and medium response can lead to numerous low p_T hadron, which explains the enhancement at small z. While at large z, the enhancement can be explained by an increase in quark fraction as gluon jets lose more energy [24, 94, 95].

Moreover, one can measure other substructure observables such as jet shape which measures the momentum distribution transverse to the jet axis, or jet mass which measures the jet virtuality (c.f. [24] for more details).

Certainly, using suppression factor as a signal for QGP formation in HIC is by itself essential; nonetheless, one should be able to employ these measurements to extract information about the medium. Using model fittings, the JET collaboration

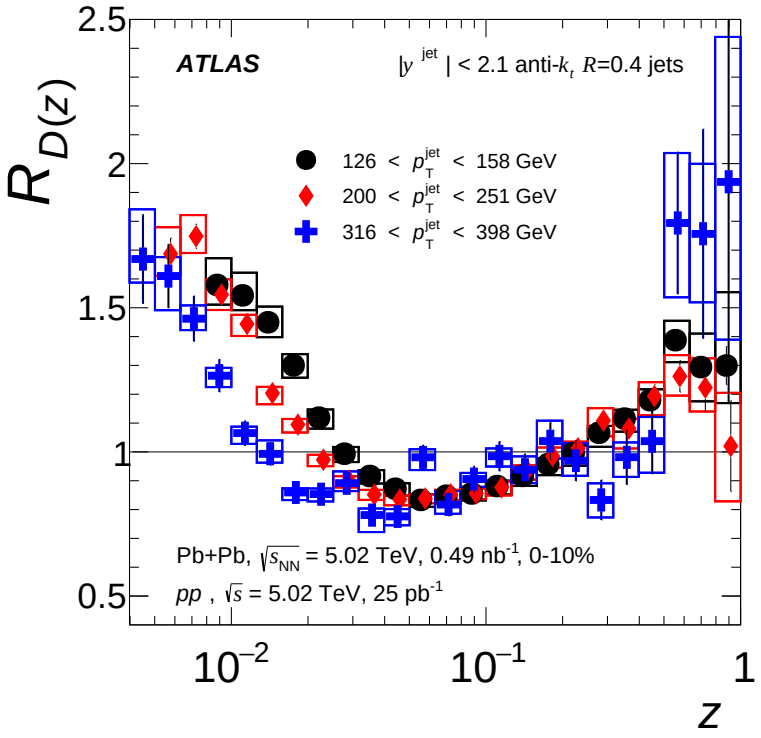

Figure 2.8: Nuclear modification of the jet fragmentation function measured in ATLAS experiment at different p_T^{jet} ranges using anti-k_T clustering algorithm with $R = 0.4$. Figure from [93].

was able to extract the transport coefficients $q_0 = 2.0 \pm 0.25\text{GeV}^2/\text{fm}$ and $2.9 \pm 0.6\text{GeV}^2/\text{fm}$ at $0-5\%$ central Au+Au collision at RHIC ($\sqrt{s} = 200\text{GeV/n}$) and $0-5\%$ central Pb+Pb collision LHC ($\sqrt{s} = 2.76\text{TeV/n}$), respectively [96]. Later on, JETSCAPE collaboration improved on the analysis using a simultaneous fit in a multi-dimensional parameter space to multiple data set at RHIC and the LHC [24, 97].

3 Effective kinetic theory of QCD

At extremely high temperatures, the interactions between quarks and gluons become weak due to the asymptotic nature of QCD. Therefore, we expect the *molecular chaos* hypothesis to hold, such that the timescale between successive collisions is well separated from the timescale of the collision itself (c.f. [98]). We ignore two particle correlations before and after each collision, two particle distributions are then given by the product of one particle distributions, truncating the BBGKY[1] hierarchy at the level of one particle distribution, and leading to an effective kinetic theory that simulates the QGP and treats QCD dynamics perturbatively [31].

Following the arguments of [31], if the QGP temperature T is high, we can ignore the rest mass of the quarks as the typical momentum p will be of order $T \gg m_{u,d}$. However, due to the interactions with the medium, thermal corrections will introduce an effective thermal mass m_{th} for both quarks and gluon of order $\mathcal{O}(gT)$. In perturbative theory the effective masses are given by

$$m^2_{\infty,g} = g^2 \int \frac{d^3p}{(2\pi)^3}\frac{1}{p}\left[N_c f_g(\boldsymbol{p}) + \sum_f (f_{q_f}(\boldsymbol{p}) + f_{\bar{q}_f}(\boldsymbol{p}))\right] \overset{\text{eq}}{=} \frac{m_D^2}{2} = \frac{g^2T^2}{2}\left(\frac{N_c}{3} + \frac{N_f}{6}\right) , \tag{3.1}$$

$$m^2_{\infty,q} = g^2 C_F \int \frac{d^3p}{(2\pi)^3}\frac{1}{p}\left[2 f_g(\boldsymbol{p}) + \sum_f (f_{q_f}(\boldsymbol{p}) + f_{\bar{q}_f}(\boldsymbol{p}))\right] \overset{\text{eq}}{=} \frac{g^2T^2}{2}\frac{C_F}{4} , \tag{3.2}$$

where $C_F = \frac{N_c^2-1}{2N_c}$ is the quadratic Casimir, we provide the result of the masses in equilibrium computed using the thermal distributions we define in the next section. Still, for a weak coupling ($gT \ll T$), it is reasonable to approximate the dispersion relation with

$$E_{g,q}(\boldsymbol{p}) = \sqrt{\boldsymbol{p}^2 + m^2_{(g,q),th}} \sim p . \tag{3.3}$$

Hence, we consider partons to be massless and assume that their de Broglie wavelength is much smaller than their mean free path, we can then define quasi-particles in the classical sense with a phase-space distribution $f(\boldsymbol{x}, \boldsymbol{p}, t) \equiv (2\pi)^3 \frac{1}{\nu_a}\frac{dN}{d^3\boldsymbol{x}d^3\boldsymbol{p}}$[2]

[1] BBGKY stands for: Bogoliubov–Born–Green–Kirkwood–Yvon.

[2] We will average over spin degrees of freedom.

which represent the number of particles at time t in the phase space volume with origin $(\boldsymbol{x}, \boldsymbol{p})$ and radius $(d^3\boldsymbol{x}, d^3\boldsymbol{p})$. Certainly, for particles to interact, their wave function will overlap, albeit, as one considers the collisions to be independent, only the incoming and outgoing states of the scattering matter and this information can be incorporated in the transition rate. We also take a *coarse-grained* time direction in such a way that the collision timescale are instantaneous. Similar *coarse-graining* is applied to positions $\boldsymbol{x}$ as well, such that particles with overlapping wavelengths are considered to be at the same space point and are allowed to interact. The phase-space distribution obeys a Boltzmann equation[31]

$$\left(\partial_t + \frac{\mathbf{p}}{|\mathbf{p}|}\nabla_{\mathbf{x}}\right) f(\boldsymbol{p}, \mathbf{x}, t) = C[\{f\}] \,, \tag{3.4}$$

where we do not take any external forces. The left-hand side represents the ideal gas evolution with only kinetic energy and no interactions, while the collision terms $C[\{f\}]$ on the right-hand side represent the transition rate, we will see later on that for leading order in high temperature QCD theory, one should consider two type of transition rates $2 \leftrightarrow 2$ and an effective $1 \leftrightarrow 2$ scattering. The Boltzmann equation is an integro-differential equation describing the out-of-equilibrium evolution of the system towards equilibrium stationary solutions, which we will define in the following sections.

3.1 General framework

Based on an effective kinetic description following the AMY approach [31], we describe the evolution and equilibration of highly energetic partons inside a thermal QGP. Both the hard particles and the thermal QGP medium are described by a phase-space distribution $f_a(p, x, t)$ of on-shell partons, with $a = g, q, \bar{q}$ denoting the parton species. Throughout this work, we will consider three quark flavors $N_f = 3$ without distinguishing between them. The time evolution of the phase space distribution functions $f_a(p, x, t)$ is governed by the Boltzmann equation

$$\left(\partial_t + \frac{\mathbf{p}}{|\mathbf{p}|}\nabla\right) f_a(\boldsymbol{p}, \mathbf{x}, t) = C_a^{2\leftrightarrow 2}[\{f_i\}] + C_a^{1\leftrightarrow 2}[\{f_i\}] \,, \tag{3.5}$$

where at leading order of the coupling constant g, one needs to include number conserving $2 \leftrightarrow 2$ processes and effective collinear $1 \leftrightarrow 2$ processes. By integrating

over the position $\mathbf{x}$, we then obtain a closed set of evolution equations for the momentum distributions $f_a(\boldsymbol{p},t) = \int d^3\mathbf{x}\; f_a(\boldsymbol{p},\mathbf{x},t)$[3] of hard partons

$$\partial_t f_a(\boldsymbol{p},t) = C_a^{2\leftrightarrow 2}[\{f_i\}]] + C_a^{1\leftrightarrow 2}[\{f_i\}] \; . \tag{3.6}$$

The free streaming term $\frac{\mathbf{p}}{|\mathbf{p}|}\nabla_{\mathbf{x}} f_a(\boldsymbol{p},\mathbf{x},t)$ will not play a role once we integrate the space direction. Since the hard partons are dilute compared to the soft thermal particles, we can describe the phase-space distribution of the hard partons $\delta f_a(\boldsymbol{p},t)$ as a linearized perturbation on top of the static medium and write

$$f_a(\boldsymbol{p},t) \;\; = \;\; n_a(p) + \delta f_a(\boldsymbol{p},t) \; , \tag{3.7}$$

where $n_a(p)$ is the thermal distribution, i.e., depending on the particle species $n_g(p) = \frac{1}{e^{p/T}-1}$ is the Bose-Einstein distribution or $n_{q/\bar{q}}(p) = \frac{1}{e^{p/T}+1}$ is the Fermi-Dirac distribution[4]. By linearizing Eq. (3.5) around thermal equilibrium, we then obtain a closed set of evolution equations for the momentum distributions of hard partons

$$\partial_t f_a(\boldsymbol{p},t) = \delta C_a^{2\leftrightarrow 2}[\{f_i\},\{\delta f_i\}] + \delta C_a^{1\leftrightarrow 2}[\{f_i\},\{\delta f_i\}] \; , \tag{3.8}$$

where δC_a is the linearized collision operator to be specified below.

3.2 Elastic collision integral

Highly energetic partons inside the thermal bath undergo number conserving (elastic) $2 \leftrightarrow 2$ collisions with the thermal bath. In general, the scattering $a(P_1)+b(P_2) \leftrightarrow c(P_3)+d(P_4)$ is described by the usual collision term [31]

$$C_a^{2\leftrightarrow 2}[\{f_i\}] = \frac{1}{2|p_1|\nu_a} \sum_{bcd} \int d\Omega^{2\leftrightarrow 2} \left|\mathcal{M}_{cd}^{ab}(\boldsymbol{p}_1,\boldsymbol{p}_2;\boldsymbol{p}_3,\boldsymbol{p}_4)\right|^2 \mathcal{F}(\boldsymbol{p}_1,\boldsymbol{p}_2;\boldsymbol{p}_3,\boldsymbol{p}_4) \; , \tag{3.9}$$

where $\nu_g = 2d_A = 16$ and $\nu_{q,\bar{q}} = 2d_F = 6$ denote the spin and color degeneracy factors of gluons and quarks. The delta function $\delta^4(P_1+P_2-P_3-P_4)$ ensures energy and momentum conservation, $\mathcal{M}_{cd}^{ab}(p_1,p_2;p_3,p_4)$ is the QCD matrix elements squared given in table 3.1 and $\mathcal{F}(p_1,p_2;p_3,p_4)$ is the statistical factor given by

$$\begin{aligned} \mathcal{F}(\boldsymbol{p}_1,\boldsymbol{p}_2,\boldsymbol{p}_3,\boldsymbol{p}_4) = & f_c(\boldsymbol{p}_3)\, f_d(\boldsymbol{p}_4)\, (1\pm f_a(\boldsymbol{p}_1))\, (1\pm f_b(\boldsymbol{p}_2)) \\ & - f_a(\boldsymbol{p}_1)\, f_b(\boldsymbol{p}_2)\, (1\pm f_c(\boldsymbol{p}_3))\, (1\pm f_d(\boldsymbol{p}_4)) \; . \end{aligned} \tag{3.10}$$

[3] Although we use the same notation to represent the momentum distributions and the full phase-space distribution, there should not be any confusion as they come with different arguments.

[4] We consider vanishing chemical potentials for all quark flavors.

$ab \longleftrightarrow cd$	$\left\|\mathcal{M}_{cd}^{ab}\right\|^2$
$q_i q_f \longleftrightarrow q_i q_f$, $q_i \bar{q}_f \longleftrightarrow q_i \bar{q}_f$, $\bar{q}_i q_f \longleftrightarrow \bar{q}_i q_f$, $\bar{q}_i \bar{q}_f \longleftrightarrow \bar{q}_i \bar{q}_f$	$8g^4 \, \frac{d_{\rm F}^2 \, C_{\rm F}^2}{d_{\rm A}} \left(\frac{s^2+u^2}{t^2} \right)$
$q_i q_i \longleftrightarrow q_i q_i$, $\bar{q}_i \bar{q}_i \longleftrightarrow \bar{q}_i \bar{q}_i$	$8g^4 \, \frac{d_{\rm F}^2 \, C_{\rm F}^2}{d_{\rm A}} \left(\frac{s^2+u^2}{t^2} + \frac{s^2+t^2}{u^2} \right) + 16g^4 \, d_{\rm F} \, C_{\rm F} \left(C_{\rm F} - \frac{C_{\rm A}}{2} \right) \frac{s^2}{tu}$
$q_i \bar{q}_i \longleftrightarrow q_i \bar{q}_i$	$8g^4 \, \frac{d_{\rm F}^2 \, C_{\rm F}^2}{d_{\rm A}} \left(\frac{s^2+u^2}{t^2} + \frac{t^2+u^2}{s^2} \right) + 16g^4 \, d_{\rm F} \, C_{\rm F} \left(C_{\rm F} - \frac{C_{\rm A}}{2} \right) \frac{u^2}{st}$
$q_i \bar{q}_i \leftrightarrow q_f \bar{q}_f$	$8g^4 \, \frac{d_{\rm F}^2 \, C_{\rm F}^2}{d_{\rm A}} \left(\frac{t^2+u^2}{s^2} \right)$
$q_i \bar{q}_i \longleftrightarrow g \, g$	$8g^4 \, d_{\rm F} \, C_{\rm F}^2 \left(\frac{u}{t} + \frac{t}{u} \right) - 8g^4 \, d_{\rm F} \, C_{\rm F} \, C_{\rm A} \left(\frac{t^2+u^2}{s^2} \right)$
$q_i \, g \longleftrightarrow q_i \, g$, $\bar{q}_i \, g \longleftrightarrow \bar{q}_i \, g$	$-8g^4 \, d_{\rm F} \, C_{\rm F}^2 \left(\frac{u}{s} + \frac{s}{u} \right) + 8g^4 \, d_{\rm F} \, C_{\rm F} \, C_{\rm A} \left(\frac{s^2+u^2}{t^2} \right)$
$g \, g \leftrightarrow g \, g$	$16g^4 \, d_{\rm A} \, C_{\rm A}^2 \left(3 - \frac{su}{t^2} - \frac{st}{u^2} - \frac{tu}{s^2} \right)$

Table 3.1: Different $2 \leftrightarrow 2$ processes in QCD and their matrix elements squared [31] written in terms of the Mandelstam variables $s = (P_1 + P_2)^2$, $t = (P_1 - P_3)^2$ and $u = (P_1 - P_4)^2$. For QCD theory with $SU(N_c)$ gauge symmetry, the fundamental representation has dimension $d_F = N_c$ and quadratic Casimir $C_F = \frac{N_c^2 - 1}{2N_c}$, while in the adjoint representation the dimension is $d_A = N_c^2 - 1$ and the quadratic Casimir is $C_A = N_c$.

The phase-space integration is given by

$$\int d\Omega^{2\leftrightarrow 2} \equiv \int \frac{d^3p_2}{(2\pi)^3}\,\frac{1}{2E_2}\int \frac{d^3p_3}{(2\pi)^3}\,\frac{1}{2E_3}\int \frac{d^3p_4}{(2\pi)^3}\,\frac{1}{2E_4}(2\pi)^4\delta^{(4)}(P_1+P_2-P_3-P_4)\ . \tag{3.11}$$

Following the parametrization in [65], one can use the three-dimensional integral to apply the momentum delta function defining $\boldsymbol{q} \equiv \boldsymbol{p}_1 - \boldsymbol{p}_3 = \boldsymbol{p}_4 - \boldsymbol{p}_2$. While the energy delta function left is cast into two delta functions, by introducing an integration over $\omega \equiv p_1 - p_3 = p_4 - p_2$ representing the energy exchange. The phase-space measure becomes

$$\begin{aligned}\int d\Omega^{2\leftrightarrow 2} =&(2\pi)\int \frac{d^3p_2}{(2\pi)^3}\int \frac{d^3q}{(2\pi)^3}\int d\omega\ \frac{1}{8E_2E_3E_4}\delta\left(p_1-\omega-|\boldsymbol{p}_1-q|\right)\\ &\delta\left(p_2+\omega-|\boldsymbol{p}_2+q|\right)\ .\end{aligned} \tag{3.12}$$

We then write the two delta functions in terms of the angles between $(\boldsymbol{p}_1, \boldsymbol{p}_2)$ and $\boldsymbol{q}$ that we denote with $(\theta_{1q}, \theta_{2q})$

$$\begin{aligned}\int d\Omega^{2\leftrightarrow 2} = (2\pi)\int \frac{d^3p_2}{(2\pi)^3}\int \frac{d^3q}{(2\pi)^3}\int d\omega\ \frac{1}{8p_1p_2^2q^2}\Theta(q-|\omega|)\Theta\left(p_1-\frac{q+\omega}{2}\right)\\ \Theta\left(p_2-\frac{q-\omega}{2}\right)\delta\left(cos\theta_{1q}-\left(\frac{\omega}{q}-\frac{\omega^2-q^2}{2p_1q}\right)\right)\delta\left(cos\theta_{2q}-\left(\frac{\omega}{q}+\frac{\omega^2-q^2}{2p_2q}\right)\right)\ .\end{aligned} \tag{3.13}$$

We leave the integration as is because for the numerical discretization we will perform another three-dimensional integral for $\boldsymbol{p}_1$ which will allow us to employ the delta functions symmetrically between $\boldsymbol{p}_1$ and $\boldsymbol{p}_2$. The elastic collision integral introduced above will be utilized in two different approach during this thesis, in Chapter 5 we will apply the small angle approximation to simplify it [99, 100] while in Chapter 6 we will use the full collision integral by only replacing the divergent parts of the bare matrix elements with a thermal treatment [31, 65].

3.3 Landau-Pomeranchuk-Migdal effect in QCD

In the study of energy loss of highly energetic partons inside the QGP medium, elastic interactions were historically considered first [25, 26]. However, due to the multiple soft scattering in the medium, radiation is induced and is further enhanced

by being nearly collinear. It turns out that this can lead to significantly more energy loss [27, 101, 102]. The study of radiative energy loss has spurred a lot of interest in recent years, during this section we will introduce the physics of medium-induced radiation based on [21, 23, 28, 77, 103–105], and we refer the interested reader to these reviews for more details.

Multiple soft scattering with the medium will kick the parton slightly off-shell, which in turn leads to a radiation of a gluon with energy ω and momentum $\boldsymbol{k}$. Because of the uncertainty principle, the gluon radiation is not instantaneous, instead the gluon separation from the parton is given by the uncertainty principle with its transverse energy

$$t_f \, E_\perp \sim 1 \,, \quad \text{with } E_\perp = \omega - k_z \simeq \frac{k_\perp^2}{2\omega} \,, \tag{3.14}$$

where we define the formation time t_f, the time it takes for the radiated gluon to form. One finds

$$t_f = \frac{2\omega}{k_\perp^2} \,, \tag{3.15}$$

where $k_\perp$ is the transverse momentum of the gluon. The elastic interactions with the medium are characterized by the momentum broadening coefficient $\hat{q} \sim m_D^2/\lambda_{\text{mfp}}$,[5] which defines the typical transverse momentum squared acquired inside the medium per mean free path. During the formation of the gluon, the typical transverse momentum it acquires is $k_\perp^2 \sim \hat{q} t_f$, the formation time can then be written

$$t_f = \sqrt{\frac{2\omega}{\hat{q}}} \,. \tag{3.16}$$

Let us define the Bethe-Heitler scale $\omega_{\text{BH}} \equiv \hat{q}\lambda_{\text{mfp}}^2$. When the gluon energy is much smaller than this scale $\omega \ll \omega_{\text{BH}}$, the formation time is shorter than mean free path $t_f \ll \lambda_{\text{mfp}}$ and the medium cannot resolve the radiated quanta until it is formed, i.e. the parton does not have time to encounter more than one scattering with the medium during the formation time.

However, when the gluon energy is larger $\omega \gg \omega_{\text{BH}}$, the formation time is longer than mean free path $t_f \gg \lambda_{\text{mfp}}$ and multiple scatterings with the medium act coherently leading to interference effects that have to be resummed, giving rise to a suppression of the radiation of high momentum gluons in the medium. This suppression is known as the Landau-Pomeranchuk-Migdal (LPM) effect, which was first developed in QED [106, 107] and later on it was extended to QCD [27, 108–111].

[5] In QCD perturbation theory, the mean free path for small angle scatterings is $\lambda_{\text{mfp}} \sim \frac{1}{g^2 T}$.

Contrary to QED, in QCD this effects not only the highly energetic parton but also the radiated gluon, as the gluon itself can scatter with the medium.

One can obtain a resummation of the multiple soft scatterings diagrams into an effective $1 \leftrightarrow 2$ rate. We proceed now to give a derivation of the rate equation following [23, 112]. We take the eikonal approximation of the medium-parton interaction, where the light-cone coordinates are $p^+ = \frac{p+p^z}{\sqrt{2}} \gg p_\perp$ and $k^+ = \frac{k+k^z}{\sqrt{2}} \gg k_\perp$. In the eikonal approximation, the kinematics of the interactions corresponds to a two-dimensional system of non-relaticistic quantum mechanics [112]; the light-cone momentum p^+ is conserved and will act as a mass. We study the propagation in terms of the transverse position $\boldsymbol{x} = (x^1, x^2)$ conjugate to the transverse momentum $\boldsymbol{p}_\perp$, the time direction will be given by the light-cone time $t = \frac{x^0+x^3}{\sqrt{2}}$. For the medium field, we take the light-cone gauge $A^+ = 0$; gluon polarization will propagate in the transverse plane, with no spin flip allowed along the trajectory. We define the background field $A_a^-(\boldsymbol{x}, t)$ obeying the correlation function

$$\langle A_a^-(\boldsymbol{x}, t) A_b^-(\boldsymbol{x}, t) \rangle = \delta^{ab} \delta(t - t') \gamma(\boldsymbol{x} - \boldsymbol{y}) \, , \tag{3.17}$$

where the model-dependent correlation function $\gamma(\boldsymbol{x})$ is given by the Fourier transform of the collisional broadening kernel $C(\boldsymbol{q})$ that we will discuss more in Chapter 6

$$\gamma(\boldsymbol{x}) = \int \frac{d^2q}{(2\pi)^2} \, e^{i\boldsymbol{x}\cdot\boldsymbol{q}} C(\boldsymbol{q}) \, . \tag{3.18}$$

We will see that the quantity that will play a role in the calculation is in fact the difference [112]

$$C(\boldsymbol{x}) = \gamma(0) - \gamma(\boldsymbol{x}) = \int \frac{d^2q}{(2\pi)^2} \, (1 - e^{i\boldsymbol{x}\cdot\boldsymbol{q}}) C(\boldsymbol{q}) \, . \tag{3.19}$$

The gluon propagator $\mathcal{G}(\boldsymbol{x}, t; \boldsymbol{y}, t')$ between two light-cone times t and t' is given by the Schrödinger equation

$$\left[i\partial_t + \frac{\partial_{\boldsymbol{x}}^2}{2p^+} + gA^-(\boldsymbol{x}, t) \right] \mathcal{G}(\boldsymbol{x}, t; \boldsymbol{y}, t') = i\delta(t - t')\delta(\boldsymbol{x} - \boldsymbol{y}) \, , \tag{3.20}$$

which can be written using the path integral

$$\mathcal{G}(\boldsymbol{x}, t; \boldsymbol{y}, t') = \int \mathcal{D}\boldsymbol{r} \; e^{i\frac{p^+}{2}\int_t^{t'} ds \; \dot{\boldsymbol{r}}^2} \mathcal{T} \exp\left[ig \int_{t'}^{t} ds \; A_a^-(\boldsymbol{r}(s), s) T^a \right] \, , \tag{3.21}$$

where $\mathcal{T}$ is time ordering and the Wilson line is integrated along the trajectory $\boldsymbol{r}(t) = \boldsymbol{x}$ and $\boldsymbol{r}(t') = \boldsymbol{y}$. In order to obtain the in-medium emission spectrum, one

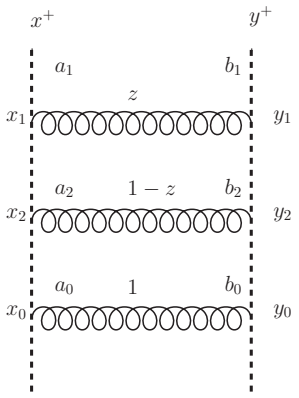

Figure 3.1: Graphical representation of an example three-point function for an in-medium gluon splitting [112].

considers the three-point function $G(\boldsymbol{y}, t_2; \boldsymbol{x}, t_1)$, as shown in Fig. 3.1 and employs the medium average Eq. 3.17 to find the spectrum [27, 108–111]

$$z\frac{dI^a_{bc}(P,z)}{dz} = \frac{\alpha_s z P_{bc}(z)}{[Pz(1-z)]^2}\mathrm{Re}\int_0^\infty dt_2 \int_0^{t_2} dt_1 \; \boldsymbol{\partial_x}\boldsymbol{\partial_y}\left[G(\boldsymbol{y}, t_2; \boldsymbol{x}, t_1) - G_0(\boldsymbol{y}, t_2; \boldsymbol{x}, t_1)\right] , \tag{3.22}$$

where we define P the momentum of the parent, and $z = \frac{k}{P}$ the momentum fraction of the radiated quanta. $P_{ab}(z)$ are the Dokshitzer-Gribov-Lipatov-Altarelli-Parisi (DGLAP) splitting functions

$$P_{gg}(z) = 2C_A\frac{[1-z(1-z)]^2}{z(1-z)} , \quad P_{qg}(z) = C_F\frac{1+(1-z)^2}{z} ,$$
$$P_{gq}(z) = \frac{1}{2}\left(z^2+(1-z)^2\right) . \tag{3.23}$$

The three-point function is given by the Schrödinger equation

$$\left[i\partial_t + \frac{\partial^2_{\boldsymbol{x}}}{2Pz(1-z)} + M_{\text{eff}} + i\Gamma_3(\boldsymbol{x})\right] G(\boldsymbol{x}, t; \boldsymbol{y}, t_1) = i\delta(t-t_1)\delta^{(2)}(\boldsymbol{x}-\boldsymbol{y}) , \tag{3.24}$$

where we have used the HTL framework to dress the free propagators with thermal mass by exchanging

$$\frac{\partial^2_{\boldsymbol{x}}}{2z(1-z)P} \to \frac{\partial^2_{\boldsymbol{x}}}{2z(1-z)P} + M_{\text{eff}} , \text{ with } M_{\text{eff}} = \frac{m_1^2}{2P} - \frac{m_z^2}{2zP} - \frac{m^2_{1-z}}{2(1-z)P} . \tag{3.25}$$

The three-body interaction is given in terms of two-body interactions

$$\Gamma_3(\boldsymbol{x}) = \left[C_1\bar{C}(\boldsymbol{x}) + C_z\bar{C}(z\boldsymbol{x}) + C_{1-z}\bar{C}((1-z)\boldsymbol{x})\right] , \tag{3.26}$$

where $\bar{C}(\boldsymbol{x}) \equiv \frac{C(\boldsymbol{x})}{C_R}$ is the broadening kernel stripped of its color factor. We define the factors $C_1 = \frac{1}{2}\left(C_z^R + C_{1-z}^R - C_1^R\right)$, $C_z = \frac{1}{2}\left(C_{1-z}^R + C_1^R - C_z^R\right)$ and $C_{1-z} = \frac{1}{2}\left(C_1^R + C_z^R - C_{1-z}^R\right)$, using color factor of the species with momentum fraction 1,z and $1-z$ respectively. $C(\boldsymbol{x})$ is the zero-substracted Fourier transform of the collisional broadening kernel (Eq. 3.19) which accounts for elastic collisions with the medium. We note also that the spectrum is defined with a subtraction of the free three-point function $G_0(\boldsymbol{y}, t_2; \boldsymbol{x}, t_1)$ to account for only medium-induced radiation without vacuum splittings.

One can obtain the equation in momentum space as well by employing a Fourier transformation. First, we define the Fourier transform of the propagator

$$K(\boldsymbol{k}, t_2; \boldsymbol{p}_b, t_1) = \int \frac{d^2\boldsymbol{y}}{(2\pi)^2}\frac{d^2\boldsymbol{x}}{(2\pi)^2}\, e^{i\boldsymbol{k}\cdot\boldsymbol{y}} e^{-i\boldsymbol{p}_b\cdot\boldsymbol{x}} G(\boldsymbol{y}, t_2; \boldsymbol{x}, t_1) . \tag{3.27}$$

After manipulation of the integral using the definition in Eq. (3.19), the three-body interactions term becomes the following convolution

$$\begin{aligned}\Gamma_3 \circ \psi(\boldsymbol{p}) = \int_{\boldsymbol{q}} \bar{C}(\boldsymbol{q}) \Bigg\{ & C_1\Big[\psi(\boldsymbol{p}) - \psi(\boldsymbol{p}-\boldsymbol{q})\Big] \\ & + C_z\Big[\psi(\boldsymbol{p}) - \psi(\boldsymbol{p}+z\boldsymbol{q})\Big] + C_{1-z}\Big[\psi(\boldsymbol{p}) - \psi(\boldsymbol{p}+(1-z)\boldsymbol{q})\Big]\Bigg\} .\end{aligned} \tag{3.28}$$

Derivatives in position space are replaced by $\partial_{\boldsymbol{x}} \to i\boldsymbol{p}_b$ and the propagator now satisfies the integro-differential equation

$$\left[i\partial_t - \delta E(z, P, \mathbf{p}_b) + i\Gamma_3(\boldsymbol{x}, t)\right] K(\boldsymbol{k}, t_2; \boldsymbol{p}_b, t_1) = i\delta(t - t_1)\delta^{(2)}(\boldsymbol{p}_b - \boldsymbol{k}) , \tag{3.29}$$

where we define the energy

$$\delta E(z, P, \boldsymbol{p}_b) = \frac{\mathbf{p}_b^2}{2Pz(1-z)} - M_{\text{eff}} . \tag{3.30}$$

The spectrum is now given by

$$\begin{aligned}z\frac{dI_{bc}^a(P,z)}{dz} = & \frac{\alpha_s z P_{bc}(z)}{[Pz(1-z)]^2}\mathrm{Re}\int_0^\infty dt_2 \int_0^{t_2} dt_1 \int \frac{d^2\boldsymbol{p}_b}{(2\pi)^2}\frac{d^2\boldsymbol{k}}{(2\pi)^2}\, \boldsymbol{k}\cdot\boldsymbol{p}_b \\ & \left[K(\boldsymbol{k}, t_2; \boldsymbol{p}_b, t_1) - K_0(\boldsymbol{k}, t_2; \boldsymbol{p}_b, t_1)\right] .\end{aligned} \tag{3.31}$$

By applying a time derivative to the spectrum in Eqns. (3.22-3.31), one obtains an effective radiation rate which can be incorporated into a Boltzmann evolution. However, solving the Schrödinger equation is not simple and one must resort to an approximation that simplify the calculations (see [113] for a review):

- One approximation is to consider the medium length to be infinite taking $t_2 \to \infty$ in the integration as was done by Arnold, Moore and Yaffe (AMY) [31], taking the HTL computed broadening kernel one can then solve the rate numerically. We will use this approach for the jet-medium evolution in Chapter 4-5.

- One can also solve the equation perturbatively in the number of scatterings which is known as the opacity expansion [103] and the first order is known as the Gyulassy, Levai and Vitev (GLV) approximation [114, 115].

- Another approach is to take the very high energy limit for the collisional broadening, which corresponds to a diffusion and leads to a Harmonic Oscillator equation [27, 116]. One can also define the HO approximation as the lowest order of the expansion and compute corrections around it [117–119].

We will compare the different approximations in the study of medium-induced radiation using the non-perturbative collision kernel in Chapter 6.

3.4 Collinear radiation

We describe now our treatment of collinear radiation when solving the Boltzmann equation for the jet-medium interactions. Generally, the interplay between vacuum-like emissions which are tied to the production vertex, and medium-induced emissions which can occur anywhere inside the medium can be rather complicated [116], and results in an explicit path length L or time t dependence of the medium-induced radiation rates [82, 116, 120, 121]. Since we are particularly interested in hard partons which lose a large fraction of their energy to the medium, there is, however, a clear separation of time scales between the initial vacuum-like shower and the subsequent energy loss of the partons inside the medium. We will therefore not include the effects of vacuum like emissions, anticipating that they can be absorbed into initial conditions or source terms for the in-medium evolution. Since we are particularly interested in the evolution on large time scales, we will also not consider the explicit path length L dependence of the medium-induced radiation rates,

and instead employ the large L limit of the medium-induced radiation rates, following the approach of AMY [31], where medium-induced radiation is described by collinear $1 \leftrightarrow 2$ splittings/mergings with an effective rate $\frac{d\Gamma^a_{bc}(p,z)}{dz}$. Starting from the nonvacuum part of Eq. 3.22 and apply a time (t_2) derivative to the spectrum to obtain a rate, and by taking the infinite medium length limit ($t_2 \to \infty$), we find the AMY in-medium rates

$$\frac{d\Gamma^a_{bc}(P,z)}{dz} = \frac{\alpha_s P_{bc}(z)}{[2Pz(1-z)]^2} \mathrm{Re} \int_0^\infty dt_1 \int \frac{d^2\boldsymbol{p}_b}{(2\pi)^2} \frac{d^2\boldsymbol{k}}{(2\pi)^2} \, 4\boldsymbol{k}\cdot\boldsymbol{p}_b K(\boldsymbol{k},\infty;\boldsymbol{p}_b,t_1) \ . \quad (3.32)$$

With the definition $\mathbf{g}_{(z,P)}(\boldsymbol{p}_b) = \int_0^\infty dt_1 \int \frac{d^2\boldsymbol{k}}{(2\pi)^2} \, 2\boldsymbol{k} K(\boldsymbol{k},\infty;\boldsymbol{p}_b,t_1)$, we can write the rate as[6] [116]

$$\frac{d\Gamma^a_{bc}(p,z)}{dz} = \frac{\alpha_s P_{bc}(z)}{[2Pz(1-z)]^2} \int \frac{d^2\boldsymbol{p}_b}{(2\pi)^2} \, \mathrm{Re}\left[2\mathbf{p}_b \cdot \mathbf{g}_{(z,P)}(\mathbf{p}_b)\right] \ , \quad (3.33)$$

where $\mathbf{g}_{(z,P)}$ is a solution to the integral equation

$$\begin{aligned} 2\mathbf{p}_b =& i\delta E(z,P,\mathbf{p}_b)\mathbf{g}_{(z,P)}(\mathbf{p}_b) + \int \frac{d^2q}{(2\pi)^2} \, \bar{C}(\boldsymbol{q}) \, \Big\{ C_1 \left[\mathbf{g}_{(z,P)}(\mathbf{p}_b) - \mathbf{g}_{(z,P)}(\mathbf{p}_b - \mathbf{q})\right] + \\ & C_z \left[\mathbf{g}_{(z,P)}(\mathbf{p}_b) - \mathbf{g}_{(z,P)}(\mathbf{p}_b - z\mathbf{q})\right] + C_{1-z} \left[\mathbf{g}_{(z,P)}(\mathbf{p}_b) - \mathbf{g}_{(z,P)}(\mathbf{p}_b - (1-z)\mathbf{q})\right] \Big\} \ , \end{aligned} \quad (3.34)$$

derived from Eq. (3.29). For the elastic broadening kernel $\bar{C}(\boldsymbol{q})$, we use the leading order expression

$$\bar{C}(\boldsymbol{q}) = \frac{g^2 T m_D^2}{q^2(q^2+m_D^2)} \ . \quad (3.35)$$

We solve Eq. (3.33) self-consistently, obtaining a resummation of multiple scatterings to all orders encompassing the Bethe-Heitler (BH) regime at low energy $z(1-z)p \lesssim \omega_{BH} \sim T$ as well as the Landau-Pomeranchuk-Migdal (LPM) regime at high energy $z(1-z)p \gg \omega_{BH} \sim T$. Based on this formalism, the effect of medium-induced

[6] We follow the notation of P. Arnold [116], and refer to [116] for comparison to other notations.

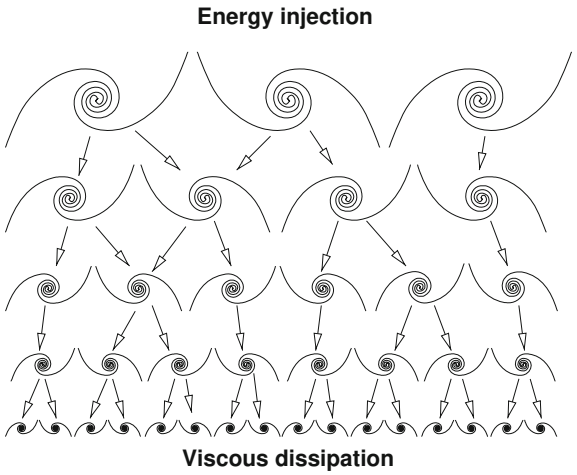

Figure 3.2: Illustration of Richardson's energy cascade (taken from [123]). The diagram demonstrates how energy is democratically and locally divided into smaller and smaller vortices all the way to the smallest scales.

radiation is then described by the $1 \leftrightarrow 2$ collision integral

$$C_a^{1\leftrightarrow 2}[\{f_i\}] = \sum_{bc}\Bigg\{ -\frac{1}{2}\int_0^1 dz \frac{d\Gamma^a_{bc}(\boldsymbol{p},z)}{dz}\Big[f_a(\boldsymbol{p})(1\pm f_b(z\boldsymbol{p}))(1\pm f_c(\bar{z}\boldsymbol{p})) \\ -f_b(z\boldsymbol{p})f_c(\bar{z}p)(1\pm f_a(\boldsymbol{p}))\Big] \\ +\frac{\nu_b}{\nu_a}\int_0^1 \frac{dz}{z^3}\frac{d\Gamma^b_{ac}(\frac{\boldsymbol{p}}{z},z)}{dz}\Big[f_b\left(\frac{\boldsymbol{p}}{z}\right)(1\pm f_a(\boldsymbol{p}))\left(1\pm f_c\left(\frac{\bar{z}}{z}\boldsymbol{p}\right)\right) \\ -f_a(\boldsymbol{p})f_c\left(\frac{\bar{z}}{z}\boldsymbol{p}\right)\left(1\pm f_b\left(\frac{\boldsymbol{p}}{z}\right)\right)\Big]\Bigg\}, \tag{3.36}$$

where $\frac{d\Gamma^a_{bc}(p,z)}{dz}$ is the effective rate for a particle a to split into b and c with energy zp and $\bar{z}p$ respectively, and we will denote $\bar{z} = 1-z$ in the following. We Fourier transform Eq. (3.33) to impact parameter space, turning the integral equation into a differential equation, which we solve numerically following a refined version of the algorithm in [122].

3.5 Wave turbulence

Before we go on to discuss the particularity of the medium cascade in the next chapters, we will use this section to briefly introduce wave turbulence, and we refer the reader to [123, 124] for more details on the subject.

Usually associated with eddies, turbulence is a complex chaotic motion sensitive to small changes in initial conditions, which is studied in the context of hydrodynamics [123, 125, 126]. When interactions occur only between eddies of similar size, an energy cascade is generated as in the Richardson cascade illustrated in Fig. 3.2. Out of the microscopic chaos emerges well-defined average quantities that can be described by the energy flux through scales. In direct energy cascade the energy is transported from large scales to small ones, e.g., in Richardson cascade, large vortices are broken up to smaller vortices in a self-similar manner until reaching the smallest scales which dissipate the energy. A cascade in the opposite direction is called an inverse cascade.

Wave turbulence is a case of turbulent behavior where the transport is described by waves instead of eddies. Specifically, for the case of weak wave turbulence where higher correlations are suppressed, one can describe the evolution using kinetic equations truncating the BBKGY hierarchy. In a system where waves interact only locally, the injection of energy at a source (k_i) far away from the sink (k_f) (where it is dissipated), generates a turbulent cascade which transports energy in a self-similar way from one scale to the next. Due to the large separation of scales in the inertial range far away from the source and sink, the system loses information about the boundaries and is naturally described by a universal behavior known as the Kolmogorov-Zakharov spectrum [123, 124]. Although wave turbulence systems are far-from-equilibrium, the generated Kolmogorov-Zakharov spectrum is a stationary solution of the kinetic equations in the inertial range, and can be obtained using analytical analysis.

A wide range of natural phenomenon can be studied using the weak wave turbulence formalism, e.g., capillary waves on water surfaces relevant for weather and ocean studies (c.f. [127]). Additionally, thermalization in field theory exhibits similar behavior [128–131] as well as parton energy loss in QCD medium [29, 30, 32] which will be relevant to our discussion in chapter 4. In order to illustrate these properties in the case of parton energy loss, following [32] we model the gluon cascade by considering only radiative emissions using an approximation of the splitting rates for high energy particles while neglecting elastic interactions and merging with

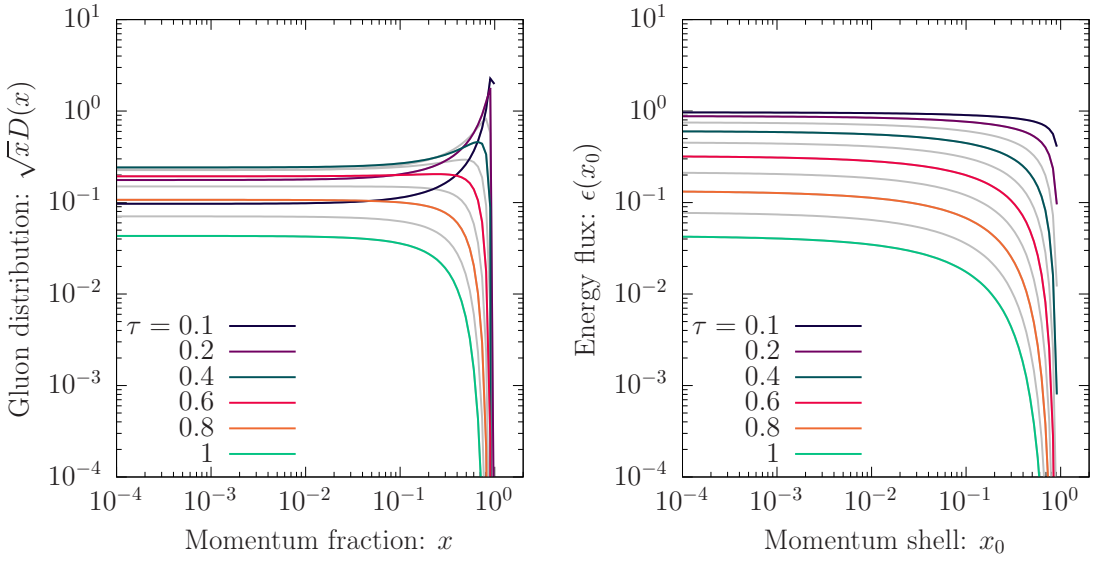

Figure 3.3: (left) Evolution of the gluon energy distribution multiplied by $\sqrt{x}$ to emphasize the Kolmogorov-Zakharov spectrum $\frac{1}{\sqrt{x}}$, at different times $\tau = 0.1 - 1$. (right) Evolution of the energy flux defined in Eq. (3.40), we observe that after time $\tau \sim 0.3$ the flux become scale independent in the inertial range $x \ll 1$.

the medium. The evolution equations are given by

$$\partial_t D(x,t) = \frac{\alpha_s N_c}{\pi t_{br}} \int_x^1 dz\ \mathcal{K}(z) \sqrt{\frac{z}{x}} D\left(\frac{x}{z}, t\right) - \frac{\alpha_s N_c}{\pi t_{br}} \int_0^1 dz\ \mathcal{K}(z) \frac{z}{\sqrt{x}} D(x,t)\ , \quad (3.37)$$

where $D(x,t) = x\frac{dN}{dx}$ is the gluon energy distribution as a function of the momentum fraction $x = \frac{|p|}{E}$. The kernel $\mathcal{K}(z)$ describes the rate of gluon radiation, and the two terms on the right-hand side represent merging ($gg \to g$) and splitting ($g \to gg$) processes. The branching time $t_{br} = \sqrt{\frac{E}{\hat{q}}}$ is the typical time it takes a leading gluon to undergo a democratic splitting ($z = \frac{1}{2}$). The simplicity of Eq. (3.37) allows us to solve for the distribution analytically if we choose the kernel to be

$$\mathcal{K}(z) = \frac{1}{[z(1-z)]^{3/2}}\ , \quad (3.38)$$

which displays the same divergences as the physical high energy kernel in sec. 4.2.2. Starting with an initial condition $D(x, t=0) = \delta(1-x)$, the rate equation is then solved by [32]

$$D(x,\tau) = \frac{\tau}{\sqrt{x}(1-x)^{3/2}} \exp\left(-\pi \frac{\tau^2}{1-x}\right)\ , \quad (3.39)$$

with $\tau = \alpha_s N_c \frac{t}{\pi t_{br}}$. At early times, the distribution displays a peak at $x = 1$ associated with the initial gluon energy as seen in Fig. 3.3. Subsequently, the energy is transported to arbitrary small scales $x \sim 0$ and a nonvanishing energy flux is generated at the origin. We can also compute the energy flux through a momentum shell x_0 as follows

$$\epsilon(x_0) = \int_{x_0}^1 dx\ D(x,\tau)\ , \quad (3.40)$$

$$= e^{-\pi\tau^2} \mathrm{erfc}\left(\sqrt{\pi}\tau \sqrt{\frac{x_0}{1-x_0}}\right)\ , \quad (3.41)$$

where $\mathrm{erfc}(x) = 1 - \frac{2}{\sqrt{\pi}} \int_0^x dt\ e^{-t^2}$ is the complementary error function. For arbitrary small scales $x_0 \ll 1$ the scale dependence drops out, and the energy flux becomes

$$\epsilon(x_0) \overset{x_0 \to 0}{\longrightarrow} e^{-\pi\tau^2}\ . \quad (3.42)$$

We see in Fig. 3.3 how the energy flux plateaus at small scales as it exponentially decays with times. Another way to describe the dynamics in the inertial range is to search for the stationary solution associated with the scale invariant energy flux.

Without the use of the analytical solution for the evolution, one can plug the ansatz $D(x) = \left(\frac{1}{x}\right)^{\lambda}$ in the evolution equations for the energy flux

$$\partial_t \epsilon(x_0) = \int_{x_0}^1 dx \ \left[\frac{\alpha_s N_c}{\pi t_{br}} \int_x^1 dz \ \mathcal{K}(z) \sqrt{\frac{z}{x}} \left(\frac{z}{x}\right)^{\lambda} - \frac{\alpha_s N_c}{\pi t_{br}} \int_0^1 dz \ \mathcal{K}(z) \frac{z}{\sqrt{x}} \left(\frac{1}{x}\right)^{\lambda}\right] . \tag{3.43}$$

By changing the order of integration and shifting the integration variable in the first term we find

$$\partial_t \epsilon(x_0) = \frac{\alpha_s N_c}{\pi t_{br}} \int_{x_0}^1 dz \ z\mathcal{K}(z) \int_{x_0/z}^1 dx \ \left(\frac{1}{x}\right)^{\lambda+\frac{1}{2}} - \frac{\alpha_s N_c}{\pi t_{br}} \int_0^1 dz \ z\mathcal{K}(z) \int_{x_0}^1 dx \ \left(\frac{1}{x}\right)^{\lambda+\frac{1}{2}} . \tag{3.44}$$

Combining the integrals we can write

$$\partial_t \epsilon(x_0) = -\frac{\alpha_s N_c}{\pi t_{br}} \int_{x_0}^1 dz \ z\mathcal{K}(z) \int_{x_0}^{x_0/z} dx \ \left(\frac{1}{x}\right)^{\lambda+\frac{1}{2}} - \frac{\alpha_s N_c}{\pi t_{br}} \int_0^{x_0} dz \ z\mathcal{K}(z) \int_{x_0}^1 dx \ \left(\frac{1}{x}\right)^{\lambda+\frac{1}{2}} , \tag{3.45}$$

for arbitrary small scales $x_0 \to 0$, we have

$$\partial_t \epsilon(x_0) \overset{x_0 \to 0}{\longrightarrow} -\frac{\alpha_s N_c}{\pi t_{br}} \int_0^1 dz \ z\mathcal{K}(z) \int_{x_0}^{x_0/z} dx \ \left(\frac{1}{x}\right)^{\lambda+\frac{1}{2}} . \tag{3.46}$$

The only way to recover a scale invariant energy flux will be to take $\lambda + \frac{1}{2} = 1$, meaning $\lambda = 1/2$ which is exactly the spectrum we see in left panel of Fig. 3.3 as well as in the analytical solution in Eq. 3.39. Although we found this spectrum using only a simplistic model for the cascade, this is the Kolmogorov-Zakharov spectrum for the in-medium cascade, which we will encounter in a more physical system in Chapter 4. That is because the existence of such spectrum does not depend on the detailed behavior of the splitting kernel, instead, it stems from the characteristic $(1/\sqrt{x})$ dependence of the rate on the momentum fraction [30].

4 Longitudinal energy loss

Recent studies revealed that hard partons lose their energy in the medium following an inverse energy cascade driven by successive radiative branchings [29, 30, 32]. These studies feature a description of the evolution which focuses solely on the hard constituents and do not properly take into account the equilibration of soft fragments and energy balance with the medium. We improve on these studies, by using the full medium-induced radiation kernel (computed in the infinite medium), and include elastic energy loss and medium recoils in the small angle approximation, allowing us to follow the jet evolution from high energies ($\sim E$) all the way to the soft medium sector ($\sim T$).

Based on the effective kinetic description introduced in the previous chapter, which parallels earlier studies in the context of jet quenching [29, 30, 32, 33] and thermalization of the QGP [34–38], we follow the in-medium energy loss of highly energetic partons starting from early collisional and radiative energy loss all the way to complete equilibration of jets inside the medium. We establish three different regimes corresponding to initial elastic and radiative energy loss, turbulent energy loss via multiple successive branchings and equilibration, and provide detailed analytical discussions of the underlying physics mechanisms in each regime. Since our evolution includes the full equilibration of the partons, we end our analysis by investigating to what extent the physics of near-equilibrium excitations is relevant to the problem of jet quenching.

4.1 Kinetic description

When investigating the in-medium evolution of the parton shower, we find it more convenient to study the re-distribution of energy, which can be quantified in terms of

$$D_a(x,t) \equiv x\frac{dN_a}{dx} = \nu_a \int \frac{d^3p}{(2\pi)^3}\,\frac{|\boldsymbol{p}|}{E}\,\delta\Big(\frac{|\boldsymbol{p}|}{E}-x\Big)\delta f_a(\boldsymbol{p},t)\;, \tag{4.1}$$

where E is the total energy of the energy distribution and $x \equiv \frac{|\boldsymbol{p}|}{E}$ is the energy fraction carried by each parton in the energy distribution. The number of degrees of

freedom are $\nu_g = 2(Nc^2-1)$ and $\nu_q = 2N_c$. We note that the distribution $D_a(x,t)$ to some extent analogous to a fragmentation function in the vacuum [30]; in particular the distributions satisfy the following sum rules, related to energy E and charge (Q_f) conservation

$$\sum_a \int dx\ D_a(x,t) = 1\ , \qquad \int \frac{dx}{x}\left(D_{q_f}(x,t) - D_{\bar{q}_f}(x,t)\right) = Q_f\ . \tag{4.2}$$

Based on Eq. (3.8), the evolution of the momentum/energy distributions of partons $D_a(x,t)$ is entirely driven by interactions with the medium constituents,

$$\partial_t D_a(x,t) = C_a^{2\leftrightarrow 2}[\{D_i\}] + C_a^{1\leftrightarrow 2}[\{D_i\}]\ , \tag{4.3}$$

where as in Eq. (4.1) we have defined $C_a[\{D_i\}] \equiv \nu_a \int \frac{d^3p}{(2\pi)^3}\ \frac{|\boldsymbol{p}|}{E}\ \delta\left(\frac{|\boldsymbol{p}|}{E} - x\right) C_a[\{f_i\},\{\delta f_i\}]$.

4.1.1 Small angle approximation

Contributions to the collision integrals for elastic $2 \leftrightarrow 2$ scattering processes can be further separated into large-angle scatterings and small-angle scatterings

$$C_a^{2\leftrightarrow 2}[\{f_i\}] = C_a^{\text{large}}[\{f_i\}] + C_a^{\text{small}}[\{f_i\}]\ , \tag{4.4}$$

by introducing a cut-off μ on the energy-momentum transfer in the t and u channels [99, 100]. When the infrared cutoff for the large-angle scattering is matched with the ultraviolet cutoff for the small-angle scattering, it can be shown that the cut-off dependence cancels, and one recovers the full in-medium matrix elements at leading and next-to-leading order [100]. Since large-angle elastic scatterings exhibit the same parametric dependencies as small angle processes [31, 34, 71], we will only consider small-angle scatterings in this chapter and leave the large angle scatterings for the next one. We then solve numerically the Boltzmann equation

$$\partial_t D_a(x,t) = C_a^{small}[\{D_i\}] + C_a^{1\leftrightarrow 2}[\{D_i\}]\ . \tag{4.5}$$

By considering the limit of small momentum transfer, the collision integral for small angle $2 \leftrightarrow 2$ scatterings reduces to a Fokker-Planck equation [99, 100] (c.f. App. A)

$$C_a^{\text{small}}[\{f_i\}] = -\nabla_p \mathcal{J}_a + S_a\ , \tag{4.6}$$

which features two distinct contributions, associated with drag and momentum diffusion ($-\nabla_p \mathcal{J}_a$) and conversion between quark and gluon degrees of freedom (S_a). Drag and momentum diffusion arise from soft u, t-channel gluon exchanges, and can be characterized by the momentum currents

$$\mathcal{J}_g = -\frac{C_A}{4}\left[\hat{\bar{q}}\nabla_{\boldsymbol{p}} f_g(\boldsymbol{p}) + \bar{\eta}_D \frac{\boldsymbol{p}}{|\boldsymbol{p}|} f_g(\boldsymbol{p})(1+f_g(\boldsymbol{p}))\right], \tag{4.7}$$

$$\mathcal{J}_{q_f} = -\frac{C_F}{4}\left[\hat{\bar{q}}\nabla_{\boldsymbol{p}} f_{q_f}(\boldsymbol{p}) + \bar{\eta}_D \frac{\boldsymbol{p}}{|\boldsymbol{p}|} f_{q_f}(\boldsymbol{p})(1-f_{q_f}(\boldsymbol{p}))\right], \tag{4.8}$$

$$\mathcal{J}_{\bar{q}_f} = -\frac{C_F}{4}\left[\hat{\bar{q}}\nabla_{\boldsymbol{p}} f_{\bar{q}_f}(\boldsymbol{p}) + \bar{\eta}_D \frac{\boldsymbol{p}}{|\boldsymbol{p}|} f_{\bar{q}_f}(\boldsymbol{p})(1-f_{\bar{q}_f}(\boldsymbol{p}))\right], \tag{4.9}$$

where $\hat{\bar{q}}$ and $\bar{\eta}_D$ are the momentum diffusion constant and the drag coefficient stripped of their respective color factor. One finds that at leading order

$$\begin{aligned}\hat{\bar{q}} \equiv & \frac{g^4}{\pi}\mathcal{L}\int \frac{d^3k}{(2\pi)^3}\left\{C_{\mathrm{A}} f_g(\boldsymbol{k})(1+f_g(\boldsymbol{k}))\right. \\ & \left. + \frac{1}{2}\sum_f \left[f_{q_f}(\boldsymbol{k})(1-f_{q_f}(\boldsymbol{k})) + f_{\bar{q}_f}(\boldsymbol{k})(1-f_{\bar{q}_f}(\boldsymbol{k}))\right]\right\},\end{aligned} \tag{4.10}$$

$$\bar{\eta}_D \equiv \frac{g^4}{\pi}\mathcal{L}\int \frac{d^3k}{(2\pi)^3}\frac{2}{|\boldsymbol{k}|}\left\{C_{\mathrm{A}} f_g(\boldsymbol{k}) + \frac{1}{2}\sum_f \left[f_{q_f}(\boldsymbol{k}) + f_{\bar{q}_f}(\boldsymbol{k})\right]\right\}, \tag{4.11}$$

where $\mathcal{L} = \int_{m_D}^{\mu} \frac{dq}{q}$ denotes the logarithmic phase-space for small angle scatterings, which we will take to be of order unity setting $\mathcal{L} = 1$ in our analysis.

Similarly, conversion terms in Eq. (4.6) stem from soft u-channel quark exchanges in the $gq \leftrightarrow gq$, $g\bar{q} \leftrightarrow g\bar{q}$ and $gg \leftrightarrow q\bar{q}$ processes, which effectively convert between particle flavors without significantly affecting their momenta. By following [99, 100], we find that the corresponding terms in the Fokker-Planck equation can be written

as

$$S_g = \frac{1}{8|\boldsymbol{p}|}\sum_f \Bigg(\Big[f_{q_f}(\boldsymbol{p})(1+f_g(\boldsymbol{p})) - f_g(\boldsymbol{p})(1-f_{\bar{q}_f}(\boldsymbol{p})) \Big] \mathcal{I}_{\bar{q}_f} + \Big[f_{\bar{q}_f}(\boldsymbol{p})(1+f_g(\boldsymbol{p})) - f_g(\boldsymbol{p})(1-f_{q_f}(\boldsymbol{p})) \Big] \mathcal{I}_{q_f} \Bigg) , \tag{4.12}$$

$$S_{q_f} = \frac{\nu_g}{\nu_q}\frac{1}{8|\boldsymbol{p}|}\Big[f_g(\boldsymbol{p})(1-f_{q_f}(\boldsymbol{p}))\mathcal{I}_{q_f} - f_{q_f}(\boldsymbol{p})(1+f_g(\boldsymbol{p}))\mathcal{I}_{\bar{q}_f} \Big] , \tag{4.13}$$

$$S_{\bar{q}_f} = \frac{\nu_g}{\nu_q}\frac{1}{8|\boldsymbol{p}|}\Big[f_g(\boldsymbol{p})(1-f_{\bar{q}_f}(\boldsymbol{p}))\mathcal{I}_{\bar{q}_f} - f_{\bar{q}_f}(\boldsymbol{p})(1+f_g(\boldsymbol{p}))\mathcal{I}_{q_f} \Big] , \tag{4.14}$$

where $\mathcal{I}_{q_f}$ and $\mathcal{I}_{\bar{q}_f}$ are given by the following moments of the phase-space distribution

$$\mathcal{I}_{q_f} = \frac{g^4 C_F \mathcal{L}}{\pi}\int \frac{d^3k}{(2\pi)^3}\frac{1}{|\boldsymbol{k}|}\Big[f_{q_f}(\boldsymbol{k})(1+f_g(\boldsymbol{k})) + f_g(\boldsymbol{k})(1-f_{\bar{q}_f}(\boldsymbol{k})) \Big] , \tag{4.15}$$

$$\mathcal{I}_{\bar{q}_f} = \frac{g^4 C_F \mathcal{L}}{\pi}\int \frac{d^3k}{(2\pi)^3}\frac{1}{|\boldsymbol{k}|}\Big[f_{\bar{q}_f}(\boldsymbol{k})(1+f_g(\boldsymbol{k})) + f_g(\boldsymbol{k})(1-f_{q_f}(\boldsymbol{k})) \Big] . \tag{4.16}$$

We note that while the conversion terms in Eq. (4.6), affect the chemistry of the QGP, they do not directly contribute to the redistribution of energy as the relevant linear combination

$$\nu_g S_g + \nu_q \sum_f (S_{q_f} + S_{\bar{q}_f}) = 0 , \tag{4.17}$$

vanishes identically.

Based on the collision integrals for small angle scattering processes in Eq. (4.6), we then proceed with the linearization around the static homogenous equilibrium background.[1] When linearizing the momentum current ($\mathcal{J}_a$) around the equilibrium distribution, one obtains two distinct types of contributions, which can be associated with changes of the phase-space density in Eqns. (4.7,4.8,4.9) or respectively with the changes of the momentum diffusion constant $\hat{\bar{q}}$ and the drag coefficient $\bar{\eta}_D$ in Eq. (4.10,4.11). Physically, the first part $\mathcal{J}_a[\{D_i\}]$ acts primarily on the hard sector, diffusing the particle momentum and dragging it to the infrared. Conversely, the second part $\delta\mathcal{J}_a[\{D_i\}]$, associated with the changes of $\hat{\bar{q}}$ and $\bar{\eta}_D$, corresponds to the

[1] Evidently the collision integral vanishes for the equilibrium background due to detailed balance.

recoil response of the medium, and describes how the energy lost from the hard sector is deposited into the softer medium particles.

Expressing the result in terms of the energy distribution $D_a(x,t)$, the hard particles currents $-\nabla_p \mathcal{J}_a[\{D_i\}]$ are given by

$$-\nabla_p \mathcal{J}_g[\{D_i\}] = \frac{C_\mathrm{A}\hat{\bar{q}}_\mathrm{eq}}{4T^2} x \left[\frac{T^2}{E^2}\partial_x x^2 \partial_x + \frac{T}{E}\partial_x x^2 (1 + 2n_B(xE))\right] \frac{D_g(x)}{x^3} \,, \tag{4.18}$$

$$-\nabla_p \mathcal{J}_{q_f}[\{D_i\}] = \frac{C_\mathrm{F}\hat{\bar{q}}_\mathrm{eq}}{4T^2} x\partial_x \left[\frac{T^2}{E^2}\partial_x x^2 \partial_x + \frac{T}{E}\partial_x x^2 (1 - 2n_F(xE))\right] \frac{D_{q_f}(x)}{x^3} \,, \tag{4.19}$$

$$-\nabla_p \mathcal{J}_{\bar{q}_f}[\{D_i\}] = \frac{C_\mathrm{F}\hat{\bar{q}}_\mathrm{eq}}{4T^2} x\partial_x \left[\frac{T^2}{E^2}\left(\partial_x x^2 \partial_x\right) + \frac{T}{E}\partial_x x^2 (1 - 2n_F(xE))\right] \frac{D_{\bar{q}_f}(x)}{x^3} \,, \tag{4.20}$$

where $\hat{\bar{q}}_\mathrm{eq}$ is the equilibrium momentum diffusion constant

$$\begin{aligned}\hat{\bar{q}}_\mathrm{eq} =& \frac{g^4}{\pi}\int \frac{d^3p}{(2\pi)^3}\left[C_\mathrm{A} n_B(p)(1+n_B(p)) + N_f n_F(p)(1-n_F(p))\right] \,, \\ =& \frac{g^4}{\pi}\frac{T^3}{2}\left(\frac{N_c}{3} + \frac{N_f}{6}\right) \,,\end{aligned} \tag{4.21}$$

and we have made use of the Einstein relation $\bar{\eta}_D = \hat{\bar{q}}_\mathrm{eq}/T$ to eliminate the drag coefficient from Eqns. (4.18,4.19,4.20). Similarly, the recoil terms $\delta\mathcal{J}_a[\{D_i\}]$ are written as

$$-\nabla_p \delta\mathcal{J}_g[\{D_i\}] = \frac{C_\mathrm{A}\hat{\bar{q}}_\mathrm{eq}}{4T^2}\frac{T\delta\bar{\eta}_D - \delta\hat{\bar{q}}}{\hat{\bar{q}}_\mathrm{eq}}\frac{\nu_g}{2\pi^2}\frac{T}{E} x\partial_x x^2 n_B(xE)(1+n_B(xE)) \,, \tag{4.22}$$

$$-\nabla_p \delta\mathcal{J}_{q_f/\bar{q}_f}[\{D_i\}] = \frac{C_F\hat{\bar{q}}_\mathrm{eq}}{4T^2}\frac{T\delta\bar{\eta}_D - \delta\hat{\bar{q}}}{\hat{\bar{q}}_\mathrm{eq}}\frac{\nu_q}{2\pi^2}\frac{T}{E} x\partial_x x^2 n_F(xE)(1-n_F(xE)) \,, \tag{4.23}$$

where the recoil coefficients are given by

$$\begin{aligned}\delta\hat{\bar{q}} =& \frac{g^4}{\pi}E^3\int dx\ \frac{1}{x}\Bigg[C_\mathrm{A}\nu_g^{-1} D_g(x)(1+2n_B(xE)) \\ &+ \frac{1}{2}\sum_f \nu_q^{-1}(D_{q_f}(x) + D_{\bar{q}_f}(x))(1-2n_F(xE))\Bigg] \,,\end{aligned} \tag{4.24}$$

$$\delta\bar{\eta}_D = \frac{g^4}{\pi}E^2\int dx\ \frac{2}{x^2}\left[C_\mathrm{A}\nu_g^{-1} D_g(x) + \frac{1}{2}\sum_f \nu_q^{-1}(D_{q_f}(x) + D_{\bar{q}_f}(x))\right] . \tag{4.25}$$

Since $\delta\hat{\bar{q}}$ and $\delta\bar{\eta}_D$ are determined by the non-equilibrium contributions from the energy distribution, they do not satisfy an Einstein relation, i.e. $\delta\bar{\eta}_D \neq \delta\hat{\bar{q}}/T$, giving rise to a finite recoil contribution in Eqns. (4.22,4.23).

Similarly, when linearizing the conversion terms around equilibrium, one finds that the contributions can be separated into conversions of hard particles $S_a[\{D_i\}]$ and (recoil) conversions of thermal constituents $\delta S_a[\{D_i\}]$ in an analogous fashion. Evaluating the action of conversions on the hard particles, one finds

$$S_g[\{D_i\}] = \nu_g \frac{\mathcal{I}^{\text{eq}}_{q_f}}{8T^2}\frac{T}{xE}\sum_f \left\{\nu_q^{-1}\Big[D_{q_f}(x)+D_{\bar{q}_f}(x)\Big](1+2n_B(xE)) - 2\nu_g^{-1}D_g(x)(1-2n_F(xE))\right\} , \tag{4.26}$$

$$S_{q_f,\bar{q}_f}[\{D_i\}] = \nu_g \frac{\mathcal{I}^{\text{eq}}_{q_f}}{8T^2}\frac{T}{xE}\left\{\nu_g^{-1}D_g(x)(1-2n_F(xE)) - \nu_q^{-1}D_{q_f,\bar{q}_f}(x)(1+2n_B(xE))\right\} , \tag{4.27}$$

where in accordance with Eqns. (4.15,4.16), we denote

$$\mathcal{I}^{\text{eq}}_{q_f} = \mathcal{I}^{\text{eq}}_{\bar{q}_f} = \frac{g^4 C_F \mathcal{L} T^2}{8\pi} , \tag{4.28}$$

for a charge neutral plasma. Due to the identity $n_F(\boldsymbol{p})(1+n_B(\boldsymbol{p})) = n_B(\boldsymbol{p})(1+n_F(\boldsymbol{p}))$ one finds that the recoil contribution to the source term S_g in Eq. (4.12) vanishes identically,

$$\delta S_g[\{D_i\}] = 0 , \tag{4.29}$$

and only the quark and antiquark channels acquire a recoil contribution given by

$$\delta S_{q_f}[\{D_i\}] = \frac{\nu_g}{2\pi^2}\frac{x^2}{8E}\left(\delta\mathcal{I}_{q_f} - \delta\mathcal{I}_{\bar{q}_f}\right)\, n_B(xE)(1-n_F(xE)) , \tag{4.30}$$

$$\delta S_{\bar{q}_f}[\{D_i\}] = \frac{\nu_g}{2\pi^2}\frac{x^2}{8E}\left(\delta\mathcal{I}_{\bar{q}_f} - \delta\mathcal{I}_{q_f}\right)\, n_B(xE)(1-n_F(xE)) , \tag{4.31}$$

where $\delta\mathcal{I}_{q_f}$ and $\delta\mathcal{I}_{\bar{q}_f}$ are the linearization of the integrals in Eqns. (4.15,4.16), whose difference is given by

$$\left(\delta\mathcal{I}_{\bar{q}_f} - \delta\mathcal{I}_{q_f}\right) = \frac{g^4 C_F \mathcal{L}}{\pi} E^2 \int dx\, \frac{1}{x^2}\,(1+2n_B(xE))\,\nu_q^{-1}\left(D_{q_f}(x) - D_{\bar{q}_f}(x)\right) . \tag{4.32}$$

Since $\sum_a \delta S_a[\{D_i\}] = 0$, the conversions of thermal constituents do not affect the energy distribution of parton fragments $\sum_a D_a(x,t)$. However, for charged partons, they do affect the distribution of valence charge, as described by the charge distributions $\frac{1}{x}(D_{q_f}(x,t) - D_{\bar{q}_f}(x,t))$.

4.1.2 Collinear radiation

We linearize the collision integral defined in Eq. 3.36, and express the contributions to the evolution equation for the energy distribution. Starting with the contributions to the evolution of the gluon distribution $D_g(x,t)$ given by the sum of $g \to gg$, $q \to qg$, $\bar{q} \to \bar{q}g$ and $g \to q\bar{q}$ processes

$$
\begin{aligned}
C_g^{g\leftrightarrow gg}[\{D_i\}] = \int_0^1 dz \frac{d\Gamma^g_{gg}(\left(\frac{xE}{z}\right), z)}{dz} \Bigg[& D_g\left(\frac{x}{z}\right)\left(1 + n_B(xE) + n_B\left(\frac{\bar{z}xE}{z}\right)\right) \\
& + \frac{D_g(x)}{z^3}\left(n_B\left(\frac{xE}{z}\right) - n_B\left(\frac{\bar{z}xE}{z}\right)\right) + \frac{D_g\left(\frac{\bar{z}xE}{z}\right)}{\bar{z}^3}\left(n_B\left(\frac{xE}{z}\right) - n_B(xE)\right)\Bigg] \\
& - \frac{1}{2}\int_0^1 dz \frac{d\Gamma^g_{gg}(xE,z)}{dz}\Bigg[D_g(x)(1 + n_B(zxE) + n_B(\bar{z}xE)) \\
& + \frac{D_g(zx)}{z^3}(n_B(xE) - n_B(\bar{z}xE)) + \frac{D_g(\bar{z}x)}{\bar{z}^3}(n_B(xE) - n_B(zxE))\Bigg],
\end{aligned} \tag{4.33}
$$

$$
\begin{aligned}
C_g^{q\leftrightarrow qg}[\{D_i\}] = \sum_f \int_0^1 dz \frac{d\Gamma^q_{gq}\left(\frac{xE}{z}, z\right)}{dz} \Bigg[& D_{q_f}\left(\frac{x}{z}\right)\left(1 + n_B(xE) - n_F\left(\frac{\bar{z}xE}{z}\right)\right) \\
& + \frac{\nu_q}{\nu_g}\frac{D_g(x)}{z^3}\left(n_F\left(\frac{xE}{z}\right) - n_F\left(\frac{\bar{z}xE}{z}\right)\right) - \frac{D_{q_f}\left(\frac{\bar{z}x}{z}\right)}{\bar{z}^3}\left(n_F\left(\frac{xE}{z}\right) + n_B(xE)\right)\Bigg],
\end{aligned} \tag{4.34}
$$

$$
\begin{aligned}
C_g^{\bar{q}\leftrightarrow\bar{q}g}[\{D_i\}] = \sum_f \int_0^1 dz \frac{d\Gamma^q_{gq}\left(\frac{xE}{z}, z\right)}{dz} \Bigg[& D_{\bar{q}_f}\left(\frac{x}{z}\right)\left(1 + n_B(xE) - n_F\left(\frac{\bar{z}xE}{z}\right)\right) \\
& + \frac{\nu_q}{\nu_g}\frac{D_g(x)}{z^3}\left(n_F\left(\frac{xE}{z}\right) - n_F\left(\frac{\bar{z}xE}{z}\right)\right) - \frac{D_{\bar{q}_f}\left(\frac{\bar{z}x}{z}\right)}{\bar{z}^3}\left(n_F\left(\frac{xE}{z}\right) + n_B(xE)\right)\Bigg],
\end{aligned} \tag{4.35}
$$

$$C_g^{g\leftrightarrow q\bar{q}}[\{D_i\}] = -\sum_f \int_0^1 dz \frac{d\Gamma^g_{q\bar{q}}(xE,z)}{dz}\Bigg[D_g(x)(1-n_F(zxE)-n_F(\bar{z}xE))$$
$$-\frac{\nu_g}{\nu_q}\frac{D_{q_f}(zx)}{z^3}(n_B(xE)+n_F(\bar{z}xE)) - \frac{\nu_g}{\nu_q}\frac{D_{\bar{q}_f}(\bar{z}x)}{\bar{z}^3}(n_B(xE)+n_F(zxE))\Bigg]. \quad (4.36)$$

where both $1 \to 2$ and inverse $2 \to 1$ processes are included along with the appropriate final state Bose enhancement and Fermi suppression, such that the above also include the (linearized) back-reaction of the high energy particles onto the medium and automatically satisfy energy-momentum conservation. Similarly, the contributions to the evolution of the energy distribution of quarks and anti-quarks $D_q(x,t)$ and $D_{\bar{q}}(x,t)$ are given by the sum of $q \to qg$ or respectively $\bar{q} \to \bar{q}g$, and $g \to q\bar{q}$ processes, which take the form

$$C_{q_f}^{q\leftrightarrow qg}[\{D_i\}] = -\int_0^1 dz \frac{d\Gamma^q_{gq}(xE,z)}{dz}\Bigg[D_{q_f}(x)(1+n_B(zxE)-n_F(\bar{z}xE))$$
$$+\frac{\nu_q}{\nu_g}\frac{D_g(zx)}{z^3}(n_F(xE)-n_F(\bar{z}xE)) - \frac{D_{q_f}(\bar{z}x)}{\bar{z}^3}(n_F(xE)+n_B(xE))\Bigg]$$
$$+\int_0^1 dz \frac{d\Gamma^q_{gq}\left(\frac{xE}{z},\bar{z}\right)}{dz}\Bigg[D_{q_f}\left(\frac{x}{z}\right)\left(1+n_B\left(\frac{\bar{z}xE}{z}\right)-n_F(xE)\right)$$
$$+\frac{\nu_q}{\nu_g}\frac{D_g\left(\frac{\bar{z}x}{z}\right)}{z^3}\left(n_F\left(\frac{x}{z}\right)-n_F\left(\frac{xE}{z}\right)\right) - \frac{D_{q_f}(x)}{\bar{z}^3}\left(n_F\left(\frac{xE}{z}\right)+n_B\left(\frac{\bar{z}xE}{z}\right)\right)\Bigg], \quad (4.37)$$

$$C_{q_f}^{g\leftrightarrow q\bar{q}}[\{D_i\}] = \int_0^1 dz \frac{d\Gamma^g_{q\bar{q}}\left(\frac{xE}{z},z\right)}{dz}\Bigg[D_g\left(\frac{x}{z}\right)\left(1-n_F(xE)-n_F\left(\frac{\bar{z}xE}{z}\right)\right)$$
$$-\frac{\nu_g}{\nu_q}\frac{D_{q_f}(x)}{z^3}\left(n_B\left(\frac{xE}{z}\right)+n_F\left(\frac{\bar{z}xE}{z}\right)\right) - \frac{\nu_g}{\nu_q}\frac{D_{\bar{q}_f}\left(\frac{\bar{z}x}{z}\right)}{\bar{z}^3}\left(n_B\left(\frac{xE}{z}\right)+n_F(xE)\right)\Bigg]. \quad (4.38)$$

and similarly for anti-quarks, with q_f replaced by $\bar{q}_f$ in the above expressions.

4.1.3 Conservation laws and scaling

Before we proceed to our analysis of the evolution of the energy distribution, we briefly note that by explicitly taking into account the back-reaction of the highly energetic particles on the thermal QGP constituents, the above evolution equations satisfy the following sum rules

$$\partial_t \sum_a \int_0^\infty dx D_a(x,t) = 0 \,, \qquad \partial_t \int_0^\infty dx \frac{1}{x} \Big(D_{q_f}(x,t) - D_{\bar{q}_f}(x,t) \Big) = 0 \,, \tag{4.39}$$

associated with energy (E) and net charge (Q_f) conservation. While for typical excitations with energies $\omega = xE \sim T$ of the order of the temperature of the QGP, all contributions of elastic and inelastic processes to the collision integrals are parametrically of the same order $\sim g^4 T$ [31, 71], the situation is markedly different for high-momentum particles with $\omega = xE \gg T$, where the various contributions to the collision integrals behave parametrically as

$$C_a^{\text{inelastic}} \sim g^4 T \sqrt{\frac{T}{xE}} D_a(x,t) \,, \tag{4.40}$$

$$C_a^{\text{Drag}} \sim g^4 T \left(\frac{T}{xE}\right) x\partial_x D_a(x,t) \,, \tag{4.41}$$

$$C_a^{\text{Conversion}} \sim g^4 T \frac{T}{xE} D_a(x,t) \,, \tag{4.42}$$

$$C_a^{\text{Diffusion}} \sim g^4 T \left(\frac{T}{xE}\right)^2 (x\partial_x)^2 D_a(x,t) \,, \tag{4.43}$$

indicating that the evolution of high-momentum particles $x \gg T/E$ will be dominated by inelastic processes, with power suppressed contributions from elastic processes. Nevertheless, including the effects of all leading order processes is important to study the evolution of softer fragments of the energy distribution all the way to the temperature scale $x \sim T/E$, where elastic and inelastic contributions eventually become comparable in magnitude [31].

4.2 Energy loss and equilibration

We study the energy loss and equilibrium of hard partons inside a thermal QGP, starting from an initial condition, where the initial energy distribution of partons $D_a(x,t)$ is given by a narrow Gaussian of width $\sigma/E = 10^{-3}/\sqrt{2}$ centered around the energy E, which is normalized to $\int dx \sum_a D_a(x,0) = 1$. Since the evolution

equations are linear, the evolution of a general solution can be decomposed into a basis set of excitations. We choose the initial condition as a Gaussian profile, which is transparent to the physics. With regard to the chemical composition, we will consider two types of initial conditions, corresponding to highly energetic gluon and quark where initially all the energy is stored either in the gluon or quark distribution respectively, Although we will refer to these two initial condition as gluon/quark jet, we would like to emphasize that they do not correspond to the usual jet definitions as this requires definitions of cones sizes which are aspects beyond the scope of this study. For a gluon jet

$$D_g^{g-jet}(x,0) = \frac{2e^{-\frac{(xE-E)^2}{2\sigma^2}}}{\sqrt{2\pi}\sigma/E\left(\mathrm{erf}\left(\frac{E}{\sqrt{2}\sigma}\right)+1\right)}\,, \qquad D_q^{g-jet}(x,0) = 0\,,$$
$$D_{\bar{q}}^{g-jet}(x,0) = 0\,, \tag{4.44}$$

whereas for a quark jet

$$D_g^{q-jet}(x,0) = 0\,, \qquad D_q^{q-jet}(x,0) = \frac{2e^{-\frac{(xE-E)^2}{2\sigma^2}}}{\sqrt{2\pi}\sigma/E\left(\mathrm{erf}\left(\frac{E}{\sqrt{2}\sigma}\right)+1\right)}\,,$$
$$D_{\bar{q}}^{q-jet}(x,0) = 0\,, \tag{4.45}$$

where the error function is given by $\mathrm{erf}(x) = \frac{2}{\sqrt{\pi}}\int_0^x dt\; e^{-t^2}$.

If not stated otherwise, we will present results for the evolution of jets with energy $E = 1000T$, and express all time scales in terms of the dimensionless time variable

$$\tau = \frac{t}{t_{\mathrm{split}}(E)} = g^4 T\sqrt{\frac{T}{E}}t\,. \tag{4.46}$$

Since $t_{\mathrm{split}}(E) = \frac{1}{g^4 T}\sqrt{\frac{E}{T}}$ corresponds to the typical timescale for an initial hard parton to undergo a quasi-democratic ($z \sim 1/2$) splitting,[2] which will ultimately dictate the energy loss [29, 34, 36, 71], we can expect that this normalization takes into account the leading dependence on the jet energy. We will further address the jet energy dependence in Sec. 4.2.2, where we compare results for different values of $E/T = 10, 30, 100, 1000$.

[2]Note that due to LPM suppression, the timescale $t_{\mathrm{split}}(E)$ is enhanced by a factor $\sqrt{\frac{E}{T}}$ relative to the typical mean free path or relaxation time $\sim \frac{1}{g^4 T}$ of near-thermal excitations.

With regard to the quark distributions, it is convenient to decompose the energy distributions $D_{q_f}(x)$ and $D_{\bar{q}_f}(x)$ into flavor singlet (S) and valence (V) distributions, which are obtained by the following linear combinations

$$D_S(x) = \sum_f D_{q_f}(x) + D_{\bar{q}_f}(x), \qquad D_{V_f}(x) = D_{q_f}(x) - D_{\bar{q}_f}(x), \tag{4.47}$$

such that the singlet distribution $D_S(x)$ characterizes the energy distribution of quarks inside the jet, whereas the valence distribution describes the distribution of valence charge inside the jet. By careful inspection of the evolution equations, one finds that at the linearized level, the evolution of $D_{V_f}(x)$ decouples from the evolution of $D_S(x)$ and $D_g(x)$, indicating that different mechanisms will ultimately be responsible for the equilibration of energy and valence charge of the jet.

Since our effective kinetic description explicitly takes into account the medium response, the total energy E as well as the set of all valence charges Q_f are explicitly conserved. Nevertheless, over the course of the evolution, jet energy and valence charge are re-distributed from high-energy ($\omega \sim E$) to low energy ($\omega \sim T$), where the soft constituents of the jet will eventually thermalize with the surrounding medium. Hence, in order to analyze jet energy loss, we define a cut-off scale $\mu = 2\pi T$, such that the hard constituents with $\omega > \mu$ are to be considered as part of the jet, whereas the soft constituents with $\omega < \mu$ are considered as part of the equilibrated medium.[3] Based on this procedure, the individual contributions of each species to the jet energy and valence charge is then evaluated as

$$E_i = \int_{\mu/E}^{\infty} dx\ D_i(x), \qquad Q_f = \int_{\mu/E}^{\infty} \frac{dx}{x}\ D_{V_f}(x). \tag{4.48}$$

We present our results for jet energy loss in Fig. 4.1, where the two upper panels show the evolution of the different contributions to the energy for quark and gluon jets. Different curves E_S, E_g in each panel, show the individual contributions of hard quarks and gluons, as well as the total energy of hard constituents E_{tot}. While initially quarks(gluons) dominate the energy budget of quark (gluon) jets, strong changes in the chemical composition of the jet take place over the course of the evolution. Eventually, by the time $\tau \gtrsim 20$ the chemical composition of quark and gluon jets becomes nearly identical; however, at this point the jet has already lost a significant fraction of its energy to the thermal medium.

By taking the time derivatives of the total energy of hard constituents E_{tot}, we can further compare the differential energy loss rate $dE/d\tau$ for quarks and gluon

[3] We note that in thermal equilibrium, around $\sim 75\%$ of the total energy are contained in the energy range $[0, 2\pi T]$.

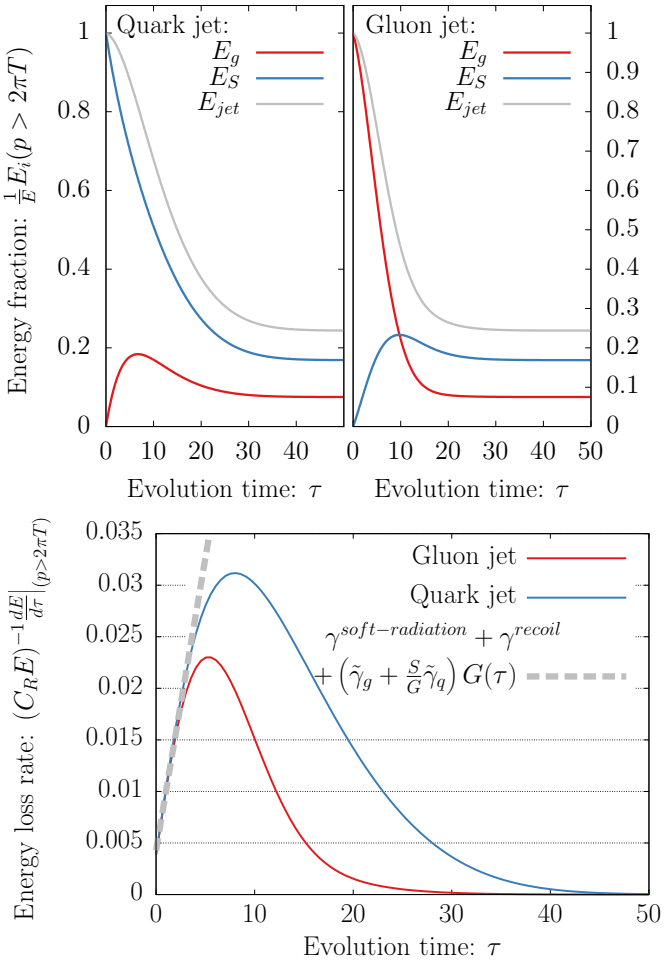

Figure 4.1: (top) Evolution of the energy carried by particles with momentum $p > 2\pi T$ for quark (left) and gluon (right) jets with $E = 1000T$. Different curves labeled $E_{g,S,jet}$ represent the energy fraction of gluons (g), quarks plus anti-quarks (S) and the sum of all species (jet). (bottom) Differential energy loss rate $dE_{\text{jet}}/d\tau$ divided by the corresponding Casimir factor ($C_R = C_A = N_c$ for gluons jets and $C_R = C_F = \frac{N_c^2-1}{2N_c}$ for quark jets).

jets, which are presented in the lower panel of Fig. 4.1. Starting from a small but non-zero energy loss rate at very early times $\tau \simeq 0$, the energy loss rate $dE/d\tau$ exhibits an approximately linear increase with evolution time τ, which follows the expected Casimir scaling such that $\frac{1}{C_F} dE/d\tau|_{q-jet} \approx \frac{1}{C_A} dE/d\tau|_{g-jet}$ at early times $\tau \lesssim 3$. Subsequently, as the hard constituents of the jet start to be significantly affected by the presence of the medium, the energy loss rate experiences a broad maximum and the Casimir scaling of the energy loss breaks down. Eventually, the energy loss rate $dE/d\tau$ decays exponentially at very late times, as the few remaining constituents equilibrate with the thermal medium.

Based on the behavior observed in Fig. 4.1, we find that the in-medium evolution of the jet can be roughly divided into three distinct stages, characterized by direct energy loss, inverse turbulent cascade, and the eventual approach to equilibrium, which we will now discuss in more detail.

4.2.1 Early stages of the evolution

During the early stages of in-medium jet evolution, elastic and inelastic processes give rise to (longitudinal) momentum broadening of the hard components of the jet, as can be seen from the widening of the distribution peak around $x \sim 1$ in Figs. 4.2 and 4.3, where we present the evolution of the energy distributions $D_g(x), D_S(x)$ and $D_V(x)$ at early times. Even though these processes initially have a small effect on the hard ($x \sim 1$) components of the jet, they can still lead to a sizeable deposition of energy into soft ($x \sim T/E$) modes due to the emission of soft radiation and recoil of the thermal medium. In order to further quantify the energy loss at early times, we can compute the energy deposition below the scale μ perturbatively, i.e. assuming that at early times $\tau \ll 1$ the distributions $D_i(x)$ of hard fragments are unmodified. By inserting the initial conditions in Eqns. (4.44, 4.45) into the evolution equations (4.22-4.25, 4.33-4.38) for the energy distribution and integrating over momentum fractions x up to the cut-off scale $\mu/E \ll 1$, one finds an approximately constant energy loss at early times

$$\left.\frac{dE}{d\tau}\right|_{\tau \ll 1} = \gamma^{\text{soft}-\text{radiation}} + \gamma^{\text{recoil}} \,, \tag{4.49}$$

where $\gamma^{\text{soft}-\text{radiation}}$ is the contribution from the emission of soft radiation and γ^{recoil} describes the contribution from elastic recoils.

Evaluating the inelastic contributions in the limit $x \ll 1$, one finds that Bose-enhancement and Fermi-suppresion factors cancel between gain and loss terms, such

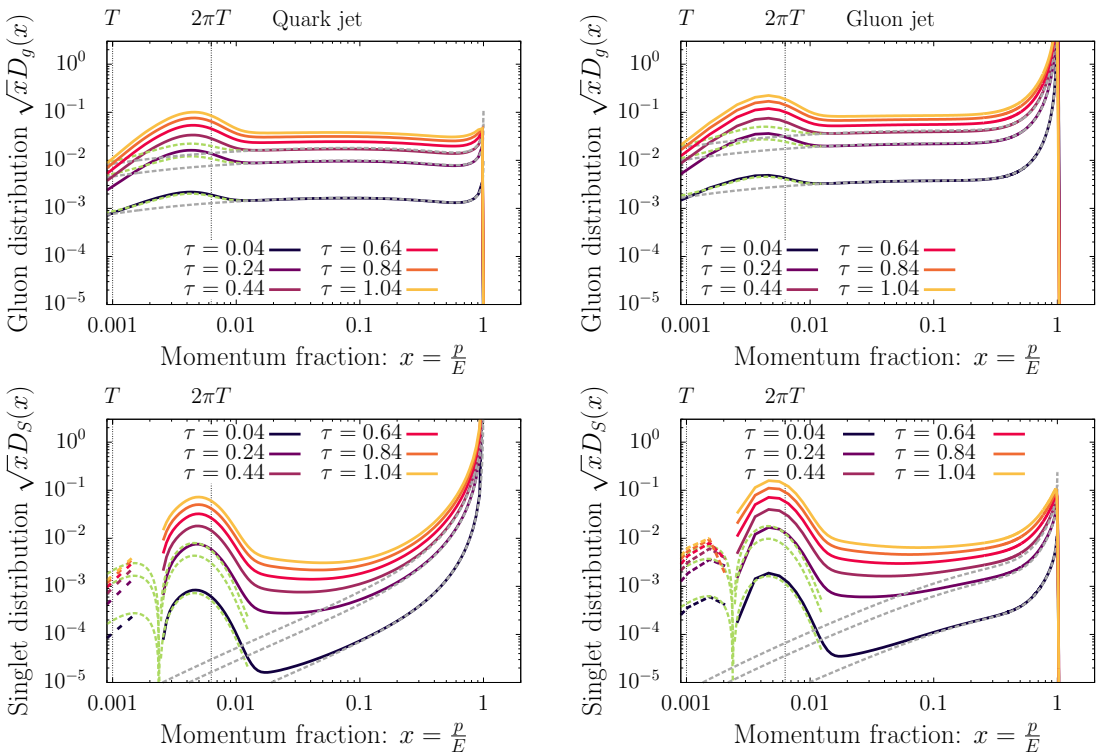

Figure 4.2: Early time behavior of the energy distribution for a quark jet (left) and a gluon jet (right). Gray dashed lines represent single splitting as written in Eqns. (4.50-4.51) and (4.52-4.53), while the green dashed lines represent the same splitting plus the elastic recoil terms from Eqns. (4.61-4.62).

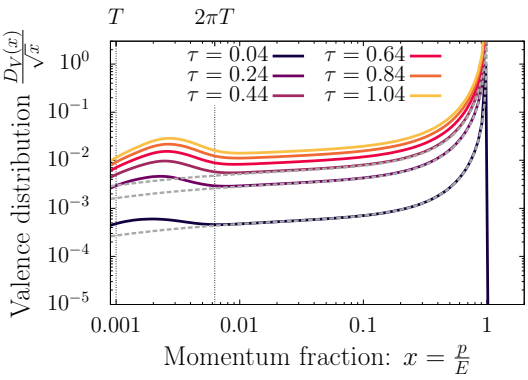

Figure 4.3: Early time behavior of the valence distribution for a quark jet. Gray dashed lines represent single splitting as written in Eqns. (4.50-4.51) and (4.52-4.53), while the green dashed lines represent the same splitting plus the elastic recoil terms from Eqns. (4.61-4.62).

that for $x \ll 1$ the radiative contributions to the energy distributions are approximately given by

$$\text{gluon jet:} \qquad D_g^{\text{soft}-\text{radiation}}(x,t) = xt \left.\frac{d\Gamma^g_{gg}(E,z)}{dz}\right|_{z=x}, \tag{4.50}$$

$$D_S^{\text{soft}-\text{radiation}}(x,t) = xtN_f \left.\frac{d\Gamma^g_{q\bar{q}}(E,z)}{dz}\right|_{z=x}, \tag{4.51}$$

$$\text{quark jet:} \qquad D_g^{\text{soft}-\text{radiation}}(x,t) = xt \left.\frac{d\Gamma^q_{gq}(E,z)}{dz}\right|_{z=x}, \tag{4.52}$$

$$D_S^{\text{soft}-\text{radiation}}(x,t) = D_V^{\text{soft}-\text{radiation}}(x,t) = xt \left.\frac{d\Gamma^q_{gq}(E,z)}{dz}\right|_{z=1-x}, \tag{4.53}$$

which is indicated in Figs. 4.2 and 4.3 by a gray dashed line for the earliest three times. Based on the above expressions, the resulting contributions to energy loss evaluate to

$$\begin{aligned}\gamma^{\text{soft}-\text{radiation}}_{g-jet} =& \frac{1}{t_{\text{split}}(E)} \int_0^\mu dx\, x \left[\left.\frac{d\Gamma^g_{gg}(E,z)}{dz}\right|_{z=x} + N_f \left.\frac{d\Gamma^g_{q\bar{q}}(E,z)}{dz}\right|_{z=x} \right], \\ =& (\underbrace{0.0072}_{g\to gg} + \underbrace{1.16\ 10^{-6}}_{g\to q\bar{q}} N_f),\end{aligned} \tag{4.54}$$

$$\gamma_{q-jet}^{\text{soft}-\text{radiation}} = \frac{1}{t_{\text{split}}(E)} \int_0^\mu dx\ x \left[\left. \frac{d\Gamma_{gq}^q(E,z)}{dz} \right|_{z=x} + \left. \frac{d\Gamma_{gq}^q(E,z)}{dz} \right|_{z=1-x} \right] , \tag{4.55}$$
$$= \underbrace{0.0038}_{q\leftrightarrow gq} ,$$

where the quoted values correspond to numerical evaluations for $E = 1000T$ and $\mu = 2\pi T$ as usual.

Similarly, from Eq.(4.22) and (4.23) we can estimate the effect of the elastic recoil at early times as

$$\gamma^{\text{recoil}} = \frac{1}{t_{\text{split}}(E)} \sum_i \int_0^\mu dx\ \delta\mathcal{J}_i[\{D_i\}] \simeq \frac{1}{t_{\text{split}}(E)} \frac{2d_A}{4TE^4} \frac{\hat{\bar{q}}}{(g^4/\pi)} \left[\delta\hat{\bar{q}} - T\delta\bar{\eta}_D \right] , \tag{4.56}$$

where in the last step we have approximated $\int_0^{2\pi} dx\ x^2 n_a(xE)(1 \pm n_a(xE)) \simeq \int_0^\infty dx\ x^2 n_a(xE)(1 \pm n_a(xE))$. Evaluating the contributions to $\delta\hat{\bar{q}}$ and $\delta\bar{\eta}_D$ based on the initial conditions for gluon and quark jets in Eq. (4.44) and (4.45), one finds that

$$\text{gluon jet:} \qquad \delta\hat{\bar{q}} = \frac{g^4}{\pi} \nu_g^{-1} C_A E^3 , \quad \delta\bar{\eta}_D = \frac{g^4}{\pi} 2\nu_g^{-1} C_A E^2 , \tag{4.57}$$

$$\text{quark jet:} \qquad \delta\hat{\bar{q}} = \frac{g^4}{\pi} \frac{\nu_q^{-1} E^3}{2} , \quad \delta\bar{\eta}_D = \frac{g^4}{\pi} \frac{2\nu_q^{-1} E^2}{2} , \tag{4.58}$$

$$\tag{4.59}$$

such that

$$\gamma^{\text{recoil}} = \frac{1}{t_{\text{split}}(E)} \frac{\hat{\bar{q}}_{\text{eq}} C_R}{4E} \left[\frac{1}{T} - \frac{2}{E} \right] \simeq \frac{\hat{\bar{q}}_{\text{eq}} C_R}{4TE} , \tag{4.60}$$

where C_R corresponds to the particle carrying all the energy in the initial condition. We also provide the behavior of the recoil contribution to the energy distribution at the early times

$$D_g^{\text{recoil}}(x,t) \simeq \frac{\hat{\bar{q}}_{\text{eq}} C_A}{4TE} x^2 t\ n_B(xE)(1 + n_B(xE)) , \tag{4.61}$$

$$D_S^{\text{recoil}}(x,t) \simeq 2\frac{\hat{\bar{q}}_{\text{eq}} C_F}{4TE} x^2 t\ n_F(xE)(1 - n_F(xE)) . \tag{4.62}$$

which is indicated in Fig. 4.2 by a green dashed line for the earliest three times. While the sum of soft radiation and recoil contributions provides an excellent description of the evolution of the energy distributions in Figs. 4.2-4.3 and the initial

energy loss rate in Fig. 4.1 at very early times, clear deviations of the spectrum at small $x \lesssim T/E$ and intermediate scales $T/E \ll x \ll 1$ start to develop rather quickly, especially in the flavor singlet quark channel (D_S). Similarly, the early-time estimate in Eq. (4.49), also fails to explain the linear rise of the energy loss rate seen in Figs. 4.2-4.3, which as we will discuss now can be attributed to multiple successive splittings, which ultimately provide a more efficient energy loss mechanism [29, 34, 36, 132].

4.2.2 Successive splittings & evolution at intermediate scales

Besides contributing to the energy loss, radiative emissions from the original hard partons in Eqns. (4.50,4.51,4.52,4.53) also establish a spectrum of intermediate energy particles, as is clearly seen from Figs. 4.2-4.3, where all intermediate scales are populated starting at early times. Such radiated quanta at intermediate energy scales $T/E \ll x \ll 1$ typically have a higher interaction rate, and they can therefore undergo subsequent interactions with the thermal medium to lose their energy.

Based on the parametric estimates in Eqns. (4.40-4.43), one expects the evolution at scales $T/E \ll x \ll 1$, to be dominated by inelastic scatterings and one can therefore approximate the collision integrals as follows

$$\begin{aligned} C_g[\{D_i\}] = &\int_0^1 dz\ \frac{d\Gamma^g_{gg}\left(\frac{xE}{z}, z\right)}{dz} D_g\left(\frac{x}{z}\right) - \frac{1}{2}\frac{d\Gamma^g_{gg}(xE,z)}{dz} D_g(x) \\ &+ \int_0^1 dz\ \frac{d\Gamma^q_{gq}\left(\frac{xE}{z}, z\right)}{dz} D_S\left(\frac{x}{z}\right) - N_f \int_0^1 dz\ \frac{d\Gamma^g_{q\bar{q}}(xE,z)}{dz} D_g(x)\ , \quad (4.63) \\ C_S[\{D_i\}] = &\int_0^1 dz\ \frac{d\Gamma^q_{gq}\left(\frac{xE}{z}, \bar{z}\right)}{dz} D_S\left(\frac{x}{z}\right) - \frac{d\Gamma^q_{gq}(xE,z)}{dz} D_S(x) \\ &+ 2N_f \int_0^1 dz\ \frac{d\Gamma^g_{q\bar{q}}\left(\frac{xE}{z}, z\right)}{dz} D_g\left(\frac{x}{z}\right)\ , \quad (4.64) \\ C_V[\{D_i\}] = &\int_0^1 dz\ \frac{d\Gamma^q_{gq}\left(\frac{xE}{z}, \bar{z}\right)}{dz} D_V\left(\frac{x}{z}\right) - \frac{d\Gamma^q_{gq}(xE,z)}{dz} D_V(x)\ , \quad (4.65) \end{aligned}$$

where we neglected the contributions from Bose enhancement and Fermi suppression, which are exponentially suppressed for energies $xE \gg T$. Since at sufficiently high jet energies the relevant splitting rates Γ^a_{bc} are in the deep LPM regime [116, 133],

they can further be approximated by the leading-log solutions [30, 116][4]

$$\frac{d\Gamma^g_{gg}(xE,z)}{dz} \simeq \frac{1}{\sqrt{x}}\mathcal{K}_{gg}(z) = \frac{\alpha_s}{2\pi}P_{gg}(z)\sqrt{\frac{\hat{\hat{q}}(xE)}{xE}}\sqrt{\frac{(1-z)C_A + z^2 C_A}{z(1-z)}}\,, \tag{4.66}$$

$$\frac{d\Gamma^q_{gq}(xE,z)}{dz} \simeq \frac{1}{\sqrt{x}}\mathcal{K}_{gq}(z) = \frac{\alpha_s}{2\pi}P_{qg}(z)\sqrt{\frac{\hat{\hat{q}}(xE)}{xE}}\sqrt{\frac{(1-z)C_A + z^2 C_F}{z(1-z)}}\,, \tag{4.67}$$

$$\frac{d\Gamma^g_{q\bar{q}}(xE,z)}{dz} \simeq \frac{1}{\sqrt{x}}\mathcal{K}_{qg}(z) = \frac{\alpha_s}{2\pi}P_{gq}(z)\sqrt{\frac{\hat{\hat{q}}(xE)}{xE}}\sqrt{\frac{C_F - z(1-z)C_A}{z(1-z)}}\,, \tag{4.68}$$

where in the above expressions $\hat{\hat{q}}(xE)$ should be fixed to match the full splitting kernel at the relevant energy scale (see Appendix B for a comparison). Based on the above expressions for the splitting rates, and the initial conditions in Eqns. (4.44) and (4.45) the single emission spectrum then takes the approximate form

$$D_g(x,t) \simeq \frac{G(t)}{\sqrt{x}}\,, \tag{4.69}$$

$$D_S(x,t) \simeq S(t)\sqrt{x}\,, \tag{4.70}$$

featuring the characteristic $1/\sqrt{x}$ and $\sqrt{x}$ power laws in the gluon and singlet quark channels with linearly rising amplitudes $G(t)$ and $S(t)$ given by

$$\text{gluon jet: } G(t) = C_A^{3/2}\frac{\alpha_s}{2\pi}\sqrt{\frac{\hat{\hat{q}}(E)}{E}}t\,, \quad S(t) = 2C_F^{1/2}N_f T_R\frac{\alpha_s}{2\pi}\sqrt{\frac{\hat{\hat{q}}(E)}{E}}t\,, \tag{4.71}$$

$$\text{quark jet: } G(t) = C_F C_A^{1/2}\frac{\alpha_s}{2\pi}\sqrt{\frac{\hat{\hat{q}}(E)}{E}}t\,, \quad S(t) = C_F^{3/2}\frac{\alpha_s}{2\pi}\sqrt{\frac{\hat{\hat{q}}(E)}{E}}t\,. \tag{4.72}$$

Beyond early times, the perturbative description in Eq. (4.71) breaks down, as the radiated quanta undergo successive splittings; the spectrum at intermediate scales $T/E \ll x \ll 1$ no longer follows the single emission spectra from hard ($x \sim 1$) primaries, but is instead determined by the dynamics of multiple successive branchings of semi-hard ($T/E \ll x \ll 1$) fragments with a continuous influx of energy and valence charge due to continued emissions from the hard ($x \sim 1$) primaries.

In this context, it is important to point out that the set of evolution equations for multiple successive branchings of semi-hard ($T/E \ll x \ll 1$) fragments in

[4] Note that this approximation is also commonly referred to as harmonic oscillator approximation, and that the functions $\mathcal{K}_{ij}$ agree with the definitions in [30].

Eqns. (4.63-4.65) features a stationary solution of the form

$$D_g(x) = \frac{G}{\sqrt{x}}\,, \quad D_S = \frac{S}{\sqrt{x}}\,, \quad D_V = V\sqrt{x}\,, \tag{4.73}$$

which following earlier works [29, 30] corresponds to the Kolmogorov-Zhakarov (KZ) spectrum of weak-wave turbulence, and is associated with the stationary transport of energy and valence charge towards lower energies, i.e. an inverse energy and respectively particle cascade. Despite the fact that the spectral shape $\propto 1/\sqrt{x}$ of the stationary gluon spectrum in Eq. (4.73) agrees with that of single gluon emission spectra in Eq. (4.71), this agreement is to some extent accidental, as the spectral shape of the KZ spectrum is determined by the characteristic energy x-dependence of the splitting rates $\Gamma(xE, z) \sim \sqrt{\frac{\hat{q}}{xE}}$ in Eq. (4.66) rather than the specific z-dependence of the splitting functions [30, 32, 123, 124]. Similarly, the stationary Kolmogorov-Zakharov spectrum for the singlet quark distribution, also features the same $\propto 1/\sqrt{x}$ behavior as the gluon distribution, with the ratio quark and gluon distributions $\frac{D_S(x)}{D_g(x)} = \frac{S}{G}$ determined by the (local) balance of $g \to q\bar{q}$ and $q \to qq$ processes[30]

$$\frac{S}{G} = \frac{2N_f \int dz\; z\; \mathcal{K}_{qg}(z)}{\int dz\; z\; \mathcal{K}_{gq}(z)} \approx 0.07 \times 2N_f \tag{4.74}$$

which is in sharp contrast to the single emission spectra in Eq.(4.71), where quark emission is power suppressed compared to gluon emission at small x.

Numerical results for the evolution of the in-medium energy distributions at intermediate times τ are presented in Fig. 4.4, where the different panels show the distributions $D_g(x), D_S(x)$ and $D_V(x)$ for quarks jets (left column) and gluon jets (right column). Despite the fact that the numerical results include both elastic and radiative processes with full in-medium splitting rates, the turbulent spectra in Eq. (4.73) are clearly visible at intermediate energy scales and persist over the entire range of evolution times shown in Fig. 4.4. Especially in the subdominant channels, i.e., for the singlet quark distribution inside a gluon jet, or the gluon distribution inside a quark jet, the turbulent spectrum persists over a large range of energy fractions $0.02 \lesssim x \lesssim 0.5$ while for the dominant channels, it is not as prominent due to the additional contributions from the jet peak around $x \sim 1$. Strong deviations from the turbulent spectrum also emerge at small $x \sim T/E$, where the effective description in Eqns. (4.73) breaks down, as other contributions from elastic and inelastic processes become equally important and ultimately lead to the thermalization of the soft fragments.

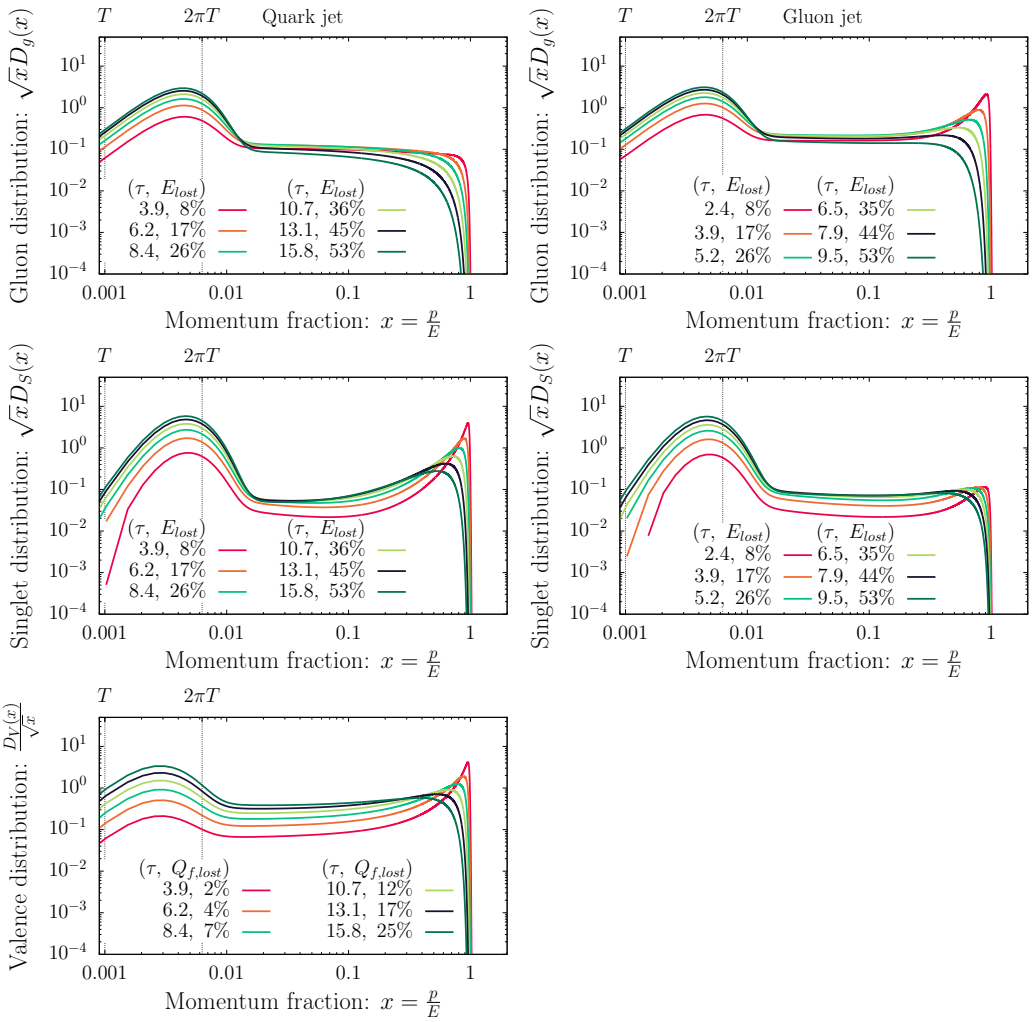

Figure 4.4: Evolution of the energy distribution at intermediate times for a quark jet (left) and a gluon jet (right). One clearly observes the Kolmogorov-Zakhrov spectra in Eq. (4.73) at intermediate energies $T/E \ll x \ll 1$.

Clearly, the onset of turbulence has important consequences for the jet energy loss [29, 30, 34, 36, 132]. Since semi-hard fragments with $T/E \ll x \ll 1$ can efficiently lose energy to the thermal bath via multiple successive quasi-democratic ($z \sim 1/2$) splittings, the energy that is injected into the cascade due to semi-hard ($T/E \ll x \ll 1$) primary emissions is efficiently transferred all the way to the scale of the thermal medium $x \sim T/E$, thus providing a highly efficient energy loss mechanism. One characteristic feature of this turbulent transport is the fact that it can be described by an energy flux

$$\frac{dE}{d\tau}(\Lambda) = \sum_i \int_{\Lambda/E}^{\infty} dx \; \partial_\tau D_i(x) \; . \tag{4.75}$$

from high-momenta ($x \sim 1$) to low momenta ($x \sim T/E$), which is independent of the momentum scale Λ where the energy flux is evaluated. Numerical results for the energy flux $\frac{dE}{d\tau}(\Lambda)$ are presented in Fig. 4.5, where we show the dependence of $\frac{dE}{d\tau}(\Lambda)$ on the momentum scale Λ for three different jet energies $E = 10, 100, 1000T$ at various stages of the evolution. When the separation of scales between the jet energy E and the medium temperature T is large, we clearly see a plateau in the energy flux, which is virtually constant within an inertial range of momenta between the jet energy and the medium temperature. Such scale invariance of the energy flux ensures the energy injected into the cascade is transported from high-energy ($x \sim 1$) to low-energy ($x \sim T/E$) fragments, without an accumulation of energy at any intermediate scale. Conversely, the variations of the energy flux with the scale Λ indicate the regions where energy is dissipated from the hard components of the jet ($x \sim 1$) and accumulated at the scale of the medium temperature $x \sim T/E$. By comparing the behavior for different jet energies in Fig. 4.5, we find that even for jets with moderately high energies, $E = 100T$, there is still a sizeable momentum range where an approximately scale invariant energy flux is formed at intermediate times, during which the jet loses most of its energy to the thermal medium. However, for very low energy jets, $E = 10T$, the energy flux strongly varies with the momentum scale Λ, indicating that without a significant separation of scales the energy of the jet is directly transferred to the medium without resorting to a turbulent energy cascade.

Based on the approximate form of the kinetic equations for $T/E \ll x \ll E$, we can estimate the energy loss $\frac{dE}{d\tau}$ in the turbulent regime as the scale invariant energy

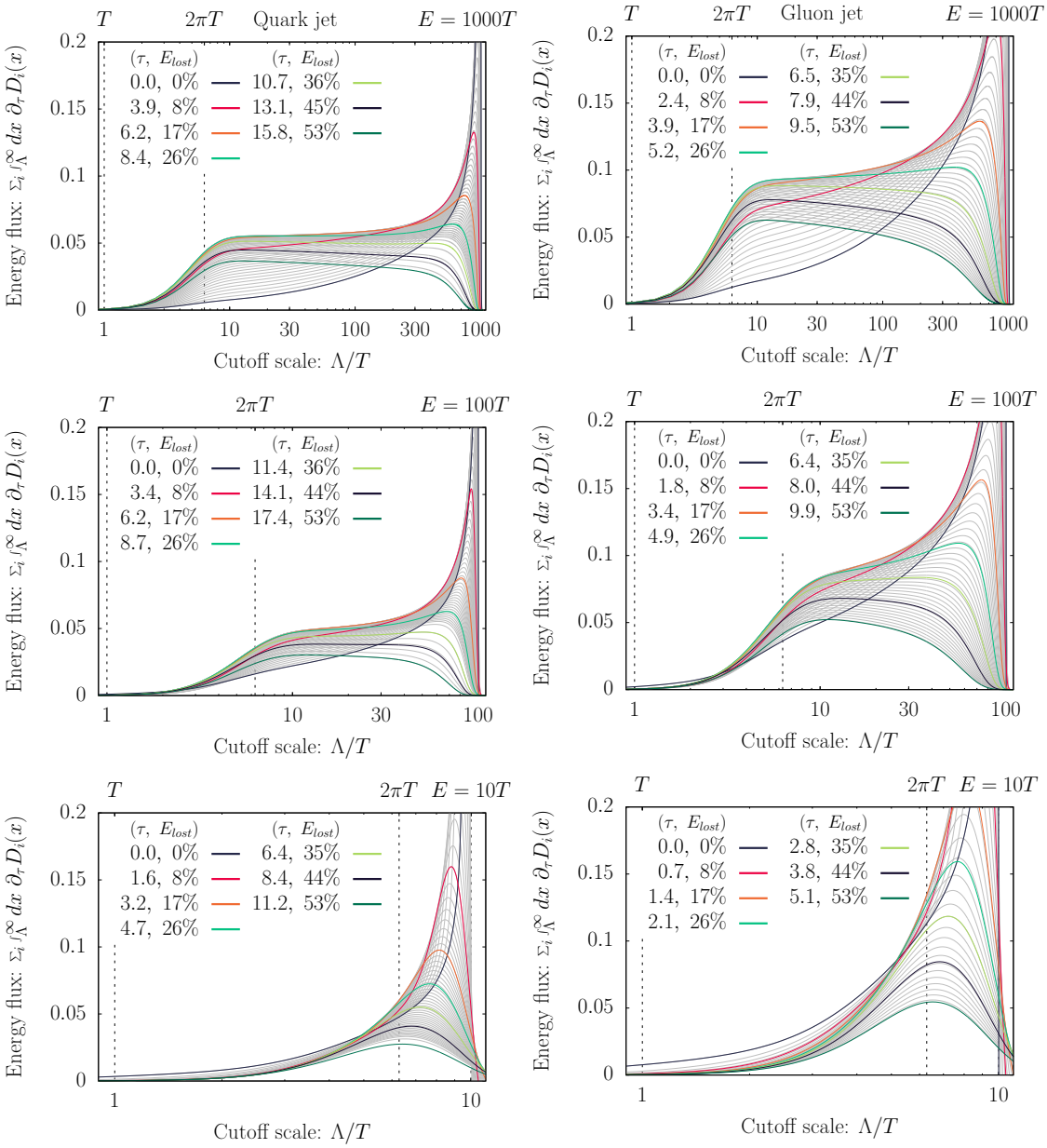

Figure 4.5: Evolution of the energy flux in Eq. 4.75 for quark (left) and a gluon (right) jets with different initial energies $E = 1000, 100, 10T$ from top to bottom. Different curves in each panel show the energy flux at different times with gray lines corresponding to intermediate times.

flux, which can be computed as

$$\begin{aligned}\frac{dE}{d\tau} =& \int_{\mu/E}^{1} dx \int_{x}^{1} dz \ [\mathcal{K}_{gg}(z) + 2N_f \mathcal{K}_{qg}(z)] \sqrt{\frac{z}{x}} D_g\left(\frac{x}{z}\right) \\ &- \int_{\mu/E}^{1} dx \int_{0}^{1} dz \ [\mathcal{K}_{gg}(z) + 2N_f \mathcal{K}_{qg}(z)] \frac{z}{\sqrt{x}} D_g(x) \ , \\ &+ \int_{\mu/E}^{1} dx \int_{x}^{1} dz \ [\mathcal{K}_{gq}(z) + \mathcal{K}_{gq}(1-z)] \sqrt{\frac{z}{x}} D_S\left(\frac{x}{z}\right) \\ &- \int_{\mu/E}^{1} dx \int_{0}^{1} dz \ \mathcal{K}_{gq}(z) \frac{1}{\sqrt{x}} D_S(x) \ , \end{aligned} \tag{4.76}$$

By changing the order of integration and performing a change of variable $x \to x/z$ to combine the gain and loss terms, the energy flux can be re-expressed as [30]

$$\begin{aligned}\frac{dE}{d\tau} =& - \int_{\mu/E}^{1} dz \ z[\mathcal{K}_{gg}(z) + 2N_f \mathcal{K}_{qg}(z)] \int_{\mu/E}^{\mu/zE} dx \ \frac{D_g(x)}{\sqrt{x}} \\ &- \int_{0}^{\mu/E} dz \ z[\mathcal{K}_{gg}(z) + 2N_f \mathcal{K}_{qg}(z)] \int_{\mu/E}^{1} dx \ \frac{D_g(x)}{\sqrt{x}} \\ &- \int_{\mu/E}^{1} dz \ 2z \left[\mathcal{K}_{gq}(z) + \mathcal{K}_{gq}(1-z)\right] \int_{\mu/E}^{\mu/zE} dx \ \frac{D_S(x)}{\sqrt{x}} \\ &- \int_{0}^{\mu/E} dz \ 2z[\mathcal{K}_{gq}(z) + \mathcal{K}_{gq}(1-z)] \int_{\mu/E}^{1} dx \ \frac{D_S(x)}{\sqrt{x}} \ . \end{aligned} \tag{4.77}$$

Such that upon making use of the explicit form of the Kolmogorov-Zhakarov spectrum in Eq. (4.73), one obtains the scale invariant energy flux in the limit $\mu/E \ll 1$ as

$$\frac{dE}{d\tau} = \tilde{\gamma}_g G + \tilde{\gamma}_q S \ , \tag{4.78}$$

with the flux constants

$$\tilde{\gamma}_g = \int_{0}^{1} dz \ z[\mathcal{K}_{gg}(z) + 2N_f \mathcal{K}_{qg}(z)] \ \log(z) = \frac{\alpha_s}{2\pi} \sqrt{\frac{\hat{\bar{q}}(\sqrt{TE})}{E}} (25.78 + 2N_f 0.177) \ , \tag{4.79}$$

$$\tilde{\gamma}_q = \int_{0}^{1} dz \ 2z[K_{gq}(z) + K_{qq}(z)] \log(z) \quad = \frac{\alpha_s}{2\pi} \sqrt{\frac{\hat{\bar{q}}(\sqrt{TE})}{E}} (11.595) \ , \tag{4.80}$$

where we chose to evaluate $\hat{\bar{q}}(\sqrt{TE})$ at an intermediate scale between the jet energy E and the medium temperature T. While the splitting functions in Eq. (4.66)

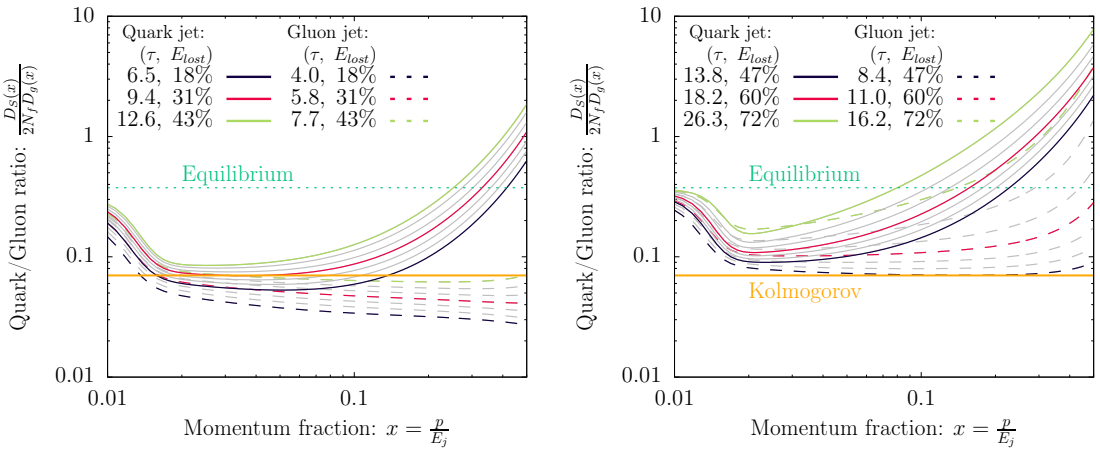

Figure 4.6: Quark to gluon ratio $D_S(x)/2N_f D_g(x)$ at different times as a function of the momentum fraction x. Different curves in each panel correspond to a quark jet (solid lines) and a gluon jet (dashed lines), at evolution times indicated by the amount of energy that the jet has lost. Horizontal lines correspond to the equilibrium ratio $D_S(x)/2N_f D_g(x) = \nu_q/\nu_g$ which is approached at small x, and the universal Kolmogorov ratio in Eq. (4.74) which is approached at intermediate values of $T/E \ll x \ll 1$ for a transient period of time.

exhibit a singular behavior for soft emissions $(z, 1-z \to 0)$, it is important to point out that the energy flux in Eqns. (4.78) is in fact dominated by quasi-democratic $(z \sim 1/2)$ splittings, and we refer the interested reader to [30] for further discussion and additional details of the above calculation.

By making the amplitude $G(\tau)$ time dependent, in order to account for the injection of energy into the cascade due to radiation from the hard $(x \sim 1)$ primaries as in Eq. (4.69), and adding the contributions from soft-radiation and recoil, the energy loss in the turbulent regime can then be estimated as

$$\frac{dE}{d\tau} = \gamma^{\text{soft}-\text{radiation}} + \gamma^{\text{recoil}} + \left(\tilde{\gamma}_g + \frac{S}{G}\tilde{\gamma}_q\right) G(\tau) \,, \tag{4.81}$$

which is shown in Fig. 4.1 as a gray dashed line and provides an excellent description of the numerical results up to times $\tau \lesssim 5$ where jets have deposited about 30% of their energy to the thermal medium.

One striking prediction of the turbulent energy loss mechanism, is the universal ratio of quark and gluon energy distributions $D_S(x)/D_g(x)$ in Eq. (4.74) within an inertial range of energy $T/E \ll x \ll 1$. Now, in order to verify to what extent this

behavior can be realized over the course of the jet medium evolution, we present our numerical results for the quark to gluon ratio in Fig. 4.6, which includes all effects due to elastic and in-elastic interactions as described in Sec. 4.1. Different curves in Fig. 4.6, show the results for $D_S(x)/2N_f D_g(x)$ for quark (solid lines) and gluon jets (dashed lines), at various stages of the evolution. Indeed, one finds that starting around the time when the jet has lost about 20% of its total energy, the quark to gluon ratio at intermediate values of $0.02 \lesssim x \lesssim 0.1$ is rather well described by the universal Kolmogorov ratio in Eq. (4.74) indicated by a solid orange line in Fig.4.6. Vice versa, for small momentum fractions $x \sim T/E$ on the order of the medium temperature, the quark to gluon ratio approaches its equilibrium value of $D_S(x)/2N_f D_g(x) = \frac{\nu_q}{\nu_g}$ indicating that the soft fragments of the jet have had sufficient time to undergo chemical equilibration. While at early times the large x components of the jet are dominated by the primary jet peak, and the jet chemistry is dominated by the primary species, i.e., by gluons for gluon jets and by quarks for quark jets, the situation is different at late times when the jet has lost a significant amount of its energy. Due to the fact that hard gluons lose their energy more efficiently compared to hard quarks, one finds that the medium effectively acts as a chemical filter, such that even for gluon jets, the hardest constituents of strongly quenched jets are more likely to be quarks, as can be inferred from the steep rise of the quark to gluon ratio in the right panel of Fig. 4.6.

4.2.3 Evolution towards equilibrium

Eventually, the hard fragments of the jet have had sufficient time to undergo multiple successive quasi-democratic branchings to deposit a significant amount of their initial energy into the thermal medium. During this last stage of the evolution depicted in Fig. 4.7, the few remaining hard fragments continue to lose energy and valence charge thereby heating up the thermal bath and doping it with the valence charge. We find that in this regime, the in-medium jet evolution follows the characteristic pattern of "bottom-up" thermalization [34–36, 72], where the low energy part of the distribution ($x \sim T/E$) is well described by the (linearized) equilibrium distributions

$$D_g^{\mathrm{eq}}(x) = \nu_g \delta T \; \partial_T n_B(xE) \; , \tag{4.82}$$

$$D_S^{\mathrm{eq}}(x) = 2N_f \nu_q \delta T \; \partial_T n_F(xE) \; , \tag{4.83}$$

$$D_{V_f}^{\mathrm{eq}}(x) = \nu_q \delta\mu_f \; \partial_\mu n_F(xE)|_{\mu=0} \; . \tag{4.84}$$

with increasing temperature δT and chemical potential $\delta\mu_f$ as a function of time, which eventually approach their final equilibrium values, indicated by the dashed

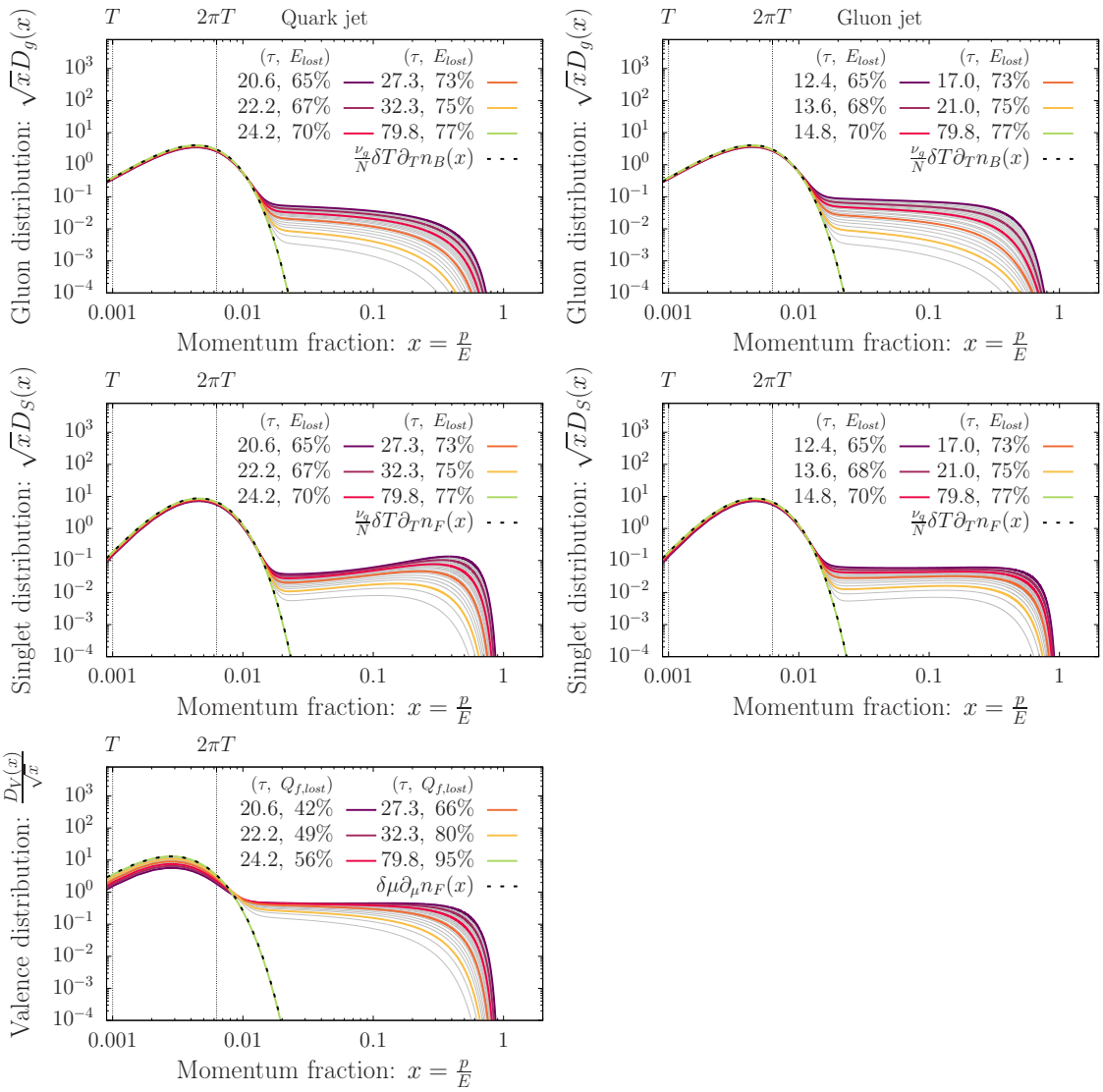

Figure 4.7: Evolution of the energy distributions at late times for quark (left) and gluon (right) jets. Dashed lines in each panel represent the asymptotic equilibrium distributions in Eq. (4.82-4.84).

lines in Fig. 4.7. While the soft sector is already thermalized, the evolution of the hard components of the distribution continues to be well described by the Kolmogorov-Zhakarov spectra in Eq. (4.73) up to the highest available momentum fractions at each instant of time; as the hard components continue to lose their energy to the thermal bath, this cascade proceeds towards lower and lower energies, in a fashion that is characteristic of decaying turbulence [29, 30, 123, 124].

Clearly, the final stages of kinetic and chemical equilibration of jets closely resemble the thermalization patterns previously observed in the context of thermalization of the QGP at early times in heavy-ion collisions [34, 37, 72]. We will now further investigate to what extent the kinetic and chemical equilibration of jets is similar to the typical excitations of the medium, encoded e.g., in the transport properties of the QGP [134]. Based on our effective kinetic description of in-medium jet evolution, the evolution of small perturbations around equilibrium can be compactly expressed as

$$\partial_t D_a(x,t) = \int dz\ \delta C_{ab}(x,z) D_b(z,t) \tag{4.85}$$

indicating that the long time behavior of the distributions $D_a(x,t)$ is determined by the low-lying spectrum of the linearized collision operator $\delta C_{ab}(x,z)$, as quantified by the following eigenvalue equation

$$\int dz\ \delta C_{ab}(x,z) D_b(z,t) = \lambda_{(k)} D_b^{(k)}(x,t) \tag{4.86}$$

We provide a compact summary of our findings in Figs. 4.8 where we show the spectrum of the low-lying eigenvalues $\lambda_{(k)}$ along with the corresponding eigenfunctions $D_a^{(k)}(x,t)$, determined by numerical diagonalization of the discretized collision operator[5].

Since the effective kinetic description in Sec.4.1, exactly conserves the energy E and valence charges Q_f, there is a total of $N_f + 1$ zero modes $\lambda_{(k)} = 0$ of the collision operator, whose eigenfunctions correspond to the equilibrium solutions in Eq. (4.82), and are correctly reproduced by our numerical analysis in Figs. 4.8. Due to the fact that energy and valence charge evolution decouple from each other in the linearized kinetic description, the linearized collision operator is block diagonal and one can further distinguish between the spectrum of modes $\lambda_{(k)}^{(E)}$ in the energy sector, spanned by the distributions (D_g, D_S), and the N_f-fold degenerate spectrum of modes $\lambda_{(k)}^{(V)}$ in the valence charge sector (D_{V_f}). Based on our analysis, we find

[5] We have checked explicitly that varying the discretization does not significantly alter the results.

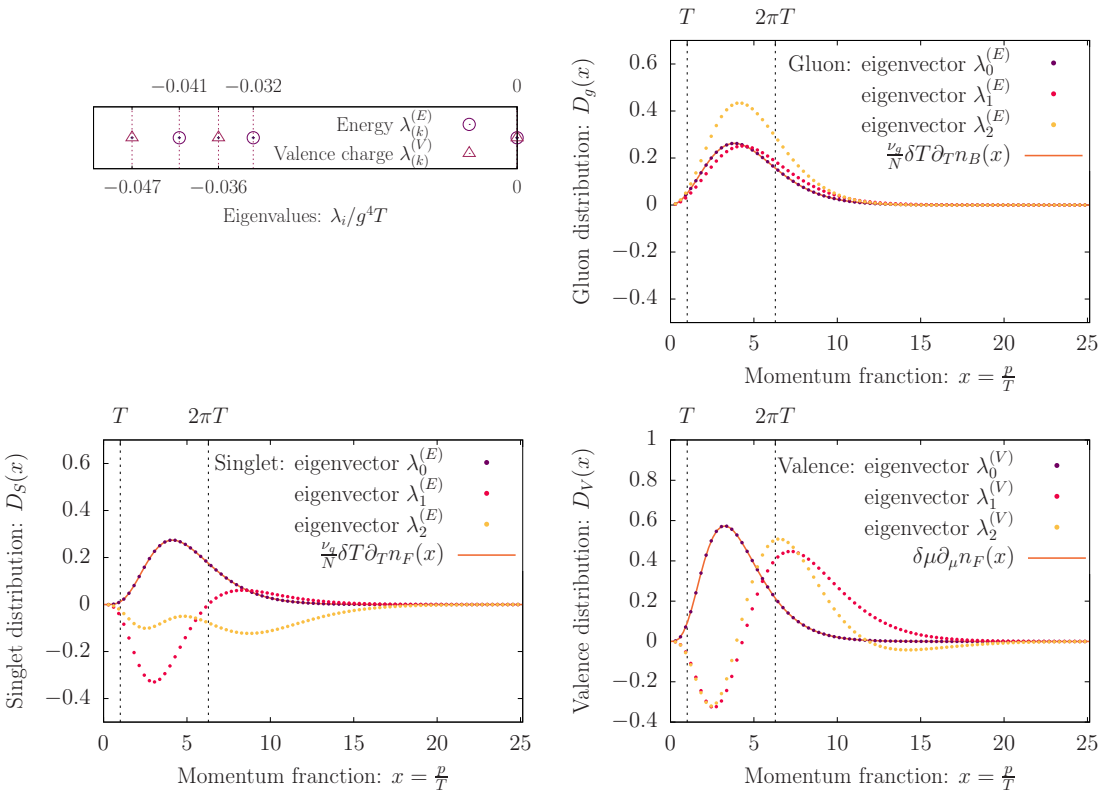

Figure 4.8: Spectrum of the linearized collision operator. Different panels show the low-lying eigenvalues (top left) as well as the associated eigenfunctions in the gluon (top right), singlet (bottom left) and valence charge (bottom right) channels. Eigenfunctions have been normalized according to $\int dx\ D_g(x)^2 + D_S(x)^2 = 1$ in the energy sector and $\int dx\ D_V(x)^2 = 1$ in the valence charge sector.

that both energy and charge sector feature a discrete low-lying spectrum with low-lying eigenvalues $\lambda_{1,2}^{(V)}$ and $\lambda_{1,2}^{(E)}$ of similar magnitude, which in accordance with our discussion determine the relaxation rates for energy and charge equilibration close to equilibrium. We also find that the corresponding eigenfunctions are localized at low energies p/T, in the sense that they decay exponentially [135] at large energies as can be inferred from Fig. 4.8.

Now that we have determined the near-equilibrium relaxation rates for energy and charge equilibrium, it is insightful to revisit the evolution of the jet energy (E) and valence charge (Q_f) loss rates. Numerical results for the time evolution of the energy and valence charge loss rates are presented in Fig. 4.9, which compactly summarize our results for quark (dashed lines) and gluon jets (solid lines), with initial energies $E = 30, 100, 300, 1000T$. By comparing the results for different energies in the top panels, which shows the rates $\frac{1}{C_R} dE/d\tau$ and $dQ_f/d\tau$ as a function of the natural timescale $\tau = t/t_{\rm split}(E)$ for jet evolution, one finds that the leading jet energy dependence is indeed determined by the timescale for hard splittings $t_{\rm split}(E)$ and correctly captured by the scaling variable. Nevertheless, with decreasing jet energy one observes a gradual change in the energy loss pattern, where the constant energy and valence charge loss due to soft radiation and recoil starts to become increasingly important compared to the turbulent jet energy loss mechanism. Bottom panels of Fig. 4.9 show the same data for energy and valence charge loss, but now in units of the natural medium timescale $1/g^4T$ of the thermal medium. Based on our above discussion, one ultimately expects that at asymptotically late times, the in-medium evolution of the jet will be governed by the near-equilibrium relaxation rates, corresponding to the lowest eigenvalues $\lambda_1^{(E)}$ and $\lambda_1^{(V)}$ of the linearized collision operator. While for low energy jets, $E = 30T$, such an exponential decay is clearly visible at late times, as indicated by the gray dashed lines in Fig. 4.9 which represent fits of the form $\frac{dE}{dt} \propto e^{\lambda_1^{(E)} t}$ and $\frac{dQ}{dt} \propto e^{\lambda_1^{(V)} t}$, it is important to note that the jets have already lost nearly all of their energy by the time that this near-equilibrium linear response treatment becomes applicable. We therefore conclude that the in-medium evolution of high-energy jets should be considered as a genuine far-from-equilibrium probe of the QGP, whose space-time dynamics can not be directly related to that of near-equilibrium excitations and generally requires a detailed microscopic description.

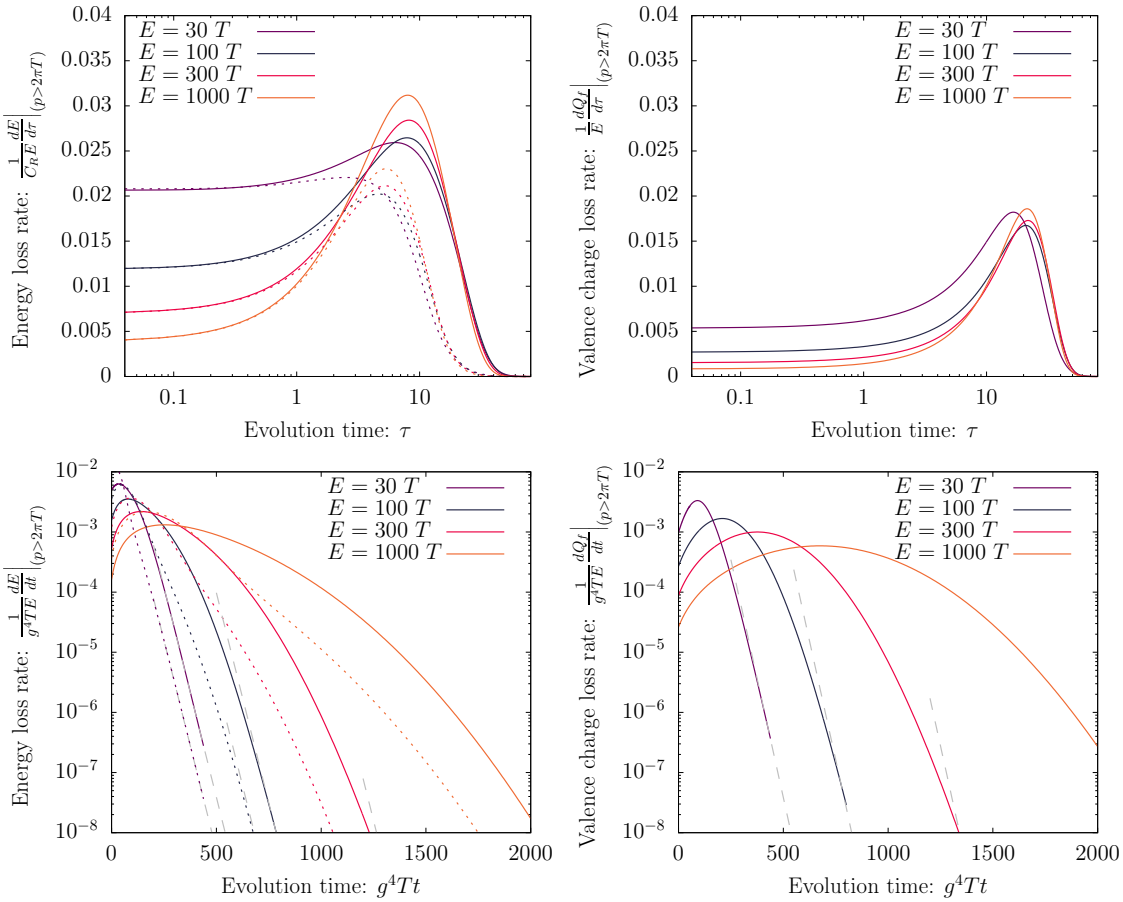

Figure 4.9: Comparison of energy and valence charge loss rates for quark (full lines) and a gluon (dashed lines) jets, with different initial jet energies $E = 30, 100, 300, 1000$. Dashed lines in the lower panel represent fits to an exponential decay using the first nonzero eigenvalues as the decay constant.

4.3 Discussion

Based on an effective kinetic description of hard partons in a thermal medium, we established a comprehensive picture of in-medium hard parton evolution, from the earliest stages of elastic and radiative energy loss all the way towards kinetic and chemical equilibration of hard partons inside the medium. By including the leading order small angle elastic and inelastic processes, that ensure energy and charge conservation and allow us to follow the evolution of the parton shower all the way towards equilibrium, we confirm earlier findings [29, 30] that the energy loss of highly energetic partons is dominated by a turbulent cascade due to successive radiative branchings. By investigating the energy flux along the cascade, we explicitly demonstrated that the turbulent cascade transports energy all the way from the energy scale of the jet $x \sim 1$ to the temperature of the thermal medium $x \sim T/E$, where all leading order kinetic processes become of comparable importance. Due to multiple successive branchings, the in-medium energy distributions become insensitive to the hard structure of the jet and display universal turbulent features in an inertial range of energy fractions $T/E \ll x \ll 1$, while the soft fragments of the distribution with $x \lesssim T/E$ rapidly thermalize inside the medium.

Even though the in-medium evolution of hard particles closely resembles the thermalization patterns observed in previous studies of the thermalization of the QGP at early times [34, 37, 72], it turns out that the dominant mechanism underlying jet quenching is quite different from the typical relaxation of near-equilibrium modes, indicating that highly energetic partons or jets $\gtrsim 30T$ should really be considered as genuine non-equilibrium probes of the QGP. Conversely, the in-medium evolution of less energetic partons or jets $\lesssim 30T$, is more sensitive to the physics at the scale of the QGP medium.

5 Out-of-cone energy loss

While the study of longitudinal energy loss in the medium allowed us to extract important dynamics and discuss the universal behavior of the cascade, our study lacked the angular structure of the evolution, which is important for the study of the out-of-cone energy loss. In this section, we proceed to extend our study to include the polar angular structure of the cascade. We keep the same treatment for the collinear cascade, but we consider the full QCD matrix element at leading order for the elastic interactions in order to follow the fragmentation all the way to large angles.

5.1 Kinetic description

Following the same approach as the last chapter, we study the re-distribution of energy, but we now take it as a function of the polar angle as well, which can be quantified in terms of

$$D_a(x,\cos\theta,t) \equiv x\frac{dN_a}{dx d\cos\theta} = \nu_a \int \frac{d^3p}{(2\pi)^3}\ \frac{|\boldsymbol{p}|}{E}\ \delta\Big(\frac{|\boldsymbol{p}|}{E}-x\Big)\delta\Big(\frac{\boldsymbol{p}\cdot\vec{e}_z}{p}-\cos\theta\Big)\delta f_a(\boldsymbol{p},t)\ , \tag{5.1}$$

where θ is the angle between the parton's momentum and the axis $\vec{e}_z$ which defines the direction of the initial parton's momentum. We note that the sum rules related to energy E, longitudinal momentum $\boldsymbol{p}_z$ and charge (Q_f) conservation, are now given by

$$\sum_a \int_{-1}^{1} d\cos\theta \int dx\ D_a(x,\cos\theta,t) = 1\ , \quad \sum_a \int_{-1}^{1} d\cos\theta \int dx\ \cos\theta D_a(x,\cos\theta,t) = 1\ , \tag{5.2}$$

$$\int_{-1}^{1} d\cos\theta \int \frac{dx}{x}\ \Big(D_{q_f}(x,t) - D_{\bar{q}_f}(x,t)\Big) = Q_f\ . \tag{5.3}$$

Based on Eq. (3.8), the evolution of the momentum/energy distributions of partons $D_a(x,\cos\theta,t)$ is entirely driven by interactions with the medium constituents,

$$\partial_t D_a(x,\cos\theta,t) = C_a^{2\leftrightarrow 2}[\{D_i\}] + C_a^{1\leftrightarrow 2}[\{D_i\}]\ , \tag{5.4}$$

where as in Eq. (5.1) we have defined

$$C_a[\{D_i\}] \equiv \nu_a \int \frac{d^3p_1}{(2\pi)^3} \frac{|\boldsymbol{p}_1|}{E} \delta\Big(\frac{|\boldsymbol{p}_1|}{E} - x\Big)\delta\Big(\frac{\boldsymbol{p}_1 \cdot \vec{e}_z}{p_1} - \cos\theta\Big) C_a[\{f_i\}, \{\delta f_i\}] \,. \quad (5.5)$$

Since we consider the radiation processes to be collinear, they are described by exactly the same equations from section 3.4 by only including the angular dependence of the distribution. However, for the treatment of elastic processes, we will consider the full matrix element as we describe in the following section.

5.1.1 Elastic scatterings

In order to account for both small and large angle scatterings, in this chapter we will use the full collision integral in Eq. 3.9 which we linearize as follows

$$C_a^{2\leftrightarrow 2}[\{f_i\}] = \frac{1}{2|p_1|\nu_a} \sum_{bcd} \int d\Omega^{2\leftrightarrow 2} \left|\mathcal{M}_{cd}^{ab}(\boldsymbol{p}_1, \boldsymbol{p}_2; \boldsymbol{p}_3, \boldsymbol{p}_4)\right|^2 \delta\mathcal{F}(\boldsymbol{p}_1, \boldsymbol{p}_2; \boldsymbol{p}_3, \boldsymbol{p}_4) \,, \quad (5.6)$$

where the statistical factor $\delta\mathcal{F}(\boldsymbol{p}_1, \boldsymbol{p}_2, \boldsymbol{p}_3, \boldsymbol{p}_4)$ is now

$$\begin{aligned} \delta\mathcal{F}(\boldsymbol{p}_1, \boldsymbol{p}_2, \boldsymbol{p}_3, \boldsymbol{p}_4) = \quad & \delta f_a(\boldsymbol{p}_1)\left[\pm_a n_c(p_3) n_d(p_4) - n_b(p_2)(1 \pm n_c(p_3) \pm n_d(p_4))\right] \\ & + \delta f_b(\boldsymbol{p}_2)\left[\pm_b n_c(p_3) n_d(p_4) - n_b(p_1)(1 \pm n_c(p_3) \pm n_d(p_4))\right] \\ & - \delta f_c(\boldsymbol{p}_3)\left[\pm_c n_a(p_1) n_b(p_2) - n_b(p_4)(1 \pm n_a(p_1) \pm n_b(p_2))\right] \\ & - \delta f_d(\boldsymbol{p}_4)\left[\pm_d n_a(p_1) n_b(p_2) - n_b(p_3)(1 \pm n_a(p_1) \pm n_b(p_2))\right] \,, \end{aligned} \quad (5.7)$$

where $\pm_i$ is plus if particle i is a boson and minus for a fermion. Since we consider the phase-space distribution to be isotropic in the azimuth angle of momentum, we write

$$\delta f_a(\boldsymbol{p}) = \int \frac{dp_\phi}{(2\pi)} \, \delta f_a(\boldsymbol{p}) = (2\pi)^2 \frac{D_a(x, \cos\theta)}{\nu_a (xE)^3} \,. \quad (5.8)$$

The statistical factor in terms of the energy distribution is given by

$$\mathcal{D}(1,2;3,4) = \delta\mathcal{F}(\boldsymbol{p}_1,\boldsymbol{p}_2,\boldsymbol{p}_3,\boldsymbol{p}_4)\ , \tag{5.9}$$

$$\begin{aligned} &= \frac{D_a(x_1,\cos\theta_1)}{\nu_a x_1^3 E^2}\left[\pm_a n_c(p_3)n_d(p_4) - n_b(p_2)(1\pm n_c(p_3)\pm n_d(p_4))\right] \\ &+ \frac{D_b(x_2,\cos\theta_2)}{\nu_b x_2^3 E^2}\left[\pm_b n_c(p_3)n_d(p_4) - n_b(p_1)(1\pm n_c(p_3)\pm n_d(p_4))\right] \\ &- \frac{D_c(x_3,\cos\theta_3)}{\nu_c x_3^3 E^2}\left[\pm_c n_a(p_1)n_b(p_2) - n_b(p_4)(1\pm n_a(p_1)\pm n_b(p_2))\right] \\ &- \frac{D_d(x_4,\cos\theta_4)}{\nu_d x_4^3 E^2}\left[\pm_d n_a(p_1)n_b(p_2) - n_b(p_3)(1\pm n_a(p_1)\pm n_b(p_2))\right]\ , \end{aligned} \tag{5.10}$$

where $x_i = \frac{p_i}{E}$ and $\cos\theta_i = \frac{\boldsymbol{p}_i\cdot\vec{e}_z}{p_i}$. The collision integral for the energy distribution is then given by

$$\begin{aligned} C_a^{2\leftrightarrow 2}[\{D_i\}] = &\sum_{bcd}\int \frac{d^3p}{(2\pi)^3}\,\frac{|\boldsymbol{p}|}{E}\,\delta\Big(\frac{|\boldsymbol{p}|}{E}-x\Big)\delta\Big(\frac{\boldsymbol{p}\cdot\vec{e}_z}{p}-\cos\theta\Big) \\ &\frac{1}{2p_1}\int d\Omega^{2\leftrightarrow 2}\left|\mathcal{M}_{cd}^{ab}(1,2;3,4)\right|^2\mathcal{D}(1,2;3,4)\ . \end{aligned} \tag{5.11}$$

The discretization of this collision integral is described in Appendix B, in the following sections we will outline our treatment of the matrix element using Hard thermal loop (HTL) propagators.

Hard thermal loop matrix element

The matrix elements in Tab. 3.1 are for particles in vacuum, which leads to an infrared divergence in the momentum exchange in the t- and u-channels[1]. For a proper treatment using thermal propagators, the divergences are cut off by the self-energies. However, as the authors of [31] argue, medium-dependent effects are only important for small angle scatterings corresponding to the regions where $-t$ or $-u$ are of the order of the thermal mass squared and the modification of the other terms can be neglected. In this section, we will follow the AMY approach [31, 65, 136] in order to re-write the divergent terms using the retarded self-energy, which cuts off the divergence.

[1]The mixed channels $s^2/(tu)$ and $u^2/(st)$ also generate divergences, but these cancel between the gain and loss term [31].

Gluon exchange: We apply the rewriting for the following t- and u-channel gluon exchange processes: $gg \leftrightarrow gg$, $q^i q^j \leftrightarrow q^i q^j$, $q^i \bar{q}^j \leftrightarrow q^i \bar{q}^j$, $\bar{q}^i \bar{q}^j \leftrightarrow \bar{q}^i \bar{q}^j$ and $q^i g \leftrightarrow q^i g$. The matrix elements in terms of Mandelstam variables can be rewritten as

$$\frac{s^2+u^2}{t^2} = \frac{1}{2} + \frac{1}{2}\frac{(s-u)^2}{t^2} , \qquad \frac{su}{t^2} = \frac{1}{4} - \frac{1}{4}\frac{(s-u)^2}{t^2} , \tag{5.12}$$

$$\frac{s^2+t^2}{u^2} = \frac{1}{2} + \frac{1}{2}\frac{(s-t)^2}{u^2} , \qquad \frac{st}{u^2} = \frac{1}{4} - \frac{1}{4}\frac{(s-t)^2}{u^2} . \tag{5.13}$$

Using thermal propagators amounts to the replacement [65]

$$\frac{(s-u)^2}{t^2} \longrightarrow |G_{\mu\nu}(P_1-P_3)(P_1+P_3)^\mu (P_2+P_4)^\nu|^2 , \tag{5.14}$$

$$\frac{(s-t)^2}{u^2} \longrightarrow |G_{\mu\nu}(P_1-P_4)(P_1+P_4)^\mu (P_2+P_3)^\nu|^2 , \tag{5.15}$$

where $G_{\mu\nu}(P_1-P_3)$ is the retarded thermal gluon propagator, computed in the HTL approximation. In the Coulomb gauge, it is given by

$$G_{\mu\nu}(\omega,\boldsymbol{q}) = \frac{-1}{q^2+\Pi_{00}(\omega,q)} , \qquad G_{ij}(\omega,\boldsymbol{q}) = \frac{\delta_{ij} - \frac{\boldsymbol{q}_i \boldsymbol{q}_j}{q^2}}{q^2-\omega^2+\Pi_T(\omega,q)} , \tag{5.16}$$

$$G_{i0}(\omega,\boldsymbol{q}) = G_{0i}(\omega,\boldsymbol{q}) = 0 . \tag{5.17}$$

The transverse and longitudinal gluon self-energies are given by

$$\Pi_{00}(\omega,q) = m_D^2 \left[1 - \frac{\omega}{2q}\left(\ln\left(\frac{q+\omega}{q-\omega}\right) - i\pi\right)\right] , \tag{5.18}$$

$$\Pi_T(\omega,q) = m_D^2 \left[\frac{\omega^2}{q^2} + \frac{\omega(q^2-\omega^2)}{4q^3}\left(\ln\left(\frac{q+\omega}{q-\omega}\right) - i\pi\right)\right] , \tag{5.19}$$

here for the t- and u-channels, the propagator with 4-momentum $Q = (\omega, \boldsymbol{q})$ is space-like (i.e., $|\omega| < q$) and the logarithm is well-behaved.

Quark exchange: The other t- and u-channel processes that require a rewriting are the quark exchange processes: $q^i \bar{q}^i \leftrightarrow gg$ and $qg \leftrightarrow qg$. The matrix elements are computed using the following replacement for the four-momentum exchange,

$$Q^\mu \to \mathcal{Q}^\mu \equiv Q^\mu - \Sigma^\mu(Q) , \tag{5.20}$$

where the quark self-energy in the Coulomb gauge is given by

$$\Sigma^0(Q) = \frac{m_F^2}{2q}\left[\ln\left(\frac{q+\omega}{q-\omega}\right) - i\pi\right] , \tag{5.21}$$

$$\boldsymbol{\Sigma}(Q) = -\boldsymbol{q}\frac{m_F^2}{q^2}\left[1 - \frac{\omega}{2q}\ln\left(\frac{q+\omega}{q-\omega}\right) - i\pi\right] . \tag{5.22}$$

The relevant matrix elements become

$$\frac{u}{t} \longrightarrow \left.\frac{4\mathrm{Re}[(P_1\cdot\mathcal{Q})(P_2\cdot\mathcal{Q}^*)] - s\mathcal{Q}\cdot\mathcal{Q}^*}{|\mathcal{Q}\cdot\mathcal{Q}|^2}\right|_{\mathcal{Q}^\mu = P_1^\mu - P_3^\mu - \Sigma^\mu(P_1-P_3)} , \tag{5.23}$$

$$\frac{t}{u} \longrightarrow \left.\frac{4\mathrm{Re}[(P_1\cdot\mathcal{Q})(P_2\cdot\mathcal{Q}^*)] - s\mathcal{Q}\cdot\mathcal{Q}^*}{|\mathcal{Q}\cdot\mathcal{Q}|^2}\right|_{\mathcal{Q}^\mu = P_1^\mu - P_4^\mu - \Sigma^\mu(P_1-P_4)} , \tag{5.24}$$

$$\frac{s}{u} \longrightarrow \left.\frac{-4\mathrm{Re}[(P_1\cdot\mathcal{Q})(P_3\cdot\mathcal{Q}^*)] - t\mathcal{Q}\cdot\mathcal{Q}^*}{|\mathcal{Q}\cdot\mathcal{Q}|^2}\right|_{\mathcal{Q}^\mu = P_1^\mu - P_4^\mu - \Sigma^\mu(P_1-P_4)} . \tag{5.25}$$

All allowed processes in Tab. 3.1 are summed numerically to obtain the full elastic collision integral ($C_a^{2\leftrightarrow 2}[\{D_i\}]$) which together with the collinear radiation ($C_a^{1\leftrightarrow 2}[\{D_i\}]$) will describe the evolution of the energy distribution.

5.2 Energy loss and equilibration

Similarly to Chapter 4, we follow the energy loss and equilibrium of hard partons inside a thermal QGP, starting from an initial condition, where the initial energy distribution of partons $D_a(x,t)$ is given by a narrow Gaussian of width $\sigma/E = 10^{-3}/\sqrt{2}$ centered around the momentum along the z-axis (taking $p = p_z = E$), which is normalized to $\int dx \int d\cos\theta \sum_a D_a(x,\cos\theta,0) = 1$. We will also consider two types of initial conditions, corresponding to a highly energetic gluon or quark, respectively. For a gluon jet

$$D_g^{g-jet}(x,\cos\theta,0) = \frac{1}{N}\exp\left\{-\frac{(xE-E)^2 + x^2E^2(1-\cos\theta^2)}{2\sigma^2}\right\} , \tag{5.26}$$

$$D_q^{g-jet}(x,\cos\theta,0) = 0 , \qquad D_{\bar{q}}^{g-jet}(x,\cos\theta,0) = 0 , \tag{5.27}$$

whereas for a quark jet

$$D_q^{q-jet}(x,\cos\theta,0) = \frac{1}{N}\exp\left\{-\frac{(xE-E)^2 + x^2E^2(1-\cos\theta^2)}{2\sigma^2}\right\} , \tag{5.28}$$

$$D_g^{q-jet}(x,\cos\theta,0) = 0 , \qquad D_{\bar{q}}^{q-jet}(x,\cos\theta,0) = 0 , \tag{5.29}$$

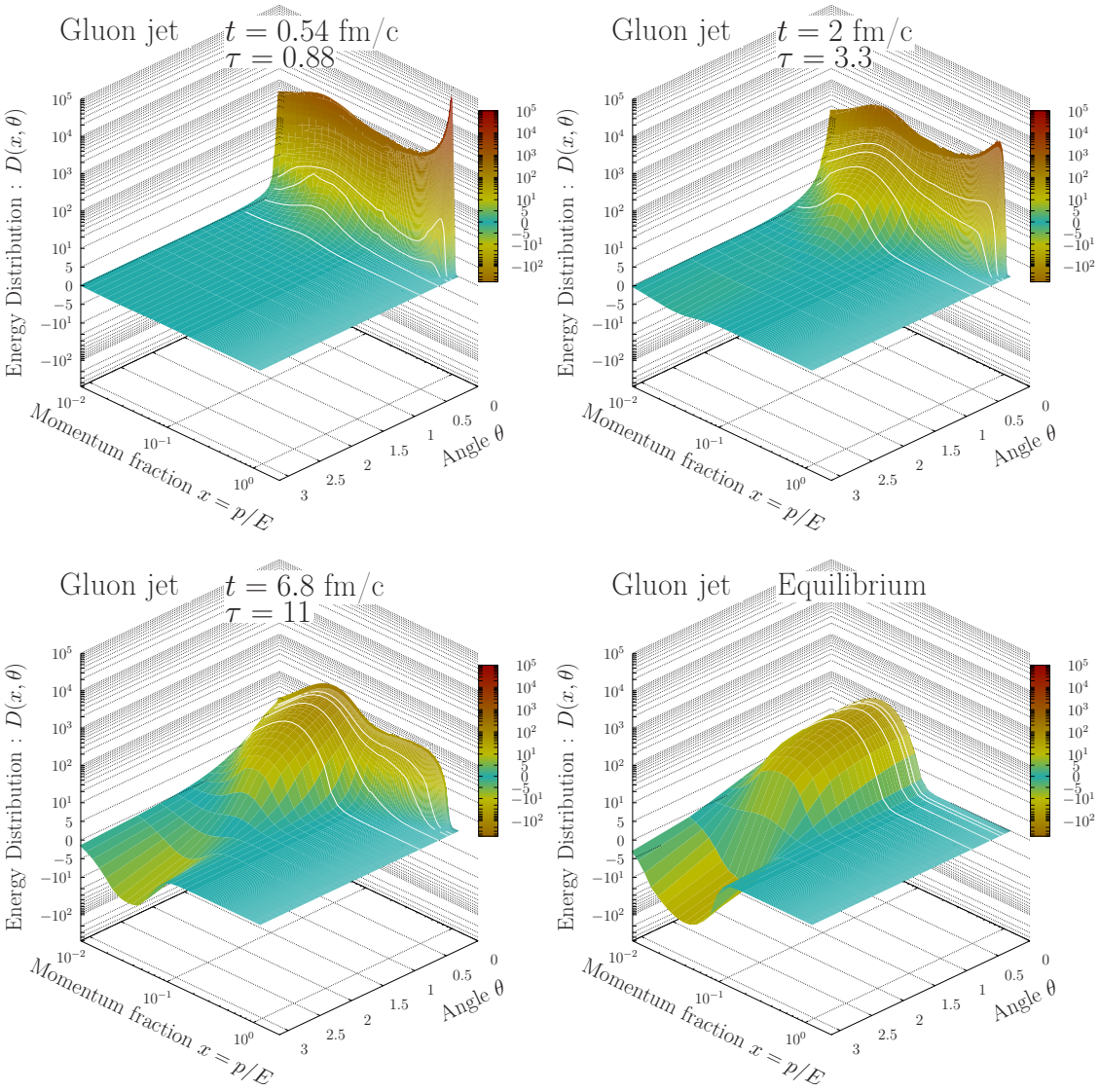

Figure 5.1: Evolution of the distributions of all species $D(x, \cos\theta) = \sum_a D_a(x, \cos\theta)$ for a gluon jet at different times $t = 0.54, 2, 3$fm/c and the equilibrium distribution as a function of momentum fraction $x = \frac{p}{E}$ and angle θ. (The white lines represent constant angles from small to large $\theta = 0.11, 0.16, 0.32, 0.62$.)

where the normalization factor is given by $N = \int_{-1}^{1} d\cos\theta \int dx\; e^{-\frac{(xE-E)^2+x^2E^2(1-\cos\theta^2)}{2\sigma^2}}$.

If not stated otherwise, throughout this chapter, we will present results for the evolution of jets with energy $E = 100T$ and take the coupling $g = 2$ which corresponds to $\alpha_s \simeq 0.31$. The time scale will be expressed in terms of both the dimensionless time variable as in the previous chapter

$$\tau = g^4 T \sqrt{\frac{T}{E}} t \,, \tag{5.30}$$

and the physical time units fm/c, where we use a thermal medium with temperature $T = 200\text{MeV}$ to set the physical scale. However, the physical time should be regarded as only an indication, since our evolution does not include relevant effects for a phenomenological study (e.g. the splitting rates are considered in an infinite medium size).

We present the evolution of the total energy distribution of all species $D(x, \cos\theta) = \sum_a D_a(x, \cos\theta)$ in figure 5.1 for a gluon jet at different times $t = 0.54, 2, 6.8\text{fm/c}$ and the equilibrium distribution as a function of momentum fraction $x = \frac{p}{E}$ and polar angle θ. At early times one identifies the leading parton peak at momentum fraction $x \sim 1$ and angle $\theta \sim 0$, which is only marginally broadened. The collinear radiation spectrum, already starts to populate the intermediate scales between the jet energy ($x \sim 1$) and the medium ($x \sim T/E$) but mainly in the collinear region ($\theta \sim 0$). In this region of small angles, the conclusions are very similar to the previous chapter where we studied the longitudinal energy loss, we observe that the energy loss follows an inverse energy cascade with a scale independent energy flux. At intermediate times, the energy starts to be transferred to large angles, but only in the low momentum sector, while in the large momentum region most of the energy is collinear ($\theta \lesssim 0.3$). We observe that the elastic interactions play a marginal role for the broadening of the hard partons, instead, the energy is first transferred collinearlly from the jet peak to the soft scale, before it broadens to large angles due to equilibration via elastic interactions. As the soft sector equilibration is rather quick, this process starts from early times and continues throughout the evolution until the energy is depleted. At late times, the peak hast lost most of its energy and the near-equilibrium sector deposits the remainder of its energy in the medium. One notes that the equilibrium distribution features a negative contribution which accounts for the medium particles that are kicked in the jet direction ensuring momentum conservation (c.f. sec. 5.2.3).

We can explore further the structure of the energy distribution by looking at the

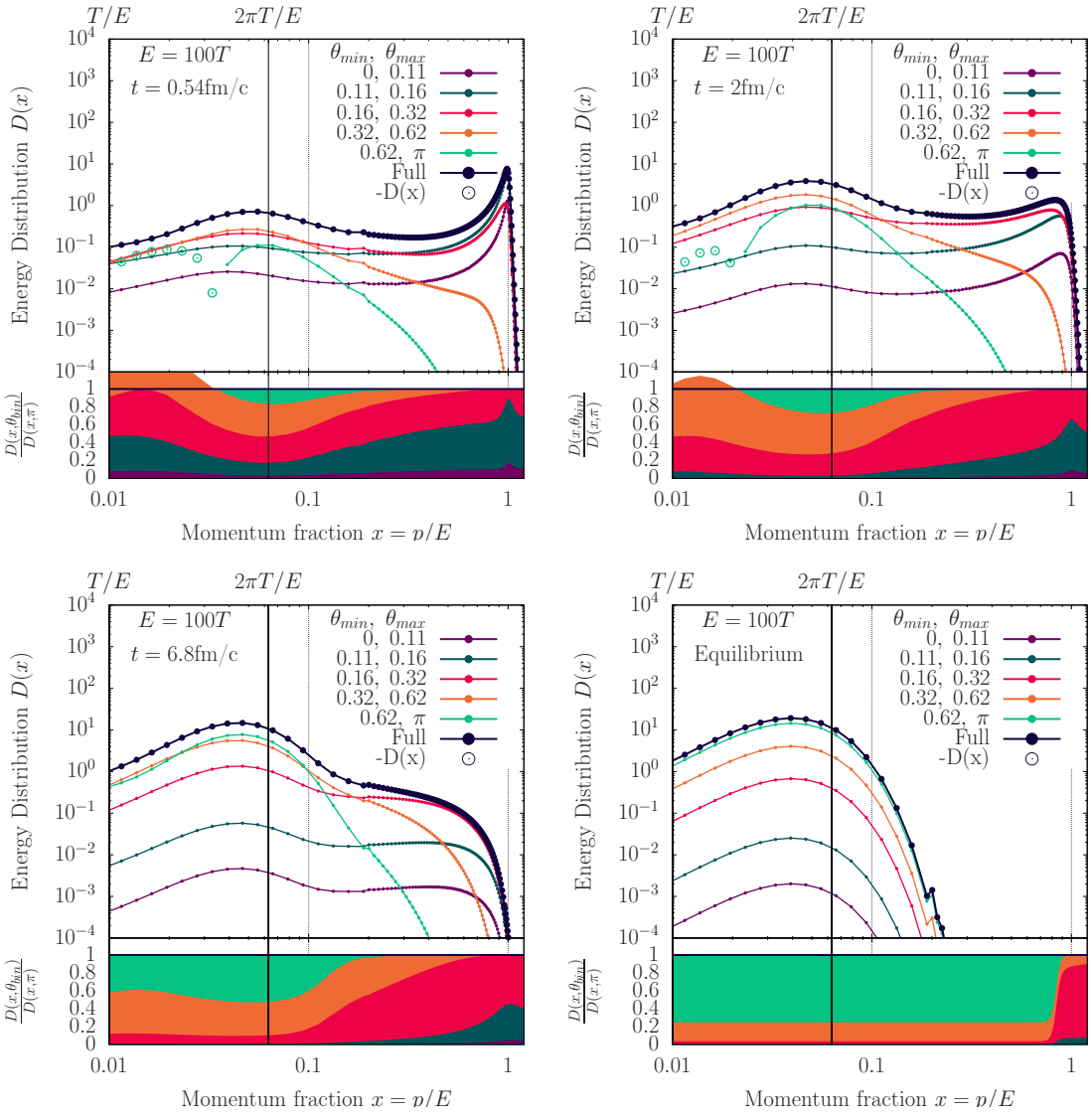

Figure 5.2: Evolution of the energy distribution as a function of the momentum fractions $x = \frac{p}{E}$ with a decomposition into different angular regions as described in Eq. (5.31). The height of each shaded region in the lower panel represents the ratio to the full distribution, displaying how the energy is distributed in different angular regions.

angular integrated energy distribution

$$D(x)|_{\theta_{\rm min}}^{\theta_{\rm max}} = \int_{\cos\theta_{\rm min}}^{\cos\theta_{\rm max}} d\cos\theta \; D(x,\cos\theta) \; . \tag{5.31}$$

We show in Fig. 5.2 the full distribution $D(x)|^{\rm Full} \equiv D(x)|_0^\pi$ together with distributions at different angular bins $D(x)|_{\theta_{\rm min}}^{\theta_{\rm max}}$ with $(\theta_{\rm min}, \theta_{\rm max}) = (0, 0.11, 0.16, 0.32, 0.62, \pi)$. The lower panel represents how the full distribution is decomposed into the different angular regions, where the height of each shaded area corresponds to the ratio $\frac{D(x)|_{\theta_{\rm min}}^{\theta_{\rm max}}}{D(x)|^{\rm Full}}$. Overall, the full energy distribution follows a similar behavior as in the previous chapter, albeit here the elastic scatterings are better represented using the full matrix element. The turbulent spectrum is recovered in the intermediate scales, not only in the full distribution but also in the small angle region where most of the collinear radiation happens. At early times, the jet peak sits at $x \sim 1$ and already energy is directly deposited in the medium at small angles, which broadens rather quickly to large angles later on. This can be seen in the lower panels, where the dark green region accounts for $\sim 25\%$ of the distribution in the soft scales ($x \sim T/E$) at $t = 0.25$fm/c and dies away ($\lesssim 10\%$) already in the following time step. The large angle region in bright green displays a negative behavior, as the direct collinear energy loss boosts the medium constituents. Afterwards, equilibration mechanisms re-distribute the momentum of the soft partons leading to a positive distribution, we will describe how energy is distributed in equilibrium in Eq. (5.40).

5.2.1 Comparison with the small angle approximation

In order to investigate the angular structure of the energy distribution, we show in Fig. 5.3 the angular distribution by integrating over the momentum fraction as follows

$$D(\cos\theta)|_{x_{\rm min}}^{x_{\rm max}} = \int_{x_{\rm min}}^{x_{\rm max}} dx \; D(x,\cos\theta) \; . \tag{5.32}$$

We compare with an evolution using the small angle approximation denoted by 'Diffusion' where we used the same procedure as the previous chapter except we also include angular diffusion mechanisms described in Appendix A. We show three different scales: large momentum sector ($xE \leq 90T$) in the left panel, intermediate scales ($10T \leq xE \leq 90T$) in the middle and soft scales ($xE \leq 10T$) in the right. The momentum broadening coefficient $\hat{q}$ used in the diffusion evolution is the equilibrium one where we take the logarithmic scale dependence to be 1 as done in the previous

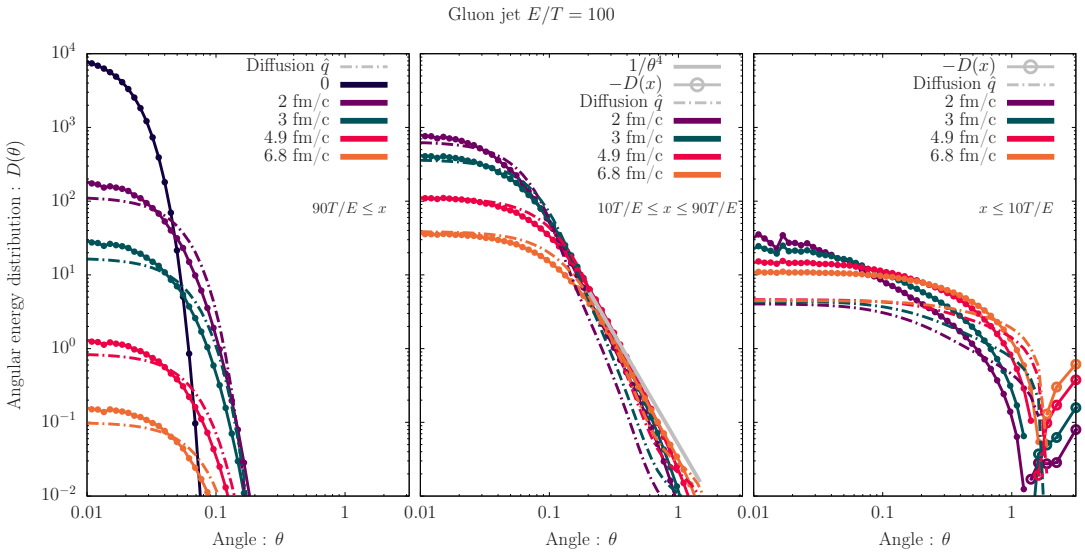

Figure 5.3: Evolution of the angular distribution in different momentum regions as described by Eq. (5.32). The dashed lines represent an evolution using only the small angle approximation by taking the logarithmic dependence to be 1 as in Chapter 4.

chapter, we recall the definition from Eq. (4.21)

$$\hat{q} = \frac{g^4 T^3 C_R}{2\pi} \left(\frac{N_c}{3} + \frac{N_f}{6} \right) . \tag{5.33}$$

We observe a small broadening of the hard particles which is much slower than their depletion due to the collinear cascade, while the soft particles broaden much more quickly and are distributed over the full range of angles even at early times. We note here once more the negative contribution at the away side ($\theta > 1$) due to momentum conservation. Evidently, using a scale independent $\hat{q}$, the broadening cannot simultaneously account for both the broadening of the hard scale and the soft scale. We find that the equilibrium $\hat{q}$ in Fig. 5.3 can account fairly well for the hard particle broadening but breaks down at medium scales.

Furthermore, rare hard scattering can take the particle out to large angles – as discussed by Molière theory for QED [137], it was also shown that such events dominate the large transverse momentum region in QCD [132]. The rare hard scatterings are described by a power-law tail known as the Molière tail, to find the exponent of the power-law we can investigate the behavior of the elastic scattering rate for highly energetic partons which has been worked out for HTL propagators

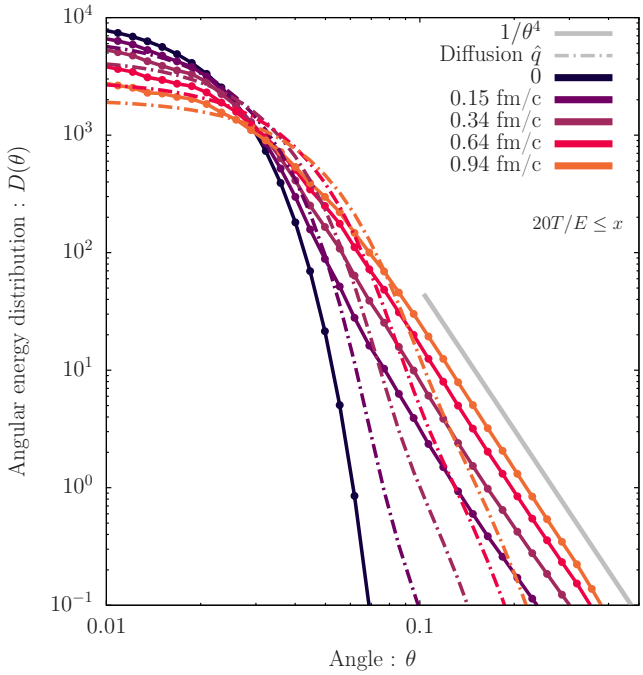

Figure 5.4: Evolution of the angular distribution for hard particles with momentum fraction $x > 20T/E$. The dashed lines represent the same 'Diffusion' evolution as in Fig. 5.3.

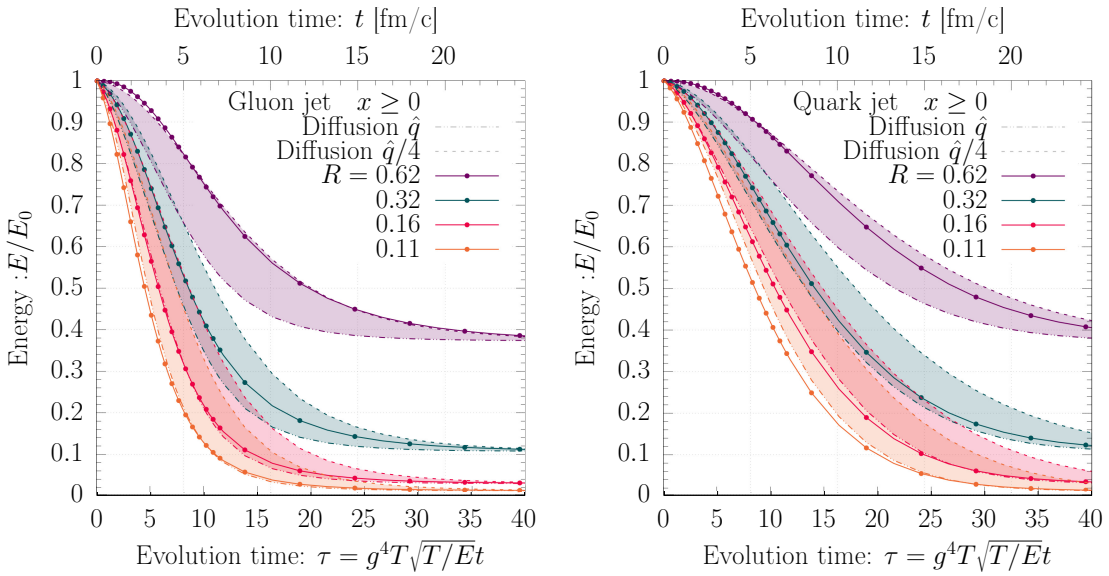

Figure 5.5: Evolution of the energy inside the cone ($\theta \leq R$) as given by Eq. (5.35), for gluon (left) and quark (right) initial jets with $E = 100T$. We compare with the 'Diffusion' approximation, taking the momentum broadening coefficient to be either $\hat{q}$ or $\frac{\hat{q}}{4}$.

as function of the transverse momentum $q_\perp$ acquired, and is given by [138]

$$\frac{d\Gamma^{\text{el}}}{d^2q_\perp} = \frac{g^2 T m_D^2}{q_\perp^2(q_\perp^2 + m_D^2)} \,. \tag{5.34}$$

Taking transverse momentum to be large ($q_\perp \gg 1$) leads to $\frac{d\Gamma^{\text{el}}}{d^2q_\perp} \sim 1/q_\perp^4$ behavior, and since $q_\perp = |q_\perp| \sin\theta$ in our evolution the distribution should go as $1/\sin^4\theta \sim 1/\theta^4$ for $\theta \ll 1$. Because the small angle scatterings lead to momentum broadening which exponentially decays at large angles, we expect the power law to dominate the large angle region. We note this behavior in the middle panel of Fig. 5.3, and it is even more apparent at the early stages of the collision in Fig. 5.4 where the absence of the power law in the 'Diffusion' approximation is more clear since the broadening is still small.

We now further explore how well 'Diffusion' can approximate the full matrix element, by comparing the energy loss as a function of cone size R. The fraction of energy remaining inside the cone ($\theta \leq R$) is given by

$$E(R,\tau) = \int dx \int_{\cos R}^{1} D(x, \cos\theta, \tau) \,. \tag{5.35}$$

For the 'Diffusion' approximation, the logarithmic dependence of the momentum broadening coefficient will affect the momentum broadening and consequently out-of-cone energy loss. In the full matrix element evolution this effect is scale dependent, however, in our 'Diffusion' simulation we do not set up a scale dependent $\hat{q}$, therefore, we will compare our results with two different values for $\hat{q}$, either taking the equilibrium value in Eq. (5.34) or taking a quarter of it ($\hat{q} \to \frac{\hat{q}}{4}$). We find that these two values provide a large enough separation to describe the range of cone dependence of the energy loss we focus on in Fig. 5.5. First, we see that, as expected, the evolution using $\frac{\hat{q}}{4}$ loses energy slower than for $\hat{q}$. Likewise, how quickly energy is lost is also dependent on the cone size, where narrower cone sizes lose energy more quickly. Comparing with the full matrix element evolution, we observe how the hard particles with narrow cones $R \sim 0.11$ are better described by $\hat{q}$ while for larger cone sizes when softer particles are more relevant the evolution is closer to $\frac{\hat{q}}{4}$, confirming our earlier conclusion that a scale independent $\hat{q}$ cannot describe the broadening at all scales. We note also that the late time limits of the different curves display the energy inside each cone size in the equilibrium distribution.

5.2.2 Energy loss

We study the effect of the soft sector on how the energy is lost out of cone, comparing the full energy inside the cone in Eq. (5.35) with the energy in the high momentum fraction region ($xE \geq 2\pi T$) as follows

$$E_{2\pi}(R,\tau) = \int_{2\pi T/E}^{\infty} dx \int_{\cos R}^{1} D(x, \cos\theta, \tau) \,. \tag{5.36}$$

Our results are shown in Fig. 5.6, we note that for narrow cones ($R \leq 0.2$) the soft sector does not play a major role and the energy loss is very similar in both momentum regions. While for larger cone sizes, a transition occurs where the soft sector not only carries a substantial fraction of the equilibrated energy at late times but also the early time energy loss diverges.

We can also study the dependence on the initial parton's energy as shown in Fig. 5.7 for two cone sizes $R = 0.32, 0.62$. We find that by taking the evolution time in terms of the splitting time t_{split}, the energy loss from inside narrow cones follows scaling behavior, which is less prominent at larger cones as medium effects start to play a role.

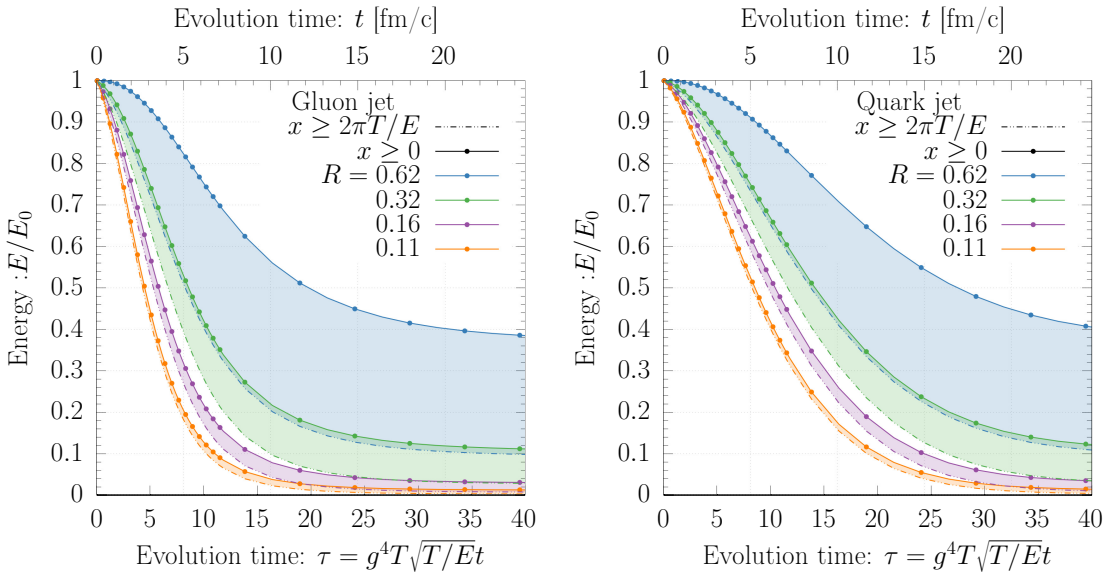

Figure 5.6: Evolution of the energy inside the cone ($\theta \leq R$) for gluon (left) and quark (right) initial jets with $E = 100T$. Full line-points represent the full momentum region as in Eq. (5.35), while the dashed lines describe only the high momentum fraction region $xE \geq 2\pi T$ as in Eq. (5.36).

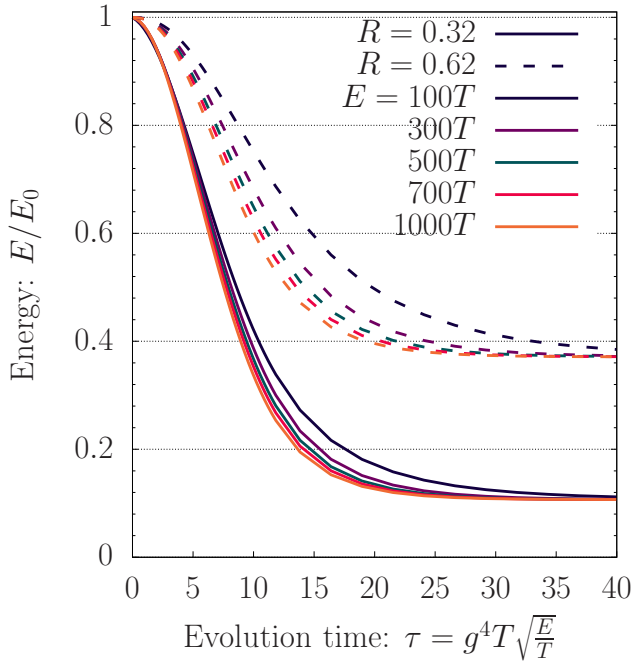

Figure 5.7: Evolution of the energy carried by particles inside cones $R = 0.32, 0.62$, for gluon jets with different initial energies $E = 100 - 1000T$.

5.2.3 Equilibration

Eventually, the hard particles lose all their energy to the medium and become part of the thermal bath. Since our description relies on a linearization over a static equilibrium background, the thermal bath does not change, rather the linear perturbation will reach an equilibrium state as a perturbation over the thermal bath. This equilibrium distribution can be obtained as a small deviation of the equilibrium distribution $n_a(p)$ written

$$D^{\rm eq}(x,\cos\theta) = x^3\delta T\partial_T n_a(xE) + x^3\frac{\delta P_z}{E}\partial_\beta n_a(xE(1-\beta\cos\theta))\Big|_{\beta\to 0} . \tag{5.37}$$

Since we start with a narrow Gaussian around $\vec{p} = E\vec{e}_z$, the energy and momentum are both normalized to one ($E = P_z = 1$), using this normalization condition we find

$$D_a^{\rm eq}(x,\cos\theta) = \frac{x^4}{N}\Big(1+3\cos\theta\Big)n_a(xE)(1\pm n_a(xE)) , \tag{5.38}$$

where $N = 2\int dx\; x^4 n_a(xE)(1\pm n_a(xE))$ is a normalization integral. When integrating the distribution over angle we recover the same longitudinal distribution from chapter 4 in Eq. (4.82-4.84).

The equilibrium distribution is recovered at late times as shown in Figs. 5.1-5.2. Specifically in Fig. 5.2, we see that most of the energy sits at large angles. In fact, thermalization of the soft sector is fast enough that as soon as energy is deposited, it starts to thermalize, as can be seen in the right panel of Fig. 5.3, where the angular structure is very close to the equilibrium $(1+3\cos\theta)$ behavior; the same happens in the momentum distribution in Fig. 5.2. We can also compute the energy inside the cone for the equilibrium distribution

$$E_{\rm eq}(R,) = \int dx \int_{\cos R}^{1} D^{\rm eq}(x,\cos\theta) , \tag{5.39}$$

$$= \frac{1}{2}(5+3\cos R)\sin^2\frac{R}{2} . \tag{5.40}$$

For small cone sizes $R \ll 1$, we have $E_{\rm eq}(R) \simeq R^2$ which describes fairly well the late time behavior in Fig. 5.5.

We note that due to momentum conservation, the equilibrium distribution is negative at the away side ($\theta \gtrsim 1.91$). Because the background equilibrium is static, this negative side reduces particles from the medium static distribution, which are then supplied back into the parton's direction. We end up with a slightly boosted medium distribution along the z direction with momentum δP_z given by

$$f_a^{\rm eq}(\boldsymbol{p}) = n_a(\boldsymbol{p}) + D_a^{\rm eq}(x,\cos\theta) . \tag{5.41}$$

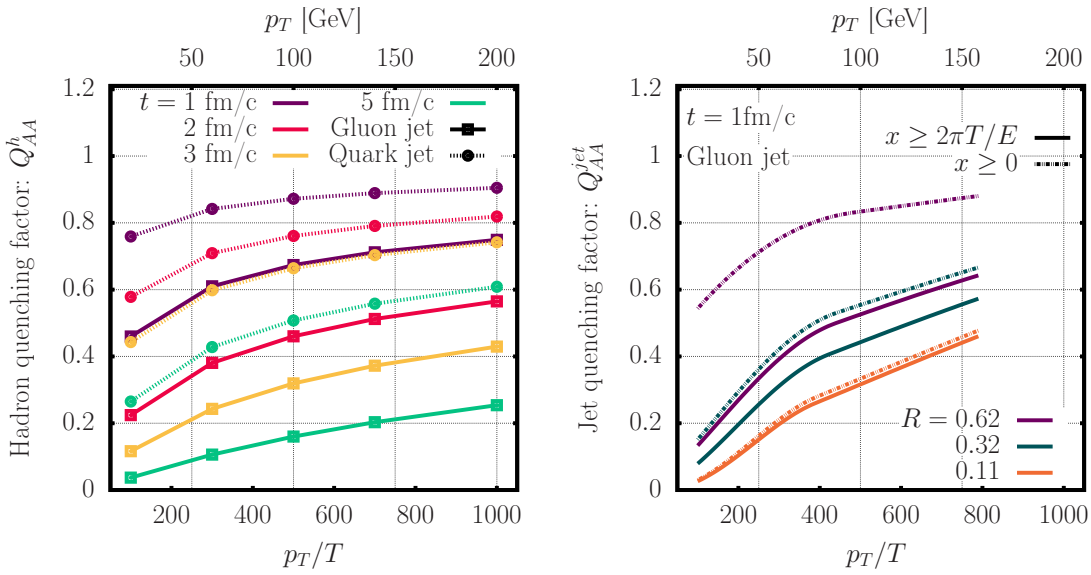

Figure 5.8: (left) Hadron quenching factor as a function of initial parton energy. (right) Jet quenching factor for a gluon jet with momentum fraction $x \geq 0$ (dashed) or $x \geq 2\pi T/E$ (solid) and different cone sizes $R = 0.62, 0.32, 0.11$ at $t = 1$fm/c. We take the medium temperature $T = 200$MeV.

5.3 Quenching factors

We stress that our evolution lacks the effects of vacuum like emissions and path length dependence of the in-medium radiation rates. While these aspects are important for phenomenological studies, we still think it is interesting to explore jet quenching using our model.

Firstly, we consider the yield of the inclusive hadron spectrum after passing through the medium which can be obtained as a convolution of the energy distribution for a given starting energy p_T^{in} with the initial parton spectrum[2] [33, 84, 139, 140]

$$\frac{d^2\sigma_{AA}}{dp_T^2}(p_T) = \int_0^\infty d^2p_T^{in} \int_0^1 \frac{dx}{x} \int_{-1}^1 d\cos\theta \; \delta^2(p_T - xp_T^{in}) \\ D\left(x, \theta, \tau \equiv g^4 T\sqrt{T/p_T^{in}}t\right) \frac{d^2\sigma_0}{d^2p_T^{in}}(p_T^{in}) \,, \tag{5.42}$$

[2]We assume parton-hadron duality, i.e., the fragmentation does not alter the leading parton so much that each leading parton leads to a high-p_T hadron in the final state.

where we make use of the rescaled the time τ [33] in order to account for the initial parton energy, which we showed to work fairly well for the hard partons in Fig. 5.7. Dividing by the vacuum spectrum, which can be approximated by a power-law $\frac{d^2\sigma_0}{dp_T^2}(p_T^{in}) \propto p_T^{-1-n}$, we define the inclusive hadron quenching factor

$$Q_{AA}^{\mathrm{h}}(p_T) = \frac{\frac{d^2\sigma_{AA}}{dp_T^2}}{\frac{d^2\sigma_0}{dp_T^2}} = \int_0^1 dx \int_{-1}^1 d\cos\theta \; D\left(x, \theta, \sqrt{x\hat{q}/p_T t}\right) \left(\frac{1}{x}\right)^{2-n} . \tag{5.43}$$

Secondly, we define a cone-size dependent inclusive spectrum, which can be regarded as a rough approximation to the jet spectrum. Starting with the following definition of the energy remaining inside a cone of radius R as a function of the initial parton energy p_T^{in}:

$$p_{T,\mathrm{rem}}(R, p_T^{in}) = p_T^{in} \int_{\cos(R)}^1 dcos(\theta) \int dx \; D(x, \theta, p_T^{in}) . \tag{5.44}$$

We define the cone-size dependent jet spectrum as a convolution between a Dirac delta function peak at energy $p_T = p_{T,\mathrm{rem}}(R, p_T^{\mathrm{in}})$, representing the remaining energy inside the cone with radius R, and the vacuum spectrum evaluated at the initial parton energy as given by

$$\frac{d^2\sigma}{d^2p_T}(R) = \int d^2p_T^{in} \; \delta^2\left(p_T - p_{T,\mathrm{rem}}(R, p_T^{in})\right) \; \frac{d^2\sigma_0}{d^2p_T^{in}} . \tag{5.45}$$

Dividing by the vacuum spectrum, we obtain

$$Q_{AA}^{jet}(p_T, R) = \int d^2\boldsymbol{p}_T^{in} \; \delta^2\left(E - p_{T,\mathrm{rem}}(R, p_T^{\mathrm{in}})\right) \; \left(\frac{p_T^{\mathrm{in}}}{p_T}\right)^{-n} , \tag{5.46}$$

$$= \left| \frac{dp_{T,\mathrm{rem}}(R, p_T^{\mathrm{in}})}{dp_T^{\mathrm{in}}} \right|^{-1}_{p_T^{\mathrm{in}}(p_T,R)} \; \left(\frac{p_T^{in}}{p_{T,\mathrm{rem}}(R, p_T^{\mathrm{in}})}\right)^{-n} \Bigg|_{p_T^{in}(p_T,R)} , \tag{5.47}$$

which we will call the jet quenching factor. One can easily see that in the case of no quenching where $p_{T,\mathrm{rem}}(R, p_T^{in}) = p_T^{in}$, we have no suppression ($Q_{AA}^{jet}(E, R) = 1$), and a fully quenched jet with $p_{T,\mathrm{rem}}(R, p_T^{in}) = 0$ will lead to full suppression ($Q_{AA}^{jet}(E, R) = 0$ since $n > 0$).

Following [94], we take $n_g = 5.66$ and $n_q = 4.19$ for gluon and quark jets, respectively. The resulting quenching factors are shown in Fig. 5.8, where on the left we show the hadron quenching factor at different times $t = 1, 2, 3, 5$fm/c and for

both gluon and quark jets, while on the right we show the jet quenching factor for a gluon jet at $t = 1\text{fm/c}$, for different cone sizes $R = 0.62, 0.32, 0.11$ and by either taking the full range of momentum fraction ($x \geq 0$) in dashed lines or only the hard sector ($x \geq 2\pi T/E$) in full lines. We will not directly compare with experimental data, still we observe a similar qualitative behavior to the suppression R_{AA} discussed in chapter 2. Both quenching factors display a suppression ($Q < 1$) in the full range of energy $p_T = 100 - 1000T$, where higher energies are less suppressed as expected. However, since we treat medium-induced splitting in the infinite medium limit which tends to overestimate the rates, the quenching factor we obtain at comparable times of heavy-ion collisions ($t \sim 5\text{fm/c}$) is much more suppressed than experimental results. Hence, other effects such as medium length and vacuum-like emissions are important to reproduce experimental observables. Nevertheless, we observe interesting features, e.g., we find that quark jets are far more suppressed than gluon jets in the hadron quenching factor, which is explained by the fact that gluons lose their energy much faster than quarks. Additionally, since $2 - n < 1$, the hadron quenching factor measures particles with a given energy, and heavily depends on the hard sector constituents which mostly sit at small angle and large momentum fraction. On the other hand, the jet quenching factor measures energy inside a cone (R), and displays a large soft sector dependence when taking wider cone sizes, while for a narrow cone size the soft sector does not significantly alter the quenching. We conclude that jet suppression depends on the soft sector which renders it much harder to compute, while hadron quenching is more sensitive to the leading parton which stays collinear and its energy loss is mainly due to the in-medium cascade.

5.4 Discussion

During this chapter, we have successfully implemented a full angular medium cascade within an effective kinetic theory of QCD following the AMY approach [31]. By extending our formalism in chapter 4 to include the full matrix elements containing both small and large angle scatterings, allowing us to study the angular structure of the energy loss in the polar angle with respect to the initial parton. Given that medium-induced radiation, which is collinear, dominates the energy loss and leads to a much faster depletion than elastic interactions with the medium, we find that the main mechanism driving the energy to large angles is the equilibration of the radiated energy in the soft sector. Therefore, while for large cone sizes the energy inside the cone is sensitive to the soft sector, hard fragments make up almost all energy inside the cone at small angles $\theta \leq 0.2$. Additionally, we compared the full

evolution against using the small angle approximation for the elastic interactions, as was done in the previous chapter. We find, as expected, that a scale independent broadening coefficient cannot simultaneously describe both the broadening at large momentum fraction and the equilibration in the soft scale. We also computed quenching factors for leading hadron and jets, where we concluded that while the hadron quenching factor depends mostly on the hard constituents, the jet quenching factor recovers energy from the soft sector when taking larger cone sizes. Consequently, hadron quenching can be used as observable to study in-medium splittings, however, to study jet quenching one must also establish a good grasp on medium response physics.

6 Non-perturbative in-medium splitting rates

Throughout the other studies, we concluded that medium energy loss of a highly energetic parton is dominated by radiative branchings. Therefore, in order to develop a better estimation for the energy loss, certainly one needs to improve the in-medium radiation rate calculation. There exist several formalisms in the literature that are used to compute the rate of medium-induced radiation [103, 114, 115, 121, 136, 140–142], each method differs in their assumptions and simplifications as well as in the treatment of the interactions with the medium (c.f. [113] for a comparison). In all the different formalisms the medium interactions are described by the collisional broadening kernel

$$C(q_\perp) \equiv \frac{(2\pi)^2 \mathrm{d}^3\Gamma}{\mathrm{d}^2 q_\perp \, \mathrm{d}L} \,, \tag{6.1}$$

which defines the rate per unit path length and $\boldsymbol{q}_\perp$ range to exchange transverse momentum $\boldsymbol{q}_\perp$ with the medium. One can also define the zero-subtracted Fourier transform[1]

$$C(b_\perp) \equiv \int \frac{\mathrm{d}^2 q_\perp}{(2\pi)^2} \left(1 - e^{i\boldsymbol{q}_\perp \cdot \boldsymbol{b}_\perp}\right) C(q_\perp) \,. \tag{6.2}$$

The three main treatments of the medium used in the literature are:

- Many random, static, screened color centers [114, 143]: $C(q_\perp) \propto \frac{1}{(q_\perp^2 + m_\mathrm{D}^2)^2}$.
- Dynamical moving charges at lowest order in perturbation theory [138]: $C(q_\perp) \propto \frac{1}{q_\perp^2 (q_\perp^2 + m_\mathrm{D}^2)}$.
- Many individually small scatterings, leading to transverse momentum diffusion [116]: $C(b_\perp) = \hat{q}\, b_\perp^2 / 4$.

[1] During this chapter, we will refer to the space dimension ($\boldsymbol{x}$) from chapter 3 as impact parameter space and use $\boldsymbol{b}_\perp$ to denote it.

Although these kernels are simple compact formulas that have successfully been used in phenomenological studies to predict high p_T and jet observables (see [23] for a review), they either stem from low-order perturbative calculations or from approximations. However, due to the infamous infrared problem of finite temperature QCD, perturbative calculations can receive large non-perturbative contributions even at small coupling [49]. One can use effective theories coupled with lattice calculations to evade the IR problem [144]. For that sake, it was shown that the Fourier transform of the momentum broadening kernel in Eq. (6.2) can be defined in terms of certain light-like Wilson loops [145], and for temperatures well above the critical temperature T_c these light-like Wilson loops can be recast in the dimensionally reduced long-distance effective theory for QCD, 3D Electrostatic QCD [146]. Using earlier studies [1, 53, 54], G. D. Moore and N. Schlusser were able to obtain continuum-extrapolated results for the broadening kernel in EQCD from lattice calculations [2]. However, because EQCD is long-distance effective theory of QCD the kernel obtained in EQCD theory is not directly the expected result for QCD at all scales, and a matching still needs to be done to obtain the right short-distance kernel.

During this chapter, we will use the lattice EQCD results [2] to construct a full broadening kernel in QCD, and we will then use it to compute the medium-induced radiation in infinite medium. Subsequently, we will Fourier transform the kernel back to momentum space, which will allow us to extend the calculation of medium-induced radiation to finite medium length, and we discuss our results.

6.1 Collisional broadening kernel

	$\frac{C(b_\perp)}{g_s^2}\Big\vert^{N_f=3}_{250\ \text{MeV}}$	$\frac{C(b_\perp)}{g_s^2}\Big\vert^{N_f=3}_{500\ \text{MeV}}$
g^2	3.725027	2.763516
$\hat{q}_0/g^6T^3$	0.1465(78)	0.185(10)

Table 6.1: Coupling constant and the constant momentum broadening coefficient for the non-perturbative kernels.

In order to obtain the full QCD broadening kernel from the EQCD lattice results in [2], following [147] we need to subtract the wrong EQCD short-distance[2]behavior and supply the right QCD behavior as follows

$$C_{\text{QCD}}(b_\perp) \approx \left(C^{\text{pert}}_{\text{QCD}}(b_\perp) - C^{\text{pert}}_{\text{EQCD}}(b_\perp)\right) + C^{\text{latt}}_{\text{EQCD}}(b_\perp)\,. \tag{6.3}$$

The leading order perturbative QCD contribution for $q_\perp \gg m_D$ is known in momentum space as [148]

$$C^{\text{pert}}_{\text{QCD}}(q_\perp) = \frac{g_{\text{s}}^4 T^3 C_{\text{R}}}{q_\perp^4} \int \frac{\mathrm{d}^3 p}{(2\pi)^3} \frac{p - p_z}{p} \left[2C_{\text{A}} n_{\text{B}}(p)\,(1+n_{\text{B}}(p')) + 4\,N_{\text{f}} T_{\text{f}}\, n_{\text{F}}(p)\,(1-n_{\text{F}}(p'))\right]. \tag{6.4}$$

For the EQCD subtraction, we only need the large momentum part

$$C^{\text{pert}}_{\text{EQCD}}(q_\perp) \xrightarrow{q_\perp \gg m_{\text{D}}} C^{\text{pert}}_{\text{subtr}}(q_\perp) = \frac{C_{\text{R}} g_{\text{s}}^2 T m_{\text{D}}^2}{q_\perp^4} - \frac{C_{\text{R}} C_{\text{A}} g_{\text{s}}^4 T^2}{16\, q_\perp^3}\,, \tag{6.5}$$

where the first term subtracts the IR behavior of the QCD kernel, while the second one will cancel the UV limit of the lattice extracted result. We obtain a fully matched kernel, however, since the lattice numerical computation is expensive, the numerical data and its errors are sparse and only exist in a finite range. Additional information about the behavior of the kernel in the range of impact parameter space not covered by the data is needed in order to compute the in-medium splitting. In the following subsections, we proceed to provide such limiting behaviors of the kernel.

Long-distance limit of the kernel

At long-distances the Wilson loop follows an area-law behavior [149] with asymptotic corrections which are important for smoothening the transition to the numerical data values

$$\frac{C_{\text{QCD}}}{g_{\text{s}}^2}(b_\perp) \xrightarrow{b_\perp \gg 1/g_{\text{s}}^2} A + \frac{\sigma_{\text{EQCD}}}{g_{\text{3d}}^4} g_{\text{3d}}^2 b_\perp + \frac{g_{\text{s}}^4 C_{\text{R}}}{\pi}\left[\frac{y}{4}\left(\frac{1}{6} - \frac{1}{\pi^2}\right) + \frac{C_{\text{A}}}{8\pi^2 g_{\text{s}}^2}\right] \log(g_{\text{3d}}^2 b_\perp)\,, \tag{6.6}$$

where σ_{EQCD} is known as the string tension of EQCD and A is a constant fitted to the data.

Short-distance limit of the kernel

At short-distances which translate to the UV limit in momentum space, the rate follow a similar behavior to the leading order QCD rate

$$\frac{C_{\text{QCD}}}{g_{\text{s}}^2}(b_\perp) \xrightarrow{b_\perp \ll 1/m_{\text{D}}} -\frac{C_{\text{R}}}{8\pi}\frac{\zeta(3)}{\zeta(2)}\left(-\frac{1}{2g_{\text{s}}^2} + \frac{3y}{2}\right)(g_{\text{3d}}^2 b_\perp)^2 \log(g_{\text{3d}}^2 b_\perp) + \frac{1}{4}\frac{\hat{q}_0}{g_{\text{3d}}^6}(g_{\text{3d}}^2 b_\perp)^2\,. \tag{6.7}$$

[2] We will refer to the small $q_\perp$ limit as ultraviolet and large $q_\perp$ as infrared IR, while in impact parameter space we will use short/long distance for small/large $\boldsymbol{b}_\perp$.

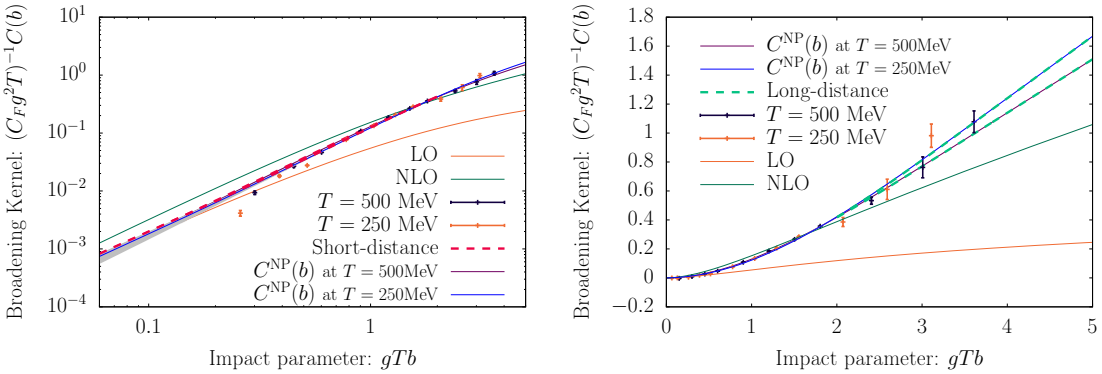

Figure 6.1: Non-perturbative elastic broadening kernel interpolation spline in the short-distance (left) and large-distance (right) regimes. We compare to both the short-distance limit from Eq. (6.7) and the long-distance limit from Eq. (6.6).

We find that to obtain $\hat{q}_0$ it is better to perform a fit to the data-points at short-distances for the non-matched lattice-EQCD-data ($C^{\rm latt}_{\rm EQCD}(b_\perp)$) and the correction ($\left(C^{\rm pert}_{\rm QCD} - C^{\rm pert}_{\rm subtr}\right)(b_\perp)$) separately. We quote the QCD result in Tab. 6.1, while for the non-matched lattice-EQCD-data it is given in [2].

6.1.1 Interpolation of lattice data

Next, in order to compute radiative rates, we construct a spline interpolation for the momentum broadening kernel. Guided by the limiting behaviors of $C_{\rm QCD}(b_\perp)$, we compute several splines by varying where we switch to the asymptotic short and long distance behavior and requiring each spline to be within a standard deviation of the data points. By taking the average of the different splines we obtain the smooth spline in Fig. 6.1 for the two different temperatures $T = 250, 500$MeV, while the gray band represents the spread of the different splines obtained. We note that the data sets for the two different temperatures show a very similar behavior when the broadening kernel $C_{\rm QCD}(b_\perp)$ and impact parameter $b_\perp$ are measured in units of $[g_{\rm s}^2 T]$ and $[g_{\rm s} T]^{-1}$, respectively, which ultimately leads to similar radiative emission rates discussed in the next section.

6.1.2 Perturbative kernel in EQCD

In addition to the non-perturbative broadening kernel, we will compare our results with the ones using broadening kernels obtained from perturbative calculations in

EQCD theory. At leading order (LO) $\mathcal{O}(g_\mathrm{s}^4)$, the QCD collisional broadening kernel can be expressed in momentum space ($q_\perp$) [148] as

$$C^{\mathrm{LO}}_{\mathrm{QCD}}(q_\perp) = \frac{g_\mathrm{s}^4 C_\mathrm{R}}{q_\perp^2(q_\perp^2+m_\mathrm{D}^2)}\int\frac{\mathrm{d}^3p}{(2\pi)^3}\frac{p-p_z}{p}\left[2C_\mathrm{A}n_\mathrm{B}(p)(1+n_\mathrm{B}(p'))\right. \\ \left.+4N_\mathrm{f}T_\mathrm{f}n_\mathrm{F}(p)(1-n_\mathrm{F}(p'))\right] , \quad (6.8)$$

with $p' = p + \frac{\boldsymbol{q}_\perp^2+2\boldsymbol{q}_\perp\cdot\boldsymbol{p}}{2(p-p_z)}$. The kernel displays the following asymptotic behaviors:

$$C^{\mathrm{LO}}_{\mathrm{QCD}}(q_\perp) = g_\mathrm{s}^2 T C_\mathrm{R}\begin{cases}\frac{m_\mathrm{D}^2-g_\mathrm{s}^2T^2C_\mathrm{A}\frac{q_\perp}{16T}}{q_\perp^2(q_\perp^2+m_\mathrm{D}^2)} , & q_\perp \ll g_\mathrm{s}T , \\ \frac{g_\mathrm{s}^2T^2}{q_\perp^4}\frac{\zeta(3)}{\zeta(2)}\left(1+\frac{N_\mathrm{f}}{4}\right) , & q_\perp \gg g_\mathrm{s}T . \end{cases} \quad (6.9)$$

Next-to-leading order (NLO) corrections are of g_s^5 order, they arise from infrared corrections that are suppressed by an additional factor of $m_\mathrm{D} \sim g_\mathrm{s}$ and can be calculated within EQCD [146]. Similarly to the treatment of the non-perturbative kernel, the NLO broadening kernel is computed using perturbative results for the soft contributions from EQCD and supplying the hard contribution by the matching (6.4) [146]. Specifically,

$$C^{\mathrm{NLO}}_{\mathrm{QCD}}(q_\perp) = C^{\mathrm{LO}}_{\mathrm{EQCD}}(q_\perp) + C^{\mathrm{NLO}}_{\mathrm{EQCD}}(q_\perp) + C^{\mathrm{pert}}_{\mathrm{QCD}}(q_\perp) - C^{\mathrm{pert}}_{\mathrm{subtr}}(q_\perp) , \quad (6.10)$$

where the leading and next-to-leading order contributions from soft modes are given by

$$C^{\mathrm{LO}}_{\mathrm{EQCD}}(q_\perp) = C_\mathrm{R}g_\mathrm{s}^2T\frac{m_\mathrm{D}^2}{q_\perp^2(q_\perp^2+m_\mathrm{D}^2)} , \quad (6.11)$$

$$\frac{C^{\mathrm{NLO}}_{\mathrm{EQCD}}(q_\perp)}{g_\mathrm{s}^4T^2C_\mathrm{R}C_\mathrm{A}} = \frac{7}{32q_\perp^3} + \frac{-m_\mathrm{D}-2\frac{q_\perp^2-m_\mathrm{D}^2}{q_\perp}\tan^{-1}\left(\frac{q_\perp}{m_\mathrm{D}}\right)}{4\pi(q_\perp^2+m_\mathrm{D}^2)^2} + \frac{m_\mathrm{D}-\frac{q_\perp^2+4m_\mathrm{D}^2}{2q_\perp}\tan^{-1}\left(\frac{q_\perp}{2m_\mathrm{D}}\right)}{8\pi q_\perp^4} \\ -\frac{\tan^{-1}\left(\frac{q_\perp}{m_\mathrm{D}}\right)}{2\pi q_\perp(q_\perp^2+m_\mathrm{D}^2)} + \frac{\tan^{-1}\left(\frac{q_\perp}{2m_\mathrm{D}}\right)}{2\pi q_\perp^3} \\ +\frac{m_D}{4\pi(q_\perp^2+m_\mathrm{D}^2)}\left[\frac{3}{q_\perp^2+4m_\mathrm{D}^2}-\frac{2}{(q_\perp^2+m_\mathrm{D}^2)}-\frac{1}{q_\perp^2}\right] . \quad (6.12)$$

$C^{\mathrm{pert}}_{\mathrm{subtr}}(q_\perp)$ from (6.5) cancels the IR divergence of the hard contribution and the UV behavior of the soft NLO contribution.

We display the different broadening kernels $C_{\mathrm{QCD}}(b_\perp)$ in Fig. 6.1. For the perturbative kernels we use the same coupling as the one for $T = 500\mathrm{MeV}$ in Tab 6.1. One notes that the leading order in Eq. (6.8) is recovered by the extrapolated spline at very short-distances $g_\mathrm{s} T b_\perp$. The NLO Eq. (6.10) result features a significantly larger value of $\hat{q}$ but has the same qualitative behavior at long-distances as the non-perturbatively determined $C_{\mathrm{QCD}}(b_\perp)$ except the difference in the string tension, i.e. the slope of the curve at large distances $gTb_\perp \gg 1$.

6.2 Infinite medium splitting rates

Before we present our results for the in-medium splitting rates, we will briefly introduce two approximations which can be used to obtain the rate at the two extremes of energy.

6.2.1 Bethe-Heitler regime

When the typical momentum of the splitting is small ($Pz(1-z) \ll \omega_{\mathrm{BH}} \sim T$), the formation time of the radiation is small and interference between scatterings can be neglected. In this so-called Bethe-Heitler regime, one can then solve the rate Eq. (3.33) in an opacity expansion, corresponding to an expansion in the number of elastic scatterings with the medium. By considering the limit of a single scattering, we obtain the following semi-analytic expressions for the rates (c.f. Appendix C)

$$\begin{aligned}
\frac{\mathrm{d}\Gamma^{BH}_{g\to gg}}{\mathrm{d}z}(P,z) =& g_\mathrm{s}^4 T P_{gg}(z)\left[\frac{C_A}{2}Q\left(\tilde{\mu}^2_{g\to gg}(z)\right)\right. \\
&\left.+\frac{C_\mathrm{A}}{2}Q\left(\tilde{\mu}^2_{g\to gg}(z)/z^2\right)+\frac{C_\mathrm{A}}{2}Q\left(\tilde{\mu}^2_{g\to gg}(z)/\bar{z}^2\right)\right], \\
\frac{\mathrm{d}\Gamma^{BH}_{q\to gq}}{dz}(P,z) =& g_\mathrm{s}^4 T P_{qg}(z)\left[\frac{C_\mathrm{A}}{2}Q\left(\tilde{\mu}^2_{q\to gq}(z)\right)\right. \\
&\left.+(C_\mathrm{F}-\frac{C_\mathrm{A}}{2})Q\left(\tilde{\mu}^2_{q\to gq}(z)/z^2\right)+\frac{C_\mathrm{A}}{2}Q\left(\tilde{\mu}^2_{q\to gq}(z)/\bar{z}^2\right)\right], \\
\frac{\mathrm{d}\Gamma^{BH}_{g\to q\bar{q}}}{\mathrm{d}z}(P,z) =& g_\mathrm{s}^4 T P_{gq}(z)\left[(C_\mathrm{F}-\frac{C_\mathrm{A}}{2})Q\left(\tilde{\mu}^2_{g\to q\bar{q}}(z)\right)\right. \\
&\left.+\frac{C_\mathrm{A}}{2}Q\left(\tilde{\mu}^2_{g\to gq}(z)/z^2\right)+\frac{C_\mathrm{A}}{2}Q\left(\tilde{\mu}^2_{q\to gq}(z)/\bar{z}^2\right)\right],
\end{aligned} \tag{6.13}$$

where, denoting $a = m^2_{\infty,q}/m^2_D$, one has

$$\tilde{\mu}^2_{g\to gg}(z) = \frac{1-z(1-z)}{2}\,, \quad \tilde{\mu}^2_{q\to gq}(z) = \frac{z}{2} + a(1-z)^2\,, \quad \tilde{\mu}^2_{g\to q\bar{q}}(z) = \frac{2a-z(1-z)}{2}\,, \tag{6.14}$$

and

$$Q(\tilde{\mu}^2) = \frac{m^2_{\rm D}}{2\pi g_{\rm s}^2 T}\int\frac{{\rm d}^2\mathbf{p}_\perp}{(2\pi)^2}\int\frac{{\rm d}^2\mathbf{q}_\perp}{(2\pi)^2}\,\bar{C}(m_D\mathbf{q}_\perp)\left[\frac{\mathbf{p}_\perp}{\mathbf{p}_\perp^2+\tilde{\mu}^2} - \frac{(\mathbf{p}_\perp-\mathbf{q}_\perp)}{(\mathbf{p}_\perp-\mathbf{q}_\perp)^2+\tilde{\mu}^2}\right]^2 . \tag{6.15}$$

While the above relation is formulated in momentum space, the integral defining $Q(\tilde{\mu}^2)$ in Eq. (6.15) can also be evaluated using the kernel in position space as show in Appendix C.

6.2.2 Deep LPM regime

Conversely, in the limit of a very high-energy parton ($P \gg T$) traversing a thick medium, the typical number of rescatterings within the formation time of bremsstrahlung can be large, indicating that interferences between many soft scatterings which contribute to the total transverse momentum transfer during the formation of the radiation need to be considered. Simplifications occur in the limit $Pz(1-z) \gg \omega_{\rm BH} \sim T$, where the splitting probes the small $b_\perp$ behavior of the momentum broadening kernel, which can be expressed as

$$C(b_\perp) = -\frac{g_{\rm s}^4 T^3}{16\pi}\mathcal{N} b_\perp^2 \log(\xi m_{\rm D}^2 b_\perp^2/4) \tag{6.16}$$

where $\mathcal{N} = \frac{\zeta(3)}{\zeta(2)}\left(1+\frac{N_{\rm f}}{4}\right)$. In accordance with the discussion in Sec. 6.1, the coefficient $\frac{g_{\rm s}^4T^2}{16\pi}\mathcal{N}b_\perp^2$ gives the leading logarithmic behavior $b_\perp\log(b_\perp^2)$ and the coefficient ξ captures the $b_\perp^2$ behavior. Specifically for the LO kernel $\xi_{\rm LO} = e^{2\gamma_{\rm E}-2} \simeq 0.429313$ can be determined analytically, while for the NLO and non-perturbative kernels, we obtain $\xi_{\rm NLO} \simeq 1.355\cdot 10^{-3}$ and $\xi_{\rm NP} = 4\frac{g_{\rm s}^4T^2}{m_{\rm D}^2}e^{-4\pi\frac{\hat{q}_0}{g_{\rm s}^4T^3\mathcal{N}}} \simeq 0.1702$ from a fit of the small $b_\perp$ behavior. Following [133], the rate equation can be solved iteratively in an inverse logarithmic expansion to obtain

$$\frac{{\rm d}\Gamma_{a\to bc}}{{\rm d}z}(P,z) = \frac{g_{\rm s}^2}{16\pi^2\sqrt{2}Pz(1-z)}\;P_{ab}(z)\;m_{\rm D}^2\mu_\perp^2(P,z)\,, \tag{6.17}$$

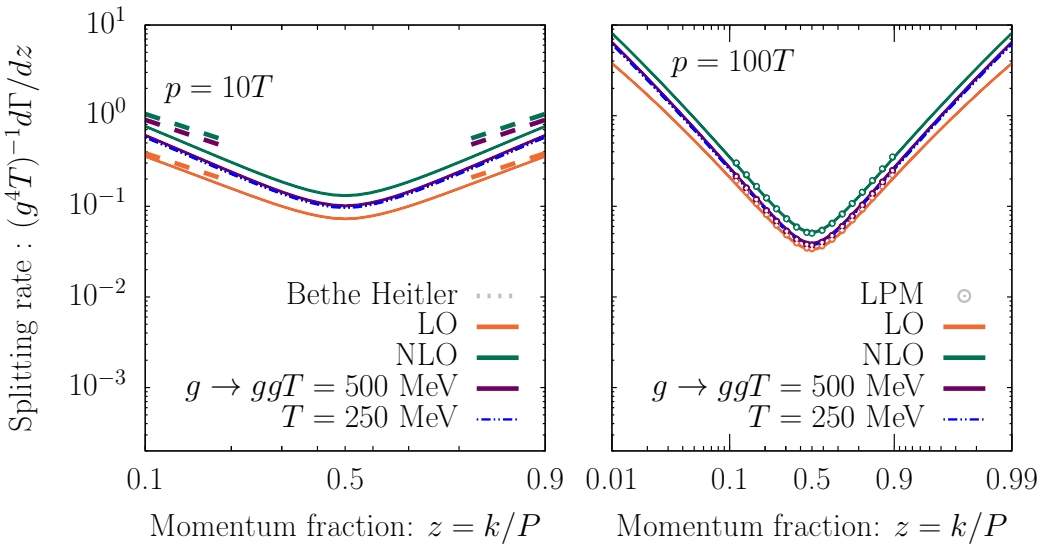

Figure 6.2: Splitting rate for process $g \to gg$ at $T = 250$MeV (dashed blue lines) and $T = 500$MeV (full purple lines). Different columns correspond to parent energies $p = 10T$ (left) and $p = 100T$ (right). We compare with rates computed using the perturbative leading order (orange) and next-to-leading order (green) elastic broadening kernels. The Bethe-Heitler rates and LPM rates are shown with dashed lines and circles, respectively, using the color of the corresponding kernel.

where $\mu_\perp^2(P,z)$ is self-consistently determined from

$$\mu_\perp^2(P,z) = \frac{g_s^2 T^2 \mathcal{N}}{m_D^2}\frac{g_s T}{m_D}\left(\frac{2}{\pi}z(1-z)\frac{P}{T}\right)^{1/2}\left(C_1 \log\left(\frac{\alpha\mu_\perp^2}{\xi}\right) + C_z z^2 \log\left(\frac{\alpha\mu_\perp^2}{\xi z^2}\right) + C_{1-z}(1-z)^2 \log\left(\frac{\alpha\mu_\perp^2}{\xi(1-z)^2}\right)\right)^{1/2}, \quad (6.18)$$

with $\alpha = e^{\gamma_e + \pi/4}$.

6.2.3 Results

We solve the full in-medium rate equation in the infinite medium length approximation as described in Chapter 3 in Eq. (3.33), where we replace the Debye screened potential with different broadening kernels in the last section. We present our results in Figs. 6.2-6.4, where we show the rates for the non-perturbative broadening

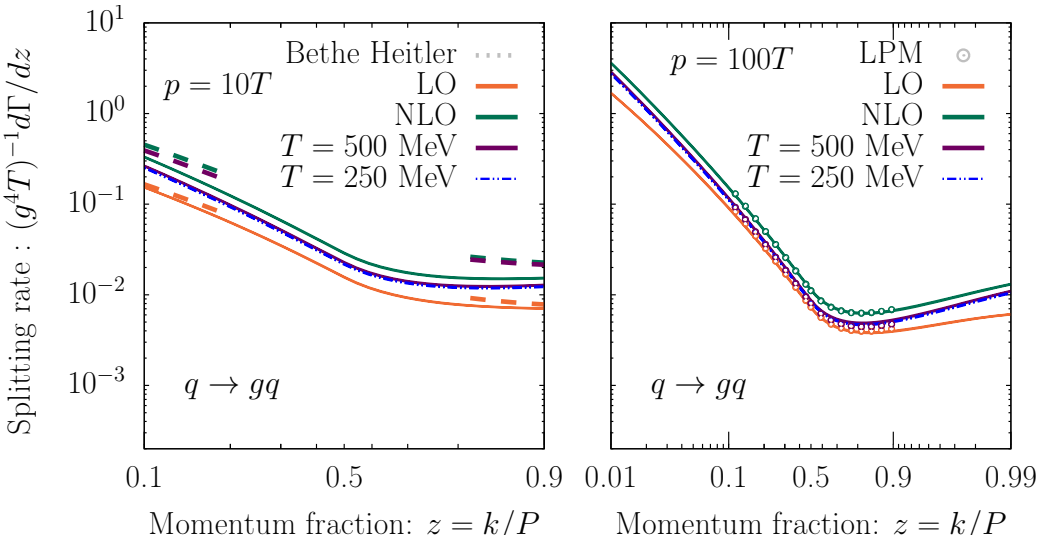

Figure 6.3: Splitting rate for process $q \to gq$ using the same color scheme as Fig. 6.2.

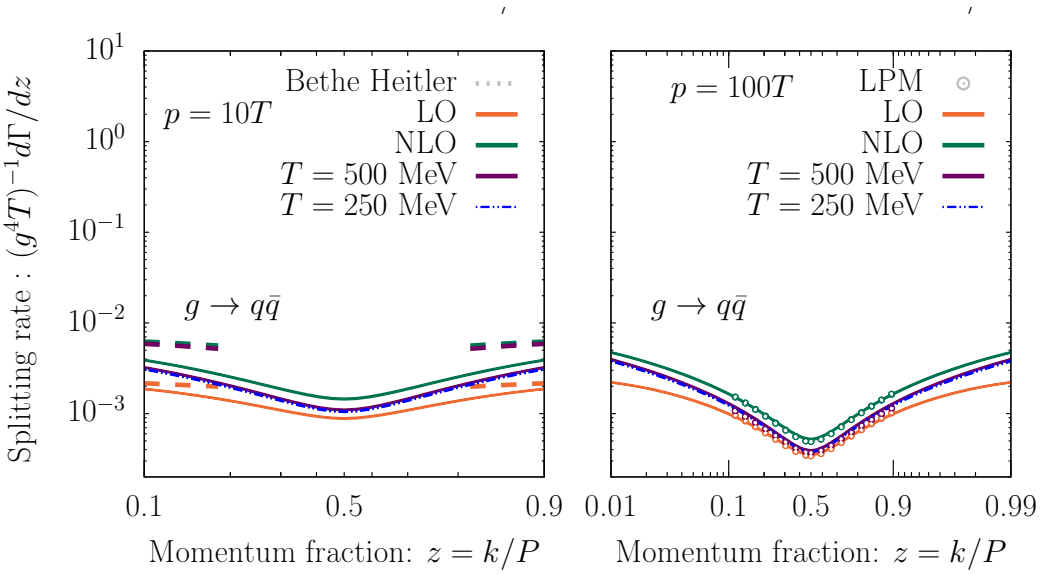

Figure 6.4: Splitting rate for the process $g \to q\bar{q}$ using the same color scheme as Fig. 6.2.

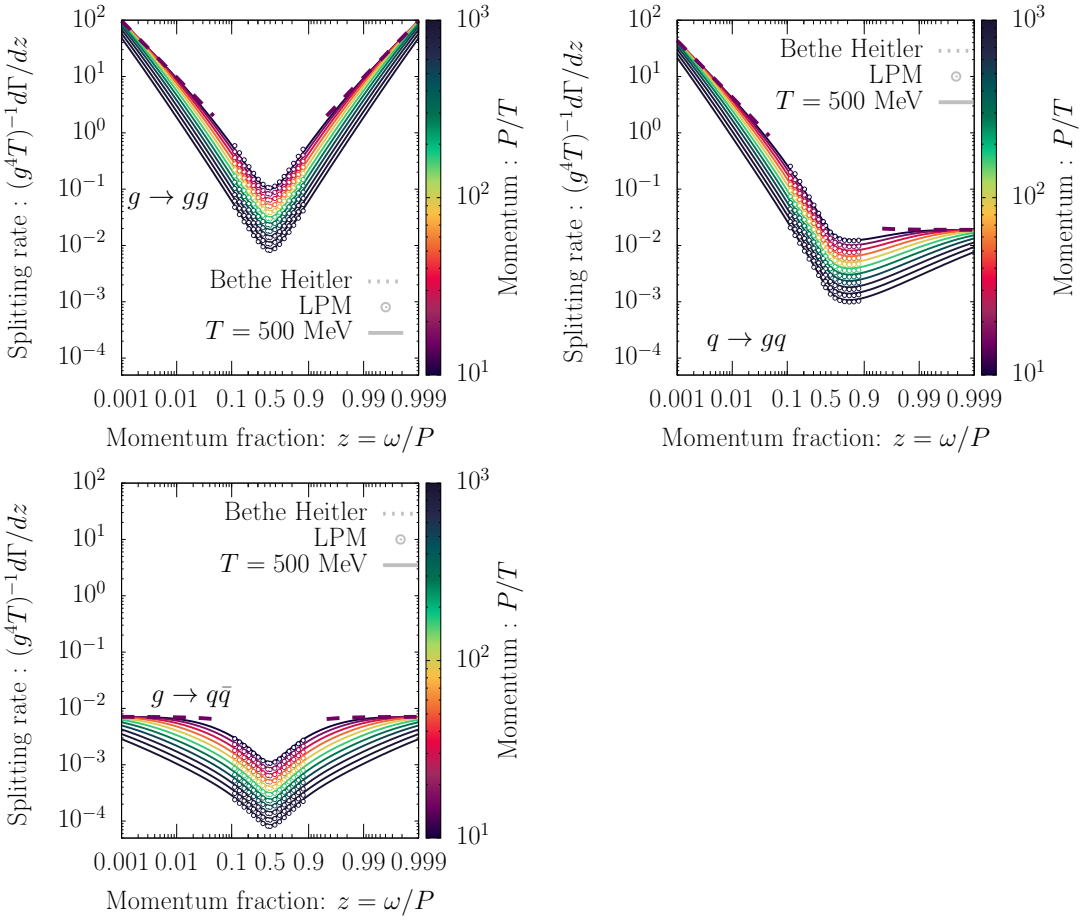

Figure 6.5: Momentum dependence of the splitting rate at $T = 500$MeV (dashed blue lines) for the processes $g \to gg$ (top left), $q \to gq$ (top right), $g \to q\bar{q}$ (bottom). Dashed lines and open circles correspond to the approximate rates in Bethe-Heitler regime (6.13) and the deep LPM regime (6.17).

kernel $C_{\rm QCD}(b_\perp)$ at $T = 250, 500$MeV (left/right columns), along with the corresponding results obtained for the leading order ($C^{\rm LO}_{\rm QCD}(b_\perp)$) and next-to-leading order ($C^{\rm NLO}_{\rm QCD}(b_\perp)$) determinations of the collisional broadening kernel. Fig. 6.2, 6.3 and 6.4 show the rates for the $g \to gg$,$q \to qg$ and $g \to q\bar{q}$ processes respectively, for different parton energies $p = 10T$ (left) and $p = 100T$ (right). The momentum dependence of the rate is shown in Fig. 6.5, for the non-perturbative kernel at $T = 500$MeV, using the color palette in a logarithmic scale to distinguish between different momentum of the parent particle $p = 10 - 1000T$. In both figures, we also show the Bethe-Heitler rates in Eq. (6.13) (dashed lines) and the deep LPM rates (circles) Eq. (6.17).

Starting with the rates in Figs. 6.2-6.4, one observes that the non-perturbatively determined splitting rates for the two different temperatures do not display any remarkable difference, leading to essentially the same emission rates in units of $[g^4T]$. As expected, the momentum dependence of the rate clearly displays LPM suppression at large typical momentum $Pz(1-z) \gg T$ as well as an unsuppressed Bethe-Heitler rate in the other limit $Pz(1-z) \ll T$ seen in Fig. 6.5. We also observe that at low energy $z(1-z)E \ll T$ where the large impact parameter (small momentum transfer) is more important, the non-perturbative result is closer to the NLO rate as they both have a similar behavior at large impact parameter, but there exists a quantitative difference due to their different string tensions. Conversely, in the LPM suppressed regime at high energy $z(1-z)E \gg T$, where small impact parameter (large momentum transfer) is relevant, the non-perturbative rate is closer to the LO rate which again agrees with the behavior of the elastic kernel (cf. Fig. 6.1).

6.3 Finite medium splitting rates

Beyond the infinite medium length limit, one can compute medium-induced radiation rates in more physical finite medium length. It turns out that, as opposed to the infinite medium limit where the calculation simplifies in impact parameter space, for finite medium, it is easier to work in momentum space where one integrates an integro-differential equation to obtain the rate [120, 121]. During this section, we will transform the broadening kernel spline to momentum space and use it to compute medium-induced radiation rate in a medium with finite length.

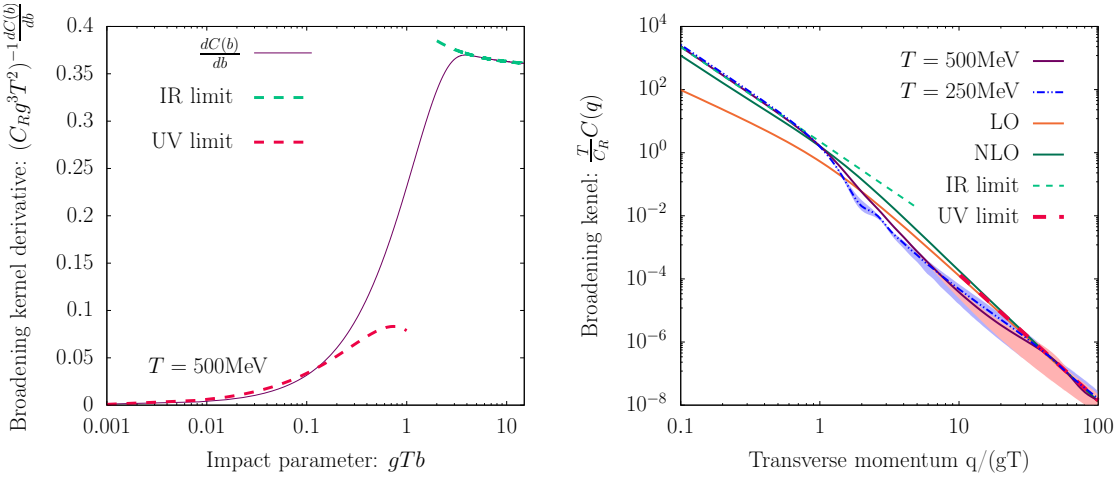

Figure 6.6: (left) Space derivative of the broadening kernel spline for $T = 500$MeV and its asymptotic behavior. (right) Elastic broadening kernel in momentum space for both $T = 250, 500$MeV, where the blue and red bands represent the error for 250MeV and 500MeV respectively. We compare to both the UV limit from Eq. (6.23) and the IR limit from Eq. (6.22).

6.3.1 Broadening kernel in momentum space

In this section we will proceed to Fourier transform the resulting spline from section 6.1.1 back to momentum space. We found that it is best to transform $\frac{\mathrm{d}C(\boldsymbol{b}_\perp)}{\mathrm{d}b_\perp}$, the coordinate space derivative of $C(b_\perp)$, using Eq. (6.2) one finds

$$\frac{\mathrm{d}C(\boldsymbol{b}_\perp)}{\mathrm{d}b_\perp} = \int \frac{\mathrm{d}^2 q_\perp}{(2\pi)^2} \mathrm{e}^{-i\boldsymbol{q}_\perp \cdot \boldsymbol{b}_\perp} \left[\frac{i\boldsymbol{q}_\perp \cdot \boldsymbol{b}_\perp}{b_\perp} C(q_\perp) \right] . \tag{6.19}$$

Exploiting the fact that $C(\boldsymbol{q}_\perp)$ does not depend on angle leads to the following Hankel transform

$$\frac{\mathrm{d}C(\boldsymbol{b}_\perp)}{\mathrm{d}b_\perp} = \int_0^\infty \frac{\mathrm{d}q_\perp}{(2\pi)} \, q_\perp J_1(b_\perp q_\perp) \left[q_\perp C(q_\perp) \right] , \tag{6.20}$$

where $J_1(x)$ is the Bessel function of the first kind of order 1. Using an inverse Hankel transform, one obtains the broadening kernel in momentum space

$$C(q_\perp) = \frac{2\pi}{q_\perp} \int_0^\infty \mathrm{d}b_\perp \, b_\perp J_1(b_\perp q_\perp) \frac{\mathrm{d}C(b_\perp)}{\mathrm{d}b_\perp} . \tag{6.21}$$

We proceed now to transform the limiting behaviors of the kernel in order to construct a picture of the momentum broadening kernel at all scales.

IR limit of $C(q_\perp)$: We transform each term of the IR limit from Eq. (6.6): the constant term does not contribute, the linear term leads to $1/q_\perp^3$ behavior[3] and the sub-leading logarithmic term leads to a $1/q_\perp^2$ behavior[4]. Collecting the terms together, one obtains the following expression in momentum space

$$C^{\rm IR}(q_\perp) = \frac{2\pi}{q_\perp^3}\frac{\sigma_{\rm EQCD}}{g_{3d}^2} + \frac{g^4 C_{\rm R}}{\pi}\left[\frac{y}{4}\left(\frac{1}{6}-\frac{1}{\pi^2}\right)+\frac{C_{\rm A}}{8\pi^2 g_{\rm s}^2}\right]\frac{2\pi}{q_\perp^2}\,. \tag{6.22}$$

UV limit of $C(q_\perp)$: The UV limit of the non-perturbative rate in Eq. (6.7) follows the same behavior as the perturbative case, one obtains the same $1/q_\perp^4$ in q-space

$$C^{\rm UV}(q_\perp) = \frac{C_{\rm R}}{8\pi}\frac{\zeta(3)}{\zeta(2)}\left(-\frac{1}{2g_{\rm s}^2}+\frac{3y}{2}\right)\frac{8\pi}{q_\perp^4}\,. \tag{6.23}$$

Transforming the spline: In order to ensure numerical convergence, we subtract the IR limit from the derivative of the rate depicted in the left panel of Fig. 6.6 as follows

$$\frac{\mathrm{d}}{\mathrm{d}b_\perp}\Delta C^{\rm NP}(\boldsymbol{b}_\perp) = \frac{\mathrm{d}C^{\rm NP}(\boldsymbol{b}_\perp)}{\mathrm{d}b_\perp} - \frac{\mathrm{d}C^{\rm IR}(\boldsymbol{b}_\perp)}{\mathrm{d}b_\perp}\,. \tag{6.24}$$

We then compute the following Hankel transform numerically

$$\Delta C^{\rm NP}(q_\perp) = \frac{2\pi}{q_\perp}\int_0^\infty \mathrm{d}b_\perp\; b_\perp J_1(b_\perp\, q_\perp)\frac{d}{db_\perp}\Delta C^{\rm NP}(b_\perp)\,, \tag{6.25}$$

and the result is supplied with the analytical transform of the IR limit

$$C^{\rm NP}(q_\perp) = \Delta C^{\rm NP}(q_\perp) + C^{\rm IR}(q_\perp)\,. \tag{6.26}$$

We obtain the rate in momentum space, shown in right panel of Fig. 6.6, where the bands represent the transformation of the different splines in the band from Fig. 6.1. We also show the limiting behaviors computed above, as well as the LO and NLO kernels. Both the data points $T = 250, 500$MeV display very similar behavior. As expected, in the IR the rate follows a $(1/q_\perp^3)$ behavior similar to the NLO kernel, however they differ by a prefactor due to the difference in the string tension. In the UV limit, all the different kernels display the same $(1/q_\perp^4)$ behavior, associated with the hard scattering contributions.

[3] One can obtain the integration using simple contour integral.

[4] To obtain this behavior we make use of the definition in Eq. (6.21).

6.3.2 Full rate calculation

With the broadening kernel in momentum space at hand, we proceed to compute the rate of medium-induced radiation. Starting point of the rate calculation is the formal expression obtained by employing a time derivative to Eq. (3.31) [121]

$$\frac{d\Gamma^a_{bc}}{dz}(P,z,t) = \frac{g^2 P^a_{bc}(z)}{4\pi P^2 z^2(1-z)^2}\mathrm{Re}\int_t^\infty dt_1 \int_{\boldsymbol{p},\boldsymbol{q}} \boldsymbol{q}.\boldsymbol{p}[K(t,\boldsymbol{q};t_1,\boldsymbol{p}) - (\mathrm{vac})] \,, \quad (6.27)$$

where $K(t,\boldsymbol{q};t_1,\boldsymbol{p})$ is the propagator satisfying the evolution Eq. (3.29). Following [121], we use an integration by part to perform the rearrangement

$$\begin{aligned}
&\int_{t_1}^\infty dt_2 \; K(t_2,\boldsymbol{q};t_1,\boldsymbol{p}) \\
=&\int_{t_1}^\infty dt_2 \; \left[\frac{d}{dt_2}\left(\frac{e^{-i\delta E(\boldsymbol{q})t_2}}{-i\delta E(\boldsymbol{q})}\right)\right] e^{-i\delta E(\boldsymbol{q})t_2} K(t_2,\boldsymbol{q};t_1,\boldsymbol{p}) \,, \quad (6.28)\\
=&\frac{1}{-i\delta E(\boldsymbol{q})}\left[K(\infty,\boldsymbol{q};t_1,\boldsymbol{p}) - K(t_1,\boldsymbol{q};t_1,\boldsymbol{p})\right] \\
&-\int_{t_1}^\infty dt_2 \; \frac{1}{-i\delta E(\boldsymbol{q})}\left[-i\delta E(\boldsymbol{q}) + \partial_{t_2}\right] K(t_2,\boldsymbol{q};t_1,\boldsymbol{p}) \,. \quad (6.29)
\end{aligned}$$

Using the evolution equation for the propagator, we simplify to obtain

$$\begin{aligned}
&\int_{t_1}^\infty dt_2 \; K(t_2,\boldsymbol{q};t_1,\boldsymbol{p}) \\
=&\frac{1}{-i\delta E(\boldsymbol{q})}\left[K(\infty,\boldsymbol{q};t_1,\boldsymbol{p}) - K(t_1,\boldsymbol{q};t_1,\boldsymbol{p})\right] \\
&+\int_{t_1}^\infty dt_2 \; \frac{i}{\delta E(\boldsymbol{q})}\Gamma_3(t_2)\circ K(t_2,\boldsymbol{q};t_1,\boldsymbol{p}) \,. \quad (6.30)
\end{aligned}$$

As argued by [121], the first term is rapidly oscillating and cancels due to a converging factor $e^{-\epsilon t}$; the second term is related to vacuum radiation, and can be canceled it against the vacuum expression. The rate is now expressed as

$$\frac{d\Gamma^a_{bc}}{dz}(P,z,t) = \frac{g^2 P^a_{bc}(z)}{4\pi P^2 z^2(1-z)^2}\mathrm{Re}\int_0^t dt_1 \int_{\boldsymbol{p},\boldsymbol{q}} \frac{i\boldsymbol{q}.\boldsymbol{p}}{\delta E(\boldsymbol{q})}\Gamma_3\circ K(t,\boldsymbol{q};t_1,\boldsymbol{p}) \,. \quad (6.31)$$

Expressing the rate using wave function

To simplify our analysis, we now re-express the rate as follows

$$\frac{d\Gamma^a_{bc}}{dz}(P,z,t) = \frac{g^2 P^a_{bc}(z)}{4\pi P^2 z^2(1-z)^2}\mathrm{Re}\int_0^t d\Delta t \int_{\boldsymbol{p}} \boldsymbol{p}\cdot\vec{\psi}(\boldsymbol{p},\Delta t) \,, \quad (6.32)$$

where we introduce the wave function

$$\vec{\psi}(\boldsymbol{p}, \Delta t = |t_1 - t|) = \int_{\boldsymbol{q}} \frac{i\boldsymbol{q}}{\delta E(\boldsymbol{q})} \Gamma_3 \circ K(t, \boldsymbol{q}; t_1, \boldsymbol{p}) \tag{6.33}$$

which follows the evolution equation

$$[\partial_{\Delta t} + \delta E(\boldsymbol{p}) + \Gamma_3 \circ] \, \vec{\psi}(\boldsymbol{p}, \Delta t) = 0 \, , \tag{6.34}$$

with the initial condition

$$\vec{\psi}(\boldsymbol{p}, \Delta t = 0) = \int_{\boldsymbol{q}} \frac{i\boldsymbol{q}}{\delta E(\boldsymbol{q})} \Gamma_3 \circ (2\pi)^2 \delta^2(\boldsymbol{p} - \boldsymbol{q}) \, , \tag{6.35}$$

$$= \Gamma_3 \circ \frac{i\boldsymbol{p}}{\delta E(\boldsymbol{p})} \, . \tag{6.36}$$

We proceed to factor out the physical scales by defining the dimensionless variables

$$\Delta\tilde{t} = \frac{m_D^2}{2Pz(1-z)} \Delta t \, , \qquad \tilde{q} = \frac{q}{m_D} \, , \quad \tilde{p} = \frac{p}{m_D} \, . \tag{6.37}$$

The energy becomes

$$\delta\tilde{E}(\tilde{\boldsymbol{p}}) = \frac{2Pz(1-z)}{m_D^2} \delta E(\boldsymbol{p}) \, . \tag{6.38}$$

The wave function can be written as

$$\vec{\psi}(\boldsymbol{p}, \Delta t) = g^2 T \frac{2Pz(1-z)}{m_D} \vec{\tilde{\psi}}(\tilde{\boldsymbol{p}}, \Delta\tilde{t}) \, . \tag{6.39}$$

If we factor out the collision integral by writing the broadening kernel as $\tilde{C}(\tilde{\boldsymbol{q}}) = \frac{m_D^2}{g^2 T} \bar{C}(\boldsymbol{q})$, we find

$$\begin{aligned} \Gamma_3 \circ \psi(\boldsymbol{p}) =& (g^2 T)^2 \frac{2Pz(1-z)}{m_D} \int_{\tilde{\boldsymbol{q}}} \tilde{C}(\tilde{\boldsymbol{q}}) \Bigg\{ C_1 \Big[\vec{\tilde{\psi}}(\tilde{\boldsymbol{p}}) - \vec{\tilde{\psi}}(\tilde{\boldsymbol{p}} - \tilde{\boldsymbol{q}}) \Big] \\ &+ C_z \Big[\vec{\tilde{\psi}}(\tilde{\boldsymbol{p}}) - \vec{\tilde{\psi}}(\tilde{\boldsymbol{p}} + z\tilde{\boldsymbol{q}}) \Big] + C_{1-z} \Big[\vec{\tilde{\psi}}(\tilde{\boldsymbol{p}}) - \vec{\tilde{\psi}}(\tilde{\boldsymbol{p}} + (1-z)\tilde{\boldsymbol{q}}) \Big] \Bigg\} \, , \end{aligned} \tag{6.40}$$

$$= (g^2 T)^2 \frac{2Pz(1-z)}{m_D} \tilde{\Gamma}_3(t) \circ \vec{\tilde{\psi}}(\tilde{\boldsymbol{p}}) \, . \tag{6.41}$$

The evolution equation for the dimensionless wave function is written

$$\left[\partial_{\Delta\tilde{t}} + \delta\tilde{E}(\tilde{\boldsymbol{p}}) + \Lambda\,\tilde{\Gamma}_3(t)\circ\right]\vec{\tilde{\psi}}(\tilde{\boldsymbol{p}}, \Delta\tilde{t}) = 0\,, \tag{6.42}$$

where $\Lambda = g^2 T \frac{2Pz(1-z)}{m_D}$, with the initial condition

$$\vec{\tilde{\psi}}(\tilde{\boldsymbol{p}}, \Delta\tilde{t} = 0) = \tilde{\Gamma}_3(t) \circ \frac{i\tilde{\boldsymbol{p}}}{\delta\tilde{E}(\tilde{\boldsymbol{p}})}\,. \tag{6.43}$$

The splitting rate becomes

$$\frac{d\Gamma^a_{bc}}{dz}(P, z, \tilde{t}) = \frac{g^4 T P^a_{bc}(z)}{\pi}\mathrm{Re}\int_0^{\tilde{t}} d\Delta\tilde{t}\int_{\tilde{\boldsymbol{p}}} \tilde{\boldsymbol{p}}\cdot\vec{\tilde{\psi}}(\tilde{\boldsymbol{p}}, \Delta\tilde{t})\,. \tag{6.44}$$

Although the solution of the rate should work at all scales for a highly energetic parton, one can get away with using approximations in certain ranges which simplifies the calculation drastically and can speed up simulation where these rates are used. Numerous approximation have been developed in the literature [108] [109] [117–119] [120], during the following sections we will review the latest developments together with some traditional approximations, which we will compare to the full rate in figure. 6.9.

6.3.3 Opacity expansion

In the region where the medium length is thin, the hard particles do not encounter many medium particles. The rate can be computed in the same way as we discussed in sec. 6.2.1. In finite medium, this expansion is also known as the Gyulassy, Levai and Vitev (GLV) approximation[5] [114, 115]. It is easier to compute the expansion in the interaction picture introduced in Appendix D, the wave function for the first order ($N = 1$) is directly the initial condition defined in Eq. (D.4) as we already take one scattering in the definition of the wave function

$$\tilde{\psi}^{(1)}_I(\tilde{p}) = \tilde{\boldsymbol{p}}\cdot\tilde{\Gamma}_3 \circ \frac{i\tilde{\boldsymbol{p}}}{\delta\tilde{E}(\tilde{\boldsymbol{p}})}\,. \tag{6.45}$$

Inserting the wave function in the definition in Eq. D.5, we write

$$\left.\frac{d\Gamma^a_{bc}}{dz}\right|_{N=1}(P, z, \tilde{t}) = \frac{g^4 T P^a_{bc}(z)}{\pi}\mathrm{Re}\int_0^{\tilde{t}} d\Delta\tilde{t}\int_{\tilde{\boldsymbol{p}}} e^{-i\delta\tilde{E}(\tilde{p})\Delta\tilde{t}}\tilde{\boldsymbol{p}}\cdot\tilde{\Gamma}_3 \circ \frac{i\tilde{\boldsymbol{p}}}{\delta\tilde{E}(\tilde{\boldsymbol{p}})}\,. \tag{6.46}$$

[5] As opposed to the GLV approximation we will not neglect thermal masses, and we will not take the soft gluon approximation.

The time integration can be done analytically and one finds

$$\left.\frac{d\Gamma^a_{bc}}{dz}\right|_{N=1}(P,z,\tilde{t}) = \frac{g^4 T P^a_{bc}(z)}{\pi}\int_{\tilde{\boldsymbol{p}}}\frac{1-\cos\left(-\delta\tilde{E}(\tilde{p})\tilde{t}\right)}{\delta\tilde{E}(\tilde{p})}\tilde{\boldsymbol{p}}\cdot\tilde{\Gamma}_3\circ\frac{i\tilde{\boldsymbol{p}}}{\delta\tilde{E}(\tilde{\boldsymbol{p}})}\,. \tag{6.47}$$

When we take the limit $\tilde{t}\to\infty$ which corresponds to neglecting the oscillatory factor $\cos\left(-\delta\tilde{E}(\tilde{p})\tilde{t}\right)$, we recover the Bethe-Heitler rate as in Eqns. (6.13) for the infinite medium case.

6.3.4 Resummed opacity expansion

Besides the straight opacity expansion, the authors of [150] developed a resummation that tries to capture additional re-scatterings with the medium. During this section we will present this procedure, starting with the second order ($N=2$) wave function which obeys the following evolution equation

$$\partial_{\Delta\tilde{t}}\tilde{\psi}^{(2)}_I(\tilde{p},s) = -\Lambda\, e^{i\delta\tilde{E}(\tilde{p})s}\tilde{\boldsymbol{p}}\cdot\tilde{\Gamma}_3\circ e^{-i\delta\tilde{E}(\tilde{p})s}\frac{\tilde{\boldsymbol{p}}}{\tilde{p}^2}\tilde{\psi}^{(1)}_I(\tilde{p})\,, \tag{6.48}$$

with initial condition $\tilde{\psi}^{(2)}_I(\tilde{p},\Delta\tilde{t}=0)=\tilde{\psi}^{(1)}_I(\tilde{p})$. Integrating the time direction, we find

$$\tilde{\psi}^{(2)}_I(\tilde{p},\Delta\tilde{t}) = \tilde{\psi}^{(1)}_I(\tilde{p}) - \Lambda\int_0^{\Delta\tilde{t}} ds\; e^{i\delta\tilde{E}(\tilde{p})s}\tilde{\boldsymbol{p}}\cdot\tilde{\Gamma}_3\circ e^{-i\delta\tilde{E}(\tilde{p})s}\frac{\tilde{\boldsymbol{p}}}{\tilde{p}^2}\tilde{\psi}^{(1)}_I(\tilde{p})\,. \tag{6.49}$$

Explicitly, the correction is given by

$$\tilde{\psi}^{(2)}_I(\tilde{p},\Delta\tilde{t}) - \tilde{\psi}^{(1)}_I(\tilde{p}) = -\Lambda\int_0^{\Delta\tilde{t}} ds\; e^{i\delta\tilde{E}(\tilde{p})s}\tilde{\boldsymbol{p}}\cdot\tilde{\Gamma}_3\circ e^{-i\delta\tilde{E}(\tilde{p})s}\frac{\tilde{\boldsymbol{p}}}{\tilde{p}^2}\tilde{\psi}^{(1)}_I(\tilde{p}) \tag{6.50}$$

$$\begin{aligned}
&= -\Lambda\int_0^{\Delta\tilde{t}} ds\; e^{i\delta\tilde{E}(\tilde{p})s}\tilde{\boldsymbol{p}}\cdot \\
&\int_{\tilde{\boldsymbol{q}}}\tilde{C}(\tilde{\boldsymbol{q}})\Bigg\{C_1\left[e^{-i\delta\tilde{E}(\tilde{p})s}\frac{\tilde{\boldsymbol{p}}}{\tilde{p}^2}\tilde{\psi}^{(1)}_I(\tilde{p}) - e^{-i\delta\tilde{E}(\tilde{p}-\tilde{q})s}\frac{\tilde{\boldsymbol{p}}-\tilde{\boldsymbol{q}}}{|\tilde{\boldsymbol{p}}-\tilde{\boldsymbol{q}}|^2}\tilde{\psi}^{(1)}_I(\tilde{p}-\tilde{q})\right] \\
&+ C_z\left[e^{-i\delta\tilde{E}(\tilde{p})s}\frac{\tilde{\boldsymbol{p}}}{\tilde{p}^2}\tilde{\psi}^{(1)}_I(\tilde{p}) - e^{-i\delta\tilde{E}(\tilde{p}+z\tilde{q})s}\frac{\tilde{\boldsymbol{p}}+z\tilde{\boldsymbol{q}}}{|\tilde{\boldsymbol{p}}+z\tilde{\boldsymbol{q}}|^2}\tilde{\psi}^{(1)}_I(\tilde{p}+z\tilde{q})\right] \\
&+ C_{1-z}\left[e^{-i\delta\tilde{E}(\tilde{p})s}\frac{\tilde{\boldsymbol{p}}}{\tilde{p}^2}\tilde{\psi}^{(1)}_I(\tilde{p}) - e^{-i\delta\tilde{E}(\tilde{p}+(1-z)\tilde{q})s}\frac{\tilde{\boldsymbol{p}}+(1-z)\tilde{\boldsymbol{q}}}{|\tilde{\boldsymbol{p}}+(1-z)\tilde{\boldsymbol{q}}|^2}\tilde{\psi}^{(1)}_I(\tilde{p}+(1-z)\tilde{q})\right]\Bigg\}\,.
\end{aligned} \tag{6.51}$$

Let us focus on the first term which can be written as

$$-\Lambda\int_0^{\Delta\tilde{t}} ds\ \int_{\tilde{\boldsymbol{q}}}\tilde{C}(\tilde{\boldsymbol{q}})C_1\Big[\tilde{\psi}_I^{(1)}(\tilde{p})-e^{i(\delta\tilde{E}(\tilde{p})-\delta\tilde{E}(\tilde{p}-\tilde{q}))s}\frac{\tilde{p}-\tilde{\boldsymbol{p}}\cdot\tilde{\boldsymbol{q}}}{|\tilde{\boldsymbol{p}}-\tilde{\boldsymbol{q}}|^2}\tilde{\psi}_I^{(1)}(\tilde{p}-\tilde{q})\Big]\ . \tag{6.52}$$

For small $\tilde{q}$ the different terms cancel each other, while for large $\tilde{q}$ the phase factor oscillate rapidly and does not contribute to the integral. If we introduce a cutoff scale M^2 for the momentum integral and define

$$\Sigma(M^2)=\int_{\tilde{\boldsymbol{q}}^2>M^2}\tilde{C}(\tilde{\boldsymbol{q}})\ , \tag{6.53}$$

one can then write

$$\begin{aligned}&-\Lambda\int_0^{\Delta\tilde{t}} ds\ \int_{\tilde{\boldsymbol{q}}}\tilde{C}(\tilde{\boldsymbol{q}})C_1\Big[\tilde{\psi}_I^{(1)}(\tilde{p})-e^{i(\delta\tilde{E}(\tilde{p})-\delta\tilde{E}(\tilde{p}-\tilde{q}))s}\frac{\tilde{p}-\tilde{\boldsymbol{p}}\cdot\tilde{\boldsymbol{q}}}{|\tilde{\boldsymbol{p}}-\tilde{\boldsymbol{q}}|^2}\tilde{\psi}_I^{(1)}(\tilde{p}-\tilde{q})\Big]\\ &=-\Lambda\int_0^{\Delta\tilde{t}} ds\ \tilde{\psi}_I^{(1)}(\tilde{p})\Sigma(M^2)\ .\end{aligned} \tag{6.54}$$

Using the same procedure for the other terms, the full correction will be written

$$\tilde{\psi}_I^{(2)}(\tilde{p},\Delta\tilde{t})-\tilde{\psi}_I^{(1)}(\tilde{p})=-\Lambda\int_0^{\Delta\tilde{t}} ds\ \tilde{\psi}_I^{(1)}(\tilde{p})\Sigma_3(M^2)\ , \tag{6.55}$$

with

$$\Sigma_3(M^2)=\Big[C_1\Sigma(M^2)+C_z\Sigma(M^2/z^2)+C_{1-z}\Sigma(M^2/(1-z)^2)\Big]\ . \tag{6.56}$$

The expansion of the splitting rate is now given by

$$\begin{aligned}\left.\frac{d\Gamma^a_{bc}}{dz}\right|_{N=X}(P,z,\tilde{t})=&\frac{g^4TP^a_{bc}(z)}{\pi}\mathrm{Re}\int_0^{\tilde{t}}d\Delta\tilde{t}\int_{\tilde{\boldsymbol{p}}}e^{-i\delta\tilde{E}(\tilde{p})\Delta\tilde{t}}\tilde{\psi}_I^{(1)}(\tilde{p})\\ &+\frac{g^4TP^a_{bc}(z)}{\pi}\mathrm{Re}\int_0^{\tilde{t}}d\Delta\tilde{t}\int_0^{\Delta\tilde{t}}ds\ \int_{\tilde{\boldsymbol{p}}}e^{-i\delta\tilde{E}(\tilde{p})\Delta\tilde{t}}\tilde{\psi}_I^{(1)}(\tilde{p})\Big(-\Lambda\Sigma_3(M^2)\Big)\\ &+\cdots\ .\end{aligned} \tag{6.57}$$

After performing the time integral (ds), we find

$$\begin{aligned}\left.\frac{d\Gamma^a_{bc}}{dz}\right|_{N=X}(P,z,\tilde{t})=&\frac{g^4TP^a_{bc}(z)}{\pi}\mathrm{Re}\int_0^{\tilde{t}}d\Delta\tilde{t}\int_{\tilde{\boldsymbol{p}}}e^{-i\delta\tilde{E}(\tilde{p})\Delta\tilde{t}}\tilde{\psi}_I^{(1)}(\tilde{p})\\ &+\frac{g^4TP^a_{bc}(z)}{\pi}\mathrm{Re}\int_0^{\tilde{t}}d\Delta\tilde{t}\int_{\tilde{\boldsymbol{p}}}e^{-i\delta\tilde{E}(\tilde{p})\Delta\tilde{t}}\tilde{\psi}_I^{(1)}(\tilde{p})\Big(-\Lambda\Sigma_3(M^2)\Delta\tilde{t}\Big)\\ &+\cdots\ .\end{aligned} \tag{6.58}$$

One notices that subsequent terms with additional time integration will exponentiate to obtain

$$\left.\frac{d\Gamma^a_{bc}}{dz}\right|_{N=X}(P,z,\tilde{t}) = \frac{g^4 T P^a_{bc}(z)}{\pi}\mathrm{Re}\int_0^{\tilde{t}} d\Delta\tilde{t}\int_{\tilde{\boldsymbol{p}}} e^{-(i\delta\tilde{E}(\tilde{p})+\Lambda\Sigma_3(\tilde{p}^2))\Delta\tilde{t}}\tilde{\psi}^{(1)}_I(\tilde{p})\ , \tag{6.59}$$

where we defined the cutoff scale $M^2 = \tilde{p}^2$ following [150].

6.3.5 Improved harmonic oscillator approximation

Analogously to the deep LPM regime we introduced in sec. 6.2.2, one can find an equivalent expression for finite medium [109]. Rather than using this approximation only, we will make use of recent calculations which try to go beyond this simple harmonic oscillator limit by including corrections perturbatively [117–119] (we will only compute the first correction).

Using the short-distance behavior defined in Eq. (6.16), one can define a scale Q^2 to evaluate the logarithm and separate it as follows

$$C(b_\perp) = \frac{g_s^4 T^3}{16\pi}\mathcal{N} b_\perp^2 \ln\left(\frac{4Q^2}{\xi m_D^2}\right) + \frac{g_s^4 T^3}{16\pi}\mathcal{N} b_\perp^2 \ln\left(\frac{1}{Q^2 b_\perp^2}\right) = C^{HO}(b_\perp) + C^{\mathrm{pert}}(b_\perp)\ , \tag{6.60}$$

where the Harmonic oscillator kernel is defined

$$C^{HO}(b_\perp) = \frac{g_s^4 T^3}{16\pi}\mathcal{N} b_\perp^2 \ln\left(\frac{4Q^2}{\xi m_D^2}\right)\ . \tag{6.61}$$

Instead of using only the short-distance limit $C^{\mathrm{pert}}(b_\perp) = \frac{g_s^4 T^3}{16\pi}\mathcal{N} b_\perp^2 \ln\left(\frac{1}{Q^2 b_\perp^2}\right)$, we find that it is better if we define the correction to the kernel as the difference

$$C^{\mathrm{pert}}(b_\perp) = C(b_\perp) - C^{HO}(b_\perp)\ , \tag{6.62}$$

where we use the full definition of $C(b_\perp)$, i.e. the numerical spline. The radiation spectrum will also be separate to the sum of the HO and the first correction

$$\frac{dI^{NLO}}{dz}(P,z,t) = \frac{dI^{HO}}{dz}(P,z,t) + \frac{dI^{(1)}}{dz}(P,z,t)\ , \tag{6.63}$$

where the correction is computed using a first order opacity expansion with the kernel $C^{\mathrm{pert}}(b_\perp)$. Following [117–119], the scale Q^2 is the typical momentum of the

radiated quanta defined self-consistently by using

$$Q^2(P,z) = \sqrt{Pz(1-z)\hat{q}_3(Q^2)}\,, \tag{6.64}$$

$$\hat{q}_{\text{eff}}(Q^2) = \frac{g_s^4 T^3}{4\pi}\mathcal{N}\left[C_1 + C_z z^2 + C_{1-z}(1-z)^2\right]\ln\left(\frac{4Q^2}{\xi m_D^2}\right)\,, \tag{6.65}$$

where $\hat{q}_{\text{eff}}(Q^2)$ is the coefficient of the three-body interaction term Γ_3, obtained by plugging $C^{HO}(b_\perp)$ in Eq. (3.26).

Leading Order

Using $C^{HO}(b_\perp)$ the rate equations can be solved analytically [27, 109, 110], historically the result was computed in terms of the spectrum

$$\frac{dI^{HO}}{dz}(P,z,t) = \frac{g^2}{4\pi^2}\ln|\cos\Omega t|\,, \tag{6.66}$$

where we define the frequency

$$\Omega = \frac{1-i}{2}\sqrt{\frac{\hat{q}_{\text{eff}}(Q^2)}{Pz(1-z)}}\,. \tag{6.67}$$

After applying a time derivative [121], we obtain the rate

$$\frac{d\Gamma^{HO}}{dz}(P,z,t) = -\frac{g^2}{4\pi^2}\text{Re}\;\Omega\tan\Omega t\,. \tag{6.68}$$

Next to Leading order

While the leading order HO term can be seen as a resummation of multiple soft scatterings with the medium, the next-to-leading order correction introduces the effect of one 'hard' scattering with the medium in an opacity expansion approach. One obtain the correction by making use of the separation in Eq. (6.63), which translates to a separation of the propagators

$$G(t,\boldsymbol{b}_\perp;t_1,\boldsymbol{p}) = G^{HO}(t,\boldsymbol{b}_\perp;t_1,\boldsymbol{y}) + G^{(1)}(t,\boldsymbol{b}_\perp;t_1,\boldsymbol{y})\,. \tag{6.69}$$

By inserting the full propagator into Eq. (3.24), and using the fact that the propagator $G^{HO}(t,\boldsymbol{q};t_1,\boldsymbol{p})$ is solution to the equation

$$\left[i\partial_t + \frac{\partial^2_{\boldsymbol{b}_\perp}}{2Pz(1-z)} + M_{\text{eff}} + i\Gamma_3^{HO}(\boldsymbol{b}_\perp)\right]G^{HO}(\boldsymbol{b}_\perp,t;\boldsymbol{y},t_1) = i\delta(t-t_1)\delta^{(2)}(\boldsymbol{b}_\perp-\boldsymbol{y})\,. \tag{6.70}$$

One finds the evolution equation of the next-to-leading order propagator $G^{(1)}(t, \boldsymbol{b}_\perp; t_1, \boldsymbol{y})$

$$\begin{aligned}&\left[i\partial_t + \frac{\partial^2_{\boldsymbol{b}_\perp}}{2Pz(1-z)} + M_{\text{eff}} + i\Gamma_3^{HO}(\boldsymbol{b}_\perp)\right] G(\boldsymbol{b}_\perp, t; \boldsymbol{y}, t_1)\\ &= -i\Gamma_3^{\text{pert}}(\boldsymbol{b}_\perp) G^{HO}(\boldsymbol{b}_\perp, t; \boldsymbol{y}, t_1)\ ,\end{aligned} \tag{6.71}$$

where we neglect the terms with $\Gamma_3^{\text{pert}}(\boldsymbol{b}_\perp)G(\boldsymbol{b}_\perp, t; \boldsymbol{y}, t_1)$. Strikingly, the evolution equation can be solved analytically to obtain the spectrum [117–119]

$$\begin{aligned}&\frac{dI^{(1)}}{dz}(P, z, t)\\ =&\frac{g^2}{4\pi^2}\text{Re}\int_0^t ds \int_0^\infty \frac{2du}{u}\left[C_1 C^{\text{pert}}(u) + C_z C^{\text{pert}}(zu) + C_{1-z}C^{\text{pert}}((1-z)u)\right] e^{k^2(s)u^2}\ ,\end{aligned} \tag{6.72}$$

$$=\frac{g^2}{4\pi^2}\text{Re}\int_0^t ds \int \frac{2du}{u} C^{\text{pert}}(u)\left[C_1 e^{k^2(s)u^2} + C_z e^{\frac{k^2(s)}{z^2}u^2} + C_{1-z}e^{\frac{k^2(s)}{(1-z)^2}u^2}\right]\ , \tag{6.73}$$

where we define

$$k^2(s) = \frac{iPz(1-z)\Omega}{2}\left[\cot\Omega s - \tan\Omega(t-s)\right]\ . \tag{6.74}$$

We integrate the spectrum and perform a numerical derivative to obtain the rate shown in Fig. 6.9.

6.3.6 Results

We obtain numerically the full in-medium radiation rate as described in App. D using different broadening kernels. We present our results for the medium-induced radiation of a gluon by a parent quark of energy $P = 300T$ in an equilibrium medium with temperature $T = 500$MeV and present the comparison in two figures (6.7-6.8). Firstly, we present the full rates as a function of the evolution time t with three gluon momentum fractions $z = 0.05, 0.25, 0.5$ in Fig. 6.7, as well as at a fixed time for a range of momentum fractions in Fig. 6.8. The lower panel of each graphic displays the ratio to the LO results. We present results for both temperature $T = 250, 500$MeV, while for the perturbative kernels, we use the same parameters as the $T = 500$MeV data point given in Tab. 6.1. Similarly to the previous section, there is only a small difference between the two temperatures, the rate for 250MeV is

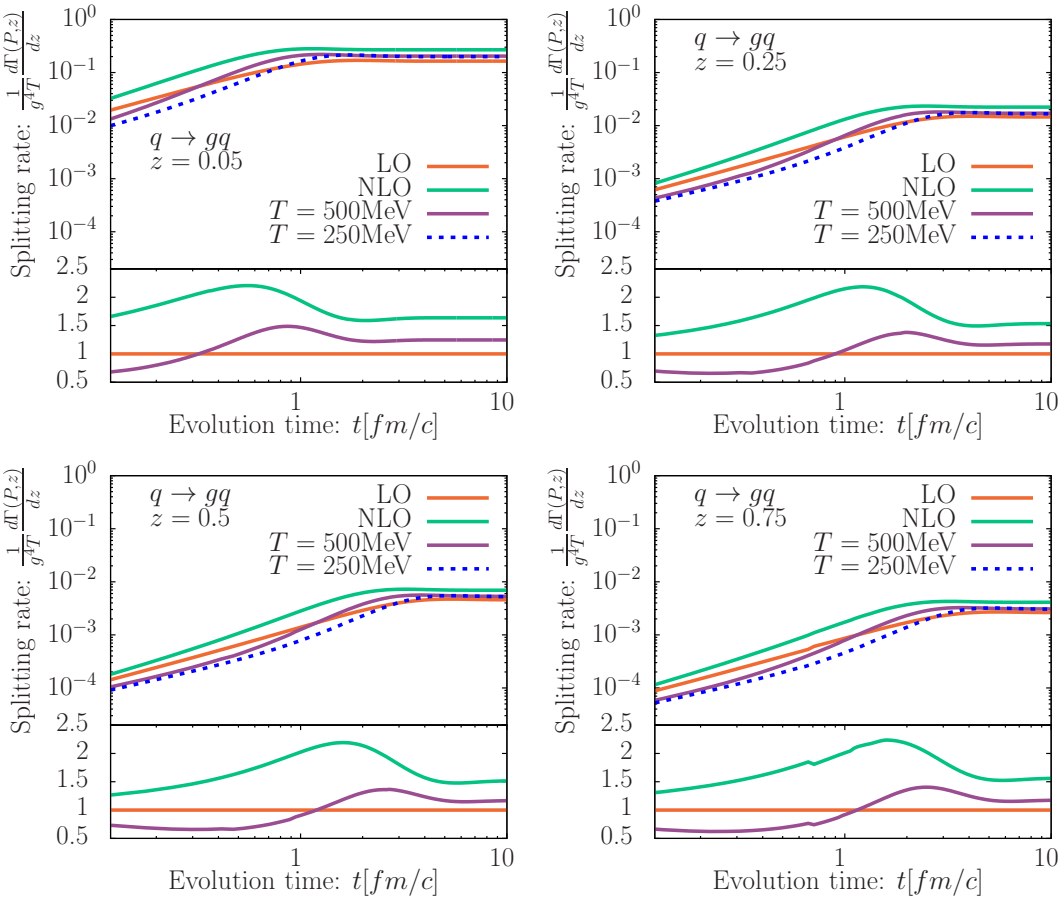

Figure 6.7: Medium-induced radiation of a gluon from a parent quark with energy $P = 300T$ in an equilibrium medium with temperature $T = 250, 500$MeV as a function of the evolution time t, each panel represent a different gluon momentum fraction $z = 0.05, 0.25, 0.5$. We compare calculation done using the different collisional broadening kernel as shown in Fig. 6.6 (the temperature and coupling constant for the perturbative results are matched to the $T = 500$MeV data in Tab. 6.1). The lower panel of each plot displays the ratio to the LO results.

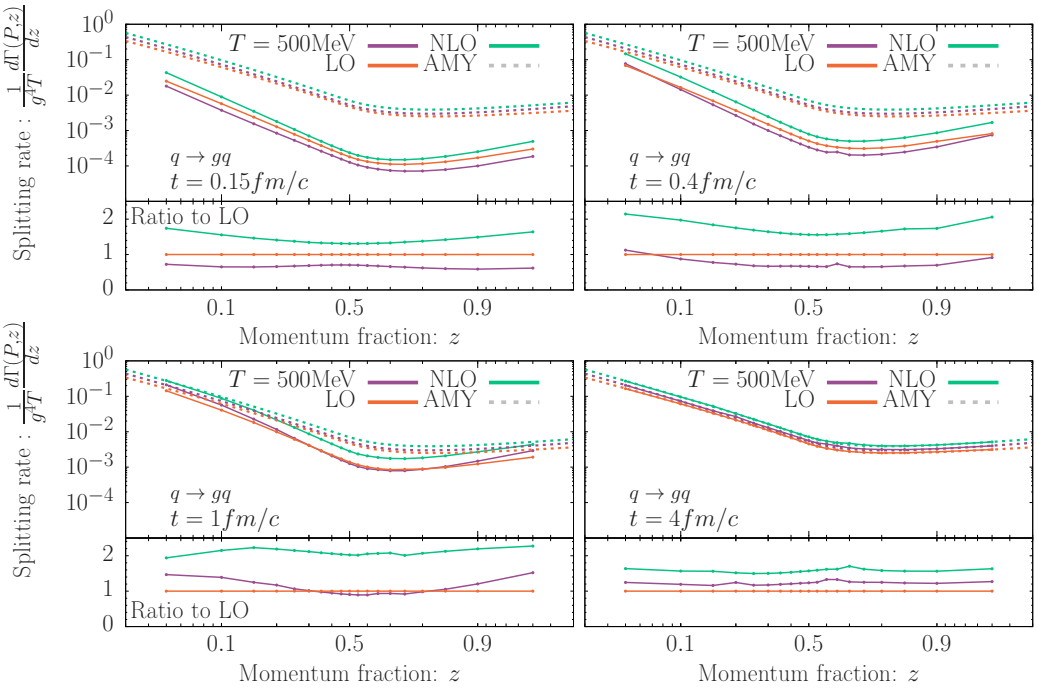

Figure 6.8: The splitting rate of a parent quark with energy $P = 300T$ in an equilibrium medium with temperature $T = 500$MeV as a function of momentum fraction of the radiated gluon z at fixed times $t = 0.15, 0.4, 1, 4fm/c$. The lower panel of each plot shows the ratio to the finite medium splitting rate computed using the LO broadening kernel.

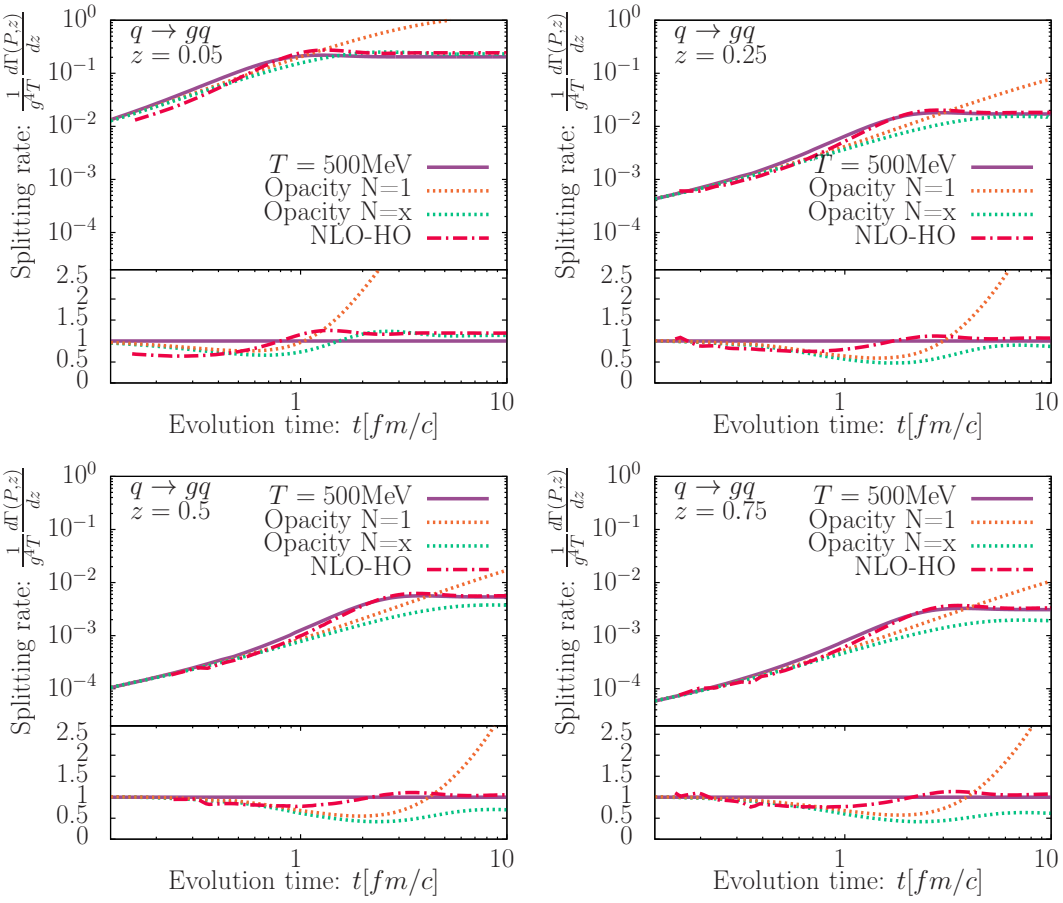

Figure 6.9: Medium-induced radiation of a gluon from a parent quark with energy $P = 300T$ in an equilibrium medium with temperature $T = 500$MeV as a function of the evolution time t, each panel represent a different gluon momentum fraction $z = 0.05, 0.25, 0.5$. We compare calculation done using the different approximation of the in-medium splitting rate: Opacity expansion at $N = 1$ Eq.(6.47), the resummed opacity rate of Eq. (6.59) and the NLO expansion around the Harmonic Oscillator Eq. (6.63) to the full result. The lower panel of each plot displays the ratio to the full rate.

only slightly shifted to the right in the time axis due to the temperature difference. Firstly, we note that all the different rates recover their respective AMY results at late times, which for the non-perturbative kernel is a nice confirmation for our Fourier transformation to momentum space. Comparing to the perturbative results, we observe that the non-perturbative result starts lower than the LO rates before it settles above the LO and below the NLO. Notably, the non-perturbative kernel does not depart from a band of $\pm 50\%$ around LO, while the NLO result becomes over $2\times$ larger than the LO.

In figure 6.9 we compare the different approximations to the in-medium splitting rates, here we only use the non-perturbative broadening kernel at $T = 500\text{MeV}$, and show again the same three gluon momentum fractions $z = 0.05, 0.25, 0.5$; the lower panel represent the ratio to the full medium splitting rate. We see that the opacity expansion works well at early times when the parton does not have time to re-scatter with the medium, but soon after it over-estimates the rate at late times. On the other hand, the NLO expansion around the NLO-HO can work fairly well at all times if one considers hard splittings ($z \sim 1/2$), while the resummed opacity expansion works better for soft splittings ($z \ll 0.5$). We conclude that for a sophisticated numerical simulation, one can reconstruct the full rate to obtain precise results; while for (semi-)analytical calculations where one is interested in different regimes to approximate parton splittings, a combination of the resummed opacity and NLO-HO rates is sufficient.

6.4 Discussion

Using recent results of the broadening kernel calculated using EQCD on a lattice, we obtained the QCD broadening kernel by matching the right short-distance behavior. Providing the right limiting behaviors we constructed a continuous spline for the full range of impact parameter space which allowed us to compute medium-induced radiation rates in the infinite medium size limit. Comparing our results to ones computed using perturbative results which are used in the literature, we see a substantial difference with the non-perturbative rates. Beyond the infinite medium calculation, we were able to successfully Fourier transform our resulting kernel to momentum space in order to compute the rate in a physical medium with finite size. We find that the Leading order perturbative rates do not depart from a band of $\pm 50\%$ from the non-perturbative rates. We also compared against different approximation in the literature. The NLO Harmonic Oscillator approximation manages better for hard splitting ($z \sim \frac{1}{2}$), while the resummed opacity expansion works for

soft splittings ($z \ll \frac{1}{2}$). Although the full radiation rate is more accurate at all scales, computing it at a large range of scales could become taxing numerically, we conclude that it would be sufficient to employ a combination of these approximations for the limiting cases to obtain reasonable (semi-)analytical estimates.

In the literature, jet quenching is commonly studied using weak coupling techniques, while due to the IR problem we believe that perturbative calculations will break down in thermal field theories. The genuine non-perturbative results we presented will be of utmost importance to test how well the weak coupling techniques hold and pin down the physics of jet quenching. Naturally, the obtained rates can then be incorporated into a jet study either using a kinetic approach as in the previous chapters [3, 30, 33] or with a MonteCarlo simulations [151–154]. Moreover, one can also utilize the same broadening kernel to include non-perturbative contributions to the elastic scatterings. What is more, a recent study using the same EQCD setting obtained non-perturbative contributions to the thermal masses [55], and it would be interesting to investigate their impact on the rate calculation specifically and jet quenching in general.

7 Conclusion

In this chapter, we provide an overall summary of the main results and an outlook on the direction of future investigations.

In recent years, heavy-ion collisions have proven to be a crucial laboratory to study QCD matter. The formation of the QGP during the collision provides an unparalleled opportunity to study the microscopic and macroscopic aspects of QCD matter in collider experiments. Hard partons that are produced at the early stages of the collision, follow an in-medium evolution, leading to modifications of their properties as well as of the medium. Certainly, by studying the modification of hard partons, they can be used as tomographic probes to extract information about the evolution of the plasma and its properties.

The main concern of this study was the evolution and equilibration of highly energetic partons in a static thermal QGP, we were able to investigate the dynamics using a linearized effective theory of QCD at leading order following the AMY approach [31]. Contrary to usual studies in the literature, we were careful in our formulation to keep both Bose enhancement and Fermi suppression in order to follow the energy from high momentum scales all the way to the medium sector, and understand the back-reaction of the hard particles onto the medium. The two main interactions that have to be considered at leading order are the number conserving elastic ($2 \leftrightarrow 2$) scatterings and multiple soft scatterings with the medium induce collinear radiation, which was resummed in an effective ($1 \leftrightarrow 2$) scattering rate.

First, in chapter 4, we focused on the longitudinal energy loss where we used the small angle approximation for the elastic interactions and extracted important dynamics of the evolution. Most notably, we confirm earlier findings that the energy loss is governed by an inverse energy cascade from high energies towards the medium scale [29, 30] akin to weak wave turbulence [124]. Driven by successive splittings, this energy cascade is associated with a scale invariant energy flux, transporting energy from the hard sector all the way to the medium scale without any deposition in intermediate scales. Due to the turbulent nature of the cascade, the inertial range is insensitive to the hard and soft scales and displays a universal Kolmogorov-Zakharov spectrum that was discussed. Although the mechanisms underlying hard particle energy loss are equivalent to the ones that thermalizes the QGP [34, 37, 72], we find

that the late time energy loss is negligible when considering the evolution of a highly energetic parton $E \gtrsim 30T$, which probe far from equilibrium dynamics. While low energetic partons $E \lesssim 30T$ are more sensitive to the QGP medium scale, and may be used to understand QGP thermalization using jet quenching studies in present and future experiments. Measurements of the correlation between jets and their recoil partner can be used to extract information about such strongly quenched jets. For example, by measuring a recoil high-p_T hadron, a recent experimental study [155] has developed a method to subtract the background and reconstruct the highly quenched jet on the away side of the hadron. These studies are of the utmost importance to explain the physics of the sPHENIX collaboration [156], which focuses on jet studies at RHIC where, unlike the LHC, the hard scattering p_T spectrum does not reach very high energies and are more sensitive to medium modifications of the parton shower. Moreover, the interactions of jets with the medium constituents lead to interesting changes of the chemical composition of medium modified jets (see also [30]), which should have experimentally observable consequences, e.g., in ratios of identified particles (K/π, Λ/π, D_0/π, Λ_c/π, ...) inside/around heavy-ion jets. Of course, to provide detailed predictions for any such observables, one also has to include the effects of vacuum like emissions and hadronization, and it will be interesting to further explore these aspects within suitable Monte-Carlo implementations of jet evolution in heavy-ion collisions [151–154], which can also account for vacuum like emissions and potentially important effects due to fluctuations of the jet shower and the medium.

Second, in chapter 5, we upgraded our formalism to account for the angular structure of the polar angle around the initial parton. We used the same formalism as the previous chapter for the inelastic interactions, however, for the elastic interactions, we used the full matrix element computed in the HTL approximation to describe energy depletion at small and large angles. At early times the jet peak, which sits at high energy and small angle ($\boldsymbol{p} \sim E\vec{e}_z$) slowly broadens due to multiple soft scatterings with the medium, while collinear radiation leads to much faster energy depletion. Additionally, rare hard scatterings with the medium lead to a power law tail in the angular distribution at large momentum fraction, which drops as θ^{-4} [132]. Consequently, most of the energy is lost due to an inverse energy cascade, which deposits energy at narrow angles and soft momentum scales. This energy is quickly equilibrated and transported to large angles, while the away side is negative as the equilibrium distribution is slightly boosted in the parton direction to account for momentum conservation. We concluded that while at high energies the distribution is mostly collinear, the energy at large angles ($\theta > 0.2$) is mainly sensitive to the soft scales. Eventually, all the initial equilibrates and the resulting equilibrium

distribution is then boosted in the parton's direction due to momentum conservation. Using our evolution results, we computed an analogue to hadron quenching and jet quenching. While for hadrons, we found that the quenching is more sensitive to the longitudinal energy cascade, which is mainly due to the multiple successive splittings and can be used to study these medium-induced splittings. However, energy loss out of the jet cone is more sensitive to soft physics, making it difficult to extract; nonetheless, it will be important to explore this angular structure using jet observables, e.g., jet shapes, which measure the momentum distribution transverse to the jet axis. For that sake, it will be crucial to study the evolution in a more dynamical background medium by including expansion [33], or using a viscous Hydrodynamic evolution [95], in order to understand how the energy deposited in the medium modifies these soft scales, and by going to large cone sizes the fragmentation functions can recover the energy of highly quenched jets experimentally [155].

Since the in-medium energy loss is dominated by radiative processes driving the energy cascade, it is only natural to strive to improve the calculation of in-medium splitting rates. Using a novel broadening kernel, which incorporate non-perturbative contributions computed using a dimensionally reduced theory of QCD on a lattice [1, 2], in chapter 6 we computed medium-induced radiation in both infinite and finite size medium lengths. We have found a sizable difference with the results using perturbative rates that are usually employed in the literature, which hints at interesting physics to investigate. Lattice EQCD methods have proven to be crucial tools for studying high temperature QCD [49, 50, 54, 144]; new computations are on going to extract non-perturbative contributions to the thermal masses [55]. It will be important to incorporate these studies as well, to investigate their effect.

Although our study was able to extract the important dynamics of energy loss and equilibration with the medium, there are several aspects that can be improved. Firstly, since we established a framework that can easily employ the small/large angle separation of the elastic scatterings, which is very handy when one needs to extend the formalism to Next-to-Leading order (NLO) introduced in [100, 157]. Alternatively, one can instead directly employ the non-perturbative elastic collisional broadening kernel for the elastic interactions with the medium as well as for computing medium-induced radiation rates. It would be important to investigate these two approaches together with the LO method we employed here, in order to compare to what extent the physics at LO is relevant for more realistic models.

Another aspect we can further improve is the treatment of radiative interactions. Since we mainly focused on the energy loss of partons on large timescales, where they lose a significant amount of their energy, we were able to approximate the radiative emission rates by considering an infinite medium length. However, one

must explicitly include the path length dependence of the medium-induced radiation rates to study parton energy loss on shorter timescales. Besides, because the evolution is linear, we argued that our results can be interpreted as a Green's function propagating a single medium-resolved highly energetic parton. Building on this, it would be important to include vacuum-like emissions as source terms to account for additional fragmentation that will be relevant to explore in-medium evolution of jet shapes. Using this effective kinetic theory framework, both soft and hard fragment evolution can be studied [30, 33, 34, 37, 72]. That being so, the long term goals of these studies would be to construct a unified description of the full energy loss picture and the back-reaction of the QGP.

A Derivation of the small-angle approximation

In this appendix, we shall explain how one finds the diffusion approximation to the elastic $2 \leftrightarrow 2$ QCD scatterings. We start from the following collision integral [100]

$$C_a[f] = \frac{1}{2|p_1|\nu_a} \sum_{bcd} \int d\Omega^{2\leftrightarrow 2} \left|\mathcal{M}^{ab}_{cd}(\boldsymbol{p}_1, \boldsymbol{p}_2; \boldsymbol{p}_3, \boldsymbol{p}_4)\right|^2 \mathcal{F}(\boldsymbol{p}_1, \boldsymbol{p}_2; \boldsymbol{p}_3, \boldsymbol{p}_4) \,, \tag{A.1}$$

where $\mathcal{M}^{ab}_{cd}(p_1, p_2; p_3, p_4)$ is the QCD matrix element and $\mathcal{F}(p_1, p_2; p_3, p_4)$ is the statistical factor given by

$$\begin{aligned} \mathcal{F}(\boldsymbol{p}_1, \boldsymbol{p}_2, \boldsymbol{p}_3, \boldsymbol{p}_4) =& f_c(\boldsymbol{p}_3)\, f_d(\boldsymbol{p}_4)\, (1 \pm f_a(\boldsymbol{p}_1))\, (1 \pm f_b(\boldsymbol{p}_2)) \\ & - f_a(\boldsymbol{p}_1)\, f_b(\boldsymbol{p}_2)\, (1 \pm f_c(\boldsymbol{p}_3))\, (1 \pm f_d(\boldsymbol{p}_4)) \,. \end{aligned} \tag{A.2}$$

A.1 Phase-space parametrization

Using the phase-space measure for $2 \leftrightarrow 2$ scatterings we obtained in Eq. (3.13) which we recall

$$\begin{aligned} \int d\Omega^{2\leftrightarrow 2} = (2\pi) \int \frac{d^3 p_2}{(2\pi)^3} \int \frac{d^3 q}{(2\pi)^3} \int d\omega \; \frac{1}{8 p_1 p_2^2 q^2} \Theta(q - |\omega|) \Theta\left(p_1 - \frac{q+\omega}{2}\right) \\ \Theta\left(p_2 - \frac{q-\omega}{2}\right) \delta\left(cos\theta_{1q} - \left(\frac{\omega}{q} - \frac{\omega^2 - q^2}{2 p_1 q}\right)\right) \delta\left(cos\theta_{2q} - \left(\frac{\omega}{q} + \frac{\omega^2 - q^2}{2 p_2 q}\right)\right) \,. \end{aligned} \tag{A.3}$$

Within this parametrization, the Mandelstam variables are given by

$$t = \omega^2 - q^2 \,, \quad s = -2 p_1 p_2 (1 - \cos\theta_{12}) \,, \quad u = -t - s \,, \tag{A.4}$$

where θ_{12} is the angle between $\boldsymbol{p}_1$ and $\boldsymbol{p}_2$. Note that here a t-channel parametrization has been used, while the u-channel can be obtained by exchanging $\boldsymbol{p}_3 \leftrightarrow \boldsymbol{p}_4$

momentum and s-channel diagrams are neglected because of the divergent nature of the t- and u-channels for small momentum exchange.

To perform the three-dimensional q integration, we write the different components in the following orthonormal basis,

$$\begin{pmatrix}\vec{e}_+\\ \vec{e}_-\\ \vec{e}_3\end{pmatrix} = \begin{pmatrix}\frac{\vec{e}_1+\vec{e}_2}{\sqrt{2+2\cos\theta_{12}}}\\ \frac{\vec{e}_1-\vec{e}_2}{\sqrt{2-2\cos\theta_{12}}}\\ \frac{\vec{e}_1\times\vec{e}_2}{|\vec{e}_1\times\vec{e}_2|}\end{pmatrix}, \quad \boldsymbol{q} \equiv \begin{pmatrix}q_+\\ q_-\\ q_\perp\end{pmatrix} = \begin{pmatrix}\frac{q(\cos\theta_{1q}+\cos\theta_{2q})}{\sqrt{2+2\cos\theta_{12}}}\\ \frac{q(\cos\theta_{1q}-\cos\theta_{2q})}{\sqrt{2-2\cos\theta_{12}}}\\ \pm\sqrt{q^2-q_1^2-q_2^2}\end{pmatrix}, \tag{A.5}$$

where θ_{1q}/θ_{2q} are the angles between $\boldsymbol{p}_1/\boldsymbol{p}_2$ and $\boldsymbol{q}$. We perform a change of integration variables from $(q_+, q_-, q_\perp)$ to $(\cos\theta_{1q}, \cos\theta_{2q}, q)$, and combine the range of $q_\perp$ integration as follows

$$\int_{-q_{\max}}^{q_{\max}} dq_\perp\ f(q_\perp) = \int_0^{q_{\max}} dq_\perp\ f(|q_\perp|) + f(-|q_\perp|)\ , \tag{A.6}$$

We then use the two delta functions to perform two integrations, obtaining

$$\int d\Omega^{2\leftrightarrow 2} = \\ 2(2\pi)\int\frac{d^3p_2}{(2\pi)^3}\int\frac{dq}{(2\pi)^3}\int d\omega\ \frac{1}{8p_1p_2^2q^2}\frac{q^3}{|q_\perp|\sqrt{1-\cos^2\theta_{12}}}\Theta\left(1-\left|\frac{q_+}{q}\right|\right)\Theta\left(1-\left|\frac{q_-}{q}\right|\right)\ , \tag{A.7}$$

for $q, w \ll p_1, p_2$ we can neglect earlier Θ functions restraining $\boldsymbol{p}_1$ and $\boldsymbol{p}_2$ integrations. We also symmetrize the integrand giving rise to a factor 2 and canceling all odd integrand of $q_\perp$.

The components of the vector $\boldsymbol{q}$ in the new parametrization are written as follows

$$q_+ = \frac{2\omega - \frac{\omega^2-q^2}{2}\left(\frac{1}{p_1}-\frac{1}{p_2}\right)}{\sqrt{2+2\cos\theta_{12}}}\ , \quad q_- = -\frac{\frac{\omega^2-q^2}{2}\left(\frac{1}{p_1}+\frac{1}{p_2}\right)}{\sqrt{2-2\cos\theta_{12}}}\ . \tag{A.8}$$

Since the QCD matrix element favors small angle exchange, we expand the different contributions to the integrand in powers of q and ω in the following sections, and we use the leading order of q to perform the integral.

A.2 Expansion of statistical terms

Before expanding the statistical term, we note that the t-channel diagrams can be written either with interaction due to a gluon exchange giving rise to the current

term in the Fokker-Planck equation these require a and c to be the same species and likewise for b and d, which cancels the 0-th order in q of the statistical term. The matrix elements for these diagrams are proportional to $\frac{s^2}{t^2} \propto q^{-4}$ necessitating expansion of the statistical term up to second order

$$\begin{aligned}\mathcal{F}^{\text{Current}}(\boldsymbol{p}_1, \boldsymbol{p}_2, \boldsymbol{q}) = q_i \left\{ -f_a(p_2)(1 \pm f_b(\boldsymbol{p}_2))\partial^i_{p_1} f_a(p_1) + f_a(\boldsymbol{p}_1)(1 \pm f_a(\boldsymbol{p}_1))\partial^i_{p_2} f_b(\boldsymbol{p}_2) \right\} \\ + \frac{q_i q_j}{2} \Big\{ f_b(\boldsymbol{p}_2)(1 \pm f_b(\boldsymbol{p}_2))\partial^i_{p_1}\partial^j_{p_1} f_a(\boldsymbol{p}_1) + f_a(\boldsymbol{p}_1)(1 \pm f_a(\boldsymbol{p}_1))\partial^i_{p_2}\partial^j_{p_2} f_b(\boldsymbol{p}_2) \\ - \partial^j_{p_2} f_b(\boldsymbol{p}_2)\partial^i_{p_1} f_a(\boldsymbol{p}_1)(1 \pm f_a(\boldsymbol{p}_1)) - \partial^j_{p_1} f_a(\boldsymbol{p}_1)\partial^i_{p_2} f_b(\boldsymbol{p}_2)(1 \pm f_b(\boldsymbol{p}_2)) \Big\} . \end{aligned} \tag{A.9}$$

Whereas the diagrams where a quark exchange takes place, give rise to the conversion processes and require a and d to be the same species instead, likewise for b and c. The matrix elements for these diagrams are proportional to $\frac{s}{t} \propto q^{-2}$, which only require to take the 0-th order expansion of the statistical term

$$\begin{aligned}\mathcal{F}^{\text{Conversion}}(\boldsymbol{p}_1, \boldsymbol{p}_2, \boldsymbol{q}) =& f_b(p_1)\, f_a(p_2)\, (1 \pm f_a(p_1))\, (1 \pm f_b(p_2)) \\ & - f_a(p_1)\, f_b(p_2)\, (1 \pm f_b(p_1))\, (1 \pm f_a(p_2)) . \end{aligned} \tag{A.10}$$

A.3 Evaluation of small angle matrix elements

By combining the statistical terms with the matrix element one finds for the current contributions

$$\begin{aligned} C_a^{\text{Current}} &= 2(2\pi) \int \frac{d^3 p_2}{(2\pi)^3} \\ & B_i \left\{ -f_b(\boldsymbol{p}_2)(1 \pm f_b(\boldsymbol{p}_2))\partial^i_{p_1} f_a(\boldsymbol{p}_1) + f_a(\boldsymbol{p}_1)(1 \pm f_a(\boldsymbol{p}_1))\partial^i_{\boldsymbol{p}_2} f_b(\boldsymbol{p}_2) \right\} \\ & + \frac{B_{ij}}{2} \Big\{ f_b(\boldsymbol{p}_2)(1 \pm f_b(\boldsymbol{p}_2))\partial^i_{\boldsymbol{p}_1}\partial^j_{p_1} f_a(\boldsymbol{p}_1) + f_a(\boldsymbol{p}_1)(1 \pm f_a(\boldsymbol{p}_1))\partial^i_{\boldsymbol{p}_2}\partial^j_{\boldsymbol{p}_2} f_b(\boldsymbol{p}_2) \\ & \qquad - \partial^j_{p_2} f_b(\boldsymbol{p}_2)\partial^i_{p_1} f_a(\boldsymbol{p}_1)(1 \pm f_a(\boldsymbol{p}_1)) - \partial^j_{p_1} f_a(\boldsymbol{p}_1)\partial^i_{p_2} f_b(\boldsymbol{p}_2)(1 \pm f_b(\boldsymbol{p}_2)) \Big\} \Big\} , \end{aligned} \tag{A.11}$$

and the conversion contributions can be expressed as

$$\begin{aligned} C_a^{\text{Conversion}} =& 2(2\pi) \int \frac{d^3 p_2}{(2\pi)^3}\; B \left\{ f_b(\boldsymbol{p}_1)\, f_a(\boldsymbol{p}_2)\, (1 \pm f_a(\boldsymbol{p}_1))\, (1 \pm f_b(\boldsymbol{p}_2)) \right. \\ & \left. - f_a(\boldsymbol{p}_1)\, f_b(\boldsymbol{p}_2)\, (1 \pm f_b(\boldsymbol{p}_1))\, (1 \pm f_a(\boldsymbol{p}_2)) \right\} . \end{aligned} \tag{A.12}$$

The above equations give rise to the three following integrals

$$B \equiv \int \frac{dq}{2\pi^2} \int_{-q_+}^{q_+} d\omega \; \frac{1}{8p_1 p_2^2 q^2} \frac{q^3}{|q_\perp|\sqrt{1-\cos^2\theta_{12}}} \frac{s}{t} \; , \tag{A.13}$$

$$B^i \equiv \int \frac{dq}{2\pi^2} \int_{-q_+}^{q_+} d\omega \; \frac{1}{8p_1 p_2^2 q^2} \frac{q^3}{|q_\perp|\sqrt{1-\cos^2\theta_{12}}} q^i \frac{s^2}{t^2} \; , \tag{A.14}$$

$$B^{ij} \equiv \int \frac{dq}{2\pi^2} \int_{-q_+}^{q_+} d\omega \; \frac{1}{8p_1 p_2^2 q^2} \frac{q^3}{|q_\perp|\sqrt{1-\cos^2\theta_{12}}} \frac{q^i q^j}{2} \frac{s^2}{t^2} \; . \tag{A.15}$$

$$\tag{A.16}$$

Taking the integration, we find at lowest order of q

$$B = \int \frac{dq}{q} \; \frac{1}{8\pi p_2} \; , \quad B^i = \int \frac{dq}{q} \; \frac{p_1}{8\pi} \left(\frac{\vec{e}_1}{p_2} - \frac{\vec{e}_2}{p_1} \right) \; , \tag{A.17}$$

$$B^{ij} = \int \frac{dq}{q} \; \frac{p_1}{16\pi} \left(\delta^{ij}(1-\cos\theta_{12}) + \frac{\boldsymbol{p}_1^i}{p_1}\frac{\boldsymbol{p}_2^j}{p_2} + \frac{\boldsymbol{p}_1^j}{p_1}\frac{\boldsymbol{p}_2^i}{p_2} \right) \; . \tag{A.18}$$

A.4 Collision integrals in small angle approximation

After combining the integrals with the statistical term, we obtain the different collision integrals. We define the current term in the gluon channel as

$$C_g^{\text{Current}}[f] = C_g^{gg \overset{g}{\longleftrightarrow} gg}[f] + \sum_f \left(C_g^{gq_f \overset{g}{\longleftrightarrow} gq_f}[f] + C_g^{g\bar{q}_f \overset{g}{\longleftrightarrow} g\bar{q}_f}[f] \right) \; , \tag{A.19}$$

where we only take the gluon exchange contribution of the (anti-)quark/gluon scatterings denoted by $\overset{g}{\longleftrightarrow}$. The different collision integrals are written,

$$C_g^{gg\overset{g}{\longleftrightarrow}gg}[f] = \frac{g^4 C_A \mathcal{L}}{4\pi}\,\partial^i_{\boldsymbol{p}_1}\int\frac{d^3p_2}{(2\pi)^3}C_A f_g(\boldsymbol{p}_2)(1+f_g(\boldsymbol{p}_2))\partial^i_{\boldsymbol{p}_1}f_g(\boldsymbol{p}_1) + C_A\frac{2f_g(\boldsymbol{p}_2)}{p_2}\frac{\boldsymbol{p}_1^i}{p_1}f_g(\boldsymbol{p}_1)(1+f_g(\boldsymbol{p}_1))\,, \tag{A.20}$$

$$C_g^{gq_f\overset{g}{\longleftrightarrow}gq_f}[f] = \frac{g^4 C_A \mathcal{L}}{4\pi}\,\partial^i_{\boldsymbol{p}_1}\int\frac{d^3p_2}{(2\pi)^3}f_{q_f}(\boldsymbol{p}_2)(1-f_{q_f}(\boldsymbol{p}_2))\partial^i_{\boldsymbol{p}_1}f_g(\boldsymbol{p}_1) + \frac{2f_{q_f}(\boldsymbol{p}_2)}{p_2}\frac{\boldsymbol{p}_1^i}{p_1}f_g(\boldsymbol{p}_1)(1+f_g(\boldsymbol{p}_1))\,, \tag{A.21}$$

$$C_g^{g\bar{q}_f\overset{g}{\longleftrightarrow}g\bar{q}_f}[f] = \frac{g^4 C_A \mathcal{L}}{4\pi}\,\partial^i_{\boldsymbol{p}_1}\int\frac{d^3p_2}{(2\pi)^3}f_{\bar{q}_f}(\boldsymbol{p}_2)(1-f_{\bar{q}_f}(\boldsymbol{p}_2))\partial^i_{\boldsymbol{p}_1}f_g(\boldsymbol{p}_1) + \frac{2f_{\bar{q}_f}(\boldsymbol{p}_2)}{p_2}\frac{\boldsymbol{p}_1^i}{p_1}f_g(\boldsymbol{p}_1)(1+f_g(\boldsymbol{p}_1))\,, \tag{A.22}$$

where we define the logarithmic enhancement $\mathcal{L} = \int_{m_D}^{\mu}\frac{dq}{q}$.

Conversely, the quark exchange contribution to the scattering lead to the conversion terms

$$C_g^{\text{Conversion}}[f] = \sum_f\left(C_g^{gq_f\overset{q}{\longleftrightarrow}gq_f}[f] + C_g^{g\bar{q}_f\overset{q}{\longleftrightarrow}g\bar{q}_f}[f] + C_g^{gg\overset{q}{\longleftrightarrow}q_f\bar{q}_f}[f]\right)\,, \tag{A.23}$$

$$= \frac{1}{8|\boldsymbol{p}|}\sum_f\Big[f_{q_f}(\boldsymbol{p}_1)(1+f_g(\boldsymbol{p}_1)) - f_g(\boldsymbol{p}_1)(1-f_{\bar{q}_f})\Big]\mathcal{I}_{q_f} + \Big[f_{\bar{q}_f}(\boldsymbol{p}_1)(1+f_g(\boldsymbol{p}_1)) - f_g(\boldsymbol{p}_1)(1-f_{q_f})\Big]\mathcal{I}_{\bar{q}_f}\,, \tag{A.24}$$

where $\mathcal{I}_{q_f}$ and $\mathcal{I}_{\bar{q}_f}$ are given by the following moments of the phase-space distribution

$$\mathcal{I}_{q_f} = \frac{g^4 C_F \mathcal{L}}{\pi}\int\frac{d^3k}{(2\pi)^3}\frac{1}{|\boldsymbol{k}|}\Big[f_{q_f}(\boldsymbol{k})(1+f_g(\boldsymbol{k})) + f_g(\boldsymbol{k})(1-f_{\bar{q}_f}(\boldsymbol{k}))\Big]\,, \tag{A.25}$$

$$\mathcal{I}_{\bar{q}_f} = \frac{g^4 C_F \mathcal{L}}{\pi}\int\frac{d^3k}{(2\pi)^3}\frac{1}{|\boldsymbol{k}|}\Big[f_{\bar{q}_f}(\boldsymbol{k})(1+f_g(\boldsymbol{k})) + f_g(\boldsymbol{k})(1-f_{q_f}(\boldsymbol{k}))\Big]\,. \tag{A.26}$$

Similarly, for the quark channel using only the gluon exchange part of the scatterings

we write the current term

$$C_{q_f}^{\text{Current}}[f] = C_{q_f}^{q_f g \overset{g}{\longleftrightarrow} q_f g}[f] + \sum_i \left(C_{q_f}^{q_f q_i \longleftrightarrow q_f q_i}[f] + C_{q_f}^{q_f \bar{q}_i \longleftrightarrow q_f \bar{q}_i}[f] \right) , \tag{A.27}$$

$$\begin{aligned} C_{q_f}^{q_f g \overset{g}{\longleftrightarrow} q_f g}[f] =& \frac{g^4 C_F \mathcal{L}}{4\pi} \partial_{\boldsymbol{p}_1}^i \int \frac{d^3 p_2}{(2\pi)^3} C_A f_g(\boldsymbol{p}_2)(1 + f_g(\boldsymbol{p}_2)) \partial_{\boldsymbol{p}_1}^i f_{q_f}(\boldsymbol{p}_1) \\ &+ C_A \frac{2 f_g(\boldsymbol{p}_2)}{p_2} \frac{\boldsymbol{p}_1^i}{p_1} f_{q_f}(\boldsymbol{p}_1)(1 + f_g(\boldsymbol{p}_1)) , \end{aligned} \tag{A.28}$$

$$\begin{aligned} C_{q_f}^{q_f q_i \longleftrightarrow q_f q_i}[f] =& \frac{g^4 C_F \mathcal{L}}{8\pi} \partial_{\boldsymbol{p}_1}^i \int \frac{d^3 p_2}{(2\pi)^3} f_{q_i}(\boldsymbol{p}_2)(1 - f_{q_i}(\boldsymbol{p}_2)) \partial_{\boldsymbol{p}_1}^i f_{q_f}(\boldsymbol{p}_1) \\ &+ \frac{2 f_{q_i}(\boldsymbol{p}_2)}{p_2} \frac{\boldsymbol{p}_1^i}{p_1} f_{q_f}(\boldsymbol{p}_1)(1 - f_{q_f}(\boldsymbol{p}_1)) , \end{aligned} \tag{A.29}$$

$$\begin{aligned} C_{q_f}^{q_f \bar{q}_i \longleftrightarrow q_f \bar{q}_i}[f] =& \frac{g^4 C_F \mathcal{L}}{8\pi} \partial_{\boldsymbol{p}_1}^i \int \frac{d^3 p_2}{(2\pi)^3} f_{\bar{q}_i}(\boldsymbol{p}_2)(1 - f_{\bar{q}_i}(\boldsymbol{p}_2)) \partial_{\boldsymbol{p}_1}^i f_{q_f}(\boldsymbol{p}_1) \\ &+ \frac{2 f_{\bar{q}_i}(\boldsymbol{p}_2)}{p_2} \frac{\boldsymbol{p}_1^i}{p_1} f_{q_f}(\boldsymbol{p}_1)(1 - f_{q_f}(\boldsymbol{p}_1)) , \end{aligned} \tag{A.30}$$

and using the quark exchange part of the scatterings we write the conversion term

$$C_{q_f}^{\text{Conversion}}[f] = C_{q_f}^{q_f g \overset{q}{\longleftrightarrow} q_f g}[f] + C_{q_f}^{q_f \bar{q}_f \overset{q}{\longleftrightarrow} g g}[f] , \tag{A.31}$$

$$= \frac{g^4 C_F^2 \mathcal{L}}{4\pi} \sum_f \int \frac{d^3 p_2}{(2\pi)^3} f_{q_f}(\boldsymbol{p}_1)(1 + f_g(\boldsymbol{p}_1)) \mathcal{I}_{q_f} - f_g(\boldsymbol{p}_1)(1 - f_{q_f}) \mathcal{I}_{\bar{q}_f} . \tag{A.32}$$

The same quark collision integrals apply to the antiquark channel after exchange of q_f with $\bar{q}_f$ and vice-versa. After summing the different contributions for each channel, one recovers the Fokker-Planck equation in section 4.1.

A.5 Angular dependent case

We will compare the medium cascade of the full matrix elements with one where we take only the diffusion approximation. Since we are considering an angle differential cascade, during this section, we will upgrade the evolution equation of the energy distribution from Chapter 3 to account for angle. Only the current term and its

recoil counter-part have to be modified. For the direct diffusion, we have

$$-\nabla_p \mathcal{J}_g[\{D_i\}] = \frac{C_\mathrm{A}\hat{\bar{q}}_\mathrm{eq}}{4T^2} x \left[\frac{T^2}{E^2} \left(\partial_x x^2 \partial_x + \partial_{\cos\theta}(1-\cos\theta^2)\partial_{\cos\theta} \right) + \frac{T}{E}\partial_x x^2 (1+2n_B(xE)) \right] \frac{D_g(x,\cos\theta)}{x^3} \,, \tag{A.33}$$

$$-\nabla_p \mathcal{J}_{q_f}[\{D_i\}] = \frac{C_\mathrm{F}\hat{\bar{q}}_\mathrm{eq}}{4T^2} x\partial_x \left[\frac{T^2}{E^2} \left(\partial_x x^2 \partial_x + \partial_{\cos\theta}(1-\cos\theta^2)\partial_{\cos\theta} \right) + \frac{T}{E}\partial_x x^2 (1-2n_F(xE)) \right] \frac{D_{q_f}(x,\cos\theta)}{x^3} \,, \tag{A.34}$$

$$-\nabla_p \mathcal{J}_{\bar{q}_f}[\{D_i\}] = \frac{C_\mathrm{F}\hat{\bar{q}}_\mathrm{eq}}{4T^2} x\partial_x \left[\frac{T^2}{E^2} \left(\partial_x x^2 \partial_x + \partial_{\cos\theta}(1-\cos\theta^2)\partial_{\cos\theta} \right) + \frac{T}{E}\partial_x x^2 (1-2n_F(xE)) \right] \frac{D_{\bar{q}_f}(x,\cos\theta)}{x^3} \,. \tag{A.35}$$

In addition to the recoil contribution that we had before in Eqns. (4.18-4.20), an angle dependent contribution is obtained

$$-\nabla_p \delta\mathcal{J}_g^{\parallel}[\{D_i\}] = \frac{C_\mathrm{A}\hat{\bar{q}}_\mathrm{eq}}{4T^2} \frac{T\delta\bar{\eta}_D^{\parallel}}{2\hat{\bar{q}}_\mathrm{eq}} \frac{\nu_g}{2\pi^2} \frac{T}{E} x^3 \cos\theta\, \partial_x n_B(xE)(1+n_B(xE)), \tag{A.36}$$

$$-\nabla_p \delta\mathcal{J}_{q_f/\bar{q}_f}^{\parallel}[\{D_i\}] = \frac{C_F\hat{\bar{q}}_\mathrm{eq}}{4T^2} \frac{T\delta\bar{\eta}_D^{\parallel}}{2\hat{\bar{q}}_\mathrm{eq}} \frac{\nu_q}{2\pi^2} \frac{T}{E} x^3 \cos\theta\, \partial_x n_F(xE)(1-n_F(xE)) \,, \tag{A.37}$$

where the recoil coefficient is given by

$$\delta\bar{\eta}_D^{\parallel} = \frac{g^4}{\pi} E^2 \int_{-1}^{1} d\cos\theta \int dx\, \frac{2\cos\theta}{x^2} \Big[C_\mathrm{A}\nu_g^{-1} D_g(x,\cos\theta) + \frac{1}{2}\sum_f \nu_q^{-1} (D_{q_f}(x,\cos\theta) + D_{\bar{q}_f}(x,\cos\theta)) \Big] \,. \tag{A.38}$$

A Derivation of the small-angle approximation

B Numerical implementation of the Boltzmann equation

Below, we provide details on the numerical implementation of the effective kinetic theory.

B.1 Basic formalism

Following the discrete-momentum method introduced in [158], we discretize the distribution using "wedge" functions basis

$$N_i^a(\tau) = \int dx\ w_i(x) \frac{D_a(x,\tau)}{x} \ , \tag{B.1}$$

where N_i^a is the wedge coefficient for the number of particle moment for the species $a = \{g, q_f, \bar{q}_f\}$ and $w_i(x)$ is the wedge function defined as

$$w_i(x) = \begin{cases} \frac{x - x_{i-1}}{x_i - x_{i-1}} \ , & x_{i-1} < x < x_i \\ \frac{x_{i+1} - x}{x_{i+1} - x_i} \ , & x_i \leq x < x_{i+1} \\ 0 \ , & x > x_{i+1} \text{ or } x < x_{i-1} \end{cases} \tag{B.2}$$

with $\{x_i\}$ the discrete node points spanning the region of interest ($\sim [0, 2]$). We note that the wedge functions display the following summation properties

$$\sum_i w_i(x) = \Theta(x_{\max} - x)\Theta(x - x_{\min}) \ , \tag{B.3}$$

$$\sum_i x_i w_i(x) = x\Theta(x_{\max} - x)\Theta(x - x_{\min}) \ . \tag{B.4}$$

By use of these properties, one finds simple relations for the number of particles and energy,

$$n_a(\tau) = \sum_i N_i^a(\tau) \ , \quad E_a(\tau) = \sum_i x_i N_i^a(\tau) \ , \tag{B.5}$$

allowing us to keep track of these quantities up to machine precision.

The collision integral is expanded in the same basis

$$C_i^a(\tau) = \int dx\ w_i(x) \frac{C_a(x,\tau)}{x} \ . \tag{B.6}$$

Because the collision integral $C_a(x,\tau)$ is linear in terms of the distribution of each species one can write $C_i^a(\tau)$ as a matrix vector product

$$C_i^a(\tau) = \sum_j \delta C_{ij}^{ab} N_j^b(\tau) = \delta \bar{C}^{ab} \vec{N}^b(\tau) \ , \tag{B.7}$$

by constructing the vector $\vec{N}$ and matrix $\bar{C}$ from the coefficients and matrices of the different species

$$\vec{N}(\tau) \equiv \begin{pmatrix} \vec{N}^g(\tau) \\ \vec{N}^{q_f}(\tau) \\ \vec{N}^{\bar{q}_f}(\tau) \end{pmatrix} \ , \quad \bar{C}(\tau) \equiv \frac{\delta C_i^a(\tau)}{\delta N_j^b(\tau)} = \begin{pmatrix} \bar{C}_{gg}(\tau) & \bar{C}_{gg_f}(\tau) & \bar{C}_{g\bar{q}_f}(\tau) \\ \bar{C}_{q_f g}(\tau) & \bar{C}_{q_f q_f}(\tau) & \bar{C}_{q_f \bar{q}_f}(\tau) \\ \bar{C}_{\bar{q}_f g}(\tau) & \bar{C}_{\bar{q}_f q_f}(\tau) & \bar{C}_{\bar{q}_f \bar{q}_f}(\tau) \end{pmatrix} \ . \tag{B.8}$$

The matrices $\bar{C}_{ab}(\tau)$ characterize the contribution of the distribution of species b to the collision integral of species a. Although $\bar{C}(\tau)$ will not depend on $N_i^b(\tau)$ because $C_a(\tau)$ is linear in $N_i^b(\tau)$, we will still keep track of $N_j^b(\tau)$ when we write the matrices in the following sections.

In order to recover the full distribution from the discrete values $N_i^a(\tau)$, we approximate the coefficient integral by taking $\frac{D_a(x,\tau)}{D_a^{\rm eq}(x)e^{xE/T}}$ to be constant between node points

$$N_i^a(\tau) = \int dx\ w_i(x) \frac{D_a(x,\tau)}{x\ D_a^{\rm eq}(x) e^{xE/T}} D_a^{\rm eq}(x) e^{xE/T} \ , \tag{B.9}$$

$$= \frac{D_a(x,\tau)}{D_a^{\rm eq}(x) e^{xE/T}} \mathcal{A}_i^a \ , \tag{B.10}$$

where $\mathcal{A}_i^a$ is the area defined as

$$\mathcal{A}_i^a \equiv \int \frac{dx}{x}\ w_i(x) D_a^{\rm eq}(x) e^{xE/T} \ . \tag{B.11}$$

We now can write the value of the distribution at the node points, and using a linear interpolation, one can write the full distribution as

$$D_a(x,\tau) = \sum_i w_i(x) N_i^a(\tau) \frac{D_a^{\rm eq}(x) e^{xE/T}}{\mathcal{A}_i^a} \ , \tag{B.12}$$

$$= \sum_i x K_i(x) N_i^a(\tau) \ , \tag{B.13}$$

we introduced the "cardinal" function $K_i^a(x) \equiv w_i(x)\frac{D_a^{\rm eq}(x)e^{xE/T}}{x\mathcal{A}_i^a}$ in the last line.

Lastly, as the basis function is constant in time, the evolution of the coefficients $\vec{N}(\tau)$ are obtained directly from the discrete collision integral as follows,

$$\partial_\tau \vec{N}(\tau) = \bar{C}\vec{N}(\tau) \ , \tag{B.14}$$

which admits the solution

$$\vec{N}(\tau) = e^{\tau\bar{C}}\vec{N}(\tau=0) \ , \tag{B.15}$$

where $e^{\tau\bar{C}}$ is a matrix exponentiation.

The integration in Eq. (B.6) is done numerically using a Monte Carlo integration scheme, where at each step we update all elements of the matrix C_{ij}, which ensures charge and energy conservation thanks to Eq. (B.3) and (B.4). Writing the collision integral as a matrix also allows us to compute the eigenvalues and eigenfunctions discussed in Section 4.2. In the following sections, we will provide the different matrices corresponding to each process from Section 4.1.

B.2 Discretization of small angle elastic collision integrals

It is straight forward to write the hard part of the current term in Eqns. (4.18-4.20) using this discretization formalism. One only needs to introduce the wedge function

integration and replace the distribution by its discrete form, we obtain

$$
\begin{aligned}
&-\nabla_{\boldsymbol{p}}\mathcal{J}^{g}_{ij} = \\
&N^{g}_{j}(\tau)C_A\frac{\hat{q}_{\rm eq}}{4T^2}\int dx\; w_i(x)\left[\frac{T^2}{E^2}(\partial_x x^2\partial_x)\frac{K_j(x)}{x^2}\frac{T}{E}(\partial_x x^2)\frac{K_j(x)}{x^2}(1\pm 2n_a(xE))\right],
\end{aligned}
\tag{B.16}
$$

$$
\begin{aligned}
&-\nabla_{\boldsymbol{p}}\mathcal{J}^{q_f}_{ij} = \\
&N^{q_f}_{j}(\tau)C_F\frac{\hat{q}_{\rm eq}}{4T^2}\int dx\; w_i(x)\left[\frac{T^2}{E^2}(\partial_x x^2\partial_x)\frac{K_j(x)}{x^2}+\frac{T}{E}(\partial_x x^2)\frac{K_j(x)}{x^2}(1\pm 2n_a(xE))\right],
\end{aligned}
\tag{B.17}
$$

$$
\begin{aligned}
&-\nabla_{\boldsymbol{p}}\mathcal{J}^{\bar{q}_f}_{ij} = \\
&N^{\bar{q}_f}_{j}(\tau)C_F\frac{\hat{q}_{\rm eq}}{4T^2}\int dx\; w_i(x)\left[\frac{T^2}{E^2}(\partial_x x^2\partial_x)\frac{K_j(x)}{x^2}+\frac{T}{E}(\partial_x x^2)\frac{K_j(x)}{x^2}(1\pm 2n_a(xE))\right],
\end{aligned}
\tag{B.18}
$$

for the quark/antiquark to ensure stability at the boundaries, we employ an integration by parts, inspired by the "weak" form of differential equations [159], and set the term fully integrated to zero according to the boundary conditions.

Using the same approach, the recoil contribution in Eqns. (4.22-4.23) are given by

$$
-\nabla_{\boldsymbol{p}}\delta\mathcal{J}^{g}_{ij} = \frac{C_{\rm A}\hat{\tilde{q}}_{\rm eq}}{4T^2}\frac{T\delta\bar{\eta}^{j}_{D}-\delta\hat{\tilde{q}}^{j}}{\hat{\tilde{q}}_{\rm eq}}\frac{\nu_g}{2\pi^2}\frac{T}{E}\int\frac{dx}{2\pi^2}w_i(x)\partial_x x^2 n_a(xE)(1\pm n_a(xE)),
\tag{B.19}
$$

$$
-\nabla_{\boldsymbol{p}}\delta\mathcal{J}^{q_f/\bar{q}_f}_{ij} = \frac{C_{\rm F}\hat{\tilde{q}}_{\rm eq}}{4T^2}\frac{T\delta\bar{\eta}^{j}_{D}-\delta\hat{\tilde{q}}^{j}}{\hat{\tilde{q}}_{\rm eq}}\frac{\nu_g}{2\pi^2}\frac{T}{E}\int\frac{dx}{2\pi^2}w_i(x)\partial_x x^2 n_a(xE)(1\pm n_a(xE)),
\tag{B.20}
$$

where the recoil coefficients are now represented by vectors written as

$$\delta\hat{\bar{q}}^j = \frac{g^4}{\pi}E^3\int dx\,\Bigg[C_{\rm A}\nu_g^{-1}N_j^g(\tau)K_j(x)(1+2n_B(xE)) + \frac{1}{2}\sum_f \nu_q^{-1}(N_j^{q_f}(\tau)K_j(x)+N_j^{\bar{q}_f}(\tau)K_j(x))(1-2n_F(xE))\Bigg]\,, \tag{B.21}$$

$$\delta\bar{\eta}_D^j = \frac{g^4}{\pi}E^2\int dx\,\frac{2}{x}\Bigg[C_{\rm A}\nu_g^{-1}N_j^g(\tau)K_j(x)+\frac{1}{2}\sum_f \nu_q^{-1}(N_j^{q_f}(\tau)K_j(x)+N_j^{\bar{q}_f}(\tau)K_j(x))\Bigg]\,. \tag{B.22}$$

Similarly for the conversion term from Eqns. (4.26,4.27) we obtain

$$S_{ij}^g = \nu_g\frac{\mathcal{I}_{q_f}^{\rm eq}}{8T^2}\int dx\,\frac{T}{xE}w_i(x)\sum_f\Big\{\nu_q^{-1}\Big[N_j^{q_f}(\tau)K_j(x)+N_j^{\bar{q}_f}(\tau)K_j(x)\Big](1+2n_B(xE)) - 2\nu_g^{-1}N_j^g(\tau)K_j(x)(1-2n_F(xE))\Big\}\,, \tag{B.23}$$

$$S_{ij}^{q_f,\bar{q}_f} = \nu_g\frac{\mathcal{I}_{q_f}^{\rm eq}}{8T^2}\int dx\,\frac{T}{xE}w_i(x)\Big\{\nu_g^{-1}N_j^g(\tau)K_j(x)(1-2n_F(xE)) - \nu_q^{-1}N_j^{q_f,\bar{q}_f}(\tau)K_j(x)(x)(1+2n_B(xE))\Big\}\,, \tag{B.24}$$

and the corresponding recoil contributions are given by

$$\delta S_{ij}^{q_f} = \frac{\nu_g}{2\pi^2}\int dx\; w_i(x)\frac{x}{8E}\left(\delta\mathcal{I}_j^{q_f}-\delta\mathcal{I}_j^{\bar{q}_f}\right)\; n_B(xE)(1-n_F(xE))\,, \tag{B.25}$$

$$\delta S_{ij}^{\bar{q}_f} = \frac{\nu_g}{2\pi^2}\int dx\; w_i(x)\frac{x}{8E}\left(\delta\mathcal{I}_j^{\bar{q}_f}-\delta\mathcal{I}_j^{q_f}\right)\; n_B(xE)(1-n_F(xE))\,, \tag{B.26}$$

where the difference of $\delta\mathcal{I}_j^{q_f}$ and $\delta\mathcal{I}_j^{\bar{q}_f}$ is given by

$$\left(\delta\mathcal{I}_j^{\bar{q}_f}-\delta\mathcal{I}_j^{q_f}\right) = \frac{g^4C_F\mathcal{L}}{\pi}E^2\int\; dx\;\frac{1}{x}\left(1+2n_B(xE)\right)\nu_q^{-1}\left(N_j^{q_f}(\tau)K_j(x)-N_j^{\bar{q}_f}(\tau)K_j(x)\right)\,. \tag{B.27}$$

B.3 Discretization of inelastic collision integrals

Before discretizing the radiative collision integrals, we will combine both merging and splitting processes in Eqns. (4.33-4.38) by introducing a delta function. Apply-

ing this to a general $1 \leftrightarrow 2$ processes, one finds

$$\begin{aligned} C_a^{1\leftrightarrow 2} =& -\frac{1}{2}\int_0^1 dz \frac{d\Gamma^a_{bc}(xE,z)}{dz}\Big[D_a(x)(1 \pm n_b(zxE) \pm n_c(\bar{z}xE)) \\ &\pm \frac{D_b(zx)}{z^3}(n_a(xE) \mp_b n_c(\bar{z}xE)) \pm \frac{D_c(\bar{z}x)}{\bar{z}^3}(n_a(xE) \mp_c n_b(zxE))\Big] \\ &+ \frac{\nu_b}{\nu_a}\int_0^1 dz\ \frac{1}{z}\frac{d\Gamma^b_{ac}(\frac{xE}{z},z)}{dz}\Big[D_b(\frac{x}{z})(1 \pm n_a(xE) \pm n_c(\frac{\bar{z}}{z}xE)) \\ &\pm \frac{D_a(x)}{z^3}(n_b(\frac{xE}{z}) \mp_a n_c(\frac{\bar{z}}{z}xE)) \pm \frac{D_a(x)}{\bar{z}^3}(n_b(\frac{xE}{z}) \mp_c n_a(\frac{xE}{z}))\Big] \qquad \text{(B.28)} \\ =& \int dy\ \int_0^1 dz \frac{d\Gamma^e_{kc}(yE,z)}{dz}\Big[D_e(y)(1 \pm n_k(zyE) \pm n_c(\bar{z}yE)) \\ &\pm \frac{D_k(zy)}{z^3}(n_e(yE) \mp_k n_c(\bar{z}yE)) \pm \frac{D_c(\bar{z}y)}{\bar{z}^3}(n_e(yE) \mp_c n_k(zyE))\Big] \\ &\times \left[\frac{\nu_b}{\nu_a} z\delta(x-zy)\delta^{e,b}_{k,a} - \frac{1}{2}\delta(x-y)\delta^{e,a}_{k,b}\right], \qquad \text{(B.29)} \end{aligned}$$

where we used $\mp_a$ to represent either a minus if particle a is a Boson or a plus if particle a is a fermion. After employing the discretization scheme, one finds for the gluon collision integrals

$$\begin{aligned} C^{g\leftrightarrow gg}_{g,ij} =& \frac{1}{2}\int dx\ \int_0^1 dz \frac{d\Gamma^g_{gg}(xE,z)}{dz}\Big[N^g_j(\tau)K_j(x)(1 + n_B(zxE) + n_B(\bar{z}xE)) \\ &+ \frac{N^g_j(\tau)K_j(zx)}{z^2}(n_B(xE) - n_B(\bar{z}xE)) \\ &+ \frac{N^g_j(\tau)K_j(\bar{z}x)}{\bar{z}^2}(n_B(xE) - n_B(zxE))\Big]\left[w_i(\bar{z}x) + w_i(zx) - w_i(x)\right], \end{aligned} \qquad \text{(B.30)}$$

$$\begin{aligned} C^{q\leftrightarrow qg}_{g,ij} =& \sum_f \int_0^1 dz \frac{d\Gamma^q_{gg}\left(\frac{xE}{z},z\right)}{dz}\Big[N^{q_f}_j(\tau)K_j(x)\left(1 + n_B(zxE) - n_F(\bar{z}xE)\right) \\ &+ \frac{\nu_q}{\nu_g}\frac{N^g_j(\tau)K_j(zx)}{z^2}(n_F(xE) - n_F(\bar{z}xE)) \\ &- \frac{N^{q_f}_j(\tau)K_j(\bar{z}x)}{\bar{z}^2}(n_F(xE) + n_B(zxE))\Big] w_i(zx), \end{aligned} \qquad \text{(B.31)}$$

$$C^{\bar{q}\leftrightarrow\bar{q}g}_{g,ij} = \sum_f \int_0^1 dz \frac{d\Gamma^q_{gq}\left(\frac{xE}{z}, z\right)}{dz} \Bigg[N_j^{\bar{q}_f}(\tau) K_j(x) \left(1 + n_B(zxE) - n_F(\bar{z}xE)\right) + \frac{\nu_q}{\nu_g} \frac{N_j^g(\tau) K_j(zx)}{z^2} (n_F(xE) - n_F(\bar{z}xE)) - \frac{N_j^{\bar{q}_f}(\tau) K_j(\bar{z}x)}{\bar{z}^2} (n_F(xE) + n_B(zxE)) \Bigg] w_i(zx) \,, \tag{B.32}$$

$$C^{g\leftrightarrow q\bar{q}}_{g,ij} = -\sum_f \int_0^1 dz \frac{d\Gamma^g_{q\bar{q}}(xE, z)}{dz} \Bigg[N_j^g(\tau) K_j(x) (1 - n_F(zxE) - n_F(\bar{z}xE)) - \frac{\nu_g}{\nu_q} \frac{N_j^{q_f}(\tau) K_j(zx)}{z^2} (n_B(xE) + n_F(\bar{z}xE)) - \frac{\nu_g}{\nu_q} \frac{N_j^{\bar{q}_f}(\tau) K_j(\bar{z}x)}{\bar{z}^2} (n_B(xE) + n_F(zxE)) \Bigg] \times w_i(x) \,, \tag{B.33}$$

where for the symmetric $g \leftrightarrow gg$ and $g \leftrightarrow q\bar{q}$ processes, we symmetrized the integrand by change of variable $z \to \bar{z}$.

Similarly, the quark collision integrals are given by

$$C^{q\leftrightarrow qg}_{q_f,ij} = \sum_f \int_0^1 dz \frac{d\Gamma^q_{gq}\left(\frac{xE}{z}, z\right)}{dz} \Bigg[N_j^{q_f}(\tau) K_j(x) \left(1 + n_B(zxE) - n_F(\bar{z}xE)\right) + \frac{\nu_q}{\nu_g} \frac{N_j^g(\tau) K_j(zx)}{z^2} (n_F(xE) - n_F(\bar{z}xE)) - \frac{N_j^{q_f}(\tau) K_j(\bar{z}x)}{\bar{z}^2} (n_F(xE) + n_B(zxE)) \Bigg] \left[w_i(\bar{z}x) - w_i(x)\right] \,, \tag{B.34}$$

$$C^{g\leftrightarrow q\bar{q}}_{q_f,ij} = \sum_f \int_0^1 dz \frac{d\Gamma^g_{q\bar{q}}(xE, z)}{dz} \Bigg[N_j^g(\tau) K_j(x) (1 - n_F(zxE) - n_F(\bar{z}xE)) - \frac{\nu_g}{\nu_q} \frac{N_j^{q_f}(\tau) K_j(zx)}{z^2} (n_B(xE) + n_F(\bar{z}xE)) - \frac{\nu_g}{\nu_q} \frac{N_j^{\bar{q}_f}(\tau) K_j(\bar{z}x)}{\bar{z}^2} (n_B(xE) + n_F(zxE)) \Bigg] w_i(zx) \,. \tag{B.35}$$

For the antiquark channel the $\bar{q} \leftrightarrow \bar{q}g$ process is the same as the quark by exchange of q_f with $\bar{q}_f$, while the $g \leftrightarrow q\bar{q}$ process is given by

$$\begin{aligned} C^{g\leftrightarrow q\bar{q}}_{\bar{q}_f,ij} = \sum_f \int_0^1 dz \frac{d\Gamma^g_{q\bar{q}}(xE,z)}{dz} \Bigg[& N^g_j(\tau) K_j(x)(1 - n_F(zxE) - n_F(\bar{z}xE)) \\ & - \frac{\nu_g}{\nu_q} \frac{N^{q_f}_j(\tau) K_j(zx)}{z^2} (n_B(xE) + n_F(\bar{z}xE)) \\ & - \frac{\nu_g}{\nu_q} \frac{N^{\bar{q}_f}_j(\tau) K_j(\bar{z}x)}{\bar{z}^2} (n_B(xE) + n_F(zxE)) \Bigg] w_i(\bar{z}x) \ . \end{aligned} \tag{B.36}$$

Using the properties of the wedge function, one can easily find that charge is conserved because

$$\sum_i C^{g\leftrightarrow q\bar{q}}_{q_f,ij} - C^{g\leftrightarrow q\bar{q}}_{\bar{q}_f,ij} \propto \sum_i w_i(zx) - w_i(\bar{z}x) = 0 \ , \tag{B.37}$$

$$\sum_i C^{(q/\bar{q}_f)\leftrightarrow(q/\bar{q}_f)g}_{(q_f/\bar{q}_f),ij} \propto \sum_i w_i(\bar{z}x) - w_i(x) = 0 \ , \tag{B.38}$$

and analogously for energy conservation, we have

$$\sum_i x_i [w_i(zx) + w_i(\bar{z}x) - w_i(x)] = 0 \ , \tag{B.39}$$

for all allowed configurations of the splitting.

B.3.1 Comparison of the in-medium splitting rate to leading-log approximation

For highly energetic parent particles the radiation rate in Eq. (3.33) is in the deep LPM regime, which can be approximated by the Harmonic Oscillator (HO) rate [116]. In order to match the HO rate, one has to choose a sensible value of $\hat{\bar{q}}$. For the early time behavior in Eqns. (4.71-4.72) we consider the parent particle to be of energy E and fit $\hat{\bar{q}}(E)$ to match, as shown in the left panel of Fig. B.1. In the same figure we show the rate in the Bethe-Heitler regime [34] which describes the splitting to soft fragments, one can see clearly how the full splitting rate interpolate between the leading-log rate for highly energetic fragments and the BH regime for soft fragments. Conversely, for the successive branchings in Eqns. (4.79-4.80) we approximate the parent particle energy by the geometric mean between the jet energy E and the temperature T and fit the value of $\hat{\bar{q}}(\sqrt{TE})$ as shown in right panel of Fig. B.1.

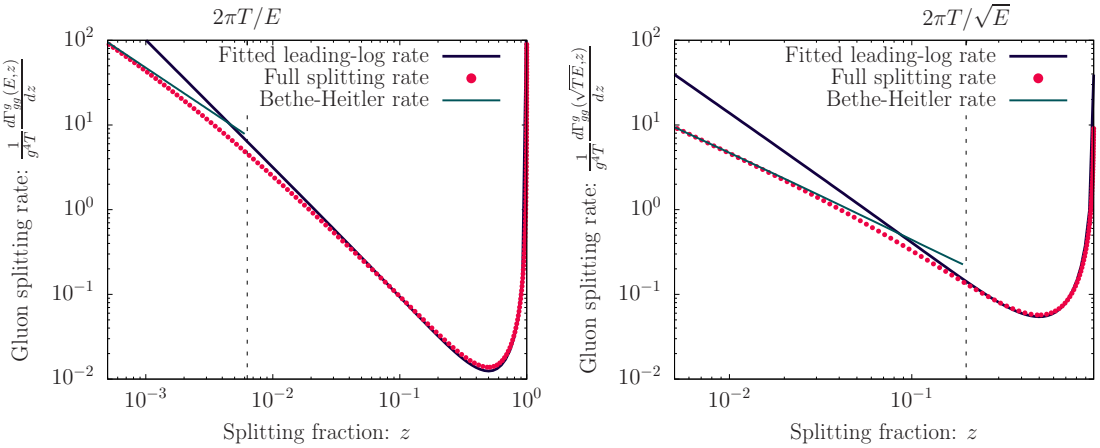

Figure B.1: Comparison of the matching of the leading-log splitting rate (blue line) to the full effective rate (red dot) for $g \leftrightarrow gg$ process. We also show the Bethe-Heitler rate (green) relevant for soft radiation. On the left panel we show for a parent particle with energy $E = 1000T$, and on the right panel for a parent particle with energy $E = \sqrt{1000}T$.

B.4 Discretization of the angular cascade

The wedge function discretization can also be employed for two-dimensional functions using double wedges, the discretization is written

$$N_k^a(\tau) = \int dx \int d\cos\theta \; w_i(x) w_j(\cos\theta) \frac{D_a(x, \cos\theta, \tau)}{x} \,, \tag{B.40}$$

here and throughout this section we will use $k = j + iN_{\cos\theta}$. Conservation of the number of particles, energy and momentum is now given by

$$n_a(\tau) = \sum_k N_k^a(\tau) \,, \quad E_a(\tau) = \sum_k x_i N_k^a(\tau) \,, \quad P_a(\tau) = \sum_k x_i \cos\theta_j N_k^a(\tau) \,. \tag{B.41}$$

Similarly, the collision integral is expanded

$$C_k^a(\tau) = \int dx \int d\cos\theta \; w_i(x) w_j(\cos\theta) \frac{C_a(x, \cos\theta, \tau)}{x} \,. \tag{B.42}$$

The vector $C_k^a(\tau)$ can again be written as a matrix vector product

$$C_k^a(\tau) = \sum_j \delta C_{kj}^{ab} N_j^b(\tau) = \delta \bar{C}^{ab} \vec{N}^b(\tau) \,, \tag{B.43}$$

using the same construction as in Eq. (B.8).

Now, to reconstruct the distribution function, we use the analogous procedure as before

$$N_k^a(\tau) = \int dx \int d\cos\theta \; w_i(x) w_j(\cos\theta) \frac{D_a(x,\cos\theta,\tau)}{x \; D_a^{\rm eq}(x) e^{xE/T}} D_a^{\rm eq}(x) e^{xE/T} \; , \tag{B.44}$$

$$= \frac{D_a(x,\cos\theta,\tau)}{D_a^{\rm eq}(x) e^{xE/T}} \mathcal{A}_k^a \; , \tag{B.45}$$

except the area $\mathcal{A}_k^a$ becomes the double integral

$$\mathcal{A}_k^a \equiv \int dx \int d\cos\theta \; w_i(x) w_j(\cos\theta) D_a^{\rm eq}(x) e^{xE/T} \; . \tag{B.46}$$

We now can write the value of the distribution at the node points, and using a linear interpolation, one can write the full distribution as

$$D_a(x,\cos\theta,\tau) = \sum_k w_i(x) w_j(x) N_k^a(\tau) \frac{D_a^{\rm eq}(x) e^{xE/T}}{\mathcal{A}_k^a} \; , \tag{B.47}$$

$$= \sum_k x K_k(x,\cos\theta) N_k^a(\tau) \; , \tag{B.48}$$

where the "cardinal" function is now $K_k^a(x,\cos\theta) \equiv w_i(x) w_j(\cos\theta) \frac{D_a^{\rm eq}(x) e^{xE/T}}{x \mathcal{A}_k^a}$.

B.4.1 Elastic scatterings

Using the discretization introduced above, we can write the $2 \leftrightarrow 2$ elastic integral, we will focus on the process $gg \leftrightarrow gg$ given by

$$C_g^{gg\leftrightarrow gg}[\{D_i\}] = \int \frac{d^3p_1}{(2\pi)^3} \; \frac{p_1}{E} \; \delta\Big(\frac{p_1}{E} - x\Big) \delta\Big(\frac{\boldsymbol{p}_1 \cdot \vec{e}_z}{p_1} - \cos\theta\Big)$$
$$\frac{1}{2p_1} \int d\Omega^{2\leftrightarrow 2} \left|\mathcal{M}_{gg}^{gg}(1,2;3,4)\right|^2 \mathcal{D}(1,2;3,4) \; . \tag{B.49}$$

Reconstruction of the statistical factor using Eq. (B.48) is straight forward, yielding

$$\begin{aligned}\mathcal{D}(1,2;3,4) = \sum_k \Bigg\{ & \\ & N_k^g(\tau)\frac{x_1 K_k^g(x_1,\cos\theta_1)}{\nu_g x_1^3 E^2}\left[n_B(p_3)n_B(p_4) - n_B(p_2)(1+n_B(p_3)+n_B(p_4))\right] \\ & + N_k^q(\tau)\frac{x_2 K_k^g(x_2,\cos\theta_2)}{\nu_g x_2^3 E^2}\left[n_B(p_3)n_B(p_4) - n_B(p_1)(1+n_B(p_3)+n_B(p_4))\right] \\ & - N_k^g(\tau)\frac{x_3 K_k^g(x_3,\cos\theta_3)}{\nu_g x_3^3 E^2}\left[n_B(p_1)n_B(p_2) - n_B(p_4)(1+n_B(p_1)+n_B(p_2))\right] \\ & - N_k^q(\tau)\frac{x_4 K_k^g(x_4,\cos\theta_4)}{\nu_g x_4^3 E^2}\left[n_B(p_1)n_B(p_2) - n_B(p_3)(1+n_B(p_1)+n_B(p_2))\right] \Bigg\} ,\end{aligned} \tag{B.50}$$

here and throughout this section, we will use x_i and $\cos\theta_i$ interchangeably with $\frac{p_i}{E}$ and $\frac{\boldsymbol{p}_i\cdot\vec{e}_z}{p_i}$. The discrete collision integral is defined as

$$C_k^g(\tau) = \int dx \int d\cos\theta \; w_i(x) w_j(\cos\theta)\frac{C_g(x,\cos\theta,\tau)}{x} . \tag{B.51}$$

We can employ the delta functions in Eq. (B.49) to obtain

$$C_k^g(\tau) = \int \frac{d^3p}{(2\pi)^3} \; w_i(x_1) w_j(\cos\theta_1)\frac{1}{2p_1}\int d\Omega^{2\leftrightarrow 2}\left|\mathcal{M}_{gg}^{gg}(1,2;3,4)\right|^2 \mathcal{D}(1,2;3,4) . \tag{B.52}$$

Using the symmetry of the system, we can rename the different momentum integrations as follows

$$\begin{aligned}C_k^g(\tau) = & \frac{1}{4}\int d\tilde{\Omega}^{2\leftrightarrow 2}\Big[w_i(x_1)w_j(\cos\theta_1) + w_i(x_2)w_j(\cos\theta_2) \\ & - w_i(x_3)w_j(\cos\theta_3) - w_i(x_4)w_j(\cos\theta_4)\Big] \\ & \left|\mathcal{M}_{gg}^{gg}(1,2;3,4)\right|^2 \mathcal{D}(1,2;3,4) ,\end{aligned} \tag{B.53}$$

where the integral measure is now

$$\int d\tilde{\Omega}^{2\leftrightarrow 2} = (2\pi)\int \frac{d^3q}{(2\pi)^3}\int \frac{d^3p_1}{(2\pi)^3}\int \frac{d^3p_2}{(2\pi)^3}\int d\omega\ \frac{1}{16p_1^2p_2^2q^2}\Theta(q-|\omega|)\Theta\left(p_1-\frac{q+\omega}{2}\right)$$
$$\Theta\left(p_2-\frac{q-\omega}{2}\right)\delta\left(cos\theta_{1q}-\left(\frac{\omega}{q}-\frac{\omega^2-q^2}{2p_1q}\right)\right)\delta\left(cos\theta_{2q}-\left(\frac{\omega}{q}+\frac{\omega^2-q^2}{2p_2q}\right)\right)\ . \tag{B.54}$$

Before we proceed, we note that particle number, energy and momentum are conserved up to machine precision thanks to the sum rules in Eqns. (B.3-B.4), which leads to

$$\sum_k \Big[w_i(x_1)w_j(\cos\theta_1)+w_i(x_2)w_j(\cos\theta_2)-w_i(x_3)w_j(\cos\theta_3)-w_i(x_4)w_j(\cos\theta_4)\Big]$$
$$=0\ , \tag{B.55}$$
$$\sum_k x_i\Big[w_i(x_1)w_j(\cos\theta_1)+w_i(x_2)w_j(\cos\theta_2)-w_i(x_3)w_j(\cos\theta_3)-w_i(x_4)w_j(\cos\theta_4)\Big]$$
$$=x_1+x_2-x_3-x_4=0\ , \tag{B.56}$$
$$\sum_k x_i\cos\theta_i\Big[w_i(x_1)w_j(\cos\theta_1)+w_i(x_2)w_j(\cos\theta_2)-w_i(x_3)w_j(\cos\theta_3)$$
$$-w_i(x_4)w_j(\cos\theta_4)\Big]=x_1\cos\theta_1+x_2\cos\theta_2-x_3\cos\theta_3-x_4\cos\theta_4=0\ . \tag{B.57}$$

We can measure the vectors $\boldsymbol{p}_1$ and $\boldsymbol{p}_2$ using $\boldsymbol{q}$ as the z-axis of spherical coordinates and employ their polar angle integrations to set

$$cos\theta_{1q}=\left(\frac{\omega}{q}-\frac{\omega^2-q^2}{2p_1q}\right)\ ,\quad cos\theta_{2q}=\left(\frac{\omega}{q}+\frac{\omega^2-q^2}{2p_2q}\right)\ . \tag{B.58}$$

We are left with the following integration

$$\int d\tilde{\Omega}^{2\leftrightarrow 2} = (2\pi)\int \frac{d^3q}{(2\pi)^3}\int_{-q}^{q} d\omega\int_{\frac{q+\omega}{2}}\frac{dp_1d\phi_1}{(2\pi)^3}\int_{\frac{q-\omega}{2}}\frac{dp_2d\phi_2}{(2\pi)^3}\ \frac{1}{16q^2}\ . \tag{B.59}$$

In the following, we provide the definitions employed to perform the integral numerically. Starting with the outgoing particles energies and momenta given by

$$\boldsymbol{p}_3=\boldsymbol{p}_1-\boldsymbol{q}\ ,\qquad \boldsymbol{p}_4=\boldsymbol{p}_2+\boldsymbol{q}\ , \tag{B.60}$$
$$p_3=p_1-\omega\ ,\qquad p_4=p_2+\omega\ . \tag{B.61}$$

The Mandelstam variables are

$$t = \omega^2 - q^2, \quad s = 2p_1p_2(1 - \cos\theta_{12}), \quad u = -t - s. \tag{B.62}$$

In order to obtain the different angles, we define the basis $(\vec{e}_1, \vec{e}_2, \vec{e}_3)$

$$\vec{e}_1 = \vec{e}_q = \frac{\mathbf{q}}{q}\,, \quad \vec{e}_2 = \frac{\vec{e}_z - \cos(\theta_q)\vec{e}_q}{|\vec{e}_z - \cos(\theta_q)\vec{e}_q|} = \frac{\vec{e}_z - \cos(\theta_q)\vec{e}_q}{\sin\theta_q}\,, \tag{B.63}$$

$$\vec{e}_3 = \frac{\vec{e}_q \times \vec{e}_z}{|\vec{e}_q \times \vec{e}_z|} = \frac{\vec{e}_q \times \vec{e}_z}{|\sin(\theta_q)|}\,, \tag{B.64}$$

where $\cos\theta_q = \vec{e}_q \cdot \vec{e}_z$. In this basis, the momenta are given by

$$\boldsymbol{p}_1 = p_1\left[\cos\theta_{1q}\vec{e}_1 + \sin\theta_{1q}(\cos\phi_1\vec{e}_2 + \sin\phi_1\vec{e}_3)\right]\,, \tag{B.65}$$

$$\boldsymbol{p}_2 = p_2\left[\cos\theta_{2q}\vec{e}_1 + \sin\theta_{2q}(\cos\phi_2\vec{e}_2 + \sin\phi_2\vec{e}_3)\right]\,, \tag{B.66}$$

The angles with the initial momentum axis (i.e., $\theta_{1,2}$) are given by

$$\cos\theta_1 = \frac{p_{1z}}{p_1} = \left[\cos\theta_{1q}\cos\theta_q + \sin\theta_{1q}\cos\phi_1\sin\theta_q\right]\,, \tag{B.67}$$

$$\cos\theta_2 = \frac{p_{2z}}{p_2} = \left[\cos\theta_{2q}\cos\theta_q + \sin\theta_{2q}\cos\phi_2\sin\theta_q\right]\,. \tag{B.68}$$

We also need the following angles

$$\frac{\boldsymbol{p}_1 \cdot \boldsymbol{p}_2}{p_1p_2} = \cos\theta_{12} = \cos\theta_{1q}\cos\theta_{2q} + \cos(\phi_1 - \phi_2)\sin\theta_{1q}\sin\theta_{2q}\,, \tag{B.69}$$

$$\frac{p_{3z}}{p_3} = \cos\theta_3 = \frac{p_1\cos\theta_1 - q\cos\theta_q}{p_1 - \omega}\,, \tag{B.70}$$

$$\frac{p_{4z}}{p_4} = \cos\theta_4 = \frac{p_2\cos\theta_2 + q\cos\theta_q}{p_2 + \omega}\,. \tag{B.71}$$

We follow the same procedure for all the different processes in Tab. 3.1 to obtain the different collision terms which are used for the evolution in Chapter 5.

C Bethe-Heitler regime at infinite medium

We solve Eq. (3.34) perturbatively following an opacity expansion in the number of elastic scatterings, such that at leading order

$$\mathbf{g}^{(0)}_{(z,P)}(\mathbf{p}_\perp) = \frac{-2i\mathbf{p}_\perp}{\delta E(z,P,\mathbf{p}_\perp)} = \frac{-4i\mathbf{p}_\perp Pz(1-z)}{\mathbf{p}_\perp^2+\mu(z)^2}\,, \tag{C.1}$$

$$\mu(z)^2 = (1-z)m^2_{\infty,(z)} + zm^2_{\infty,(1-z)} - z(1-z)m^2_{\infty,(1)}\,, \tag{C.2}$$

which is entirely imaginary and thus does not contribute to the splitting rate. Hence, the first non-trivial contribution comes from

$$\begin{aligned} 2\mathbf{p}_\perp \mathbf{g}^{(1)}_{(z,P)}(\mathbf{p}_\perp) =& \frac{2i\mathbf{p}_\perp}{\delta E(z,P,\mathbf{p}_\perp)} \int \frac{\mathrm{d}^2\mathbf{q}_\perp}{(2\pi)^2}\, \bar{C}(\mathbf{q}_\perp) \Big\{ C_1 \left[\mathbf{g}^0_{(z,P)}(\mathbf{p}_\perp) - \mathbf{g}^0_{(z,P)}(\mathbf{p}_\perp - \mathbf{q}_\perp)\right] \\ &+ C_z \left[\mathbf{g}^0_{(z,P)}(\mathbf{p}_\perp) - \mathbf{g}^0_{(z,P)}(\mathbf{p}_\perp - z\mathbf{q}_\perp)\right] \\ &+ C_{1-z} \left[\mathbf{g}^0_{(z,P)}(\mathbf{p}_\perp) - \mathbf{g}^0_{(z,P)}(\mathbf{p}_\perp - \bar{z}\mathbf{q}_\perp)\right] \Big\}\,. \end{aligned} \tag{C.3}$$

By plugging in the leading order one finds

$$\begin{aligned} 2\mathbf{p}_\perp \mathbf{g}^{(1)}_{(z,P)}(\mathbf{p}_\perp) =& 16P^2z^2(1-z)^2 \int \frac{\mathrm{d}^2\mathbf{q}_\perp}{(2\pi)^2}\, \bar{C}(\mathbf{q}_\perp)\, \frac{1}{\mathbf{p}_\perp^2+\mu^2(z)} \times \\ & \Bigg\{ C_1 \left[\frac{\mathbf{p}_\perp^2}{\mathbf{p}_\perp^2+\mu(z)^2} - \frac{\mathbf{p}_\perp(\mathbf{p}_\perp-\mathbf{q}_\perp)}{(\mathbf{p}_\perp-\mathbf{q}_\perp)^2+\mu(z)^2}\right] \\ & + C_z \left[\frac{\mathbf{p}_\perp^2}{\mathbf{p}_\perp^2+\mu(z)^2} - \frac{\mathbf{p}_\perp(\mathbf{p}_\perp-z\mathbf{q}_\perp)}{(\mathbf{p}_\perp-z\mathbf{q}_\perp)^2+\mu(z)^2}\right] \\ & + C_{1-z} \left[\frac{\mathbf{p}_\perp^2}{\mathbf{p}_\perp^2+\mu(z)^2} - \frac{\mathbf{p}_\perp(\mathbf{p}_\perp-\bar{z}\mathbf{q}_\perp)}{(\mathbf{p}_\perp-\bar{z}\mathbf{q}_\perp)^2+\mu(z)^2}\right] \Bigg\}\,, \end{aligned} \tag{C.4}$$

such that the rate is given by

$$\begin{aligned}\frac{\mathrm{d}\Gamma_{ij}^{BH}}{\mathrm{d}z}(P,z) = g_{\mathrm{s}}^4 T P_{ij}(z)\frac{1}{\pi}\int\frac{\mathrm{d}^2\mathbf{p}_\perp}{(2\pi)^2}\int\frac{\mathrm{d}^2\mathbf{q}_\perp}{(2\pi)^2}\frac{1}{g_{\mathrm{s}}^2 T}\,\bar{C}(\mathbf{q}_\perp)\,\frac{1}{\mathbf{p}_\perp^2+\mu(z)^2}\\ \times\left\{C_1\left[\frac{\mathbf{p}_\perp^2}{\mathbf{p}_\perp^2+\mu(z)^2}-\frac{\mathbf{p}_\perp(\mathbf{p}_\perp-\mathbf{q}_\perp)}{(\mathbf{p}_\perp-\mathbf{q}_\perp)^2+\mu(z)^2}\right]\right.\\ +C_z\left[\frac{\mathbf{p}_\perp^2}{\mathbf{p}_\perp^2+\mu(z)^2}-\frac{\mathbf{p}_\perp(\mathbf{p}_\perp-z\mathbf{q}_\perp)}{(\mathbf{p}_\perp-z\mathbf{q}_\perp)^2+\mu(z)^2}\right]\\ \left.+C_{1-z}\left[\frac{\mathbf{p}_\perp^2}{\mathbf{p}_\perp^2+\mu(z)^2}-\frac{\mathbf{p}_\perp(\mathbf{p}_\perp-\bar{z}\mathbf{q}_\perp)}{(\mathbf{p}_\perp-\bar{z}\mathbf{q}_\perp)^2+\mu(z)^2}\right]\right\}. \qquad \text{(C.5)}\end{aligned}$$

We perform the re-arrangement

$$\begin{aligned}&\int\frac{\mathrm{d}^2\mathbf{p}_\perp}{(2\pi)^2}\frac{1}{\mathbf{p}_\perp^2+\mu^2(z)}\left[\frac{\mathbf{p}_\perp^2}{\mathbf{p}_\perp^2+\mu(z)^2}-\frac{\mathbf{p}_\perp(\mathbf{p}_\perp-\mathbf{q}_\perp)}{(\mathbf{p}_\perp-\mathbf{q}_\perp)^2+\mu(z)^2}\right] &\text{(C.6)}\\ =\;&\frac{1}{2}\int\frac{\mathrm{d}^2\mathbf{p}_\perp}{(2\pi)^2}\left(\frac{\mathbf{p}_\perp}{\mathbf{p}_\perp^2+\mu(z)^2}-\frac{(\mathbf{p}_\perp-\mathbf{q}_\perp)}{(\mathbf{p}_\perp-\mathbf{q}_\perp)^2+\mu(z)^2}\right)^2. &\text{(C.7)}\end{aligned}$$

To re-write the terms in a manifestly positive definite form, we can re-express the rate as

$$\frac{\mathrm{d}\Gamma_{ij}^{BH}}{\mathrm{d}z}(P,z) = g_{\mathrm{s}}^4 T P_{ij}(z)\;Q^{BH}(z,m_{\mathrm{D}}^2,m_\infty^2)\,, \qquad \text{(C.8)}$$

where $Q^{BH}(z,m_{\mathrm{D}}^2,m_\infty^2)$ is a dimensionless integral given by

$$\begin{aligned}Q^{BH}(z,m_{\mathrm{D}}^2,m_\infty^2) = \frac{m_{\mathrm{D}}^2}{2\pi g_{\mathrm{s}}^2 T}\int\frac{\mathrm{d}^2\mathbf{p}_\perp}{(2\pi)^2}\int\frac{\mathrm{d}^2\mathbf{q}_\perp}{(2\pi)^2}\,\bar{C}(m_{\mathrm{D}}\mathbf{q}_\perp)\\ \times\left\{C_1\left[\frac{\mathbf{p}_\perp}{\mathbf{p}_\perp^2+\tilde{\mu}(z)^2}-\frac{(\mathbf{p}_\perp-\mathbf{q}_\perp)}{(\mathbf{p}_\perp-\mathbf{q}_\perp)^2+\tilde{\mu}(z)^2}\right]^2\right.\\ +C_z\left[\frac{\mathbf{p}_\perp}{\mathbf{p}_\perp^2+\tilde{\mu}(z)^2}-\frac{(\mathbf{p}_\perp-z\mathbf{q}_\perp)}{(\mathbf{p}_\perp-z\mathbf{q}_\perp)^2+\tilde{\mu}(z)^2}\right]^2\\ \left.+C_{1-z}\left[\frac{\mathbf{p}_\perp}{\mathbf{p}_\perp^2+\tilde{\mu}(z)^2}-\frac{(\mathbf{p}_\perp-\bar{z}\mathbf{q}_\perp)}{(\mathbf{p}_\perp-\bar{z}\mathbf{q}_\perp)^2+\tilde{\mu}(z)^2}\right]^2\right\}, \qquad \text{(C.9)}\end{aligned}$$

with $\tilde{\mu}(z)^2 = \mu(z)^2/m_{\mathrm{D}}^2$. By re-scaling $\mathbf{p}_\perp$ in the second and third term, the three terms can be expressed in terms of a single integral

$$Q^{BH}(z, m_{\mathrm{D}}^2, m_\infty^2) = C_1 Q\Big(\tilde{\mu}^2(z)\Big) + C_z Q\Big(\frac{\tilde{\mu}^2(z)}{z^2}\Big) + C_z Q\Big(\frac{\tilde{\mu}^2(z)}{(1-z)^2}\Big)\,, \tag{C.10}$$

where

$$Q(\tilde{\mu}^2) = \frac{m_{\mathrm{D}}^2}{2\pi g_{\mathrm{s}}^2 T}\int\frac{\mathrm{d}^2\mathbf{p}_\perp}{(2\pi)^2}\int\frac{\mathrm{d}^2\mathbf{q}_\perp}{(2\pi)^2}\,\bar{C}(m_{\mathrm{D}}\mathbf{q}_\perp)\left[\frac{\mathbf{p}_\perp}{\mathbf{p}_\perp^2+\tilde{\mu}^2} - \frac{(\mathbf{p}_\perp-\mathbf{q}_\perp)}{(\mathbf{p}_\perp-\mathbf{q}_\perp)^2+\tilde{\mu}^2}\right]^2 \tag{C.11}$$

Now evaluating $\tilde{\mu}(z)^2$ for the different channels, we get

$$\tilde{\mu}^2_{g\to gg}(z) = (1-z)\frac{m^2_{\infty,(g)}}{m_{\mathrm{D}}^2} + z\frac{m^2_{\infty,(g)}}{m_{\mathrm{D}}^2} - z(1-z)\frac{m^2_{\infty,(g)}}{m_{\mathrm{D}}^2} = \frac{1-z(1-z)}{2}\,, \tag{C.12}$$

$$\tilde{\mu}^2_{q\to gq}(z) = (1-z)\frac{m^2_{\infty,(g)}}{m_{\mathrm{D}}^2} + z\frac{m^2_{\infty,(q)}}{m_{\mathrm{D}}^2} - z(1-z)\frac{m^2_{\infty,(q)}}{m_{\mathrm{D}}^2} = \frac{1-z}{2} + az^2\,, \tag{C.13}$$

$$\tilde{\mu}^2_{g\to q\bar{q}}(z) = (1-z)\frac{m^2_{\infty,(q)}}{m_{\mathrm{D}}^2} + z\frac{m^2_{\infty,(q)}}{m_{\mathrm{D}}^2} - z(1-z)\frac{m^2_{\infty,(g)}}{m_{\mathrm{D}}^2} = \frac{2a-z(1-z)}{2}\,, \tag{C.14}$$

where $a = m^2_{\infty,q}/m_{\mathrm{D}}^2$, such that the rates can be compactly expressed as

$$\begin{aligned}
&\frac{\mathrm{d}\Gamma^{BH}_{g\to gg}}{\mathrm{d}z}(P,z) = g_{\mathrm{s}}^4 T P_{g\to gg}(z)\times \\
&\left[\frac{C_A}{2}Q\left(\frac{1-z(1-z)}{2}\right) + \frac{C_{\mathrm{A}}}{2}Q\left(\frac{1-z(1-z)}{2z^2}\right) + \frac{C_{\mathrm{A}}}{2}Q\left(\frac{1-z(1-z)}{2(1-z)^2}\right)\right]\,, \\
&\frac{d\Gamma^{BH}_{q\to gq}}{dz}(P,z) = g_{\mathrm{s}}^4 T P_{q\to gq}(z)\times \\
&\left[\frac{C_{\mathrm{A}}}{2}Q\left(\frac{1-z+2az^2}{2}\right) + \left(C_{\mathrm{F}}-\frac{C_{\mathrm{A}}}{2}\right)Q\left(\frac{1-z+2az^2}{2z^2}\right) + \frac{C_{\mathrm{A}}}{2}Q\left(\frac{1-z+2az^2}{2(1-z)^2}\right)\right]\,, \\
&\frac{d\Gamma^{BH}_{g\to q\bar{q}}}{dz}(P,z) = g_{\mathrm{s}}^4 T P_{g\to q\bar{q}}(z)\times \\
&\left[\left(C_{\mathrm{F}}-\frac{C_{\mathrm{A}}}{2}\right)Q\left(\frac{2a-z(1-z)}{2}\right) + \frac{C_{\mathrm{A}}}{2}Q\left(\frac{2a-z(1-z)}{2z^2}\right) + \frac{C_{\mathrm{A}}}{2}Q\left(\frac{2a-z(1-z)}{2(1-z)^2}\right)\right]\,.
\end{aligned} \tag{C.15}$$

C.1 Evaluating the integral in impact-parameter space

In this section, we show how to compute the $Q(\tilde{\mu}^2)$ integral in $\boldsymbol{b}_\perp$-space. We start by rewriting the integral in Eq. (C.11) as follows:

$$Q(\tilde{\mu}^2) = \frac{1}{g_s^2 T}\int\frac{\mathrm{d}^2\mathbf{p}_\perp}{(2\pi)^2}\,\vec{\psi}(\mathbf{p}_\perp)\int\frac{\mathrm{d}^2\mathbf{q}_\perp}{(2\pi)^2}\,\bar{C}(\mathbf{q}_\perp)\left(\vec{\psi}(\mathbf{p}_\perp)-\vec{\psi}(\mathbf{p}_\perp-\mathbf{q}_\perp)\right)\,, \tag{C.16}$$

where we introduce the function $\vec{\psi}(\mathbf{p}_\perp) = \frac{\mathbf{p}_\perp}{\mathbf{p}_\perp^2+\tilde{\mu}^2}$. Its Fourier transform is given by,

$$\vec{\psi}(\boldsymbol{b}_\perp) = \int\frac{\mathrm{d}^2\mathbf{q}_\perp}{(2\pi)^2}e^{-i\mathbf{q}_\perp\cdot\boldsymbol{b}_\perp}\vec{\psi}(\mathbf{q}_\perp) = -\frac{i}{2\pi}\tilde{\mu}K_1(\tilde{\mu}b_\perp)\frac{\boldsymbol{b}_\perp}{b_\perp}\,, \tag{C.17}$$

where $K_1(x)$ is the modified Bessel function of the second kind. Inserting the Fourier transform to the $Q(\tilde{\mu}^2)$ integral and using the definition of the broadening kernel in Eq. (6.2) we obtain

$$\begin{aligned}
Q(\tilde{\mu}^2) &= \frac{1}{g_s^2 T}\int\mathrm{d}^2\boldsymbol{b}_\perp\int\frac{\mathrm{d}^2\mathbf{p}_\perp}{(2\pi)^2}\,\vec{\psi}(\mathbf{p}_\perp)\int\frac{\mathrm{d}^2\mathbf{q}_\perp}{(2\pi)^2}\,\bar{C}(\mathbf{q}_\perp)e^{i\mathbf{p}_\perp\cdot\boldsymbol{b}_\perp}\left(1-e^{-i\boldsymbol{b}_\perp\cdot\mathbf{q}_\perp}\right)\vec{\psi}(\boldsymbol{b}_\perp)\\
&= \frac{1}{g_s^2 T}\int\mathrm{d}^2\boldsymbol{b}_\perp\int\frac{\mathrm{d}^2\mathbf{p}_\perp}{(2\pi)^2}\,\vec{\psi}(\mathbf{p}_\perp)\,\bar{C}(\boldsymbol{b}_\perp)e^{i\mathbf{p}_\perp\cdot\boldsymbol{b}_\perp}\vec{\psi}(\boldsymbol{b}_\perp)\\
&= \frac{1}{g_s^2 T}\int\mathrm{d}^2\boldsymbol{b}_\perp\,\bar{C}(\boldsymbol{b}_\perp)\vec{\psi}(-\boldsymbol{b}_\perp)\cdot\vec{\psi}(\boldsymbol{b}_\perp)\\
&= \frac{1}{g_s^2 T}\int_0^\infty\frac{\mathrm{d}b_\perp}{2\pi}\,\bar{C}(b_\perp)\,b_\perp\tilde{\mu}^2K_1(\tilde{\mu}b_\perp)^2\,.
\end{aligned} \tag{C.18}$$

This last integral is equivalent to Eq. (C.11). However, being in position space, we can use it to obtain the rate in the Bethe-Heitler regime for the non-perturbative kernel without a Fourier transformation.

D Finite medium splitting rate calculation

Following the approach of [121], we show in this appendix how we obtain the finite medium rate numerically.

D.1 Interaction picture

We take the wave function defined in Eq. (6.43) to be isotropic and define the interaction picture wave function and the inverse, as follows

$$\tilde{\psi}_I(\tilde{p},\Delta\tilde{t}) = e^{i\delta\tilde{E}(\tilde{p})\Delta\tilde{t}}\tilde{\boldsymbol{p}}\cdot\vec{\tilde{\psi}}(|\tilde{p}|,\Delta\tilde{t}) \,, \tag{D.1}$$

$$\vec{\tilde{\psi}}(|\tilde{p}|,\Delta\tilde{t}) = e^{-i\delta\tilde{E}(\tilde{p})\Delta\tilde{t}}\frac{\tilde{\boldsymbol{p}}}{\tilde{p}^2}\tilde{\psi}_I(\tilde{p},\Delta\tilde{t}) \,, \tag{D.2}$$

which follows the evolution equation

$$\left[\partial_{\Delta\tilde{t}} + \Lambda\, e^{i\delta\tilde{E}(\tilde{p})\Delta\tilde{t}}\tilde{\boldsymbol{p}}\cdot\tilde{\Gamma}_3\circ e^{-i\delta\tilde{E}(\tilde{p})\Delta\tilde{t}}\frac{\tilde{\boldsymbol{p}}}{\tilde{p}^2}\right]\tilde{\psi}_I(\tilde{p},\Delta\tilde{t}) = 0 \,, \tag{D.3}$$

with the initial condition

$$\tilde{\psi}_I(\tilde{p},\Delta\tilde{t}=0) = \tilde{\boldsymbol{p}}\cdot\tilde{\Gamma}_3\circ\frac{i\tilde{\boldsymbol{p}}}{\delta\tilde{E}(\tilde{\boldsymbol{p}})} \,. \tag{D.4}$$

The splitting rate is now given by

$$\frac{d\Gamma^a_{bc}}{dz} = \frac{g^4 T P^a_{bc}(z)}{\pi}\mathrm{Re}\int_0^{\tilde{t}} d\Delta\tilde{t}\int_{\tilde{\boldsymbol{p}}} e^{-i\delta\tilde{E}(\tilde{p})\Delta\tilde{t}}\tilde{\psi}_I(\tilde{p},\Delta\tilde{t}) \,. \tag{D.5}$$

Using a standard Euler solver, we evolve the wave function from $\Delta\tilde{t}=0$ to $\Delta\tilde{t}=\tilde{t}$ with the differential equation (D.3) and use our results to perform the integral in Eq. (D.5).

D.2 Separating the soft scale

When solving the evolution equation using the NLO and non-perturbative broadening kernels, we find that the $1/q^3$ behavior at small momentum leads to numerical instabilities. In order to stabilize this evolution, we will consider the soft interactions in the collision integral separately. By introducing an intermediate cut in the momentum exchange $\boldsymbol{q}$, the collision integral is separated to hard and soft interactions

$$C[\tilde{\psi}_I] = C_{\text{hard}}[\tilde{\psi}_I] + C_{\text{soft}}[\tilde{\psi}_I] \ . \tag{D.6}$$

The soft interaction can be treated in a diffusion approximation using an expansion in momentum exchange $\boldsymbol{q}$. We specifically expand the following term from Eq. (D.3) of the collision integral

$$\begin{aligned}\frac{\tilde{p}^2 - \tilde{\boldsymbol{p}}\cdot\tilde{\boldsymbol{q}}}{|\tilde{\boldsymbol{p}}-\tilde{\boldsymbol{q}}|^2}\tilde{\psi}_I(\tilde{p},\Delta\tilde{t}) &= \tilde{\psi}(\tilde{p}) + \frac{q\cos\theta}{\tilde{p}}\left[\tilde{\psi}(\tilde{p}) - \tilde{p}\tilde{\psi}'(\tilde{p})\right] \\ &+ \frac{q^2}{2\tilde{p}^2}\left[(4\cos^2\theta - 2)\tilde{\psi}(\tilde{p}) + (\tilde{p} - 3\tilde{p}\cos^2\theta)\tilde{\psi}'(\tilde{p}) + \tilde{p}^2\cos^2\theta\tilde{\psi}''(\tilde{p})\right] \ ,\end{aligned} \tag{D.7}$$

where θ is the angle between $\tilde{\boldsymbol{p}}$ and $\tilde{\boldsymbol{q}}$. Plugging the expansion to the collision integral and performing the angular integral, we find

$$\begin{aligned}C_{\text{soft}}[\tilde{\psi}_I] &= \tilde{\psi}(p)\left(I_1^{(0)}(p) - I_1^{(2)}(p) + I_2(p) + 2I_3(p)\right) \\ &+ \frac{p}{2}\tilde{\psi}_I'(p)\left(I_1^{(2)}(p) - 2I_2(p) - 3I_3(p)\right) + \frac{p^2}{2}\tilde{\psi}_I''(p)I_3(p) \ ,\end{aligned} \tag{D.8}$$

where I_i are the following integral moments

$$I_1^{(0)}(p) = \int_0^{q^*} dq\ q\ n \left[C_1 C(q) + \frac{C_z}{z^2} C\left(\frac{q}{z}\right) + \frac{C_{1-z}}{1-z} C\left(\frac{q}{1-z}\right) \right] \left[1 - e^{-i\Delta t \frac{q^2}{2Pz(1-z)}} \mathcal{J}_0\left(\Delta t \frac{pq}{Pz(1-z)}\right) \right] , \tag{D.9}$$

$$I_1^{(2)}(p) = \int_0^{q^*} dq\ [..] \frac{q^2}{p^2} e^{-i\Delta t \frac{q^2}{2Pz(1-z)}} \mathcal{J}_0\left(\Delta t \frac{pq}{Pz(1-z)}\right) , \tag{D.10}$$

$$I_2(p) = \int_0^{q^*} dq\ [..] \frac{q}{p} i e^{-i\Delta t \frac{q^2}{2Pz(1-z)}} \mathcal{J}_1\left(\Delta t \frac{pq}{Pz(1-z)}\right) , \tag{D.11}$$

$$I_3(p) = \int_0^{q^*} dq\ [..] \frac{q^2}{p^2} e^{-i\Delta t \frac{q^2}{2Pz(1-z)}} \left[\frac{Pz(1-z)}{\Delta t pq} \mathcal{J}_1\left(\Delta t \frac{pq}{Pz(1-z)}\right) - \mathcal{J}_2\left(\Delta t \frac{pq}{Pz(1-z)}\right) \right] . \tag{D.12}$$

These integrals are then performed numerically and together with the hard component will make up the full collision integral in Eq. D.3, which can be used to evolve the wave function.

Bibliography

[1] Guy D. Moore and Niels Schlusser. "Full O(a) improvement in electrostatic QCD". In: *Phys. Rev.* D100.3 (2019), p. 034510. DOI: 10.1103/PhysRevD.100.034510. arXiv: 1905.09708 [hep-lat].

[2] Guy D. Moore and Niels Schlusser. "Transverse momentum broadening from the lattice". In: *Phys. Rev.* D101.1 (2020), p. 014505. DOI: 10.1103/PhysRevD.101.014505. arXiv: 1911.13127 [hep-lat].

[3] Soeren Schlichting and Ismail Soudi. "Medium-induced fragmentation and equilibration of highly energetic partons". en. In: *Journal of High Energy Physics* 2021.7 (July 2021), p. 77. ISSN: 1029-8479. DOI: 10.1007/JHEP07(2021)077.

[4] Guy D. Moore et al. "Non-perturbative determination of collisional broadening and medium induced radiation in QCD plasmas". In: (May 2021). arXiv: 2105.01679 [hep-ph].

[5] Soeren Schlichting and Ismail Soudi. "Energy loss and equilibration of jets in a QCD plasma". In: *10th International Conference on Hard and Electromagnetic Probes of High-Energy Nuclear Collisions: Hard Probes 2020*. Sept. 2020. arXiv: 2009.02973 [hep-ph].

[6] Richard P Feynman. *Photon-hadron interactions*. CRC Press, 2018.

[7] Michael E. Peskin and Daniel V. Schroeder. *An Introduction to quantum field theory*. Reading, USA: Addison-Wesley, 1995. ISBN: 978-0-201-50397-5.

[8] David J. Gross and Frank Wilczek. "Ultraviolet Behavior of Nonabelian Gauge Theories". In: *Phys. Rev. Lett.* 30 (1973). Ed. by J. C. Taylor, pp. 1343–1346. DOI: 10.1103/PhysRevLett.30.1343.

[9] H. David Politzer. "Reliable Perturbative Results for Strong Interactions?" In: *Phys. Rev. Lett.* 30 (1973). Ed. by J. C. Taylor, pp. 1346–1349. DOI: 10.1103/PhysRevLett.30.1346.

[10] Y. Aoki et al. "The Order of the quantum chromodynamics transition predicted by the standard model of particle physics". In: *Nature* 443 (2006), pp. 675–678. DOI: 10.1038/nature05120. arXiv: hep-lat/0611014.

[11] Johannes Kirsch et al., eds. *Discoveries at the Frontiers of Science: From Nuclear Astrophysics to Relativistic Heavy Ion Collisions*. Vol. 6/2020. FIAS Interdisciplinary Science Series. Mar. 2020. ISBN: 978-3-030-34233-3, 978-3-030-34234-0. DOI: 10.1007/978-3-030-34234-0.

[12] Dominik J. Schwarz. "The first second of the universe". In: *Annalen Phys.* 12 (2003), pp. 220–270. DOI: 10.1002/andp.200310010. arXiv: astro-ph/0303574.

[13] Rudolf Baier et al. "Relativistic viscous hydrodynamics, conformal invariance, and holography". In: *JHEP* 04 (2008), p. 100. DOI: 10.1088/1126-6708/2008/04/100. arXiv: 0712.2451 [hep-th].

[14] Bjoern Schenke, Sangyong Jeon, and Charles Gale. "(3+1)D hydrodynamic simulation of relativistic heavy-ion collisions". In: *Phys. Rev. C* 82 (2010), p. 014903. DOI: 10.1103/PhysRevC.82.014903. arXiv: 1004.1408 [hep-ph].

[15] Edmond Iancu. "QCD in heavy ion collisions". In: *2011 European School of High-Energy Physics*. May 2012. DOI: 10.5170/CERN-2014-003.197. arXiv: 1205.0579 [hep-ph].

[16] Xin-Nian Wang, ed. *Quark-Gluon Plasma 5*. New Jersey: World Scientific, 2016. ISBN: 978-981-4663-70-0. DOI: 10.1142/9533.

[17] J.D. Bjorken. "Energy Loss of Energetic Partons in Quark - Gluon Plasma: Possible Extinction of High p(t) Jets in Hadron - Hadron Collisions". In: (Aug. 1982).

[18] G. Kramer. *THEORY OF JETS IN ELECTRON POSITRON ANNIHILATION*. Vol. 102. 1984.

[19] R. Keith Ellis, W. James Stirling, and B. R. Webber. *QCD and collider physics*. Vol. 8. Cambridge University Press, Feb. 2011. ISBN: 978-0-511-82328-2, 978-0-521-54589-1.

[20] Ahmed Ali and Gustav Kramer. "Jets and QCD: A Historical Review of the Discovery of the Quark and Gluon Jets and its Impact on QCD". In: *Eur. Phys. J. H* 36 (2011), pp. 245–326. DOI: 10.1140/epjh/e2011-10047-1. arXiv: 1012.2288 [hep-ph].

[21] Urs Achim Wiedemann. "Jet Quenching in Heavy Ion Collisions". In: *Landolt-Bornstein* 23 (2010). Ed. by R. Stock, p. 521. DOI: 10.1007/978-3-642-01539-7_17. arXiv: 0908.2306 [hep-ph].

[22] A. Majumder and M. Van Leeuwen. "The Theory and Phenomenology of Perturbative QCD Based Jet Quenching". In: *Prog. Part. Nucl. Phys.* 66 (2011), pp. 41–92. DOI: 10.1016/j.ppnp.2010.09.001. arXiv: 1002.2206 [hep-ph].

[23] Yacine Mehtar-Tani, Jose Guilherme Milhano, and Konrad Tywoniuk. "Jet physics in heavy-ion collisions". In: *Int. J. Mod. Phys. A* 28 (2013), p. 1340013. DOI: 10.1142/S0217751X13400137. arXiv: 1302.2579 [hep-ph].

[24] Shanshan Cao and Xin-Nian Wang. "Jet quenching and medium response in high-energy heavy-ion collisions: a review". In: (Feb. 2020). arXiv: 2002.04028 [hep-ph].

[25] Eric Braaten and Markus H. Thoma. "Energy loss of a heavy quark in the quark - gluon plasma". In: *Phys. Rev. D* 44.9 (1991), R2625. DOI: 10.1103/PhysRevD.44.R2625.

[26] Eric Braaten and Markus H. Thoma. "Energy loss of a heavy fermion in a hot plasma". In: *Phys. Rev. D* 44 (1991), pp. 1298–1310. DOI: 10.1103/PhysRevD.44.1298.

[27] R. Baier et al. "Radiative energy loss of high-energy quarks and gluons in a finite volume quark - gluon plasma". In: *Nucl. Phys. B* 483 (1997), pp. 291–320. DOI: 10.1016/S0550-3213(96)00553-6. arXiv: hep-ph/9607355.

[28] R. Baier, D. Schiff, and B. G. Zakharov. "Energy loss in perturbative QCD". In: *Ann. Rev. Nucl. Part. Sci.* 50 (2000), pp. 37–69. DOI: 10.1146/annurev.nucl.50.1.37. arXiv: hep-ph/0002198 [hep-ph].

[29] Jean-Paul Blaizot, Edmond Iancu, and Yacine Mehtar-Tani. "Medium-induced QCD cascade: democratic branching and wave turbulence". In: *Phys. Rev. Lett.* 111 (2013), p. 052001. DOI: 10.1103/PhysRevLett.111.052001. arXiv: 1301.6102 [hep-ph].

[30] Yacine Mehtar-Tani and Soeren Schlichting. "Universal quark to gluon ratio in medium-induced parton cascade". In: *JHEP* 09 (2018), p. 144. DOI: 10.1007/JHEP09(2018)144. arXiv: 1807.06181 [hep-ph].

[31] Peter Brockway Arnold, Guy D. Moore, and Laurence G. Yaffe. "Effective kinetic theory for high temperature gauge theories". In: *JHEP* 01 (2003), p. 030. DOI: 10.1088/1126-6708/2003/01/030. arXiv: hep-ph/0209353 [hep-ph].

[32] Jean-Paul Blaizot and Yacine Mehtar-Tani. "Energy flow along the medium-induced parton cascade". In: *Annals Phys.* 368 (2016), pp. 148–176. DOI: 10.1016/j.aop.2016.01.002. arXiv: 1501.03443 [hep-ph].

[33] Souvik Priyam Adhya et al. "Medium-induced cascade in expanding media". In: *JHEP* 07 (2020), p. 150. DOI: 10.1007/JHEP07(2020)150. arXiv: 1911.12193 [hep-ph].

[34] Soeren Schlichting and Derek Teaney. "The First fm/c of Heavy-Ion Collisions". In: *Ann. Rev. Nucl. Part. Sci.* 69 (2019), pp. 447–476. DOI: 10.1146/annurev-nucl-101918-023825. arXiv: 1908.02113 [nucl-th].

[35] Aleksi Kurkela and Egang Lu. "Approach to Equilibrium in Weakly Coupled Non-Abelian Plasmas". In: *Phys. Rev. Lett.* 113.18 (2014), p. 182301. DOI: 10.1103/PhysRevLett.113.182301. arXiv: 1405.6318 [hep-ph].

[36] R. Baier et al. "'Bottom up' thermalization in heavy ion collisions". In: *Phys. Lett. B* 502 (2001), pp. 51–58. DOI: 10.1016/S0370-2693(01)00191-5. arXiv: hep-ph/0009237.

[37] Aleksi Kurkela and Aleksas Mazeliauskas. "Chemical equilibration in weakly coupled QCD". In: *Phys. Rev. D* 99.5 (2019), p. 054018. DOI: 10.1103/PhysRevD.99.054018. arXiv: 1811.03068 [hep-ph].

[38] Aleksi Kurkela et al. "Matching the Nonequilibrium Initial Stage of Heavy Ion Collisions to Hydrodynamics with QCD Kinetic Theory". In: *Phys. Rev. Lett.* 122.12 (2019), p. 122302. DOI: 10.1103/PhysRevLett.122.122302. arXiv: 1805.01604 [hep-ph].

[39] M. Tanabashi et al. "Review of Particle Physics". In: *Phys. Rev. D* 98.3 (2018), p. 030001. DOI: 10.1103/PhysRevD.98.030001.

[40] J. I. Kapusta and Charles Gale. *Finite-temperature field theory: Principles and applications*. Cambridge Monographs on Mathematical Physics. Cambridge University Press, 2011. ISBN: 978-0-521-17322-3, 978-0-521-82082-0, 978-0-511-22280-1. DOI: 10.1017/CBO9780511535130.

[41] Kenneth G. Wilson. "Confinement of Quarks". In: *Phys. Rev. D* 10 (1974). Ed. by J. C. Taylor, pp. 2445–2459. DOI: 10.1103/PhysRevD.10.2445.

[42] M. Creutz. "Monte Carlo Study of Quantized SU(2) Gauge Theory". In: *Phys. Rev. D* 21 (1980), pp. 2308–2315. DOI: 10.1103/PhysRevD.21.2308.

[43] A. Bazavov et al. "Equation of state in (2+1)-flavor QCD". In: *Phys. Rev. D* 90 (2014), p. 094503. DOI: 10.1103/PhysRevD.90.094503. arXiv: 1407.6387 [hep-lat].

[44] Matthias Troyer and Uwe-Jens Wiese. "Computational complexity and fundamental limitations to fermionic quantum Monte Carlo simulations". In: *Phys. Rev. Lett.* 94 (2005), p. 170201. DOI: 10.1103/PhysRevLett.94.170201. arXiv: cond-mat/0408370.

[45] Philippe de Forcrand. "Simulating QCD at finite density". In: *PoS* LAT2009 (2009). Ed. by Chuan Liu and Yu Zhu, p. 010. DOI: 10.22323/1.091.0010. arXiv: 1005.0539 [hep-lat].

[46] Sz. Borsanyi et al. "QCD equation of state at nonzero chemical potential: continuum results with physical quark masses at order mu^2". In: *JHEP* 08 (2012), p. 053. DOI: 10.1007/JHEP08(2012)053. arXiv: 1204.6710 [hep-lat].

[47] Thomas Appelquist and Robert D. Pisarski. "High-Temperature Yang-Mills Theories and Three-Dimensional Quantum Chromodynamics". In: *Phys. Rev.* D23 (1981), p. 2305. DOI: 10.1103/PhysRevD.23.2305.

[48] Sudhir Nadkarni. "Dimensional Reduction in Hot QCD". In: *Phys. Rev.* D27 (1983), p. 917. DOI: 10.1103/PhysRevD.27.917.

[49] Andrei D. Linde. "Infrared Problem in Thermodynamics of the Yang-Mills Gas". In: *Phys. Lett.* 96B (1980), pp. 289–292. DOI: 10.1016/0370-2693(80)90769-8.

[50] Mikko Laine and Aleksi Vuorinen. *Basics of Thermal Field Theory*. Vol. 925. Springer, 2016. DOI: 10.1007/978-3-319-31933-9. arXiv: 1701.01554 [hep-ph].

[51] Eric Braaten and Agustin Nieto. "Free energy of QCD at high temperature". In: *Phys. Rev. D* 53 (1996), pp. 3421–3437. DOI: 10.1103/PhysRevD.53.3421. arXiv: hep-ph/9510408.

[52] K. Kajantie et al. "The Pressure of hot QCD up to g6 ln(1/g)". In: *Phys. Rev.* D67 (2003), p. 105008. DOI: 10.1103/PhysRevD.67.105008. arXiv: hep-ph/0211321 [hep-ph].

[53] Marco Panero, Kari Rummukainen, and Andreas Schäfer. "Lattice Study of the Jet Quenching Parameter". In: *Phys. Rev. Lett.* 112.16 (2014), p. 162001. DOI: 10.1103/PhysRevLett.112.162001. arXiv: 1307.5850 [hep-ph].

[54] Michela D'Onofrio, Aleksi Kurkela, and Guy D. Moore. "Renormalization of Null Wilson Lines in EQCD". In: *JHEP* 03 (2014), p. 125. DOI: 10.1007/JHEP03(2014)125. arXiv: 1401.7951 [hep-lat].

[55] Guy D. Moore and Niels Schlusser. "The nonperturbative contribution to asymptotic masses". In: *Phys. Rev. D* 102.9 (2020), p. 094512. DOI: 10.1103/PhysRevD.102.094512. arXiv: 2009.06614 [hep-lat].

[56] Siegfried Bethke. "Experimental tests of asymptotic freedom". In: *Prog. Part. Nucl. Phys.* 58 (2007), pp. 351–386. DOI: 10.1016/j.ppnp.2006.06.001. arXiv: hep-ex/0606035.

[57] Alexandre Deur, Stanley J. Brodsky, and Guy F. de Teramond. "The QCD Running Coupling". In: *Nucl. Phys.* 90 (2016), p. 1. DOI: 10.1016/j.ppnp.2016.04.003. arXiv: 1604.08082 [hep-ph].

[58] Philippe Gros. "Identifying charged hadrons on the relativistic rise using the ALICE TPC at LHC". PhD thesis. Lund U., 2011.

[59] Li Yi. "Study of quark gluon plasma by particle correlations in heavy ion collisions". PhD thesis. Purdue U., 2014. DOI: 10.1007/978-1-4939-6487-1.

[60] Helmut Satz. *Extreme states of matter in strong interaction physics. An introduction*. Vol. 841. New York: Springer Verlag, 2012. ISBN: 978-3-642-23907-6. DOI: 10.1007/978-3-642-23908-3.

[61] Robert D. Pisarski. "Computing Finite Temperature Loops with Ease". In: *Nucl. Phys. B* 309 (1988), pp. 476–492. DOI: 10.1016/0550-3213(88)90454-3.

[62] Eric Braaten and Robert D. Pisarski. "Soft Amplitudes in Hot Gauge Theories: A General Analysis". In: *Nucl. Phys. B* 337 (1990), pp. 569–634. DOI: 10.1016/0550-3213(90)90508-B.

[63] Jens O. Andersen, Eric Braaten, and Michael Strickland. "Hard thermal loop resummation of the free energy of a hot gluon plasma". In: *Phys. Rev. Lett.* 83 (1999), pp. 2139–2142. DOI: 10.1103/PhysRevLett.83.2139. arXiv: hep-ph/9902327.

[64] Jean-Paul Blaizot and Edmond Iancu. "The Quark gluon plasma: Collective dynamics and hard thermal loops". In: *Phys. Rept.* 359 (2002), pp. 355–528. DOI: 10.1016/S0370-1573(01)00061-8. arXiv: hep-ph/0101103.

[65] Peter Brockway Arnold, Guy D Moore, and Laurence G. Yaffe. "Transport coefficients in high temperature gauge theories. 2. Beyond leading log". In: *JHEP* 05 (2003), p. 051. DOI: 10.1088/1126-6708/2003/05/051. arXiv: hep-ph/0302165.

[66] K.J.H. Phillips. *Guide to the Sun*. Cambridge University Press, 1995. ISBN: 9780521397889. URL: https://books.google.de/books?id=idwBChjVP0gC.

[67] Mohamed Abdallah et al. "Measurement of the sixth-order cumulant of net-proton multiplicity distributions in Au+Au collisions at $\sqrt{s_{NN}} = 27$, 54.4, and 200 GeV at RHIC". In: (May 2021). arXiv: 2105.14698 [nucl-ex].

[68] Andrea Dainese et al., eds. *Report on the Physics at the HL-LHC,and Perspectives for the HE-LHC*. Vol. 7/2019. CERN Yellow Reports: Monographs. Geneva, Switzerland: CERN, 2019. ISBN: 978-92-9083-549-3. DOI: 10.23731/CYRM-2019-007.

[69] Francois Gelis et al. "The Color Glass Condensate". In: *Ann. Rev. Nucl. Part. Sci.* 60 (2010), pp. 463–489. DOI: 10.1146/annurev.nucl.010909.083629. arXiv: 1002.0333 [hep-ph].

[70] F. Gelis. "Color Glass Condensate and Glasma". In: *Int. J. Mod. Phys. A* 28 (2013), p. 1330001. DOI: 10.1142/S0217751X13300019. arXiv: 1211.3327 [hep-ph].

[71] Aleksi Kurkela and Guy D. Moore. "Thermalization in Weakly Coupled Nonabelian Plasmas". In: *JHEP* 12 (2011), p. 044. DOI: 10.1007/JHEP12(2011)044. arXiv: 1107.5050 [hep-ph].

[72] Aleksi Kurkela et al. "Effective kinetic description of event-by-event pre-equilibrium dynamics in high-energy heavy-ion collisions". In: *Phys. Rev. C* 99.3 (2019), p. 034910. DOI: 10.1103/PhysRevC.99.034910. arXiv: 1805.00961 [hep-ph].

[73] Xiaojian Du and Sören Schlichting. "Equilibration of weakly coupled QCD plasmas". In: (Dec. 2020). arXiv: 2012.09079 [hep-ph].

[74] Björn Schenke. "The smallest fluid on earth". In: (Feb. 2021). arXiv: 2102.11189 [nucl-th].

[75] Guido Altarelli and G. Parisi. "Asymptotic Freedom in Parton Language". In: *Nucl. Phys. B* 126 (1977), pp. 298–318. DOI: 10.1016/0550-3213(77)90384-4.

[76] V.N. Gribov and L.N. Lipatov. "Deep inelastic e p scattering in perturbation theory". In: *Sov. J. Nucl. Phys.* 15 (1972), pp. 438–450.

[77] Jean-Paul Blaizot and Yacine Mehtar-Tani. "Jet Structure in Heavy Ion Collisions". In: *Int. J. Mod. Phys. E* 24.11 (2015), p. 1530012. DOI: 10.1142/S021830131530012X. arXiv: 1503.05958 [hep-ph].

[78] Abhijit Majumder. "Incorporating Space-Time Within Medium-Modified Jet Event Generators". In: *Phys. Rev. C* 88 (2013), p. 014909. DOI: 10.1103/PhysRevC.88.014909. arXiv: 1301.5323 [nucl-th].

[79] Nestor Armesto, Leticia Cunqueiro, and Carlos A. Salgado. "Q-PYTHIA: A Medium-modified implementation of final state radiation". In: *Eur. Phys. J. C* 63 (2009), pp. 679–690. DOI: 10.1140/epjc/s10052-009-1133-9. arXiv: 0907.1014 [hep-ph].

[80] Thorsten Renk. "A Comparison study of medium-modified QCD shower evolution scenarios". In: *Phys. Rev. C* 79 (2009), p. 054906. DOI: 10.1103/PhysRevC.79.054906. arXiv: 0901.2818 [hep-ph].

[81] Jorge Casalderrey-Solana et al. "New picture of jet quenching dictated by color coherence". In: *Phys. Lett. B* 725 (2013), pp. 357–360. DOI: 10.1016/j.physletb.2013.07.046. arXiv: 1210.7765 [hep-ph].

[82] Yacine Mehtar-Tani and Konrad Tywoniuk. "Sudakov suppression of jets in QCD media". In: *Phys. Rev. D* 98.5 (2018), p. 051501. DOI: 10.1103/PhysRevD.98.051501. arXiv: 1707.07361 [hep-ph].

[83] P. Caucal et al. "Vacuum-like jet fragmentation in a dense QCD medium". In: *Phys. Rev. Lett.* 120 (2018), p. 232001. DOI: 10.1103/PhysRevLett.120.232001. arXiv: 1801.09703 [hep-ph].

[84] Yacine Mehtar-Tani and Konrad Tywoniuk. "Jet (de)coherence in Pb–Pb collisions at the LHC". In: *Phys. Lett. B* 744 (2015), pp. 284–287. DOI: 10.1016/j.physletb.2015.03.041. arXiv: 1401.8293 [hep-ph].

[85] Xin-Nian Wang. "Effect of jet quenching on high p_T hadron spectra in high-energy nuclear collisions". In: *Phys. Rev. C* 58 (1998), p. 2321. DOI: 10.1103/PhysRevC.58.2321. arXiv: hep-ph/9804357.

[86] Michael L. Miller et al. "Glauber modeling in high energy nuclear collisions". In: *Ann. Rev. Nucl. Part. Sci.* 57 (2007), pp. 205–243. DOI: 10.1146/annurev.nucl.57.090506.123020. arXiv: nucl-ex/0701025.

[87] Serguei Chatrchyan et al. "Study of high-pT charged particle suppression in PbPb compared to *pp* collisions at $\sqrt{s_{NN}} = 2.76$ TeV". In: *Eur. Phys. J. C* 72 (2012), p. 1945. DOI: 10.1140/epjc/s10052-012-1945-x. arXiv: 1202.2554 [nucl-ex].

[88] David d'Enterria. "Jet quenching". In: *Landolt-Bornstein* 23 (2010). Ed. by R. Stock, p. 471. DOI: 10.1007/978-3-642-01539-7_16. arXiv: 0902.2011 [nucl-ex].

[89] Shreyasi Acharya et al. "Measurements of inclusive jet spectra in pp and central Pb-Pb collisions at $\sqrt{s_{\mathrm{NN}}} = 5.02$ TeV". In: *Phys. Rev. C* 101.3 (2020), p. 034911. DOI: 10.1103/PhysRevC.101.034911. arXiv: 1909.09718 [nucl-ex].

[90] Gavin P. Salam. "Towards Jetography". In: *Eur. Phys. J. C* 67 (2010), pp. 637–686. DOI: 10.1140/epjc/s10052-010-1314-6. arXiv: 0906.1833 [hep-ph].

[91] Matteo Cacciari, Gavin P. Salam, and Gregory Soyez. "FastJet User Manual". In: *Eur. Phys. J. C* 72 (2012), p. 1896. DOI: 10.1140/epjc/s10052-012-1896-2. arXiv: 1111.6097 [hep-ph].

[92] Simone Marzani, Gregory Soyez, and Michael Spannowsky. *Looking inside jets: an introduction to jet substructure and boosted-object phenomenology*. Vol. 958. Springer, 2019. DOI: 10.1007/978-3-030-15709-8. arXiv: 1901.10342 [hep-ph].

[93] Morad Aaboud et al. "Measurement of jet fragmentation in Pb+Pb and *pp* collisions at $\sqrt{s_{NN}} = 5.02$ TeV with the ATLAS detector". In: *Phys. Rev. C* 98.2 (2018), p. 024908. DOI: 10.1103/PhysRevC.98.024908. arXiv: 1805.05424 [nucl-ex].

[94] Martin Spousta and Brian Cole. "Interpreting single jet measurements in Pb + Pb collisions at the LHC". In: *Eur. Phys. J. C* 76.2 (2016), p. 50. DOI: 10.1140/epjc/s10052-016-3896-0. arXiv: 1504.05169 [hep-ph].

[95] Yasuki Tachibana et al. "Jet substructure modifications in a QGP from multi-scale description of jet evolution with JETSCAPE". In: *PoS* HardProbes2018 (2018). Ed. by David d'Enterria, Andreas Morsch, and Philippe Crochet, p. 099. DOI: 10.22323/1.345.0099. arXiv: 1812.06366 [nucl-th].

[96] Karen M. Burke et al. "Extracting the jet transport coefficient from jet quenching in high-energy heavy-ion collisions". In: *Phys. Rev. C* 90.1 (2014), p. 014909. DOI: 10.1103/PhysRevC.90.014909. arXiv: 1312.5003 [nucl-th].

[97] Ron Soltz. "Bayesian extraction of $\hat{q}$ with multi-stage jet evolution approach". In: *PoS* HardProbes2018 (2019). Ed. by David d'Enterria, Andreas Morsch, and Philippe Crochet, p. 048. DOI: 10.22323/1.345.0048.

[98] Rashmi C. Desai. "Noëlle Pottier: Nonequilibrium Statistical Physics, Linear Irreversible Processes". en. In: *Journal of Statistical Physics* 142.2 (Jan. 2011), pp. 439–440. ISSN: 1572-9613. DOI: 10.1007/s10955-010-0114-6. URL: https://doi.org/10.1007/s10955-010-0114-6 (visited on 07/16/2021).

[99] Jean-Paul Blaizot, Bin Wu, and Li Yan. "Quark production, Bose–Einstein condensates and thermalization of the quark–gluon plasma". In: *Nucl. Phys.* A930 (2014), pp. 139–162. DOI: 10.1016/j.nuclphysa.2014.07.041. arXiv: 1402.5049 [hep-ph].

[100] Jacopo Ghiglieri, Guy D. Moore, and Derek Teaney. "Jet-Medium Interactions at NLO in a Weakly-Coupled Quark-Gluon Plasma". In: *JHEP* 03 (2016), p. 095. DOI: 10.1007/JHEP03(2016)095. arXiv: 1509.07773 [hep-ph].

[101] Sangyong Jeon and Guy D. Moore. "Energy loss of leading partons in a thermal QCD medium". In: *Phys. Rev. C* 71 (2005), p. 034901. DOI: 10.1103/PhysRevC.71.034901. arXiv: hep-ph/0309332.

[102] M. Gyulassy, P. Levai, and I. Vitev. "NonAbelian energy loss at finite opacity". In: *Phys. Rev. Lett.* 85 (2000), pp. 5535–5538. DOI: 10.1103/PhysRevLett.85.5535. arXiv: nucl-th/0005032.

[103] Urs Achim Wiedemann. "Gluon radiation off hard quarks in a nuclear environment: Opacity expansion". In: *Nucl. Phys. B* 588 (2000), pp. 303–344. DOI: 10.1016/S0550-3213(00)00457-0. arXiv: hep-ph/0005129.

[104] Peter Brockway Arnold. "Quark-Gluon Plasmas and Thermalization". In: *Int. J. Mod. Phys. E* 16 (2007). Ed. by Debora Peres Menezes et al., pp. 2555–2594. DOI: 10.1142/S021830130700832X. arXiv: 0708.0812 [hep-ph].

[105] Guang-You Qin and Xin-Nian Wang. "Jet quenching in high-energy heavy-ion collisions". In: *Int. J. Mod. Phys. E* 24.11 (2015). Ed. by Xin-Nian Wang, p. 1530014. DOI: 10.1142/S0218301315300143. arXiv: 1511.00790 [hep-ph].

[106] L. D. Landau and I. Pomeranchuk. "Limits of applicability of the theory of bremsstrahlung electrons and pair production at high-energies". In: *Dokl. Akad. Nauk Ser. Fiz.* 92 (1953), pp. 535–536.

[107] A. B. Migdal. "Bremsstrahlung and pair production in condensed media at high-energies". In: *Phys. Rev.* 103 (1956), pp. 1811–1820. DOI: 10.1103/PhysRev.103.1811.

[108] R. Baier et al. "Radiative energy loss and p(T) broadening of high-energy partons in nuclei". In: *Nucl. Phys. B* 484 (1997), pp. 265–282. DOI: 10.1016/S0550-3213(96)00581-0. arXiv: hep-ph/9608322.

[109] B. G. Zakharov. "Fully quantum treatment of the Landau-Pomeranchuk-Migdal effect in QED and QCD". In: *JETP Lett.* 63 (1996), pp. 952–957. DOI: 10.1134/1.567126. arXiv: hep-ph/9607440.

[110] B. G. Zakharov. "Radiative energy loss of high-energy quarks in finite size nuclear matter and quark - gluon plasma". In: *JETP Lett.* 65 (1997), pp. 615–620. DOI: 10.1134/1.567389. arXiv: hep-ph/9704255.

[111] B. G. Zakharov. "Light cone path integral approach to the Landau-Pomeranchuk-Migdal effect". In: *Phys. Atom. Nucl.* 61 (1998). [Yad. Fiz.61,924(1998)], pp. 838–854. arXiv: hep-ph/9807540 [hep-ph].

[112] Jean-Paul Blaizot et al. "Medium-induced gluon branching". In: *JHEP* 01 (2013), p. 143. DOI: 10.1007/JHEP01(2013)143. arXiv: 1209.4585 [hep-ph].

[113] Nestor Armesto et al. "Comparison of Jet Quenching Formalisms for a Quark-Gluon Plasma 'Brick'". In: *Phys. Rev. C* 86 (2012), p. 064904. DOI: 10.1103/PhysRevC.86.064904. arXiv: 1106.1106 [hep-ph].

[114] Miklos Gyulassy, Peter Levai, and Ivan Vitev. "Jet quenching in thin quark gluon plasmas. 1. Formalism". In: *Nucl. Phys. B* 571 (2000), pp. 197–233. DOI: 10.1016/S0550-3213(99)00713-0. arXiv: hep-ph/9907461.

[115] M. Gyulassy, P. Levai, and I. Vitev. "Reaction operator approach to non-Abelian energy loss". In: *Nucl. Phys. B* 594 (2001), pp. 371–419. DOI: 10.1016/S0550-3213(00)00652-0. arXiv: nucl-th/0006010.

[116] Peter Brockway Arnold. "Simple Formula for High-Energy Gluon Bremsstrahlung in a Finite, Expanding Medium". In: *Phys. Rev.* D79 (2009), p. 065025. DOI: 10.1103/PhysRevD.79.065025. arXiv: 0808.2767 [hep-ph].

[117] Yacine Mehtar-Tani. "Gluon bremsstrahlung in finite media beyond multiple soft scattering approximation". In: *JHEP* 07 (2019), p. 057. DOI: 10.1007/JHEP07(2019)057. arXiv: 1903.00506 [hep-ph].

[118] Yacine Mehtar-Tani and Konrad Tywoniuk. "Improved opacity expansion for medium-induced parton splitting". In: *JHEP* 06 (2020), p. 187. DOI: 10.1007/JHEP06(2020)187. arXiv: 1910.02032 [hep-ph].

[119] João Barata and Yacine Mehtar-Tani. "Improved opacity expansion at NNLO for medium induced gluon radiation". In: (Apr. 2020). arXiv: 2004.02323 [hep-ph].

[120] Carlota Andres, Liliana Apolinário, and Fabio Dominguez. "Medium-induced gluon radiation with full resummation of multiple scatterings for realistic parton-medium interactions". In: (Feb. 2020). DOI: 10.1007/JHEP07(2020)114. arXiv: 2002.01517 [hep-ph].

[121] Simon Caron-Huot and Charles Gale. "Finite-size effects on the radiative energy loss of a fast parton in hot and dense strongly interacting matter". In: *Phys. Rev. C* 82 (2010), p. 064902. DOI: 10.1103/PhysRevC.82.064902. arXiv: 1006.2379 [hep-ph].

[122] Alexey Anisimov, Denis Besak, and Dietrich Bodeker. "Thermal production of relativistic Majorana neutrinos: Strong enhancement by multiple soft scattering". In: *JCAP* 03 (2011), p. 042. DOI: 10.1088/1475-7516/2011/03/042. arXiv: 1012.3784 [hep-ph].

[123] Sergey Nazarenko. *Wave turbulence*. Springer, 2011.

[124] Vladimir E Zakharov, Victor S L'vov, and Gregory Falkovich. *Kolmogorov spectra of turbulence I: Wave turbulence*. Springer Science & Business Media, 2012.

[125] Uriel Frisch and Andreĭ Nikolaevich Kolmogorov. *Turbulence: The Legacy of A. N. Kolmogorov*. en. Cambridge University Press, Nov. 1995. ISBN: 9780521457132.

[126] Isara Chantesana. "Strong Wave Turbulence and Non-Thermal Fixed Points in a Kinetic Theory". PhD thesis. U. Heidelberg (main), 2018. DOI: 10.11588/heidok.00024189.

[127] Sergey Nazarenko and Sergei Lukaschuk. "Wave Turbulence on Water Surface". In: *Annual Review of Condensed Matter Physics* 7.1 (2016), pp. 61–88. DOI: 10.1146/annurev-conmatphys-071715-102737. eprint: https://doi.org/10.1146/annurev-conmatphys-071715-102737. URL: https://doi.org/10.1146/annurev-conmatphys-071715-102737.

[128] Jurgen Berges and Denes Sexty. "Strong versus weak wave-turbulence in relativistic field theory". In: *Phys. Rev. D* 83 (2011), p. 085004. DOI: 10.1103/PhysRevD.83.085004. arXiv: 1012.5944 [hep-ph].

[129] J. Berges et al. "Turbulent thermalization process in heavy-ion collisions at ultrarelativistic energies". In: *Phys. Rev. D* 89.7 (2014), p. 074011. DOI: 10.1103/PhysRevD.89.074011. arXiv: 1303.5650 [hep-ph].

[130] Jürgen Berges et al. "Turbulent thermalization process in high-energy heavy-ion collisions". In: *Nucl. Phys. A* 931 (2014). Ed. by Peter Braun-Munzinger, Bengt Friman, and Johanna Stachel, pp. 348–353. DOI: 10.1016/j.nuclphysa.2014.08.103. arXiv: 1409.1638 [hep-ph].

[131] Jürgen Berges et al. "Thermalization in QCD: theoretical approaches, phenomenological applications, and interdisciplinary connections". In: (May 2020). arXiv: 2005.12299 [hep-th].

[132] Aleksi Kurkela and Urs Achim Wiedemann. "Picturing perturbative parton cascades in QCD matter". In: *Phys. Lett. B* 740 (2015), pp. 172–178. DOI: 10.1016/j.physletb.2014.11.054. arXiv: 1407.0293 [hep-ph].

[133] Peter Brockway Arnold and Caglar Dogan. "QCD Splitting/Joining Functions at Finite Temperature in the Deep LPM Regime". In: *Phys. Rev. D* 78 (2008), p. 065008. DOI: 10.1103/PhysRevD.78.065008. arXiv: 0804.3359 [hep-ph].

[134] Jacopo Ghiglieri, Guy D. Moore, and Derek Teaney. "Second-order Hydrodynamics in Next-to-Leading-Order QCD". In: *Phys. Rev. Lett.* 121.5 (2018), p. 052302. DOI: 10.1103/PhysRevLett.121.052302. arXiv: 1805.02663 [hep-ph].

[135] Kevin Dusling, Guy D. Moore, and Derek Teaney. "Radiative energy loss and v(2) spectra for viscous hydrodynamics". In: *Phys. Rev. C* 81 (2010), p. 034907. DOI: 10.1103/PhysRevC.81.034907. arXiv: 0909.0754 [nucl-th].

[136] Peter Brockway Arnold, Guy D. Moore, and Laurence G. Yaffe. "Photon and gluon emission in relativistic plasmas". In: *JHEP* 06 (2002), p. 030. DOI: 10.1088/1126-6708/2002/06/030. arXiv: hep-ph/0204343.

[137] Gert Moliere. "THEORY OF SCATTERING OF FAST CHARGED PARTICLES: PART II. PLURAL AND MULTIPLE SCATTERING". In: (Oct. 1947).

[138] P. Aurenche, F. Gelis, and H. Zaraket. "A Simple sum rule for the thermal gluon spectral function and applications". In: *JHEP* 05 (2002), p. 043. DOI: 10.1088/1126-6708/2002/05/043. arXiv: hep-ph/0204146.

[139] R. Baier et al. "Quenching of hadron spectra in media". In: *JHEP* 09 (2001), p. 033. DOI: 10.1088/1126-6708/2001/09/033. arXiv: hep-ph/0106347.

[140] Carlos A. Salgado and Urs Achim Wiedemann. "Calculating quenching weights". In: *Phys. Rev. D* 68 (2003), p. 014008. DOI: 10.1103/PhysRevD.68.014008. arXiv: hep-ph/0302184.

[141] Miklos Gyulassy et al. "Jet quenching and radiative energy loss in dense nuclear matter". In: (Feb. 2003). Ed. by R. C. Hwa and X. N. Wang. DOI: 10.1142/9789812795533_0003. arXiv: nucl-th/0302077.

[142] Magdalena Djordjevic and Ulrich W. Heinz. "Radiative energy loss in a finite dynamical QCD medium". In: *Phys. Rev. Lett.* 101 (2008), p. 022302. DOI: 10.1103/PhysRevLett.101.022302. arXiv: 0802.1230 [nucl-th].

[143] Xin-Nian Wang and Miklos Gyulassy. "Gluon shadowing and jet quenching in A + A collisions at s**(1/2) = 200-GeV". In: *Phys. Rev. Lett.* 68 (1992), pp. 1480–1483. DOI: 10.1103/PhysRevLett.68.1480.

[144] Eric Braaten and Agustin Nieto. "Effective field theory approach to high temperature thermodynamics". In: *Phys. Rev.* D51 (1995), pp. 6990–7006. DOI: 10.1103/PhysRevD.51.6990. arXiv: hep-ph/9501375 [hep-ph].

[145] Jorge Casalderrey-Solana and Derek Teaney. "Transverse Momentum Broadening of a Fast Quark in a N=4 Yang Mills Plasma". In: *JHEP* 04 (2007), p. 039. DOI: 10.1088/1126-6708/2007/04/039. arXiv: hep-th/0701123 [hep-th].

[146] Simon Caron-Huot. "O(g) plasma effects in jet quenching". In: *Phys. Rev. D* 79 (2009), p. 065039. DOI: 10.1103/PhysRevD.79.065039. arXiv: 0811.1603 [hep-ph].

[147] Jacopo Ghiglieri and HyungJoo Kim. "Transverse momentum broadening and collinear radiation at NLO in the $\mathcal{N} = 4$ SYM plasma". In: *JHEP* 12 (2018), p. 049. DOI: 10.1007/JHEP12(2018)049. arXiv: 1809.01349 [hep-ph].

[148] Peter Brockway Arnold and Wei Xiao. "High-energy jet quenching in weakly-coupled quark-gluon plasmas". In: *Phys. Rev. D* 78 (2008), p. 125008. DOI: 10.1103/PhysRevD.78.125008. arXiv: 0810.1026 [hep-ph].

[149] M. Laine. "A non-perturbative contribution to jet quenching". In: *Eur. Phys. J. C* 72 (2012), p. 2233. DOI: 10.1140/epjc/s10052-012-2233-5. arXiv: 1208.5707 [hep-ph].

[150] Carlota Andres, Fabio Dominguez, and Marcos Gonzalez Martinez. "From soft to hard radiation: the role of multiple scatterings in medium-induced gluon emissions". In: *JHEP* 03 (2021), p. 102. DOI: 10.1007/JHEP03(2021)102. arXiv: 2011.06522 [hep-ph].

[151] Paul Caucal et al. "A new pQCD based Monte Carlo event generator for jets in the quark-gluon plasma". In: *PoS* HardProbes2018 (2019). Ed. by David d'Enterria, Andreas Morsch, and Philippe Crochet, p. 028. DOI: 10.22323/1.345.0028. arXiv: 1812.05393 [hep-ph].

[152] Wei Chen et al. "Effects of jet-induced medium excitation in γ-hadron correlation in A+A collisions". In: *Phys. Lett. B* 777 (2018), pp. 86–90. DOI: 10.1016/j.physletb.2017.12.015. arXiv: 1704.03648 [nucl-th].

[153] J.H. Putschke et al. "The JETSCAPE framework". In: (Mar. 2019). arXiv: 1903.07706 [nucl-th].

[154] Bjoern Schenke, Charles Gale, and Sangyong Jeon. "MARTINI: An Event generator for relativistic heavy-ion collisions". In: *Phys. Rev. C* 80 (2009), p. 054913. DOI: 10.1103/PhysRevC.80.054913. arXiv: 0909.2037 [hep-ph].

[155] L. Adamczyk et al. "Measurements of jet quenching with semi-inclusive hadron+jet distributions in Au+Au collisions at $\sqrt{s_{NN}} = 200$ GeV". In: *Phys. Rev. C* 96.2 (2017), p. 024905. DOI: 10.1103/PhysRevC.96.024905. arXiv: 1702.01108 [nucl-ex].

[156] A. Adare et al. "An Upgrade Proposal from the PHENIX Collaboration". In: (Jan. 2015). arXiv: 1501.06197 [nucl-ex].

[157] Tianyu Dai et al. "Parton energy loss in a hard-soft factorized approach". In: (Dec. 2020). arXiv: 2012.03441 [hep-ph].

[158] Mark C. Abraao York et al. “UV cascade in classical Yang-Mills theory via kinetic theory”. In: *Phys. Rev. D* 89.7 (2014), p. 074036. DOI: 10.1103/PhysRevD.89.074036. arXiv: 1401.3751 [hep-ph].

[159] John P Boyd. *Chebyshev and Fourier spectral methods*. Courier Corporation, 2001.

Acknowledgment

> "*The Holy Quran enjoins us to reflect on the verities of Allah's created laws of nature; however, that our generation has been privileged to glimpse a part of His design is a bounty and a grace for which I render thanks with a humble heart.*"– Abdus Salam

I truly believe in what A. Salam said, and I feel extremely grateful to Allah for not only being born in this golden age of high-energy physics but also being able to discover it as a passion first and now a career.

Certainly, learning by myself would not be enjoyable, and I would like to take the opportunity to express my appreciation to my supervisor Soeren Schlichting. I am thankful that I have met such an energetic physicist, with whom my three years of work were very pleasant. Throughout my stay in Bielefeld, he introduced me to this research through many insightful discussions and supported me in different aspects. I also would like to thank him for pushing me to give talks and attend numerous conferences and schools, which were important to expand my knowledge. I will stay eager to work together with him again on future projects.

Furthermore, I had the pleasure to work with insightful physicists as collaborators, I would like to thank Yacine Mehtar-Tani, Guy D. Moore and Niels Schlusser for various discussions and important insights, their contribution to this work is much appreciated. I am saddened that I did not have the chance to work in person with them, but I look forward to a more traditional collaboration in the future.

I would like to express my gratitude to Carsten Greiner with whom I had vital PhD committee meetings. I am thankful for his contribution and insightful discussions, forcing me to think about the bigger picture of this project. Moreover, I thank Nicolas Borghini for agreeing to be a second referee for this thesis and I hope he is enjoying this reading.

I acknowledge support by the Deutsche Forschungsgemeinschaft (DFG, German Research Foundation) through the CRC-TR 211 'Strong-interaction matter under extreme conditions'– project number 315477589 – TRR 211. Numerical computations were performed using the Paderborn Center for Parallel Computing (PC2) and the National Energy Research Scientific Computing Center (NERSC), a DOE Office

of Science User Facility supported by the Office of Science of the U.S. Department of Energy under Contract No. DE-AC02-05CH1123.

Additionally, I would like to thank my colleagues from the non-equilibrium QCD group: Xiaojian Du, Frederic Klette, Stephan Ochsenfeld, Philip Plaschke, Pragya Singh and Clemens Werthmann for interesting discussions and for contributing to such a comfortable (virtual) working environment. A special thanks is dedicated to Pragya Singh, with whom I found a pleasant company in long trips to far away conferences.

I am thankful for the administrative support I received from Gudrun Eickmeyer, Irene Kehler, Susi v. Reder and the international office of Bielefeld University who made living in a country without speaking its language much easier.

My journey to physics was conceived much before this thesis and for that I must thank my parents Latifa Mouradi and Jaouad Soudi, I am grateful for their encouragement and support without which I would not be here. I am also thankful for their devotion to provide me with such a good education by making knowledge essential throughout my upbringing[1]. Additional support I received was from my sisters Najoua and Zineb, who helped me in various stages of my life and to whom I am immensely grateful. Last but not least, I am of course very grateful for the huge support I received from the person who became my wife within these three years. Gintarė, I especially thank you for being there for me in these times, home-office during the pandemic would not have been as enjoyable without you.

[1] Mother, I am sorry this thesis is about physics not medicine :).

Versicherung

Name: Soudi

Vorname: Ismail

Ich versichere, dass ich diese Doktorarbeit selbständig verfasst und keine anderen als die angegebenen Quellen benutzt habe.
Die den benutzten Quellen wörtlich oder inhaltlich entnommenen Stellen habe ich als solche kenntlich gemacht.
Diese Versicherung gilt auch für alle gelieferten Datensätze, Zeichnungen, Skizzen oder grafischen Darstellungen.
Des Weiteren versichere ich, dass ich das Merkblatt zum Umgang mit Plagiaten (http://phoenix.wiwi.uni-bielefeld.de/organisation/pamt/uploads/PlagiatInfoBlattStudenten.pdf) gelesen habe.

Bielefeld, den 12. August 2021

Unterschrift